Title
Improving RR Lyrae Distance Indicators Through Instrumentation, Observation, and Calibration

Author
Klein, Christopher Robert

Publication Date
2014

Peer reviewed|Thesis/dissertation

Improving RR Lyrae Distance Indicators Through Instrumentation, Observation, and Calibration

By

Christopher Robert Klein

A dissertation submitted in partial satisfaction of the

requirements for the degree of

Doctor of Philosophy

in

Astrophysics

in the

Graduate Division

of the

University of California, Berkeley

Committee in charge:

Professor Joshua S. Bloom, Chair
Professor Daniel Kasen
Professor John Rice

Spring 2014

Improving RR Lyrae Distance Indicators Through Instrumentation, Observation, and Calibration

Abstract

Improving RR Lyrae Distance Indicators Through Instrumentation, Observation, and Calibration

by

Christopher Robert Klein

Doctor of Philosophy in Astrophysics

University of California, Berkeley

Professor Joshua S. Bloom, Chair

Due to technological limitations and peculiarities of Nature, classes of astronomical distance indicators are applicable only in specific distance ranges. The Cosmic Distance Ladder is the framework by which we link together distance indicators, climbing from one rung to the next, in order to measure physical distance on an absolute scale. The object of this dissertation is one category of distance indicators, called RR Lyrae pulsating variable stars, which has commanded substantial scientific study for more than a century.

RR Lyrae stars are low mass ($M \approx 0.7$ $M_\odot$), old (age $> 10^{10}$ yr) Population II objects that are found mixed in with any stellar population of requisite age. They are unstable to radial harmonic oscillations (pulsations) because of their specific mass, metallicity content, and interior composition. It has been empirically determined, and theoretically justified, that the pulsation periods of individual RR Lyrae stars are correlated with their intrinsic luminosity; hereafter referred to as the RR Lyrae period–luminosity relation. Thus, if one can measure the period of a star (a relatively straightforward task given sufficient observations), then one can use that star as a standard candle and infer its distance.

The work in this dissertation is aimed at improving our understanding of the period–luminosity relation of RR Lyrae stars, and particularly at improving the precision of RR Lyrae distance measurements. By leveraging (and advancing) new observational facilities, gathering an abundance of new classical observations, and developing new statistical methods to combine a wealth of multi-wavelength data, this goal has been accomplished. In this dissertation I describe the involved methodology and report distances to a calibration sample of 134 RR Lyrae stars with a median fractional distance error of 0.66 per cent.

In the following chapters I describe the arc of this research. First, I present an instrumentation development project that contributed to a new simultaneous multi-band imaging camera which is well-suited to study RR Lyrae stars and accumulate the invaluable near-infrared photometry necessary for highly-precise distance measurements. Then, I present a series of RR Lyrae period–luminosity relation studies that iteratively combine more and more

data (increasing both in calibration sample size and number of wavebands) while simultaneously developing the necessary statistical models and computational methods. Finally, as an application of the results of these earlier investigations, I combine catalog data with new, longer-wavelength observations of the Large Magellanic Cloud (LMC) to measure the three-dimensional shape of the distribution of RR Lyrae stars in the LMC and derive a new distance measurement to the LMC of 50.2482 ± 0.0546 (statistical) ± 0.4628 (systematic) kpc, which is a fractional distance error of 1.03 per cent.

To those who come after, may this work be of some use.

Contents

List of Figures

List of Tables

Acknowledgments

First and foremost, I would like to acknowledge and thank my advisor, Professor Joshua Bloom, for his support, guidance, and scientific mentorship. When I found myself satisfied with my progress on a project or my approach to an analysis problem, after explaining it to Josh he would, more often than not, easily refer me to an improved method or identify some overlooked line of inquiry. His scientific adaptability and willingness to plunge into the trenches during crunch time serves as an inspiring example for me. I am also grateful for the observing opportunities made possible through membership in the Bloom research group, particularly through my involvement with PAIRITEL.

I also happily acknowledge the assistance and comradeship of other Bloom research group members. When I was still new and learning the ropes I constantly called upon Dan Starr's technical expertise and limitless patience. Nat Butler and Brad Cenko both freely provided guidance and advice, and I am gladdened to have continued collaborations with each of them after they were promoted out of the postdoc holding pattern. Dan Perley has been a great friend and role model (and a dependable StarCraft II teammate). Adam Miller, in addition to being an exceptional observing companion, was always happy to discuss research and brought a valuable outside perspective to much of my RR Lyrae work. I have relied consistently on my good friend and classmate Adam Morgan for empathetic commiseration.

The research presented in this dissertation would not have been possible without the *Wide-field Infrared Survey Explorer* and the fantastic data catalogs produced by the NASA/IPAC Infrared Science Archive. I specifically thank *WISE* team members Peter Eisenhardt, Ned Wright, Roc Cutri, and Doug Hoffman.

I thank the support staff at the Fred Lawrence Whipple Observatory (home of PAIRITEL), particularly Wayne Peters, Ted Groner, Perry Fredkin, Mike Calkins, and Emilio Falco. These guys were vital to the maintenance and operations of PAIRITEL, which provided important light curve data for my research.

I am grateful for my community of friends and support structure in Berkeley. My officemate (and cubemate) Aaron Lee has been a reliable friend and, as a brilliant theorist, has always been willing to take a look at math which stumped me. My housemates Kasey Lindsay, Travis Ford, and Scott Konishi have been my second family. Charles and Becky Milzchansen have provided invaluable respite from the research grind through nearly-weekly Games Nights, and they have also served as an encouraging example of the joyful life that awaits after graduate school. Amber Janda has been a supportive, loving, and tolerant com-

panion and has immeasurably enhanced my quality of life. I always knew I had the capacity to love a woman more than astronomy, and I am very relieved to have found her before becoming even more curmudgeonly.

Of course, my greatest debt of gratitude is due to my parents, Robert and Regina. They gave me the foundation and support to pursue my dreams, and the childhood character-building experiences to prepare me for the journey. I am so fortunate to have them. I like to think that I can take most of the credit for my accomplishments, but, honestly, my amazing and dedicated parents have been a tremendous advantage.

Shout out to Peter Williams and thanks for providing the awesome ucastrothesis LaTeX template with which this dissertation was typeset.

Chapter 1

Introduction

1.1 Preface

The main goal of astronomy, maybe more so than any other scientific discipline, is to study the Universe – literally everything except our own terrestrial speck – in the hopes of understanding our place, of putting humanity in context. This is accomplished by investigating extreme and unusual physical phenomena; cataloging the immense diversity of planetary, stellar, nebular, and galactic systems; and probing cosmic history to unravel the origins of everything we observe in the present and predict how the Universe will evolve in the future. Of all the axes on which we study the Universe and our position within it all, the most direct and informative, and often the most difficult, is relative three-dimensional physical location. Where does the Earth exist within the Solar System? Where does our sun exist within the Milky Way? What is the distribution of our neighboring galaxies within the Local Group?

The history of naked-eye astronomy is dominated by observations of stellar positions on the two-dimensional celestial sphere, a field called astrometry (the mapping of stars). Attempts were made to infer a three-dimensional map of the Universe from these two-dimensional data, and they were woefully inadequate, leading to a misguided view of the scale and distribution of matter in the Universe (see Fig. 1.1). Advances in instrumentation and methodology allow us to now also measure distance and formulate a true three-dimensional map of the Universe. Compare Fig. 1.1 with Fig. 1.2, a face-on map of the Milky Way produced in 2008 by Robert Hurt of the Spitzer Science Center.

We now have accurate data informing our astrometric maps, but the precision of our distance measurements decreases significantly with increasing distance (not just in absolute error, but also in fractional error). Besides their cartographic use, distance measurements are necessary to place the physical size and luminosity of astronomical objects on an absolute scale. To precisely convert our observations of an object's angular size and apparent brightness into physical size and intrinsic luminosity, we need a precise distance to the object of interest. The aim of the research conducted as part of this dissertation is to significantly improve one important method by which astronomical distances are measured.

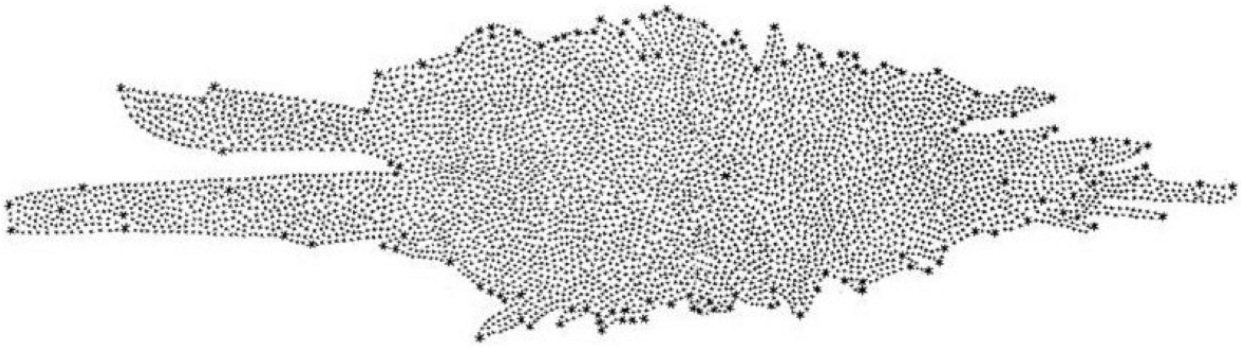

Figure 1.1: William Herschel's map of stars within the Milky Way, published in Herschel (1785). The larger black star to the right of center is the Sun.

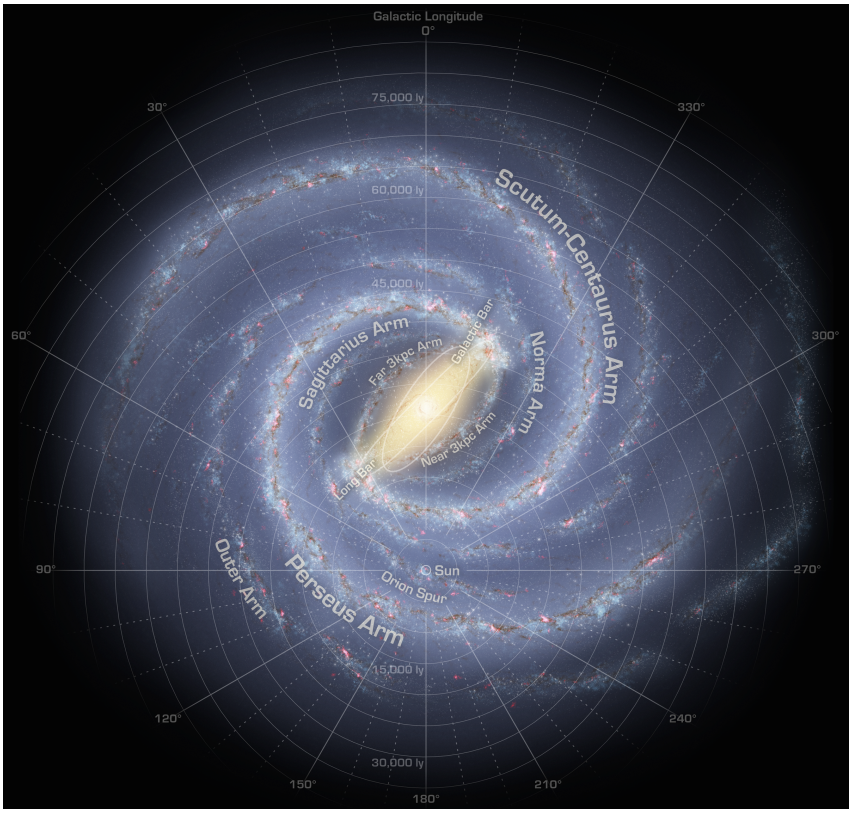

Figure 1.2: Robert Hurt's annotated map of the Milky Way produced in 2008. The Sun is noted at the center of the coordinate system. This illustrated map incorporates ground-based optical imaging from a variety of telescopes and surveys, ground-based near-infrared imaging (primarily from the Two Micron All Sky Survey), space-based mid-infrared imaging from the *Spitzer Space Telescope*, and ground-based radio-telescope surveys (primarily at 20 cm) of Milky Way gas. Image accessed from http://www.spitzer.caltech.edu/images/1925-ssc2008-10b-A-Roadmap-to-the-Milky-Way-Annotated-. Credit: NASA/JPL-Caltech/R. Hurt (SSC/Caltech).

1.2 Cosmic Distance Ladder

Over the years a cornucopia of astronomical distance measuring methods have been developed, many based upon unique classes of objects with well-understood *a priori* physical sizes or intrinsic luminosities (the former are called standard rulers and the latter standard candles). No single method is applicable at all distances. In fact, most methods can only give relative distances within their operating range. To measure the absolute distance to objects outside the Solar System we must calibrate the methods used for farther distances by using the findings of the methods applicable at closer distances. This system is called the Cosmic Distance Ladder because the higher rungs are propped up by the lower rungs, and they all work together to allow us to figuratively reach out towards distant stars.

Applications of the Cosmic Distance Ladder vary depending on the included methods or distance indicators. However, essentially all astronomical distance measurements are rooted in radar measurements to Solar System planets (defining the astronomical unit, AU, very precisely) and then trigonometric parallax measurements (which define the parsec based upon the radius of the Earth's orbit around the Sun). One parsec is thusly

$$1 \text{ pc} = \left(60\frac{\text{arcsec}}{\text{arcmin}}\right) \times \left(60\frac{\text{arcmin}}{\text{deg}}\right) \times \left(\frac{180 \text{ deg}}{\pi \text{ rad}}\right) \text{ AU} = 206,264.806 \text{ AU}. \tag{1.1}$$

Trigonometric parallax is the the most precise astronomical distance measuring method, but it is technologically limited by the ability of our instruments to measure the exact angular positions of point sources. In the early 1990s the European Space Agency's *Hipparcos* satellite measured parallax angles for more than one hundred thousand nearby stars (catalog published in Perryman & ESA 1997). The median accuracy of its parallax angle measurements was slightly better than 1 milliarcsec. In other words, *Hipparcos* parallax measurements are only reliable out to about 1 kpc in distance. In December 2013 the ESA launched *Gaia* (Clark & Quartz 2012), which is expected to release a final catalog in 2021 with fractional distance errors of less than 1 per cent for 20 million stars within 3 kpc. *Gaia* will determine the distances to an additional 200 million (fainter/farther) stars with 10 per cent error (up to about 10 kpc in distance).

While parallax is indisputably the most direct method for nearby distance measurement within the Milky Way, there is no foreseeable technical advance that can provide for the application of trigonometric parallax to more distant galaxies. Thus, parallax serves as an excellent local distance method and is vitally important for calibrating (or anchoring) the next rung of the Cosmic Distance Ladder, called primary distance indicators.

The focus of this dissertation is one class of primary distance indicator called RR Lyrae pulsating variable stars. RR Lyrae stars have well-known *a priori* mean intrinsic luminosities (which are calibrated using parallax measurements), and so they can be used as standardizable candles to measure their distance. Fig. 1.3 illustrates a Cosmic Distance Ladder that is anchored with trigonometric parallax and uses RR Lyrae stars to extend out to neighboring galaxies. The RR Lyrae stars are then used to calibrate the Tip of the Red Giant Branch

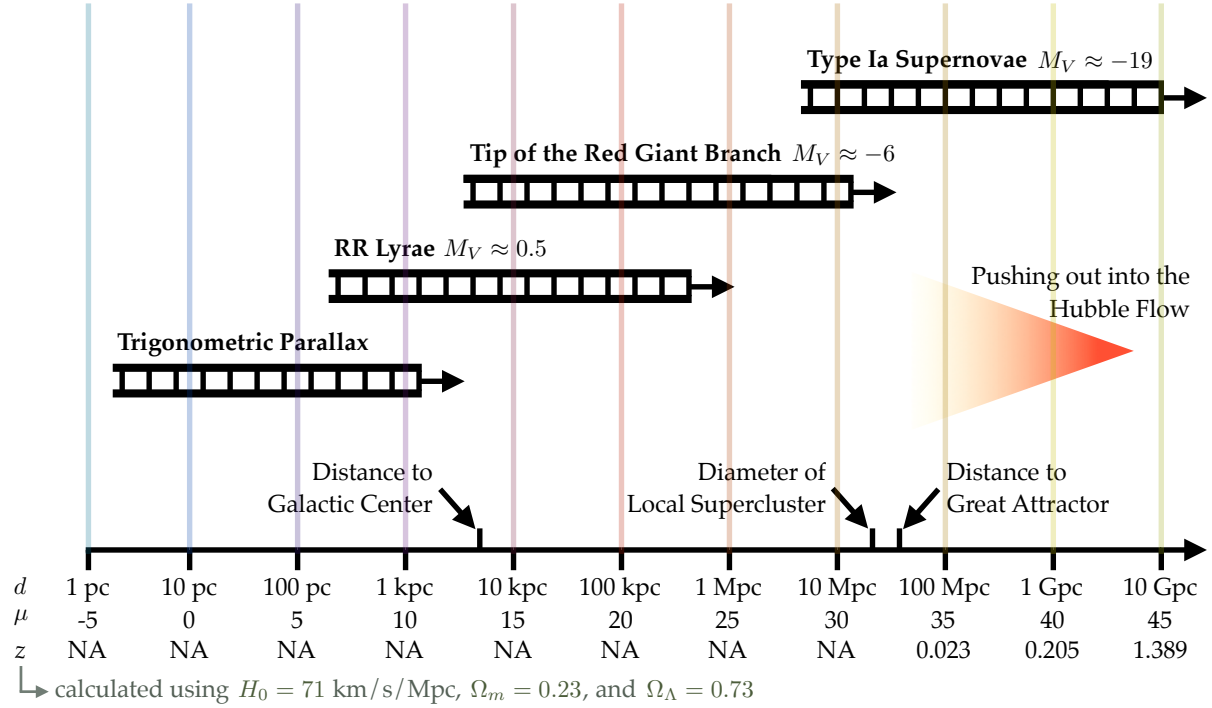

Figure 1.3: Selected distance measurement methods forming an RR Lyrae-based Cosmic Distance Ladder. See Webb (1999) for an extensive, if slightly dated, review of distance measurement methods and the variety of ladder paths to H_0.

method, which in turn is used to calibrate the luminosity of Type Ia supernovae (SNe Ia). SNe Ia are so distant that the rate of universal expansion dominates their observed redshift z, and thus they provide a calibration of physical distance as a function of z and ultimately inform studies of cosmology and Hubble's Constant H_0.

While essentially all Cosmic Distance Ladder applications are rooted in trigonometric parallax, the higher rungs (primary and secondary indicators) can vary based on intended application or preferred methodology. Cepheid variable stars are similar to RR Lyrae stars and are often preferred to RR Lyrae stars in the Cosmic Distance Ladder because they are intrinsically brighter (they are hotter and larger) and can thus be observed at much greater distances. The distance ladders used by Riess et al. (2011) and Freedman et al. (2012) to measure H_0 both employ Cepheids for this very reason. However, because Cepheids are more massive, there are less than 10 per cent as many as there are RR Lyrae stars in most mixed stellar populations. Cepheids are younger than RR Lyrae stars and exist within regions of relatively new star birth, such as the Galactic Disk; RR Lyrae stars are more diffusely positioned in the Disk, Bulge, and Halo. In the nearby regime where both RR Lyrae and Cepheid variable stars are observable (the Milky Way and Local Group galaxies), RR Lyrae stars are much more useful. They essentially provide higher resolution three-dimensional maps (more individual points comprising the maps) and through their shear abundance they

provide significantly higher precision distances to coherent populations (such as star clusters and galaxies).

One additional important reason for improving the precision of RR Lyrae distances is that they can serve as the bridge that enables a distance ladder independent from Cepheids. We can be much more confident of conclusions based upon the Cosmic Distance Ladder if different formulations of the ladder lead to agreeing measurements. Or, perhaps if they disagree (which is always more scientifically exciting) then we have the opportunity to investigate what went wrong and potentially learn something completely unexpected.

1.3 RR Lyrae Stars as Standardizable Candles

RR Lyrae stars are low mass ($M \approx 0.7$ M$_\odot$) stars that have evolved off the Main Sequence to become giants. They exist on the region of the Hertzsprung-Russell diagram called the instability strip of the Horizontal Branch and fuse shell hydrogen and core helium. Their core mass is ≈ 0.5 M$_\odot$, their radii are $4-6$ R$_\odot$, and their surface temperature is $6100-7400$ K. A low mass star requires about 10^{10} yr to evolve from the Zero Age Main Sequence to the RR Lyrae phase, and it exists as an RR Lyrae star for about 10^8 yr. RR Lyrae stars are useable as standard candles because their pulsation period (which for the class ranges between 0.2 and 0.9 d) is correlated with their intrinsic luminosity. This relationship is commonly referred to as the period–luminosity relation, or period–magnitude relation if considering brightness as measured in one designated waveband. The specifics of this relationship will be discussed and investigated in the ensuing chapters, but for now I describe the physics and nomenclature of standard candles and the RR Lyrae pulsation mechanism. Both Preston (1964) and Smith (1995) provide excellent reviews of RR Lyrae pulsating variable stars for the reader desiring further detail.

1.3.1 RR Lyrae Pulsation Mechanism

The pulsation of RR Lyrae variable stars is caused by the κ-mechanism, also called the Eddington Valve. It is named after κ because it is a valve that operates by changing opacity within the star (opacity being traditionally represented by the Greek letter κ). The opacity is related to density and temperature through Kramer's opacity law, $\kappa \propto \rho T^{-7/2}$. In most stars Kramer's law means that a compressed layer of stellar material will actually have a lower opacity due to the temperature rise associated with the compression. However, in RR Lyrae stars and other pulsating variables the heat generated during a layer's compression is absorbed by ionizing a species. For RR Lyrae stars this is the second ionization of helium (He II to He III), but the specific ionizing species varies for different variable classes. This ionization permits the layer to compress while increasing in opacity, and thus trap or store up energy beneath it. The sequential diagram shown in Fig. 1.4 illustrates this cyclical process and the steps are described below.

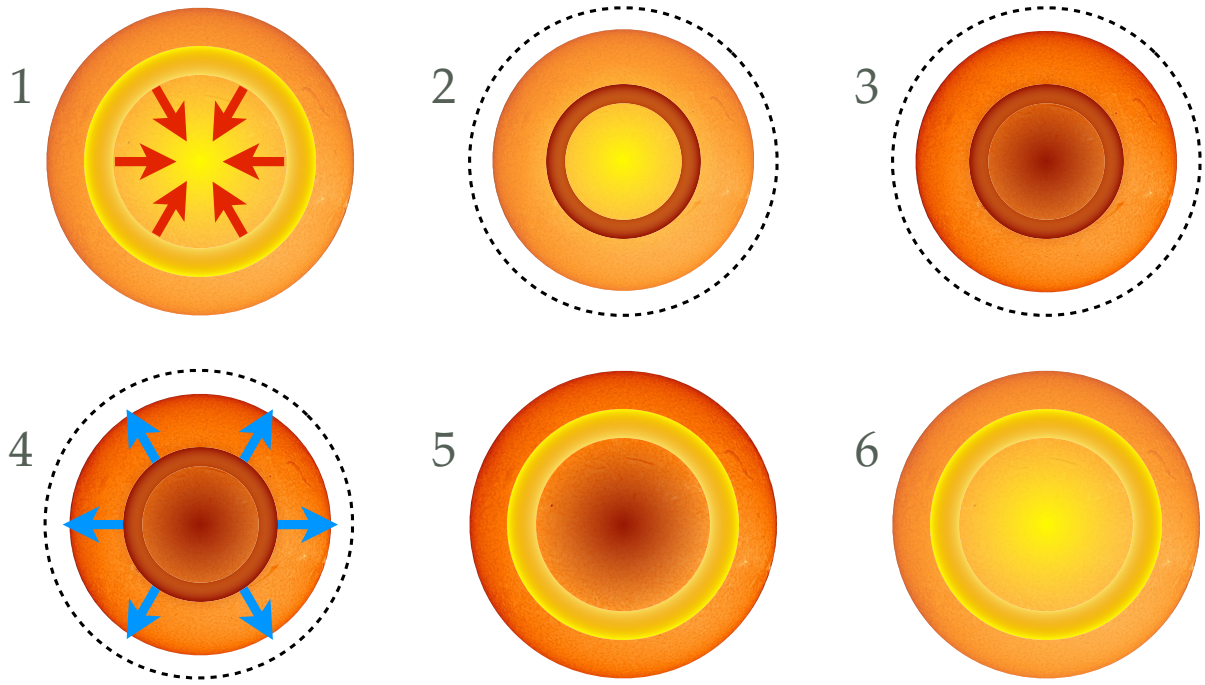

Figure 1.4: Schematic of the RR Lyrae pulsation cycle, driven by the κ-mechanism. The enumerated stages are described in the text.

1. At one point in the pulsation cycle, a layer of stellar material loses support against the star's gravity and falls inward.

2. This inward motion tends to compress the layer, which gains energy and ionizes He II to He III. Thus, during the infall the layer's density increases while the temperature remains relatively constant, and the opacity increases.

3. Since radiation diffuses more slowly through this now higher-opacity layer, heat builds up beneath it. The stored up energy is represented by the redder glow.

4. As energy is built up below the layer, the pressure rises and begins pushing outwards. The luminosity peaks shortly after the star begins expanding.

5. As it moves outwards, the layer expands, loses internal energy (He III captures free electrons to become He II), and becomes more transparent to radiation.

6. Energy can now escape from below the layer and pressure beneath the layer drops. This then leads the layer to fall inwards again and the cycle repeats.

1.4 Applications

1.4.1 Local Milky Way Mapping

Because RR Lyrae stars are old and common, they are excellent tracers of stellar mass distribution. Eyer et al. (2012) predicts $\sim$ 100,000 RR Lyrae stars in the Milky Way will be detected by *Gaia*, but the third phase of the Optical Gravitational Lensing Experiment (OGLE III, Udalski et al. 2008a,b; Soszyński et al. 2009) identified more than 20,000 RR Lyrae stars in the Large Magellanic Cloud (LMC) alone. The LMC is a nearby ($d \approx 50$ kpc) galaxy with less than 1 per cent the mass of the Milky Way. Assuming similar stellar initial mass functions and star formation histories for the Milky Way and the LMC, the OGLE findings imply the existence of 2 million Milky Way RR Lyrae stars, of which *Gaia*, an optical telescope with collecting area 0.725 m^2, will only detect the brightest 5 per cent. In the 2020s many of these extra 1.9 million RR Lyrae stars will be detected by the Large Synoptic Survey Telescope (LSST) and, particularly in the highly extincted Galactic mid-plane, by the *Wide-Field Infrared Survey Telescope* (*WFIRST*).

Gaia will be fantastic for mapping the near side of the Milky Way within about 5 kpc, but, due to optical extinction through the Galactic Plane, it will not be able to provide precise distance measurements for targets near the Galactic Center, or any detections at all for mid-plane targets in the far side of the Galaxy. Infrared observations of RR Lyrae stars, however, will be able to provide highly precise distances to populations throughout the Milky Way. In the following chapters I demonstrate how *Hipparcos* and *Hubble Space Telescope* (*HST*) parallax distances can be used to calibrate the RR Lyrae period–luminosity relation and measure the distances to individual RR Lyrae stars with better than 1 per cent fractional error. In the near future similar period–luminosity relation calibrations will be possible with highly-precise nearby RR Lyrae distances furnished by *Gaia*.

There are substantial and diverse science goals which will be advanced by Milky Way mapping via RR Lyrae stars, an obvious general benefit being higher precision distances for clusters and groupings of stars that are interesting in their own right. The most important benefit may be that a three-dimensional map of RR Lyrae stars could be used to produce a three-dimensional dust map of the Milky Way. This would enable accurate and independent extinction corrections for brightness measurements of targets embedded within the Galaxy (as opposed to the dust maps of Schlegel et al. 1998 and Schlafly & Finkbeiner 2011 which provide the extinction along an entire line of sight, including that from dust behind a target Milky Way object). An accurate understanding of the distribution of foreground dust is increasingly becoming necessary for experiments and surveys attempting to make precise cosmological measurements (see, for example, the recent BICEP2 results presented in BICEP2 Collaboration et al. 2014). In addition to this immensely useful practical application, such a three-dimensional dust map would facilitate investigations of how dust is distributed in the Milky Way, helping us to understand dust formation and destruction processes.

1.4.2 Distances to Neighboring Galaxies

Although RR Lyrae stars are relatively dim compared to other distance indicators ($L_{\rm RRL} \approx 40$ L$_\odot$ and $L_{\rm Cepheid} \approx 20,000$ L$_\odot$), they are sufficiently luminous for easy detection in neighboring galaxies (within about 100 kpc). The two largest and historically most important neighboring galaxies are the Small and Large Magellanic Clouds (SMC and LMC), at distances of roughly 60 and 50 kpc, respectively. OGLE III identified 24,906 RR Lyrae stars in the LMC (Soszyński et al. 2009) and 2,475 in the SMC (Soszyński et al. 2010a). These systems are far off the Galactic plane and thus suffer little optical extinction. Furthermore, because their individual stars all lie at roughly the same distance, precisely measuring that distance has a wide impact on improving the accuracy of inferred intrinsic luminosities and physical sizes for targets within the Magellanic Clouds.

Besides the Magellanic Clouds, there is increasing interest in studying dwarf galaxies that orbit in the Milky Way Halo at radii of up to ~ 100 kpc (Mateo 1998 presents a review of the field and Bullock 2010 discusses the "missing satellites problem"). Even though RR Lyrae stars are relatively numerous in general, and these old, dormant galaxies typically quenched their star formation more than 10^{10} yr ago, their very low mass supports only a handful of RR Lyrae stars per galaxy. Fortunately, only one RR Lyrae star is needed to infer a precise distance. Furthermore, since these galaxies are so difficult to identify simply by stellar density (clustering on the sky), their easily identified RR Lyrae members (found through time-domain surveys) can help us to find many more of these dim, sparse dwarf galaxies. One interesting application within this field is mapping the tidal disruption streams of dwarf galaxies that are pulled apart by the Milky Way's gravity (Łokas et al. 2013 describes the formation of tidal tails). As a dwarf galaxy's stars are spread out in a tidal arc, its RR Lyrae stars are mixed in, too. By identifying the tidal stream and measuring the three-dimensional positions of RR Lyrae stars embedded in the stream (as is done in Sesar et al. 2010), we can reconstruct the history of the encounter. These types of investigations will help us draw conclusions about the Milky Way's smaller galactic companions as a population, and will also inform our understanding of galaxy formation.

1.4.3 Propagation up the Distance Ladder

As mentioned above, the higher rungs of the Cosmic Distance Ladder depend upon calibrations provided by the lower rungs. Through this process the distance measurement errors of contributing methods (primary indicators) must be factored in to distance measurements made using calibrated secondary indicators. One expression of this is that SNe Ia distances will always be less precise than closer distances determined by RR Lyrae stars, Cepheids, or the Tip of the Red Giant Branch method. It is therefore very important that primary distance indicators are developed to be as precise as possible (or, at least as precise as needed to satisfy the science goals of precision cosmology). Ichikawa & Takahashi 2008 demonstrates how minimization of the error in H_0 is necessary to better constrain other cosmological parameters such as Ω_m, w_0, and w_1.

RR Lyrae stars, through their infrared period–magnitude relations in particular, offer exceptionally precise distance measurements. While it is true that RR Lyrae stars cannot directly calibrate SNe Ia[1], they can precisely calibrate the Tip of the Red Giant Branch method or Cepheid luminosities (in lieu of Cepheid parallax measurements, of which only a handful are currently available). Both of these methods can in turn be used to precisely calibrate SNe Ia luminosities.

The primary indicators in this formulation of the Cosmic Distance Ladder can be calibrated solely with Milky Way targets, but the Magellanic Clouds can (and should) be incorporated as well. Historically the SMC and LMC have been very important stepping-stones for the extension of the Cosmic Distance Ladder out beyond 50 kpc. Because of the scarcity and uncertain optical extinction of Milky Way Cepheids, the SMC and LMC are often studied as anchor calibration points for the Cepheid period–luminosity relation (the Leavitt Law). OGLE III identified 3,361 Cepheids in the LMC (Soszyński et al. 2008) and 4,630 in the SMC (Soszyński et al. 2010b). A significant portion of the errors in deriving Cepheid distances for even farther galaxies is due to uncertainty in the distances to the Magellanic Clouds. In this dissertation I analyze observations of LMC RR Lyrae stars to measure a new, precise distance to the LMC which can be used to better calibrate the Leavitt Law.

The ultimate goal of extending the Cosmic Distance Ladder in this fashion is to support increased precision in derived cosmological parameters, the most significant of which being H_0. Recently a conflict has emerged between measurements of H_0 based on the Cosmic Distance Ladder and the measurement resulting from the Plank Collaboration's analysis of Cosmic Microwave Background data from the *Planck* satellite. The distance ladder-based methods measured H_0 to be 73.8 ± 2.4 km s^{-1} Mpc^{-1} (Riess et al. 2011) and 74.3 ± 2.1 km s^{-1} Mpc^{-1} (Freedman et al. 2012), whereas the *Planck* analysis resulted in a statistically significnatly lower value of 67.3 ± 1.2 km s^{-1} Mpc^{-1} (Planck Collaboration et al. 2013). An independent analysis of the *Planck* data found 68.0 ± 1.1 km s^{-1} Mpc^{-1} (Spergel et al. 2013a), which is still in significant disagreement with the distance ladder-based measurements. Clearly additional study on both sides is merited to resolve this tension and attribute responsibility to poorly understood systematics or, barring that, motivate the development of new physics.

1.5 Outline

In this dissertation I present multiple projects that all contribute towards improved RR Lyrae period–magnitude relations. In Chapter 2 I describe an instrumentation development project I led to support the Reionization And Transients InfraRed (RATIR) camera. UC Berkeley's contribution to RATIR was funded in part through a series of grants from NASA (PI: J. Bloom) and RATIR is being led by former Berkeley postdoc N. Butler (now at Arizona State University). I have been a key member of the instrument team since joining in 2008 November. My main contribution, detailed in Chapter 2, was the development of infrared

[1]SNe Ia are too rare for a sufficiently nearby population to be produced in human timescales.

data-taking software and instrument diagnostic systems. In 2012 April-May I assisted in the installation and commissioning of RATIR on the robotocized 1.5-m Harold Johnson telescope at the Observatorio Astronómico Nacional in San Pedro Mártir, Baja California, México. RATIR has now been successfully operating for two years and, although it was designed for Gamma-Ray Burst followup, it is well-suited for autonomous observations of RR Lyrae stars.

In Chapter 3 I present the first published study of mid-infrared RR Lyrae period–magnitude relations. This work made use of the Preliminary Data Release (PDR) of the *Wide-field Infrared Survey Explorer* (*WISE*), which was made public 2011 April 14. The original manuscript of this study was submitted to The Astrophysical Journal on 2011 April 30. In addition to providing the first calibration of RR Lyrae period–magnitude relations at wavebands between 3 and 12 μm, through this research I also developed a new simultaneous Bayesian linear regression formalism for fitting the period–magnitude relation parameters and the individual star distances.

I provide a technical description of the simultaneous Bayesian period–magnitude relation fitting methodology in Chapter 4. Here I describe the statistical model and the fitting approach in more detail, and also compare the results of the *WISE* PDR study with waveband-independent least squares fits. After the study of Chapter 3 was published on 2011 August 25, new *HST*-based parallax measurements for four of the calibration sample RR Lyrae stars were announced via arXiv e-print on 2011 September 26 (later published as Benedict et al. 2011). In Chapter 4 I also compare the predicted distances from the period–luminosity relation fit performed in Chapter 3 with the improved *HST* parallax measurements and find significant agreement which serves as a strong endorsement of my Bayesian methodology.

After the AllWISE Data Release was made public on 2013 November 13, I rederived new mid-infrared period–magnitude relations using this much larger and improved dataset. The description of this study is presented in Chapter 5. This expanded calibration sample had nearly 70 per cent more RR Lyrae stars, which allowed me to sub-divide the period–magnitude relation fits on RR Lyrae star subclass (fundamental mode RRab stars and first overtone RRc stars).

Chapter 6 describes my multi-year, multi-wavelength investigation of RR Lyrae period–magnitude relations. Between 2009 April and 2013 February I collected photometry data of nearby northern-hemisphere RR Lyrae stars in nine wavebands using the 1.3-m Peters Automated Infrared Telescope (PAIRITEL) and the Lick Observatory Nickel 1-m optical telescope. In this study I combine these observations with the data from *Hipparcos* and *WISE* to simultaneously calibrate 13 band-specific period–magnitude relations and fit for the distances to and color excesses of the 134 RR Lyrae stars in my calibration sample. In support of this analsyis I also substantially augmented the simultaneous Bayesian linear regression methodology to accommodate significantly more data and to also fit for color excess. The median fractional distance error for RR Lyrae stars in my calibration sample is 0.66 per cent.

In Chapter 7 I apply the period–magnitude relations derived in Chapter 6 to fit a new, precise distance to the LMC and study the three-dimensional shape of the distribution of

LMC RR Lyrae stars. To accomplish this I leverage V- and I-band data from the OGLE III catalog of LMC RR Lyrae stars (Udalski et al. 2008b; Soszyński et al. 2009) and combine them with new z-band observations of the LMC made with the Dark Energy Camera (DECam) through a Science Verification program.

In Chapter 8 I discuss the primary conclusions of my dissertation research and consider their implications for the future of RR Lyrae stars as distance indicators.

Chapter 2

Software Solution for Autonomous Observations with H2RG Detectors and SIDECAR ASICs for the RATIR Camera

An earlier version of this chapter was previously published as Proc. SPIE 8453, High Energy, Optical, and Infrared Detectors for Astronomy V, 84532S with coauthors Petr Kubánek, Nathaniel R. Butler, Ori D. Fox, Alexander S. Kutyrev, David A. Rapchun, Joshua S. Bloom, Alejandro Farah, Neil Gehrels, Leonid Georgiev, J. Jesús González, William H. Lee, Gennadiy N. Lotkin, Samuel H. Moseley, J. Xavier Prochaska, Enrico Ramirez-Ruiz, Michael G. Richer, Frederick D. Robinson, Carlos Román-Zúñiga, Mathew V. Samuel, Leroy M. Sparr, Corey Tucker, and Alan M. Watson.[1]

Abstract

The Reionization And Transients InfraRed (RATIR) camera has been built for rapid Gamma-Ray Burst (GRB) followup and will provide quasi-simultaneous imaging in the u, g, r, i, Z, Y, J, and H wavebands. The optical component uses two 2048×2048 pixel Finger Lakes Imaging ProLine detectors, one optimized for the SDSS u, g, and r bands and one optimized for the SDSS i band. The infrared portion incorporates two 2048×2048 pixel Teledyne HgCdTe HAWAII-2RG detectors, one with a 1.7-micron cutoff and one with a 2.5-micron cutoff. The infrared detectors are controlled by Teledyne's SIDECAR (System for Image Digitization Enhancement Control And Retrieval) ASICs (Application Specific Integrated Circuits). While other ground-based systems have used the SIDECAR before, this system also utilizes Teledyne's JADE2 (JWST ASIC Drive Electronics) interface

[1] Klein et al. (2012b): Copyright 2012, SPIE.

card and IDE (Integrated Development Environment). Here we present a summary of the software developed to interface the RATIR detectors with Remote Telescope System, 2nd Version (RTS2) software. RTS2 is an integrated open source package for remote observatory control under the Linux operating system and will autonomously coordinate observatory dome, telescope pointing, detector, filter wheel, focus stage, and dewar vacuum compressor operations. Where necessary we have developed custom interfaces between RTS2 and RATIR hardware, most notably for cryogenic focus stage motor drivers and temperature controllers. All detector and hardware interface software developed for RATIR is freely available and open source as part of the RTS2 distribution.

2.1 Introduction

The Reionization And Transients InfraRed (RATIR) camera is a multi-band imager designed for autonomous, queue-scheduled observing and automatic, rapid photometric identification of high-redshift gamma-ray bursts (GRBs; $z > 8$). The instrument is a collaboration between the University of California at Berkeley, NASA Goddard Space Flight Center (GSFC), and the Instituto de Astronomía of the Universidad Nacional Autónoma de México (UNAM). It is mounted on the 1.5-m Harold Johnson telescope of the Observatorio Astronómico Nacional in San Pedro Mártir, Baja California, México, and is currently in the commissioning process.

RATIR employs three dichroics to simultaneously expose four detectors at wavelengths ranging 0.3 to 1.8 μm. Two of the detectors are 2048 $\times$ 2048 pixel Finger Lakes Imaging (FLI) ProLine cameras with Fairchild 3041 CCDs which operate at optical wavelengths, and two are 2048 $\times$ 2048 pixel Teledyne mercury-cadmium-telluride (HgCdTe) HAWAII-2RG detectors (H2RGs) which operate at near-infrared wavelengths. The dichroics split the light such that the bluest FLI camera operates with a SDSS r filter, although shorter-wavelength and narrow-bandwidth filters can be selected from its filterwheel. The redder FLI camera is permanently mated with a SDSS i filter, and each of the H2RGs are behind split filters, Z/Y and J/H. To minimize dark current and thermal background the FLI cameras are water cooled and the H2RGs are operated in a helium-cooled cryostat. A simplified diagram of the RATIR data-taking and cryostat hardware connections is given in Fig. 2.1. Although the system uses separate computers for optical data-taking (`opticalpc`), infrared data-taking (`irpc`), and cryostat operations (`cryostat`), all of these provide control of their connected hardware to the master telescope control computer, `tcs`.

In this paper we present the software employed and developed to support autonomous observations with RATIR. High-level telescope scheduling, pointing, and operations are coordinated by the open source Remote Telescope System, 2nd Version (RTS2) software (Kubánek et al. 2004)[2], as described in Section 2.2. In Section 2.3 we outline the straight-forward integration of the RATIR FLI cameras with RTS2. In Section 2.4 we detail the software used and developed to expose operating control of the Teledyne SIDECAR ASICs and H2RGs

[2] http://rts2.org/

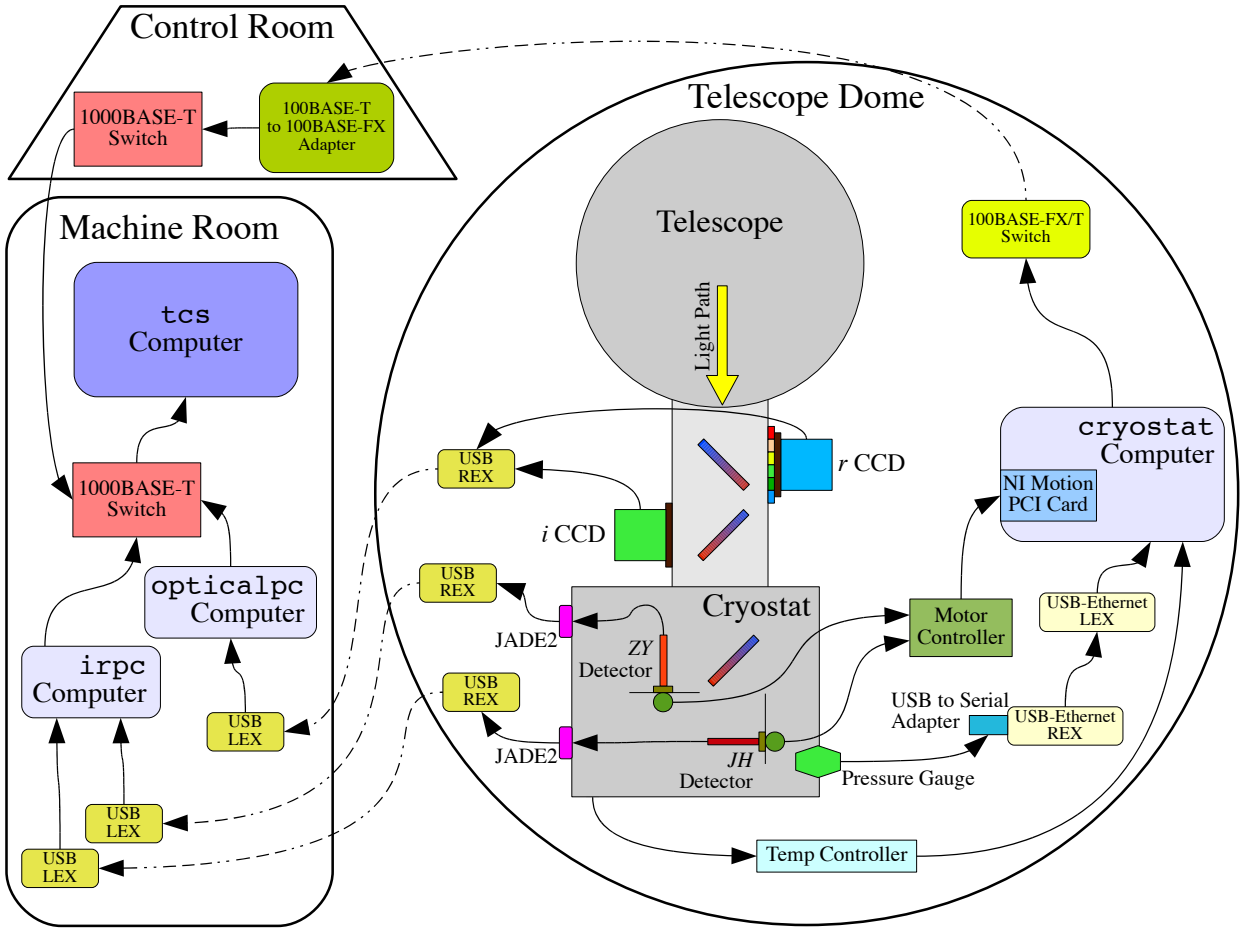

Figure 2.1: Data-taking and cryostat hardware connections. Dot-dashed connector lines indicate fiber optic cables, which electrically isolate the Telescope Dome as a lightning strike precaution. The small green circles in the cryostat represent the cryogenic focus motors, which are attached to the SIDECAR ASICs and H2RGs on the focus stages. The three slanted, red-blue bars along the optical axis represent the three dichroics. Through the computer network connections and using RTS2, the `tcs` computer is capable of operating all data-taking cameras and cryostat subsystems.

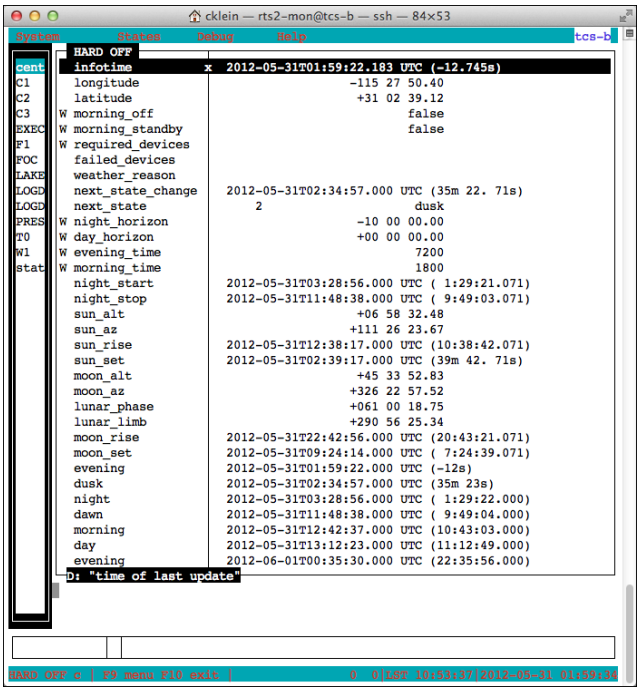

Figure 2.2: RTS2 monitor display, `rts2-mon`.

to RTS2. In Section 2.5 we explain the software developed to operate the cryogenic focus stages and monitor cryostat conditions from within RTS2. Finally, Section 2.6 summarizes the RATIR data-taking software system and its capabilities. A full description of mechanical, optical, electrical, and cryogenic components, as well as the telescope automation and first light results are described elsewhere (see Butler et al. 2012, Farah et al. 2012, Fox et al. 2012, and Watson et al. 2012).

2.2 RTS2 Telescope Control Software

RTS2 is an integrated open source package for remote observatory control under the Linux operating system written in C++. It is introduced in Kubánek et al. (2004), and later improvements are described in Kubánek et al. (2006) and Kubánek (2010). RTS2 is used to coordinate all autonomous scheduling, telescope pointing, data-taking, and instrument hardware monitoring for RATIR. Complex operations such as telescope focusing or dithered observation sequences can be scripted, and the scripts themselves can be procedurally generated. While there is no traditional graphical user interface, the `rts2-mon` program displays a monitor of all the connected devices. An example of this display provided in Fig. 2.2 shows the RATIR system with multiple devices: cameras, focusers, cryostat temperature controller, pressure gauge, etc.

The RTS2 software package is divided into five primary executable types:

1. `rts2-centrald` is the name resolver and observatory housekeeper. This process keeps track of the observatory state (off, standby, or on) and if it is day or night.

2. Individual device dameons (also referred to as device drivers) operate the individual connected devices. They share a common code for communicating over TCP/IP with `rts2-centrald`. Device drivers implement the hardware interacting layer either through their own code or through an external library. Device daemons run dome shutters, telescope mount drives, cameras, and everything else that needs to be controlled autonomously or provide sensor information to RTS2.

3. Executing daemons interacting with the scheduling database to select the next target (`rts2-selector`), execute an observation (`rts2-executor`), process images (`rts2-imgproc`), or wait and process a high-priority target of opportunity (such as for a GRB with `rts2-grb`).

4. Client-side monitoring programs included in RTS2 facilitate development and testing, as well as provide information when a human must check in on the operations of the telescope. The above described `rts2-mon` is an example of this class of RTS2 program, and others that display information through other console and graphics systems are available.

5. The observation scheduling system of RTS2 is based on a PostgreSQL database and the final class of executables handle database querying and updating.

Individual hardware components can be operated by device drivers written to integrate into RTS2. For simple devices, such as the cryostat pressure gauge which uses a common serial port, hardware communication can be completely encapsulated in the RTS2 device driver code. However, complex components require the device driver code to employ lower-level interface libraries to communicate with the hardware.

RTS2 can run in a coordinated fashion on multiple networked computers. RATIR makes use of this capability to divide up functionality among three hardware-interfacing computers (`opticalpc`, `irpc`, and `cryostat`) which all serve their RTS2 devices to the master control computer, `tcs`. To protect the instrument against lightning strikes, we use the dome as a Faraday cage. The `cryostat` computer in the dome provides interfaces only to hardware which must communicate over copper; the `irpc` and `opticalpc` computers communicate with the detectors using optical fiber USB extenders; and the `cryostat` computer is placed on the network using 100BASE-FX Ethernet over optical fibers. This scheme maintains electrical isolation of the dome but allows us to minimize thermal dissipation in the dome.

2.3 Optical Data-taking

Each RATIR optical camera is an off-the-shelf unit from Finger Lakes Imaging called ProLine PL4240. Each uses a 2048×2048 pixel Fairchild 3041 CCD. The i channel camera

has a broadband optimized QE ($> 95\%$ at i), while the r channel has a UV optimized QE ($> 95\%$ in r and $\approx 70\%$ at 300 nm). Both cameras have a shutter (65 mm from Uniblitz) and focus stage (Precision Digital Focuser). The blue-optimized CCD also has a custom FLI filter wheel. Each camera houses a USB 2.0 hub which joins the camera with its shutter, focus stage, and, if available, filter wheel. This greatly simplifies the wiring and allows for both FLI cameras to be operated by `opticalpc` through one fiber optic USB extender pair (LEX for local, and REX for remote, as labeled in Fig. 2.1).

The RTS2 drivers for the FLI cameras were written into RTS2 for prior applications. The hardware communications library is `libfli`. The version used by RTS2 is slightly modified from the official FLI Sofware Development Kit[3] and can be obtained from the RTS2 software repository. Once `libfli` is compiled, RTS2 can be compiled with the option to include support for FLI cameras, focusers, and filter wheels. The devices can then be specified in the RTS2 devices list (`/etc/rts2/devices`) and are then available for use by RTS2. When a FLI CCD is read out, imaging data is transmitted via the USB 2.0 connection as a byte stream and reformatted by RTS2 into a Flexible Image Transport System (FITS) file. RTS2 also automatically adds telescope and instrument metadata into the FITS headers.

2.4 Infrared Data-taking

2.4.1 Infrared Detector Hardware

The HgCdTe H2RG infrared detectors are mated with SIDECAR (System Image, Digitizing, Enhancing, Controlling, and Retrieving) ASIC (Application-Specific Integrated Circuits) readout and control electronics on the Focal Plane Arrays (FPAs). See Loose et al. (2003), Loose et al. (2005), and Dorn et al. (2008) for a detailed description of the ASIC architecture and properties. To provide a computer-compatible interface the SIDECAR ASICs are joined with JWST ASIC Drive Electronics (JADE2) cards that are attached to the outside of the cryostat and provide a USB 2.0 connection. The full H2RG–SIDECAR ASIC–JADE2 system is manufactured by Teledyne Imaging Sensors.

The primary advantage of using the SIDECAR ASIC is that its close proximity to the H2RG array permits a very short analog data transmission path, thus reducing the noise that can accrue before the analog values are digitized. The SIDECAR ASIC performs detector operations and readouts according to microcode (also referred to as assembly code) uploaded from the operating computer system. Through this assembly code a tremendous depth of control over the readout process is exposed to the user.

2.4.2 Teledyne Software

Teledyne provides Windows XP compatible software for interacting with the SIDECAR ASIC and programming the assembly code that runs on the ASIC. The actual interface

[3] `http://www.flicamera.com/software/`

program is the Human Abstraction Layer (HAL) Server. The HAL Server communicates with the JADE2 (and SIDECAR ASIC) over the USB connection, using a QuickUSB Device Driver.

Teledyne also provides an Integrated Development Environment (IDE) for manual operation of the SIDECAR ASIC, and programming and compiling of assembly code. A user can manually set ASIC parameters such as voltages or timing variables through the IDE using a graphical floorplan of the ASIC or by editing the assembly code. The IDE is used to develop and test assembly code and empowers the user to tailor SIDECAR ASIC operations to a specific goal or to meet specific requirements (such as dynamic range, amplifier gain, or bias level). Each time the H2RGs and SIDECAR ASICs are powered up, the IDE must initialize the devices before data-taking can proceed. This initialization process consists of uploading assembly code to the SIDECAR ASIC and firmware to the JADE2. The process takes less than two minutes and can be repeated with different assembly code to configure the detectors for different observing conditions or targets. In practice, however, RATIR will employ a single, vetted assembly code for all data-taking.

One layer above the IDE is the HxRG Socket Server. This is an IDL Runtime Application that presents the user with a data-taking GUI and executes the appropriate commands on the SIDECAR ASIC through the IDE and HAL Server. When a special variant of assembly code, called HxRG, is loaded onto the SIDECAR ASIC the HxRG Socket Server is able to modify many higher-level parameters of the readout electronics, such as clocking mode or gain settings. Furthermore, the HxRG Socket Server can execute arbitrarily complex readout sequences through the Up The Ramp exposure mode. The user can specify the readout sequence parameters to define the sequence of resets, read frames, drop frames, groups, and ramps that make up an exposure. Standard Fowler Sampling is also supported and the IDL code automatically calculates the resultant image in this mode. During an exposure sequence, imaging data is written out to the Windows XP filesystem by the HxRG Socket Server as FITS files with pertinent metadata included in the headers.

Since RATIR is an autonomous observing project, a sophisticated GUI, while beneficial for instrument development, is not necessary during normal operations. The HxRG Socket Server addresses this by providing a TCP/IP interface to all of the functionality present in the GUI. The H2RG–SIDECAR ASIC–JADE2 detector hardware can be initialized, the exposure mode selected, all of the high-level parameters adjusted, and data acquisition controlled through TCP/IP commands sent to the HxRG Socket Server.

2.4.3 RTS2 HxRG Socket Server Interface

To provide control of the SIDECAR ASICs to RTS2 we wrote a new RTS2 device driver for the HxRG Socket Server. At its core, this device driver interfaces with the HxRG Socket Server through TCP/IP. The most common subset of modifiable parameters are supported: exposure mode and associated sequencing parameters, gain, preamp KTC removal, warm/cold test, idle mode, and clocking mode. This device driver is now included in the RTS2 software distribution as `rts2/src/camd/sidecar.cpp`.

In addition to supporting the SIDECAR ASICs with a custom RTS2 device driver, a custom data-taking case was created in RTS2 for these devices. Unlike the FLI cameras which transfer the pixel data to RTS2 directly as byte code, the HxRG Socket Server generates the FITS images itself and saves them in a directory path it creates named after the ASIC identifier, exposure mode, and local exposure date-time (for example, `Z:\data1\H2RG-C001-ASIC-2-32\UpTheRamp\20120515233046`). This convention cannot be changed within the HxRG Socket Server without modifying the IDL source code, which was not made available. Only the top-level directory (`Z:\data1` in the example) can be specified in the HxRG Socket Server System Configuration. To work within these limitations we adapted RTS2 to identify the most recently created data directory and import the pre-made FITS files into the RTS2 system. RTS2 then adds further telescope and instrument metadata to the headers.

2.4.4 IR Data-taking "Blackbox"

For deployment at the telescope the SIDECAR ASIC interface software must run reliably on a "blackbox" system. In case of software crashes or necessary hardware resets, an observatory staff member must be able to restart the software and establish RTS2 control over the two RATIR SIDECAR ASIC devices without actually accessing `irpc`, the computer that serves the infrared camera devices to the master control computer, `tcs`. This is partly to keep the autonomous system simple to restart when needed, but primarily because access to the Teledyne software (on `irpc`) is governed by US International Traffic in Arms Regulations (ITAR), and restricted to authorized personnel only.

All of the Teledyne software for each infrared camera – HAL Server, IDE, and HxRG Socket Server – runs on an emulated Windows XP Operating System (a virtual machine, VM) using VMPlayer[4] on `irpc`. Each of these two VMs is assigned its own internal IP address on the host Linux system, and this is the address that the RTS2 device drivers (which are run on the Linux host) use to communicate with the HxRG Socket Servers. The VMs are assigned USB ports to which the JADE2 cards are connected via a USB-fiber optic extender pair for each camera. The VMs themselves are run from within a Virtual Network Computer (VNC) instance, which permits easy access to the HxRG Socket Servers for US collaborators. Fig. 2.3 illustrates these software connections within `irpc`.

To permit easy imaging data sharing between the Windows XP VMs and the Linux host, two dedicated shared network drives are allocated on `irpc` (`/data1` and `/data2`). These hard drives are also shared with `tcs`, which is where the actual data-taking RTS2 scripts are executed.

A complete SIDECAR ASIC interface software restart can be accomplished through a Linux shell script and a Windows XP automation script (using AutoIt[5]). First, the shell script kills any VNC instances and creates a new VNC on display 1. When the VNC starts up, it is configured to automatically open two instances of VMPlayer running Windows XP VMs, one for each camera. When the Windows XP operating systems boot up, their AutoIt

[4] http://www.vmware.com/products/player
[5] http://www.autoitscript.com/site/autoit/

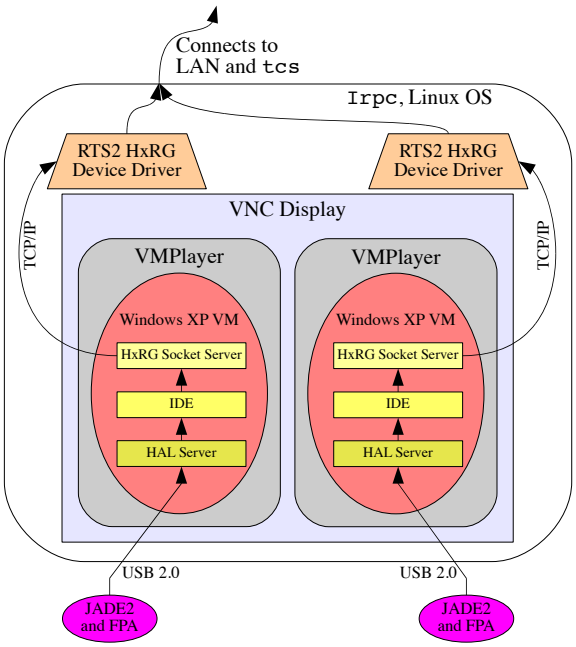

Figure 2.3: Software connections within `irpc` and external links to the FPAs and LAN.

automation scripts start up the HxRG Socket Servers and run a Python script to send the TCP/IP commands to initialize the JADE2 and SIDECAR ASIC hardware for each camera, as well as collect telemetry from the devices for logging. After a suitable wait time for the VMs to initialize the camera hardware, the shell script then starts the RTS2 SIDECAR ASIC device drivers on the Linux host and serves the devices to `tcs`. The SIDECAR ASIC interface software restart shell script is run as a cronjob every ten minutes, but it only proceeds with the actual restart if two text files, `/data1/kill_hxrg` and `/data2/kill_hxrg`, both contain "true". These text files are located on shared drives and accessible from `tcs` so that observatory staff can easily initiate a restart if the infrared cameras are not available as RTS2 devices on `tcs`.

2.5 Cryostat Focus Stages and System Monitoring

2.5.1 National Instruments Focus Motor Controller

The infrared FPAs are mounted on Newport 433 Series cryogenized 1D transport stages driven by ARSAPE AM1524 cryogenic motors. The focus motors are powered by a National Instruments MID-7604 integrated stepper motor power drive and controlled by a National Instruments PCI-7332 motion controller (a Peripheral Component Interconnect card installed within `cryostat`). The PCI-7332 card is connected to the MID-7604 with a proprietary cable that cannot be extended with fiber optic adapters. The MID-7604 is directly connected to each focus motor with four bundled copper wires which run through a port in the cryostat

wall.

Control of the motors is handled fully by the PCI-7332 card through its control of the MID-7604. The MID-7604 supplies motor drive power and provides a manual switch to enable and disable the electrical current to the motors. National Instruments provides documentation for communication with the PCI-7332 motion controller, but poor Linux support.[6] A custom driver for the PCI-7332 motion controller was written into RTS2 for RATIR and it exposes both focus motors through one RTS2 device. The RTS2 driver reads the current motor velocity, stores the current position, and sets acceleration, velocity, and target position parameters for each motor. The PCI-7332 motion controller can store the motor positions only while electrically powered, so RTS2's "autosave" device option is employed to also store motor positions in a text file on `cryostat`'s hard drive.

When powered on, the electrical current in the focus motors introduces additional electronic noise into images captured with the H2RGs and the SIDECAR ASICs. Additionally, the dissipation of this electrical current releases a small amount of heat into the cryostat. To minimize these unwanted effects, the focus motors can be "enabled" only when needed for focussing. The RTS2 driver can command the PCI-7332 card to set an individual motor to be disabled by the MID-7604 power drive. During focus operations the motors will be enabled, but during normal science observations they will be unpowered.

2.5.2 Lakeshore Temperature Controller

For cryostat temperature monitoring and control RATIR uses a Lakeshore Model 340 cryogenic temperature controller with additional 8 Channel Scanner Card and GPIB-USB-HS adapter. The Lakeshore unit's USB adapter provides a convenient USB connection directly to the `cryostat` computer. A RTS2 device driver was written to interface with the Lakeshore 340 through the General Purpose Interface Bus (GPIB). The core functionality of the driver was previously developed to support other Lakeshore models, and thus the driver written for RATIR was primarily an adaptation of this preexisting software to support the expanded feature set of the Model 340.

The Lakeshore Model 340 provides 10 temperature sensors and 2 effective heaters with independent control loops. The RTS2 driver provides access to temperature readings for all 10 of these sensors, as well as the parameters and options that define the 2 control loops. The control loops can operate in multiple different modes: manual PID,[7] open loop, and variants of an autotuned PID. Adjustable parameters include the target setpoint temperature, maximum positive and negative slopes, electrical current and range for the heater, and the P, I, and D values.

Temperature fluctuations at the H2RGs of $\gtrsim 0.01$ K during an exposure ramp introduce non-negligible detector noise. The heater loops are capable of maintaing the infrared detectors at a slightly elevated, but temporally stable temperature to eliminate this thermal

[6] Some motion drivers are available through third parties, but those seems to be outdated and do not work on modern Linux distributions.

[7] proportional-integral-derivative controller feedback mechanism

noise. During commissioning, however, it was found that the H2RG temperature stability meets this requirement without active heating control.

2.5.3 Pressure Gauge

A vacuum is created within the cryostat to assist in maintaining the cryogenic interior temperature. A 925 MicroPirani Vacuum Transducer (pressure gauge) is used to monitor the interior pressure. The pressure gauge range extends down to 10^{-5} Torr, and the cryostat can operate safely at up to 5×10^{-3} Torr. The gauge communicates over a serial (RS232) port. The serial cable is connected to a USB extender pair with a USB-serial adapter, with a USB connection to `cryostat` at the LEX end. A very basic RTS2 device driver was written for the pressure gauge using the standard C++ serial communication library, with the only command being a request for the current pressure reading. To ensure that RTS2 could properly identify the USB-serial adapter, a basic *udev* rule was set up on `cryostat`.

2.6 Summary

We have presented the data-taking and cryostat monitoring software employed and developed to support autonomous observations with RATIR. All of the hardware devices are operated by RTS2, which also coordinates telescope slewing and observation scheduling. We divide the data-taking and cryostat monitoring tasks among RTS2 device drivers run on three computers – `opticalpc`, `irpc`, and `cryostat` – which serve control of their hardware devices to the master telescope control computer, `tcs`. This software system is robust to the loss of any hardware component and is capable of operating a partially functional instrument in the unfortunate and improbable case of inoperable camera subsystems. The RTS2 software developed in this effort has been added to the project's *subversion* repository for distribution to all other telescopes utilizing RTS2.

Acknowledgments

We thank Rob Simcoe of MIT for assistance with identifying the sources of HxRG Socket Server overhead time, John Capone of the University of Maryland for assistance with the RTS2 Lakeshore Model 340 interface, and Jing Chen of Teledyne Imaging Sensors for technical support during the early phases of the project. The automation of the OAN/SPM 1.5-meter Harold Johnson telescope was financed by the Instituto de Astronomía of the UNAM, by UNAM/DGAPA/PAPIIT project 113810, and by CONACyT project INFR-2009-01-122785. Additional funding was provided through CONACyT grant CB-128556. ODF thanks the NASA Postdoctoral Program (NPP) fellowship for financial support. The design and construction of the RATIR instrument was partially financed by NASA grants NNX09AH71G, NNX09AT02G, NNX10AI27G, and NNX12AE66G. This research has made use of NASA's Astrophysics Data System.

Chapter 3

Mid-infrared Period–Luminosity Relations of RR Lyrae Stars Derived from the *WISE* Preliminary Data Release

An earlier version of this chapter was previously published as ApJ 738, 185 with coauthors Joseph W. Richards, Nathaniel R. Butler, and Joshua S. Bloom.[1]

Abstract

Interstellar dust presents a significant challenge to extending parallax-determined distances of optically observed pulsational variables to larger volumes. Distance ladder work at mid-infrared wavebands, where dust effects are negligible and metallicity correlations are minimized, have been largely focused on few-epoch Cepheid studies. Here we present the first determination of mid-infrared period–luminosity relations of RR Lyrae stars from phase-resolved imaging using the preliminary data release of the Wide-Field Infrared Survey Explorer (*WISE*). We present a novel statistical framework to predict posterior distances of 76 well-observed RR Lyrae that uses the optically constructed prior distance moduli while simultaneously imposing a power-law period–luminosity relation to *WISE*-determined mean magnitudes. We find that the absolute magnitude in the bluest *WISE* filter is $M_{W1} = (-0.421 \pm 0.014) - (1.681 \pm 0.147)\log_{10}(P/0.50118\text{ day})$, with no evidence for a correlation with metallicity. Combining the results from the three bluest *WISE* filters, we find that a typical star in our sample has a distance measurement uncertainty of 0.97% (statistical) plus 1.17% (systematic). We do not fundamentalize the periods of RRc stars to improve their fit to the relations. Taking the *Hipparcos*-derived mean V-band magnitudes, we use the distance posteriors to determine a new optical metallicity-luminosity relation which we present in Section 3.5. The results of this analysis will soon be tested by *HST*

[1] Klein et al. (2011): Copyright 2011, American Astronomical Society.

parallax measurements and, eventually, with the *Gaia* astrometric mission.

3.1 Introduction

RR Lyrae pulsating variable stars are standardizable distance indicators at optical and near-infrared wavebands. In V-band, their brightnesses are nearly standard, with a small metallicity dependence and deviation about $\langle M_V \rangle$ of $\sim$0.12–0.15 mag (Hawley et al. 1986; Fernley et al. 1998; Chaboyer 1999; Sandage & Tammann 2006). At near-infrared wavebands RR Lyrae star brightnesses are a well-fit function of pulsation period, with an apparently negligible metallicity dependence (at K-band) and mean scatter from a period-luminosity relation of $\sim$0.15 mag (Longmore et al. 1986; Sollima et al. 2006). The ability to infer distance to an RR Lyrae star is chiefly restricted by the confidence in these empirically derived luminosity-metallicity and period–luminosity relations.

There is good observational and theoretical motivation to believe that infrared photometry offers the ability to derive more tightly constrained period–luminosity relations for pulsational variable stars in general. It has been argued (Madore & Freedman 1998) and demonstrated (Freedman et al. 2008; Feast et al. 2008) that the scatter in these empirical relations is decreased at infrared wavelengths. Madore & Freedman (1998) cite the advantages: (1) The sensitivity of surface brightness to temperature is a steeply declining function of wavelength; (2) The interstellar extinction curve decreases as a function of increasing wavelength (being almost linear with $1/\lambda$ at optical and near-infrared wavelengths); (3) At the temperatures typical of horizontal-branch stars, metallicity effects predominate in the UV, blue, and visual parts of the spectrum, where most of the line transitions occur, with declining effects at longer wavelengths. The overall insensitivity of infrared magnitudes of RR Lyrae, Cepheid, and Mira variables to each of these effects results in decreased amplitudes for individual pulsating variables, as well as a decreased scatter in the apparent period–luminosity relations.

In this paper we present the first published mid-infrared period–luminosity relations for RR Lyrae variables. This is the first such work primarily because the requisite observational data has not existed previously. Since the farther reach of (brighter) Cepheid period–luminosity relations makes their study potentially more influential, the *Spitzer Space Telescope* has been used to derive mid-infrared period–luminosity relations for Galactic (Marengo et al. 2010) and Magellanic Clouds (Madore et al. 2009) Cepheids (the latter making use of SAGE survey data; Meixner et al. 2006; Madore et al. 2009). These studies of Galactic (Magellanic Clouds) Cepheid mid-infrared period–luminosity relations reported best-fit dispersions of $\sim$0.2 mag ($\sim$0.12 mag).

RR Lyrae variables are particularly important local distance indicators because they are more numerous than Cepheids, and are observable within the Galactic disk and halo, within Galactic and some extragalactic globular clusters, and in the halos of neighboring dwarf galaxies (most notably, the LMC). Importantly, RR Lyrae variables can be used as stellar density tracers (e.g., Vivas et al. 2001; Sesar et al. 2010) to map the structure of stellar

distributions.

In this article we derive mid-infrared RR Lyrae period–luminosity relations by analyzing observations of 76 RR Lyrae pulsating variable stars conducted with the Wide-field Infrared Survey Explorer (*WISE*) satellite (Wright et al. 2010) and made available through the preliminary data release of the first 105 days of science data.[2] We use a modified Lomb-Scargle (Lomb 1976; Barning 1963; Scargle 1982) period-finding algorithm to calculate the pulsation periods from both the *WISE* data and the very well-observed *Hipparcos* light curves of the same sources. We derive mean flux-weighted *WISE* magnitudes from the best-fit harmonic models of this Lomb-Scargle analysis; these observed magnitudes, along with the *Hipparcos* estimated periods, are used to estimate the *WISE* period–luminosity relations. The actual period–luminosity relation fitting is conducted through a Bayesian approach using *a priori* distance information and simultaneously fits the W1, W2, and W3 period–luminosity relations. Our methods have general applicability, and can be used to robustly fit period–luminosity relations at other spectral wavebands. Our resulting mid-infrared period–luminosity relations are tightly constrained with absolute magnitude prediction uncertainties as small as 0.016, 0.016, and 0.076 mag at 3.4, 4.6, and 12 μm, respectively.

The paper is outlined as follows. We present a brief description of the *WISE* and ancillary data in Section 3.2, followed by an explanation of our analysis methods in Section 3.3. (In Section 3.7 we demonstrate the viability of period recovery with *WISE* data, and highlight the potential for discovery of new RR Lyrae variables and other short-period variables with the *WISE* single exposure database.) We describe the Bayesian method of deriving mid-infrared period–luminosity relations in Section 3.4 and discuss the results in Section 3.5. Finally, we present conclusions in Section 3.6.

3.2 Data Description

WISE has imaging capabilities in four mid-infrared bands: W1 centered at 3.4 μm, W2 at 4.6 μm, W3 at 12 μm, and W4 at 22 μm. The satellite is in a polar orbit and scans the sky in great circles with a center located at the Sun and with a precession rate of 180° every six months (Wright et al. 2010). *WISE* completes about 15 orbits a day and the field of view of the detectors is 47 arcmin on a side. This configuration allowed *WISE* to scan the entire sky in six months, with a minimum of 8 (median 12) single-frame exposures. Sources near ecliptic poles receive the most repeat coverage in time and sources near the ecliptic have the smallest number of observed epochs. *WISE* was launched on 2009 December 14 and operated until 2011 February 17. This mission duration provided two full scans of the sky. However, the hydrogen coolant ran out in 2010 October, halting data acquisition in the W3 and W4 bands.

The present study was conducted using data from the single-exposure database of the *WISE* preliminary data release, which was made public on 2011 April 14 through the

[2] http://wise2.ipac.caltech.edu/docs/release/prelim/

NASA/IPAC Infrared Science Archive.[3] The preliminary data release includes the first 105 days of mission data and covers about 57% of the sky.

The catalog of RR Lyrae variables used in the present study is derived from work by Fernley et al. (1998). The catalog contains 144 relatively local ($\leq$2.5 kpc) RR Lyrae variables selected from the *Hipparcos* catalog (Perryman & ESA 1997) with color excess and metallicity measurements from previous literature. Of the 144 RR Lyrae variables in our starting catalog, 77 were associated with sources in the *WISE* preliminary data release. We reject one light curve (V*EZLyr) because the reported *WISE* photometry does not indicate a periodic source (using the *Hipparcos* period; the source is also a strong outlier from our period–luminosity relation fits). All target sources, save the prototype RR Lyrae star itself (V*RRLyr), are too faint for *WISE* to produce reliable W4 photometry and so we must ignore the longest wavelength data in the subsequent analysis.

To perform a proper analysis of the mid-infrared period–luminosity relation, in addition to the periods and observed *WISE* magnitudes of each RR Lyrae star, we also need a prior guess of the distance to each object. Here, we describe how we determine a prior distribution on the distance modulus of each RR Lyrae star. First, we compute the *Hipparcos* periods and mean flux-weighted magnitudes ($m_{\rm hip}$) using the same Lomb-Scargle based methods that we apply to the *WISE* light curve data (see Section 3.3). Discrepancies with the published periods of Fernley et al. (1998) were minimal (see Section 3.7). Unlike Sollima et al. (2006), we do not find that the periods of RRc type RR Lyrae variables need to be fundamentalized by adding a constant term ($\Delta \log_{10} P \approx 0.13$) in order to improve the period–luminosity relation scatter. Following Gould & Popowski (1998) we determine values of the apparent Johnson V-band magnitude (m_V) and the effective extinction, $A_{\rm V,eff}$, that differ slightly from Fernley et al. (1998). This is achieved by making use of the line-of-sight extinction from the Schlegel et al. (1998) (SFD) dust maps and by assuming a Galactic scale-height model for the dust (such that not all SFD dust lies in between us and the RR Lyrae star). In particular, we determine an effective extinction for the ith RR Lyrae star in the sample as:

$$E(B-V)_{\rm eff,i} = E(B-V)_{\rm SFD,i}\,(1-\exp[-|z_i|/h])\,, \tag{3.1}$$

where $E(B-V)_{\rm SFD,i}$ is the differential SFD extinction towards source i, z_i is the scale height of ith source above the Galactic plane,[4] and $h = 130$ pc is the exponential scale height assumed for the dust in the disk (Gould & Popowski 1998). To convert $m_{\rm hip}$ to m_V we adopt the prescription from Gould & Popowski (1998):

$$m_{V,i,\rm eff} = m_{\rm hip,i} - X - 0.2E(B-V)_{\rm eff,i} \tag{3.2}$$

where $X = 0.09$ for RRab types and $X = 0.06$ for RRc types. We assume a 15% error on $E(B-V)_{\rm eff,i}$. Finally, we produce an extinction corrected magnitude $m^*_{V,i} = m_{V,i,\rm eff} - A_{V,\rm eff,i}$,

[3] http://irsa.ipac.caltech.edu/

[4] Note that z_i will depend on the value of distance determined, however, we simply use the coordinate information provided by Maintz & de Boer (2005) when available or transform the sky coordinates using the Fernley et al. (1998) distance results when necessary. Our results are not sensitive to the precise value of z_i.

where $A_{V,\mathrm{eff},i} = 3.1 \times E(B-V)_{\mathrm{eff},i}$, and the factor $R = A_V/E(B-V) = 3.1$ from Schultz & Wiemer (1975). These values of extinction-corrected V-band magnitudes (and associated errors) are reported in Table 3.1.

To determine the prior distance modulus, $\mu_{0,i}$, for the ith source, we need a prescription for determining the absolute V-band magnitude given the metallicity of the star (there is no known relationship of period and luminosity at V-band for RR Lyrae variables). We adopt the M_V–metallicity relation given in Chaboyer (1999), where we use the metallicity data as provided in Fernley et al. (1998). Explicitly, the M_V-[Fe/H] relation used is

$$M_V = (0.23 \pm 0.04)([\mathrm{Fe/H}] + 1.6) + (0.56 \pm 0.12). \tag{3.3}$$

The calculated values of $M_{V,i}$ for each source are given in Table 3.1.

Finally, we compute the prior mean of the distance modulus of the ith RR Lyrae star as $\mu_{0,i} = m^*_{V,i} - M_{V,i}$, with the uncertainty in this quantity propagated assuming the errors on $m^*_{V,i}$ and $M_{V,i}$ are Gaussian and uncorrelated. The values of $\mu_{0,i}$ (and $\sigma_{\mu_{0,i}}$) (Table 3.1) represent our best estimates of the distances (and errors) using the body of work on RR Lyrae variables at visual bands *prior* to analyzing the *WISE* data and *prior* to the *Hubble Space Telescope* (*HST*) parallax result on V*RRLyrae itself. Note however that our prior estimate on distance modulus to V*RRLyrae ($\mu_0 = 7.042 \pm 0.125$) is consistent with that found directly from *HST* parallax measurements ($\mu = 7.090 \pm 0.063$; Benedict et al. 2002).

3.3 Light Curve Analysis Methods

In order to determine the period–luminosity relations for *WISE*, we need to calculate an apparent brightness. Following common practice (Fernley et al. 1998; Liu & Janes 1990), we define the brightness of each source as the mean flux, converted to a magnitude. As we expect possible poor phase sampling in the *WISE* data, we use a model — based on a modified Lomb-Scargle algorithm (Richards et al. 2011), which allows for data uncertainty and a mean flux offset — instead of the observed data points, to determine this mean (see Fig. 3.1 for an example). At significant peaks in the periodogram, this model construction attempts to fit as many as 8 harmonic components — at frequencies which are multiples of the fundamental frequency — in addition to the fundamental frequency component. Complex models are penalized using generalized cross validation (e.g., Hastie et al. 2009) to prevent over-fitting. The resulting model curves are smooth, typically dominated by the presence of 4–6 harmonics for *Hipparcos* data, and can be used to calculate the flux integral and its uncertainty. For the case of *Hipparcos*, we find that the difference between our flux estimates and those from Fernley et al. (1998) exhibit an rms scatter of 1.4% with no systematic difference.

Applied directly to the *WISE* data, our period finding framework accurately recovers the majority of the RR Lyrae periods directly from the *WISE* data (see Section 3.7). For all *WISE* mean-magnitude estimates, we force the Lomb-Scargle model to use the best-fit *Hipparcos* periods as the fundamental frequency. We note that our mean-magnitude estimates remain unchanged, within their uncertainties, if we instead use the best-fit *WISE* periods.

Table 3.1: Input into the period–luminosity relation fit.

Name	Class[a]	[Fe/H][a]	Period[b] [d]	$A_{V,\mathrm{eff}}$[c] [mag]	m_V^*[d] [mag]	μ [mag]	M_V [mag]	m_{W1}[e] [mag]	m_{W2}[e] [mag]	m_{W3}[e] [mag]
V*AACMi	RRab	−0.150	0.476323	0.237±0.007	11.337±0.011	10.443±0.138	0.893±0.138	10.240±0.008	10.232±0.008	10.171±0.049
V*AEBoo	RRc	−1.390	0.314896	0.083±0.004	10.577±0.008	9.969±0.125	0.608±0.125	9.722±0.008	9.730±0.008	9.665±0.033
V*AFVir	RRab	−1.330	0.483722	0.075±0.004	11.726±0.012	11.104±0.126	0.622±0.125	10.683±0.009	10.689±0.008	10.430±0.074
V*AMVir[g]	RRab	−1.370	0.615088	0.226±0.005	11.293±0.010	10.680±0.126	0.613±0.125	10.101±0.009	10.089±0.009	10.030±0.058
V*ANSer	RRab	−0.070	0.522069	0.130±0.002	10.816±0.010	9.904±0.139	0.912±0.139	9.787±0.008	9.802±0.008	9.759±0.033
V*APSer	RRc	−1.580	0.340789	0.130±0.003	10.981±0.007	10.417±0.125	0.565±0.125	10.171±0.007	10.177±0.007	10.118±0.047
V*ARHer[g]	RRab	−1.300	0.469970	0.038±0.001	11.247±0.008	10.618±0.126	0.629±0.125	10.271±0.007	10.264±0.007	10.234±0.042
V*ARPer	RRab	−0.300	0.425549	0.571±0.012	9.909±0.014	9.050±0.136	0.859±0.135	8.568±0.007	8.574±0.006	8.534±0.014
V*ATSer	RRab	−2.030	0.746568	0.123±0.002	11.356±0.011	10.895±0.126	0.461±0.126	10.158±0.007	10.164±0.007	10.196±0.049
V*AUVir	RRc	−1.500	0.343230	0.091±0.001	11.514±0.009	10.931±0.125	0.583±0.125	10.758±0.009	10.764±0.010	10.612±0.106
V*BBEri	RRab	−1.320	0.569896	0.154±0.006	11.363±0.010	10.739±0.126	0.624±0.125	10.200±0.005	10.199±0.005	10.099±0.030
V*BCDra	RRab	−2.000	0.719576	0.210±0.011	11.377±0.013	10.909±0.127	0.468±0.126	10.082±0.005	10.082±0.005	9.967±0.027
V*BNPav	RRab	−1.320	0.567173	0.260±0.007	12.304±0.018	11.679±0.127	0.624±0.125	11.282±0.014	11.282±0.012	11.079±0.105
V*BNVul	RRab	−1.610	0.594125	0.983±0.033	9.983±0.034	9.425±0.130	0.558±0.125	8.635±0.007	8.605±0.006	8.529±0.013
V*BPPav	RRab	−1.480	0.527128	0.202±0.008	12.347±0.019	11.759±0.126	0.588±0.125	11.303±0.006	11.300±0.006	11.073±0.082
V*CGLib	RRc	−1.190	0.306789	0.686±0.045	10.828±0.046	10.173±0.134	0.654±0.126	10.132±0.008	10.128±0.008	10.063±0.055
V*CIAnd	RRab	−0.690	0.484718	0.208±0.007	12.077±0.013	11.308±0.131	0.769±0.130	11.000±0.009	10.994±0.009	10.896±0.095
V*CNLyr	RRab	−0.580	0.411382	0.544±0.023	10.900±0.024	10.106±0.133	0.795±0.131	9.856±0.006	9.861±0.007	9.816±0.031
V*DDHya	RRab	−0.970	0.501818	0.075±0.002	12.169±0.016	11.464±0.128	0.705±0.127	11.105±0.009	11.089±0.009	10.777±0.113
V*FWLup	RRab	−0.200	0.484171	0.280±0.009	8.758±0.011	7.876±0.137	0.882±0.137	7.645±0.007	7.661±0.007	7.627±0.009
V*HHPup	RRab	−0.500	0.390746	0.474±0.017	10.794±0.019	9.981±0.134	0.813±0.132	9.887±0.006	9.881±0.006	9.749±0.021
V*HKPup	RRab	−1.110	0.734254	0.576±0.021	10.753±0.022	10.080±0.128	0.673±0.126	9.866±0.008	9.854±0.007	9.769±0.032
V*IOLyr	RRab	−1.140	0.577122	0.206±0.014	11.641±0.016	10.975±0.127	0.666±0.126	10.501±0.006	10.496±0.006	10.393±0.043
V*MSAra	RRab	−1.480	0.524958	0.369±0.006	11.688±0.012	11.101±0.126	0.588±0.125	10.598±0.008	10.588±0.008	10.511±0.068
V*MTTel	RRc	−1.850	0.316899	0.138±0.007	8.844±0.010	8.341±0.126	0.502±0.125	8.067±0.007	8.077±0.007	8.036±0.011
V*RRGem[g]	RRab	−0.290	0.397316	0.201±0.003	11.159±0.012	10.297±0.136	0.861±0.135	10.226±0.008	10.223±0.008	10.046±0.052
V*RRLyr[g]	RRab	−1.390	0.566805	0.102±0.003	7.650±0.007	7.090±0.063[f]	0.608±0.125	6.519±0.008	6.486±0.005	6.431±0.006
V*RSBoo[g]	RRab	−0.360	0.377337	0.044±0.003	10.339±0.007	9.494±0.135	0.845±0.134	9.411±0.009	9.398±0.009	9.386±0.028
V*RVCet[g]	RRab	−1.600	0.623428	0.097±0.002	10.828±0.007	10.268±0.120	0.560±0.120	9.568±0.012	9.563±0.011	9.483±0.044
V*RVCrB	RRc	−1.690	0.331593	0.134±0.005	11.284±0.008	10.744±0.125	0.539±0.125	10.468±0.007	10.481±0.008	10.365±0.051
V*RVOct	RRab	−1.710	0.571130	0.520±0.035	10.434±0.036	9.899±0.130	0.535±0.125	9.449±0.006	9.444±0.006	9.385±0.020
V*RWCnc[g]	RRab	−1.670	0.547193	0.067±0.003	11.788±0.017	11.244±0.126	0.544±0.125	10.665±0.008	10.683±0.008	10.456±0.066
V*RWDra[g]	RRab	−1.550	0.442898	0.040±0.002	11.709±0.009	11.137±0.125	0.572±0.125	10.662±0.005	10.664±0.005	10.545±0.039
V*RWTrA	RRab	−0.130	0.374035	0.258±0.007	11.129±0.010	10.231±0.138	0.898±0.138	10.041±0.007	10.038±0.007	10.112±0.043
V*RXCol[g]	RRab	−1.700	0.593733	0.243±0.006	12.420±0.022	11.883±0.127	0.537±0.125	11.241±0.006	11.232±0.007	10.964±0.098
V*RXEri	RRab	−1.330	0.587246	0.194±0.006	9.484±0.008	8.862±0.126	0.622±0.125	8.316±0.005	8.318±0.005	8.243±0.008
V*RYCol[g]	RRab	−0.910	0.478857	0.090±0.004	10.830±0.008	10.111±0.128	0.719±0.128	9.786±0.005	9.794±0.005	9.728±0.021
V*RYOct	RRab	−1.830	0.563469	0.354±0.010	11.675±0.013	11.168±0.126	0.507±0.125	10.725±0.007	10.718±0.007	10.628±0.063
V*RZCep	RRc	−1.770	0.308645	0.864±0.014	8.557±0.015	8.036±0.126	0.521±0.125	7.858±0.006	7.871±0.006	7.710±0.009
V*RZCet	RRab	−1.360	0.510613	0.096±0.003	11.721±0.012	11.106±0.126	0.615±0.125	10.587±0.009	10.595±0.009	10.456±0.071
V*SAra[g]	RRab	−0.710	0.451888	0.347±0.007	10.423±0.010	9.658±0.130	0.765±0.130	9.521±0.008	9.526±0.008	9.444±0.029
V*SSOct[g]	RRab	−1.600	0.621825	1.008±0.020	10.862±0.021	10.302±0.122	0.560±0.120	9.729±0.006	9.704±0.006	9.610±0.024

Continued on Next Page...

Table 3.1 – Continued

Name	Class[a]	[Fe/H][a]	Period[b] [d]	$A_{V,\mathrm{eff}}$[c] [mag]	m_V^*[d] [mag]	μ [mag]	M_V [mag]	m_{W1}[e] [mag]	m_{W2}[e] [mag]	m_{W3}[e] [mag]
V*STBoo[g]	RRab	−1.760	0.622291	0.062±0.001	10.947±0.007	10.424±0.125	0.523±0.125	9.798±0.010	9.787±0.009	9.740±0.035
V*STVir	RRab	−0.670	0.410820	0.129±0.002	11.397±0.011	10.624±0.131	0.774±0.130	10.562±0.009	10.556±0.008	10.502±0.079
V*SUDra	RRab	−1.800	0.660419	0.030±0.002	9.726±0.008	9.212±0.125	0.514±0.125	8.593±0.006	8.585±0.007	8.514±0.015
V*SVEri	RRab	−1.700	0.713863	0.282±0.008	9.653±0.012	9.116±0.126	0.537±0.125	8.546±0.008	8.553±0.007	8.483±0.015
V*SXFor	RRab	−1.660	0.605333	0.044±0.003	11.075±0.007	10.528±0.125	0.546±0.125	9.829±0.007	9.832±0.007	9.744±0.031
V*SZGem	RRab	−1.460	0.501136	0.135±0.002	11.609±0.012	11.016±0.126	0.592±0.125	10.637±0.009	10.623±0.009	10.470±0.077
V*TTCnc[g]	RRab	−1.570	0.563450	0.199±0.006	11.122±0.013	10.555±0.126	0.567±0.125	9.935±0.007	9.930±0.006	9.952±0.043
V*TTLyn	RRab	−1.560	0.597438	0.055±0.002	9.809±0.010	9.240±0.125	0.569±0.125	8.568±0.008	8.573±0.007	8.502±0.014
V*TVCrB	RRab	−2.330	0.584611	0.122±0.004	11.755±0.011	11.363±0.129	0.392±0.128	10.704±0.008	10.690±0.008	10.663±0.070
V*TWHer	RRab	−0.690	0.399601	0.131±0.004	11.143±0.008	10.374±0.130	0.769±0.130	10.231±0.006	10.220±0.006	10.114±0.037
V*TWLyn	RRab	−0.660	0.481853	0.143±0.002	11.855±0.015	11.079±0.131	0.776±0.130	10.727±0.008	10.735±0.009	10.629±0.088
V*TYAps	RRab	−0.950	0.501692	0.414±0.019	11.429±0.020	10.719±0.129	0.710±0.128	10.346±0.006	10.338±0.006	10.278±0.042
V*TZAur	RRab	−0.790	0.391675	0.197±0.003	11.717±0.014	10.970±0.130	0.746±0.129	10.780±0.008	10.795±0.008	10.707±0.092
V*ULep	RRab	−1.780	0.581474	0.103±0.005	10.465±0.009	9.947±0.125	0.519±0.125	9.405±0.005	9.415±0.005	9.405±0.020
V*UPic	RRab	−0.720	0.440371	0.031±0.001	11.367±0.010	10.604±0.130	0.762±0.130	10.332±0.005	10.337±0.005	10.317±0.032
V*UVOct[g]	RRab	−1.740	0.542625	0.250±0.002	9.243±0.006	8.715±0.125	0.528±0.125	8.175±0.006	8.167±0.005	8.077±0.008
V*UYBoo	RRab	−2.560	0.650845	0.113±0.004	10.854±0.007	10.514±0.131	0.339±0.131	9.706±0.009	9.691±0.009	9.592±0.034
V*UYCam	RRc	−1.330	0.267042	0.079±0.003	11.461±0.007	10.838±0.126	0.622±0.125	10.822±0.009	10.847±0.008	10.991±0.092
V*V413CrA	RRab	−1.260	0.589324	0.258±0.010	10.333±0.012	9.695±0.126	0.638±0.126	9.111±0.008	9.107±0.007	9.059±0.023
V*V440Sgr	RRab	−1.400	0.477474	0.263±0.006	10.051±0.012	9.445±0.126	0.606±0.125	9.040±0.009	9.054±0.008	8.981±0.027
V*V445Oph	RRab	−0.190	0.397023	0.928±0.027	10.082±0.030	9.198±0.140	0.884±0.137	9.191±0.008	9.183±0.007	9.168±0.023
V*V455Oph	RRab	−1.070	0.453918	0.454±0.016	11.877±0.019	11.195±0.128	0.682±0.127	10.947±0.008	10.949±0.008	10.851±0.094
V*V499Cen	RRab	−1.430	0.521210	0.241±0.007	10.863±0.012	10.263±0.126	0.599±0.125	9.830±0.013	9.815±0.009	9.744±0.036
V*V675Sgr	RRab	−2.280	0.642289	0.424±0.011	9.877±0.014	9.473±0.129	0.404±0.128	8.912±0.008	8.915±0.008	8.892±0.022
V*VInd	RRab	−1.500	0.479591	0.148±0.003	9.809±0.008	9.226±0.125	0.583±0.125	8.827±0.009	8.821±0.009	8.792±0.016
V*VXHer	RRab	−1.580	0.455373	0.151±0.006	10.532±0.009	9.967±0.125	0.565±0.125	9.589±0.009	9.586±0.007	9.478±0.027
V*VYLib	RRab	−1.340	0.533938	0.561±0.018	11.137±0.020	10.518±0.127	0.620±0.125	10.044±0.009	10.001±0.011	10.008±0.056
V*VYSer	RRab	−1.790	0.714094	0.129±0.002	9.998±0.008	9.482±0.125	0.516±0.125	8.752±0.008	8.738±0.007	8.678±0.017
V*VZHer	RRab	−1.020	0.440326	0.096±0.002	11.389±0.008	10.696±0.127	0.693±0.127	10.475±0.007	10.463±0.006	10.397±0.048
V*WYPav	RRab	−0.980	0.588580	0.326±0.003	11.854±0.011	11.151±0.128	0.703±0.127	10.542±0.008	10.540±0.007	10.256±0.051
V*XAri	RRab	−2.430	0.651139	0.610±0.018	8.935±0.022	8.566±0.131	0.369±0.129	7.875±0.007	7.885±0.007	7.815±0.011
V*XXAnd	RRab	−1.940	0.722742	0.138±0.002	10.541±0.008	10.060±0.126	0.482±0.126	9.374±0.008	9.385±0.007	9.252±0.025
V*XXPup	RRab	−1.330	0.517198	0.196±0.003	11.042±0.010	10.420±0.126	0.622±0.125	9.996±0.008	9.989±0.009	9.988±0.038
V*XZAps	RRab	−1.060	0.587277	0.446±0.022	11.937±0.025	11.253±0.129	0.684±0.127	10.835±0.006	10.828±0.006	10.884±0.067

[a]From Fernley et al. (1998).
[b]Period determined herein using *Hipparcos* data.
[c]Effective extinction using SFD dust models and the Gould & Popowski (1998) Galactic dust model. See Section 3.2.
[d]Extinction-corrected apparent magnitude.
[e]Determined from the *WISE* data following Section 3.3.
[f]Adopted from *HST* parallax measurements (Benedict et al. 2002). The *Hipparcos*-based determination (Section 3.2) yields $\mu = 7.042 \pm 0.125$.
[g]Blazhko-affected star following from http://www.univie.ac.at/tops/blazhko/Blazhkolist.html.

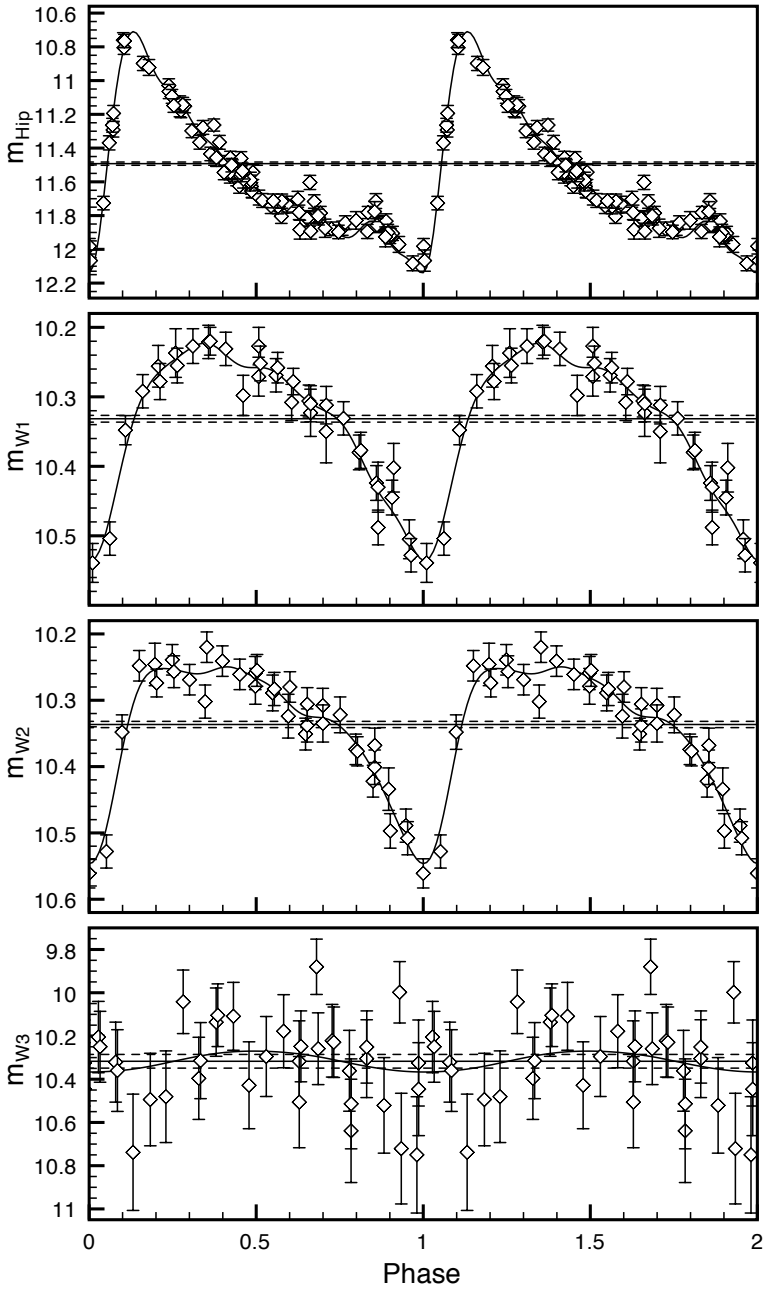

Figure 3.1: *Hipparcos* and *WISE* light curves of V*UPic with fitted models. The solid horizontal line is at the mean flux magnitude and the dashed lines represent the uncertainty of this mean magnitude. The model fitted to the *Hipparcos* (*WISE* W1) data uses 8 (7) harmonics. V*UPic is our best observed *WISE* source with 35 observations over ∼2.3 days. The data is phase-shifted so that the minimum of the model in each band is at phase = 1.

3.4 Deriving the Period–Luminosity Relations

Using the full sample of 76 *WISE* RR Lyrae variables, we derive the empirical period–luminosity relationship in each of the bands W1, W2, and W3. For each RR Lyrae star in the sample, we estimate the observed magnitude, m_{ij}, and pulsational period, P_i, using the methods outlined in Section 3.3. Here, $i = 1, ..., n$ indexes the RR Lyrae variables and $j = 1, 2, 3$ indexes the *WISE* bands.

Our statistical model of the period–luminosity relationship is[5]

$$m_{ij} = \mu_i + M_{0,j} + \alpha_j \log_{10}(P_i/P_0) + \epsilon_{ij}, \tag{3.4}$$

where μ_i is the distance modulus for ith RR Lyrae star, $M_{0,j}$ is the absolute magnitude zero point for the jth *WISE* band at $P = P_0$, where $P_0 = 0.50118$ day is the mean period of the sample, and α_j is the slope of the period–luminosity relationship in the jth band. We assume that any extinction is negligible in these bands. The error terms ϵ_{ij} are independent zero-mean Gaussian random deviates with variance $(\sigma\sigma_{m_{ij}})^2$, which describe the intrinsic scatter in the m_{ij} about the model, where σ is a free parameter which is an unknown scale factor on the known measurement errors, $\sigma_{m_{ij}}$.[6] We fit the model (equation 3.4) using a Bayesian procedure, described below.

A Bayesian approach to this problem is appropriate because for each RR Lyrae star we have *a priori* distance information from previous V-band RR Lyrae studies. For each RR Lyrae star in our sample, we determine a prior on its distance modulus using the steps outlined in Section 3.2. For the star V*RRLyr, we adopt the *HST* distance estimate of Benedict et al. (2002) as our prior. These priors encompass the full amount of information that we have about each source's distance *before* looking at the *WISE* data. The key in our analysis is that while the distance to any RR Lyrae star could be changed within its prior to fit a perfect period–luminosity relation in a single band, the simultaneous fitting of a power-law period–luminosity relation in all bands (with as little intrinsic scatter as possible) tightly constrains the distance of each source. Bayesian fitting of the period–luminosity relation model allows us to obtain:

- posterior distributions on the distance to each RR Lyrae star, given the *WISE* data,
- posterior distributions on the absolute magnitude zero point and slope of the period–luminosity relationship in each *WISE* band, and
- an estimate of the amount of intrinsic spread of the data around the period–luminosity relationship.

The end goal, of course, is to use the estimated period–luminosity relationship to accurately *predict* the distance to each newly observed RR Lyrae star from its period and observed

[5] In principle, there could be a metallicity dependence, but we found such a dependence was negligible in the *WISE* bands. See Section 3.5.

[6] The average measurement error, σ_m, is 0.013, 0.013, and 0.045 mag in W1, W2, and W3, respectively.

WISE light curve. Furthermore, we want to make these predictions with an accurate notion of the amount of error in each predicted distance, as those errors will propagate to subsequent studies.

Bayesian fitting of linear models is thoroughly described in Gelman et al. (2003). Here, we summarize our procedure for analysis of the *WISE* period–luminosity relationship. First, we assume a normal (Gaussian) prior distribution on each of the distance moduli with mean $\mu_{0,i}$ and standard deviation $\sigma_{\mu_{0,i}}$, as described above. For the other parameters in our model (equation 3.4), we assume a flat, noninformative prior distribution. For convenience, we rewrite the model in matrix form as $m = \mathbf{X}\beta + \epsilon$, where m is a vector of the $3n$ measured *WISE* mean-magnitudes, β is a vector of the $n + 6$ parameters (μ, M_0, α) in the period–luminosity relation model, $\mathbf{X}$ is the appropriate $3n$ by $n + 6$ design matrix for equation 3.4, and ϵ is a vector of the zero-mean, normally distributed random errors with covariance matrix $\sigma^2\mathrm{diag}(\sigma_m^2)$.

Including an informative prior on μ is equivalent to adding extra prior "data points" to the analysis. In our model, these "data points" are $\mu_{0,i} = \mu_i + \sigma_{\mu_{0,i}}\epsilon_i$, where ϵ_i is a normal random variate with mean 0 and variance 1. This prior information on μ induces the model $m_* = \mathbf{X}_*\beta + \epsilon_*$, where

$$m_* = \begin{pmatrix} m \\ \mu_0 \end{pmatrix}, \tag{3.5}$$

$$\mathbf{X}_* = \begin{pmatrix} \mathbf{X} \\ (I_n, 0_{n,6}) \end{pmatrix}, \tag{3.6}$$

$$\Sigma_* = \begin{pmatrix} \sigma^2\mathrm{diag}(\sigma_m^2) & 0_{3n,n} \\ 0_{n,3n} & \mathrm{diag}(\sigma_{\mu_0}^2) \end{pmatrix}, \tag{3.7}$$

$\epsilon_* \sim N(0, \Sigma_*)$, and N denotes the multivariate normal distribution. Here, I_n indicates the $n \times n$ identity matrix and $0_{m,n}$ is the $m \times n$ matrix of 0s.

Posterior distributions for the parameters of interest can be derived in a straightforward manner using the entities in equations 3.5–3.7. The joint posterior distribution, $P(\beta, \sigma|m, P)$, can be sampled by first drawing from $P(\sigma|m, P)$ and then, conditional on that draw, selecting from $P(\beta|m, P, \sigma)$. The posterior distribution for β, conditional on the value of σ, follows the multivariate normal distribution,

$$\beta|m, P, \sigma \sim N(\widehat{\beta}, (\mathbf{X}'_*\Sigma_*^{-1}\mathbf{X}_*)^{-1}) \tag{3.8}$$

where $\widehat{\beta}$ is the standard maximum likelihood (weighted least squares) solution,

$$\widehat{\beta} = (\mathbf{X}'_*\Sigma_*^{-1}\mathbf{X}_*)^{-1}\mathbf{X}'_*\Sigma_*^{-1}m_*. \tag{3.9}$$

Unlike the posterior distribution of β (given σ), the posterior distribution of σ does not follow a simple conjugate distribution. Instead, the distribution follows the form

$$P(\sigma^2|m, P) \propto \frac{P(\beta)P(\sigma^2)L(m|P, \beta, \sigma)}{P(\beta|m, P, \sigma)} \tag{3.10}$$

where the prior on β is proportional to the informative prior on μ, the flat prior on σ is $P(\sigma^2) \propto \sigma^{-2}$, and the data likelihood L is the product, over all observed magnitudes, of the Gaussian likelihood of the data given the model (equation 3.4) with all parameters specified.

We draw samples from our joint posterior distribution $P(\beta, \sigma|m, P)$ using equations 3.8 and 3.10 in conjunction. In practice, we compute[7] $P(\sigma^2|m, P)$ over a fine grid of σ values using equation 3.10, and then draw a sample of σ from this density. For each sampled σ, we subsequently draw a β from equation 3.8, conditional on the drawn σ value. We repeat this process 10,000 times to characterize the joint posterior distribution. Using a large sample from this joint posterior distribution, we can compute quantities of interest such as the maximum *a posteriori* slopes and zero points of the period–luminosity relationship of each *WISE* band, the intrinsic scatter of the data around the period–luminosity relationship in each band, and the spread in the *a posteriori* distribution of the period–luminosity relation parameters (see Figs. 3.2–3.4).

3.5 Period–Luminosity Relations Discussion

Bayesian analysis of the *WISE* RR Lyrae variables shows a strong period–luminosity relationship in each of the three bands. The maximum *a posteriori* estimates (and corresponding errors) of the slopes and absolute magnitude zero points for each of the three bands (equation 3.4) and the joint posterior distributions of these parameters are plotted in Figs. 3.2, 3.3, and 3.4 (see also Section 3.6). At the mean period ($P_0 = 0.50118$ day) of the sample, we achieve an absolute magnitude prediction error of 0.016, 0.016, and 0.076 mag in W1, W2, and W3, respectively. Therefore, for an RR Lyrae star of period near 0.5 day observed in *WISE* W1 or W2 bands, we can predict the absolute magnitude of that object to within 0.016 mag, which corresponds to a fractional distance error of 0.7%.

The width of the absolute magnitude prediction bands becomes slightly larger as one moves to larger or smaller periods, as the model is less constrained in those regions. However, the prediction uncertainty remains low throughout the full period range, even at the extremes. For example, at a period of 0.3 day, the absolute magnitude prediction error is 0.037, 0.037, and 0.084 mag (1.7, 1.7, and 3.9% fractional distance error); at a period of 0.7 day, the prediction errors are 0.026, 0.026, and 0.079 mag (1.2, 1.2, and 3.6% fractional distance error) for W1, W2, and W3, respectively. Fig. 3.5 plots the estimated period–luminosity relationship in each *WISE* band, plus the $\pm 1\sigma$ prediction intervals. For each newly observed RR Lyrae star, the true absolute magnitude is expected to reside within the prediction interval.

[7] Assuming that $\beta = \widehat{\beta}$. Several iterations show that the posterior distribution of σ is insensitive to the assumed choice of β.

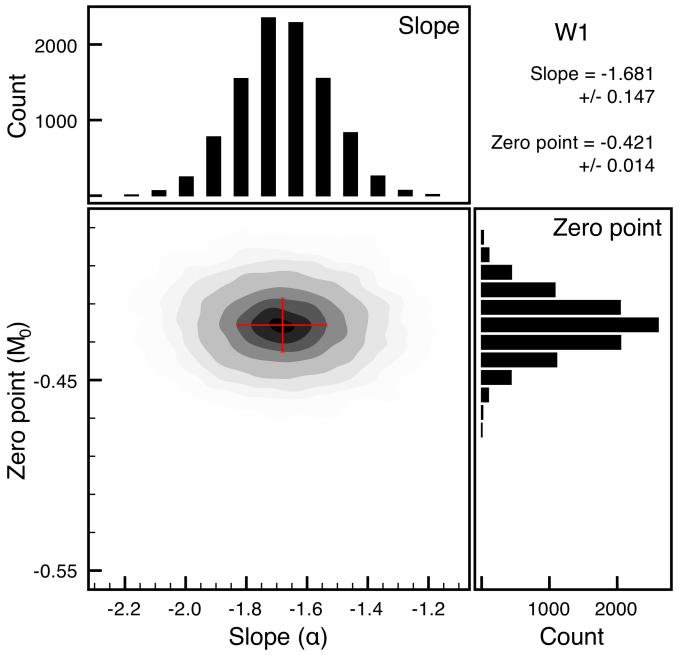

Figure 3.2: Contour plot and histograms of 10,000 samples from the posterior distribution of the slope (α_1) and absolute magnitude zero point ($M_{0,1}$) of the period-luminosity relation for W1. Our data constrain α_1 to -1.681 ± 0.147 and $M_{0,1}$ to -0.421 ± 0.014, with negligible correlation between those parameters. Levels in the 2D contour plot are at the 99.9, 99, 97.5, 95, 90, 85, 80, and 70th percentile.

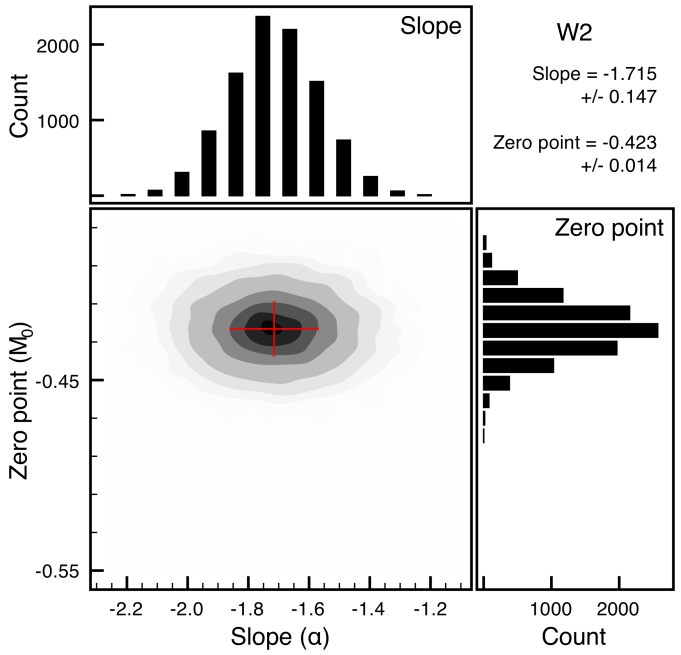

Figure 3.3: Same as in Fig. 3.2, for W2. Our data constrain α_2 to -1.715 ± 0.147 and $M_{0,2}$ to -0.423 ± 0.014, with negligible correlation between those parameters.

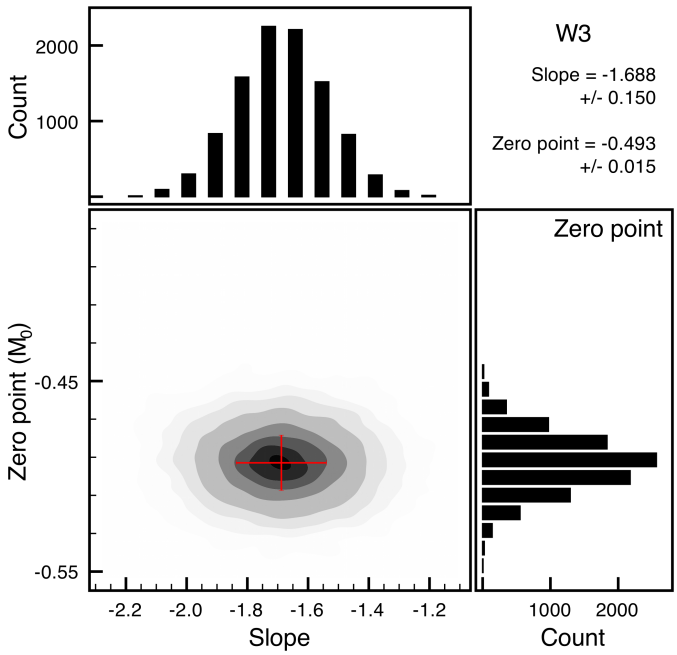

Figure 3.4: Same as in Fig. 3.2, for W3. Our data constrain α_3 to -1.688 ± 0.150 and $M_{0,3}$ to -0.493 ± 0.015, with negligible correlation between those parameters.

Along with estimating the period–luminosity relationship for each band, our fitting procedure supplies a posterior distribution for the distances of each of the RR Lyrae star in our sample. In Table 3.2 we report the posterior means along with the 68% and 95% posterior credible sets for the distance to each of the 76 RR Lyrae stars used to fit the period–luminosity relationships. We also list the separation between prior and posterior distance moduli in units of σ, defined as

$$\Delta(\mu_{\rm prior} - \mu_{\rm post}) = \frac{\bar{\mu}_{\rm prior} - \bar{\mu}_{\rm post}}{\sqrt{\sigma^2_{\mu_{\rm prior}} + \sigma^2_{\mu_{\rm post}}}},$$

where $\bar{\mu}$ and σ_μ denote the means and standard deviations of the distributions, respectively. We note that there is, for most RR Lyrae variables, a close correspondence between the prior and posterior distances, as $|\Delta| < 2$ for all but 2 sources in our sample (V*ANSer and V*HKPup). Fig. 3.6 shows a plot of prior versus posterior distance moduli, including a residuals plot, which shows again that, within their errors, the posterior distance distributions are consistent with the prior distance distributions for almost all the RR Lyrae stars.

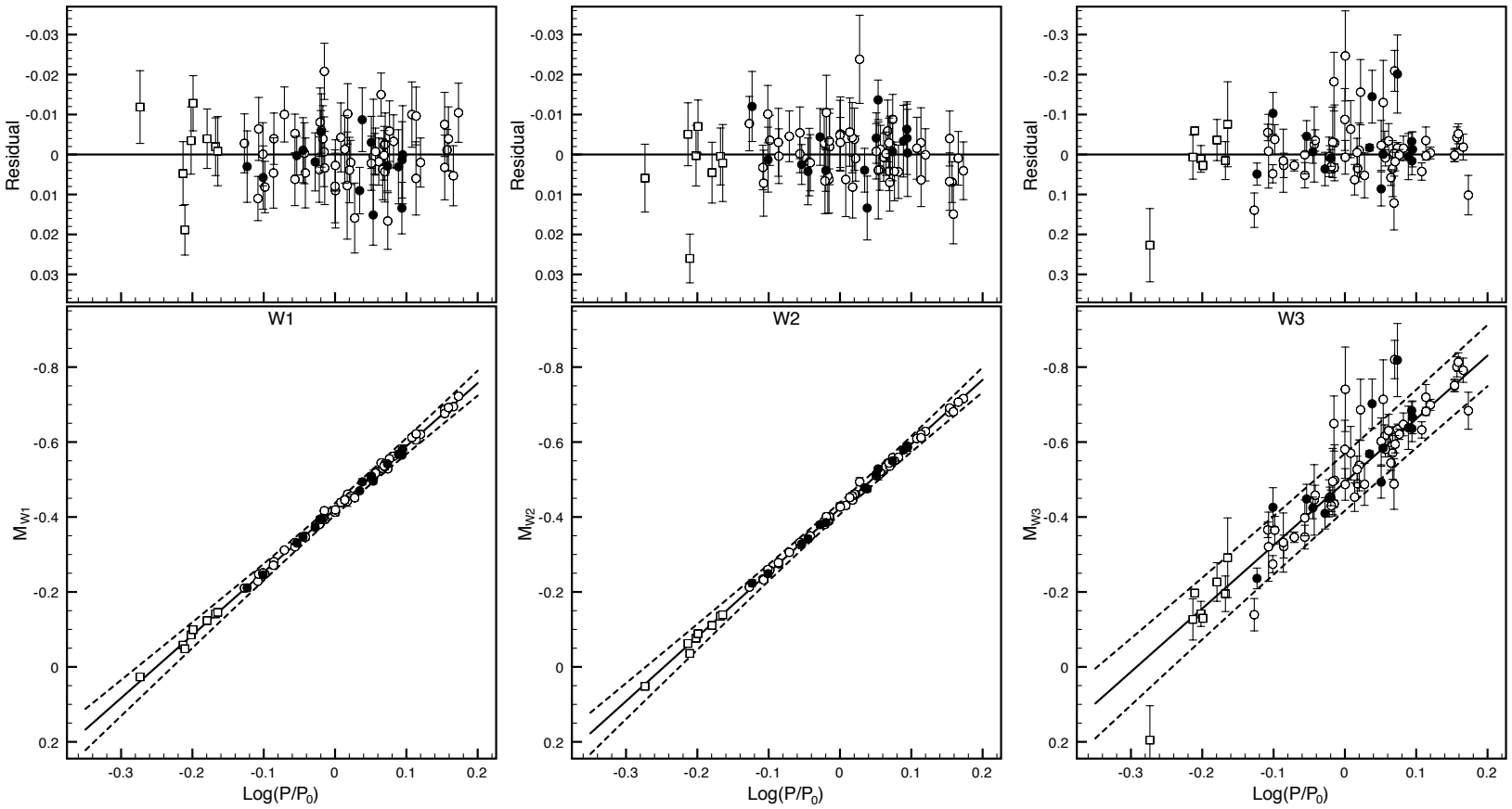

Figure 3.5: Period-luminosity relations for W1, W2, and W3 (left to right), as found by our Bayesian fitting method. In each figure, the solid line shows our model's prediction of the RR Lyrae absolute magnitude, as a function of RR Lyrae period. The dashed lines show the $\pm 1\sigma$ prediction intervals; we expect the true absolute magnitude to fall within the dashed lines for 68% of all newly observed RR Lyrae variables. The top panel of each plot shows the residual spread around the best fit model, showing the small variance, σ^2, in the intrinsic scatter around the period–luminosity relations. In the figure, RRab are plotted as circles and RRc as squares. Blazhko-affected RR Lyrae stars are indicated by filled points.

Table 3.2: RR Lyrae distance and M_V posteriors from Bayesian analysis.

Name	d_{best} [a] [pc]	$[d-1\sigma, d+1\sigma]$ [pc]	$[d-2\sigma, d+2\sigma]$ [pc]	$\Delta(\mu_{prior}-\mu_{post})$ [b] [No. of σ]	M_V [c] [mag]
V*AACMi	1330.7	[1320.4, 1341.1]	[1310.1, 1351.6]	1.27	0.716±0.020
V*AEBoo	914.9	[900.6, 929.5]	[886.6, 944.2]	−1.25	0.770±0.035
V*AFVir	1643.8	[1631.2, 1656.6]	[1618.6, 1669.4]	−0.20	0.647±0.021
V*AMVir	1360.2	[1347.3, 1373.2]	[1334.5, 1386.4]	−0.09	0.625±0.023
V*ANSer	1120.8	[1112.3, 1129.3]	[1103.8, 1137.9]	2.44	0.569±0.019
V*APSer	1154.9	[1139.2, 1170.8]	[1123.6, 1187.0]	−0.81	0.668±0.031
V*ARHer	1344.8	[1334.4, 1355.4]	[1324.0, 1366.0]	0.20	0.604±0.019
V*ARPer	597.1	[591.8, 602.4]	[586.6, 607.7]	−1.24	1.029±0.024
V*ATSer	1499.6	[1479.3, 1520.3]	[1459.2, 1541.2]	−0.11	0.476±0.032
V*AUVir	1515.7	[1495.2, 1536.5]	[1475.0, 1557.6]	−0.22	0.611±0.031
V*BBEri	1389.6	[1378.4, 1400.9]	[1367.3, 1412.4]	−0.19	0.648±0.020
V*BCDra	1424.1	[1406.2, 1442.2]	[1388.5, 1460.6]	−1.09	0.610±0.031
V*BNPav	2283.5	[2263.4, 2303.8]	[2243.4, 2324.2]	0.89	0.511±0.026
V*BNVul	680.4	[674.6, 686.4]	[668.7, 692.4]	−1.99	0.819±0.039
V*BPPav	2248.3	[2231.5, 2265.3]	[2214.8, 2282.3]	0.00	0.587±0.025
V*CGLib	1091.5	[1073.7, 1109.6]	[1056.2, 1128.0]	0.12	0.638±0.059
V*CIAnd	1899.9	[1885.2, 1914.8]	[1870.6, 1929.7]	0.65	0.683±0.021
V*CNLyr	1065.1	[1055.0, 1075.3]	[1044.9, 1085.6]	0.23	0.764±0.032
V*DDHya	2011.6	[1996.2, 2027.2]	[1980.9, 2042.9]	0.41	0.651±0.023
V*FWLup	409.7	[406.7, 412.7]	[403.7, 415.7]	1.34	0.696±0.019
V*HHPup	1054.3	[1043.3, 1065.5]	[1032.5, 1076.7]	0.99	0.679±0.030
V*HKPup	1294.6	[1277.5, 1311.9]	[1260.6, 1329.4]	3.66	0.192±0.036
V*IOLyr	1601.8	[1588.4, 1615.4]	[1575.1, 1629.0]	0.38	0.618±0.024
V*MSAra	1621.3	[1608.9, 1633.8]	[1596.5, 1646.4]	−0.41	0.639±0.021
V*MTTel	429.7	[423.1, 436.4]	[416.6, 443.2]	−1.35	0.678±0.035
V*RRGem	1242.5	[1229.8, 1255.4]	[1217.2, 1268.3]	1.26	0.687±0.025
V*RRLyr	252.9	[250.9, 254.9]	[248.9, 256.9]	−1.16	0.636±0.018
V*RSBoo	840.2	[830.7, 849.8]	[821.3, 859.6]	0.93	0.718±0.026
V*RVCet	1070.8	[1060.1, 1081.6]	[1049.6, 1092.5]	−0.98	0.680±0.023
V*RVCrB	1313.1	[1294.3, 1332.2]	[1275.7, 1351.5]	−1.18	0.692±0.032
V*RVOct	984.3	[976.3, 992.4]	[968.4, 1000.5]	0.50	0.469±0.040
V*RWCnc	1704.9	[1691.3, 1718.6]	[1677.8, 1732.4]	−0.67	0.629±0.024
V*RWDra	1579.6	[1566.5, 1592.9]	[1553.5, 1606.2]	−1.14	0.716±0.020
V*RWTrA	1122.5	[1109.5, 1135.6]	[1096.7, 1148.8]	0.14	0.879±0.027
V*RXCol	2272.3	[2252.3, 2292.4]	[2232.5, 2312.7]	−0.78	0.637±0.029
V*RXEri	590.1	[585.1, 595.1]	[580.2, 600.1]	−0.06	0.630±0.020
V*RYCol	1086.1	[1078.0, 1094.3]	[1070.0, 1102.5]	0.53	0.651±0.018
V*RYOct	1761.4	[1747.2, 1775.7]	[1733.0, 1790.2]	0.48	0.446±0.022
V*RZCep	381.3	[375.2, 387.6]	[369.2, 393.9]	−0.99	0.650±0.038
V*RZCet	1604.0	[1591.8, 1616.3]	[1579.6, 1628.8]	−0.63	0.695±0.020
V*SAra	941.0	[933.3, 948.8]	[925.6, 956.6]	1.60	0.555±0.020
V*SSOct	1144.8	[1133.9, 1155.8]	[1123.1, 1167.0]	−0.07	0.569±0.030
V*STBoo	1188.8	[1177.2, 1200.5]	[1165.7, 1212.3]	−0.38	0.572±0.022
V*STVir	1468.1	[1453.9, 1482.4]	[1439.8, 1496.9]	1.59	0.564±0.024
V*SUDra	696.2	[688.8, 703.7]	[681.4, 711.3]	0.01	0.513±0.025
V*SVEri	702.4	[693.6, 711.2]	[685.0, 720.2]	0.91	0.420±0.030
V*SXFor	1197.5	[1186.6, 1208.5]	[1175.9, 1219.5]	−1.08	0.683±0.021
V*SZGem	1622.1	[1609.7, 1634.6]	[1597.5, 1647.1]	0.27	0.558±0.020
V*TTCnc	1227.2	[1217.3, 1237.3]	[1207.5, 1247.3]	−0.87	0.677±0.022
V*TTLyn	667.7	[661.9, 673.7]	[656.0, 679.7]	−0.92	0.686±0.022
V*TVCrB	1764.9	[1749.7, 1780.2]	[1734.7, 1795.6]	−1.00	0.522±0.022
V*TWHer	1246.4	[1233.8, 1259.1]	[1221.4, 1271.9]	0.79	0.665±0.023
V*TWLyn	1677.6	[1664.7, 1690.6]	[1651.9, 1703.7]	0.34	0.732±0.023
V*TYAps	1422.3	[1411.8, 1432.9]	[1401.3, 1443.6]	0.35	0.664±0.026
V*TZAur	1605.2	[1588.2, 1622.4]	[1571.3, 1639.8]	0.44	0.689±0.027
V*ULep	976.8	[968.6, 985.1]	[960.4, 993.5]	0.02	0.516±0.020
V*UPic	1357.3	[1346.1, 1368.6]	[1334.9, 1380.0]	0.45	0.703±0.021

Continued on Next Page...

Table 3.2 – Continued

Name	d_{best} [a] [pc]	$[d-1\sigma, d+1\sigma]$ [pc]	$[d-2\sigma, d+2\sigma]$ [pc]	$\Delta(\mu_{prior}-\mu_{post})$ [b] [No. of σ]	M_V [c] [mag]
V*UVOct	535.8	[531.8, 539.8]	[527.8, 543.9]	−0.56	0.598±0.017
V*UYBoo	1154.2	[1141.9, 1166.6]	[1129.8, 1179.1]	−1.53	0.542±0.024
V*UYCam	1442.5	[1413.8, 1471.7]	[1385.6, 1501.6]	−0.32	0.665±0.044
V*V413CrA	852.3	[844.9, 859.8]	[837.5, 867.3]	−0.33	0.680±0.022
V*V440Sgr	770.5	[764.6, 776.5]	[758.8, 782.5]	−0.09	0.617±0.020
V*V445Oph	773.5	[765.5, 781.5]	[757.7, 789.6]	1.72	0.640±0.037
V*V455Oph	1816.7	[1801.8, 1831.8]	[1787.0, 1847.0]	0.78	0.581±0.026
V*V499Cen	1133.1	[1124.2, 1142.1]	[1115.4, 1151.1]	0.06	0.591±0.021
V*V675Sgr	803.2	[795.1, 811.5]	[787.0, 819.8]	0.39	0.353±0.026
V*VInd	698.9	[693.6, 704.2]	[688.3, 709.6]	−0.03	0.587±0.018
V*VXHer	970.8	[963.0, 978.7]	[955.2, 986.7]	−0.25	0.596±0.020
V*VYLib	1256.2	[1246.2, 1266.2]	[1236.3, 1276.3]	−0.17	0.642±0.027
V*VYSer	768.6	[759.1, 778.3]	[749.6, 788.1]	−0.41	0.569±0.028
V*VZHer	1442.2	[1430.0, 1454.4]	[1417.9, 1466.8]	0.77	0.594±0.020
V*WYPav	1641.2	[1627.0, 1655.7]	[1612.8, 1670.2]	−0.58	0.778±0.022
V*XAri	500.5	[495.3, 505.8]	[490.2, 511.1]	−0.52	0.438±0.032
V*XXAnd	1030.7	[1017.5, 1044.1]	[1004.4, 1057.6]	0.05	0.476±0.029
V*XXPup	1225.1	[1215.9, 1234.4]	[1206.7, 1243.8]	0.16	0.601±0.019
V*XZAps	1880.7	[1864.6, 1897.1]	[1848.5, 1913.5]	0.91	0.565±0.031

[a] Best distance posteriors from the analysis described in Section 3.4.
[b] The number of σ discrepancy between the prior and posterior mean, defined as $\Delta(\mu_{prior}-\mu_{post}) = \frac{\bar{\mu}_{prior}-\bar{\mu}_{post}}{\sqrt{\sigma^2_{\mu_{prior}}+\sigma^2_{\mu_{post}}}}$.
[c] Absolute V-band magnitudes calculated with posterior μ from the period–luminosity relation analysis (Section 3.4) and m^*_V from converted, extinction corrected *Hipparcos* mean-magnitude, (Section 3.3; Table 3.1).

Recall that for V*RRLyr we use the well-measured *HST* parallax result, which corresponds to 262 ± 7.5 pc. Our posterior fit distance for V*RRLyr is 253 ± 2 pc, which is consistent with the *HST* distance at a level of 1.2σ. We also get a consistent prediction for V*RRLyr if we do not use V*RRLyr itself in the period–luminosity relation analysis (Fig. 3.7). That our analysis for the source with the most highly constrained distance prior is consistent with those results is further evidence of its accuracy and applicability.

To check the sensitivity of our results to the prior distances used, we analyze the changes in our posterior distance estimates under systematic prior offsets. We first note that the prior μ estimate for V*RRLyr using the *HST* parallax result differs by 0.05 dex from the *Hipparcos* V-band estimate. To estimate the amount of systematic error in our posterior distance estimates, we inflate the prior mean distance modulus by 0.05 dex for a random 50% of the RR Lyrae stars before running our Bayesian period–luminosity relation model fitting. As a result, the posterior distance moduli increase by an average of 0.023 dex, implying a systematic error of 1.17% on distance estimation. We take this to be a reasonable estimate of the systematic error.

As a further sanity check, in Fig. 3.7 we compare the prior, posterior, and prediction μ densities for a few RR Lyrae variables. The prediction density for each RR Lyrae star was computed by holding out that particular star during the model fitting, and then applying the fitted model to predict the distance modulus of that source. We find that these "cross-

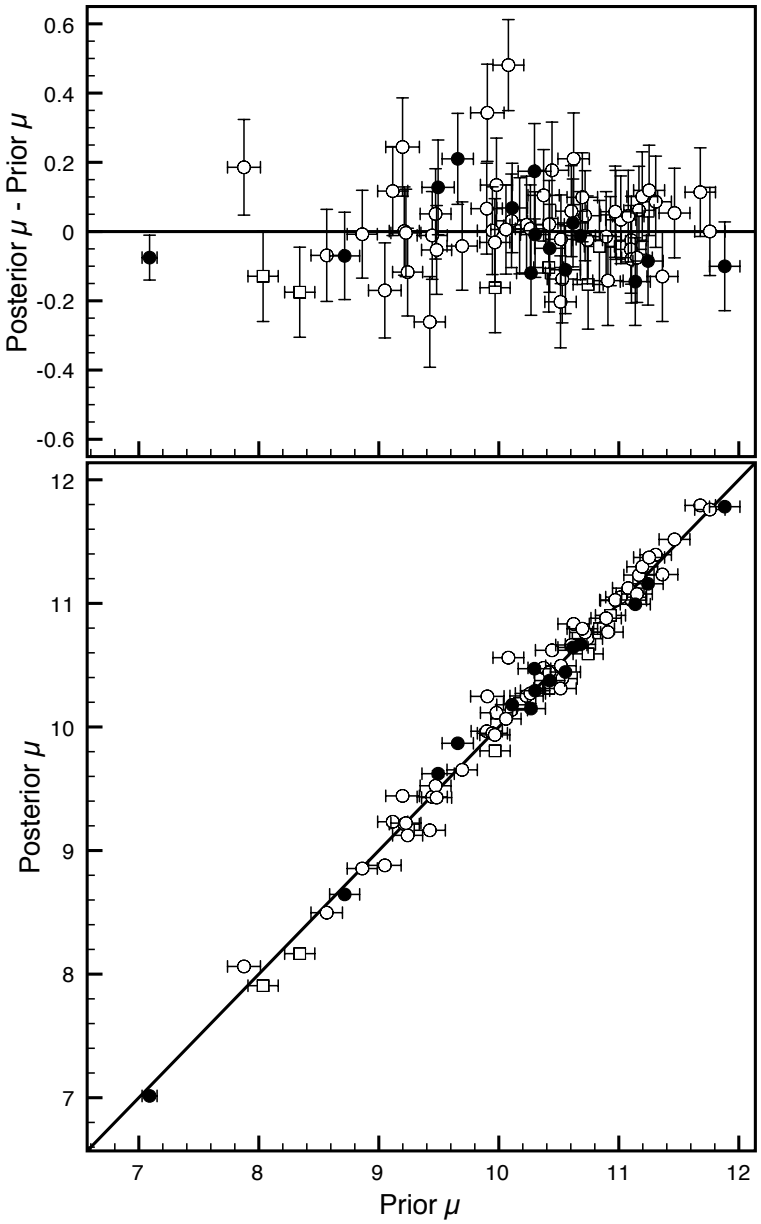

Figure 3.6: Prior versus posterior distance moduli (bottom) and residual difference (top). The posterior distance modulus distribution is determined by sampling from the density in equation 3.8, which considers the evidence in all three *WISE* bands as well as the prior distance information. As is evident, the posterior distances are consistent with the prior distance distribution, within their errors. In the figure, RRab are plotted as circles and RRc as squares. Blazhko-affected RR Lyrae stars are indicated by filled points.

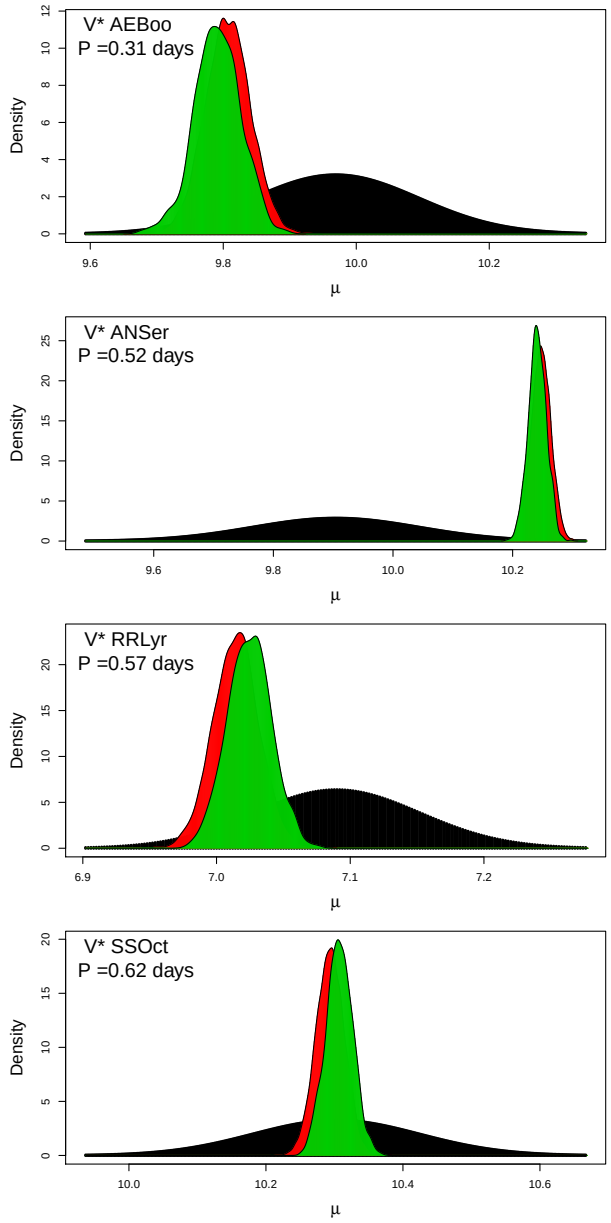

Figure 3.7: Comparison of the prior, posterior, and prediction density for the distance modulus, μ, for 4 RR Lyrae stars in our sample. From top to bottom, these sources are V*AEBoo, V*ANSer, V*RRLyr, and V*SSOct. In each plot, the broad black curve represents the prior μ density, the red (hidden) curve is the posterior density of μ, and the green (foreground) curve is the prediction density for μ, which is found by holding that source out during model fitting and then predicting its μ with the built model. For three of the four stars, the posterior densities are in good agreement with the prior; V*ANSer is the second most discrepant star in our sample (after V*HKPup). In all cases, the posterior and predictive densities are much more precise than the prior densities and are in very close agreement to one another.

validated" μ prediction densities are very consistent with the posterior μ densities, suggesting that the model is stable and that small changes in the set of RR Lyrae stars used to fit the model do not cause any substantial differences in the model. Furthermore, those densities are much more narrow than the prior densities, showing that the *WISE* data can constrain the distances to a great degree. Additionally, we see that both the posterior and prediction densities fall within high-probability regions of the prior distribution for three of the four stars, meaning that our model is in good agreement with the prior distances. Note that the one discrepant star plotted, V*ANSer, has the second largest discrepancy between prior and posterior μ densities, after V*HKPup (Table 3.2).

We also test whether including RR Lyrae metallicity into the model improves the period–luminosity relationship fits. To do this, we add an additional term, $\gamma_j Z_i$, to our model (3.4), where Z_i is the metallicity of RR Lyrae star i and γ_j is the slope of the magnitude-metallicity relationship for the jth *WISE* band. Fitting this model, we find that γ_j has a significantly positive value, but that the predictive power of the new model, as measured by the width of the prediction intervals around the absolute magnitudes, does not differ from the original model which neglected metallicity. Furthermore, if we first subtract from the absolute magnitudes the fit of the model that uses only period, we find no relationship between the residuals and metallicity (slope of -0.00034 ± 0.00151). Including only period in the model achieves significantly better fits than including only metallicity, with half as much residual scatter. These results suggest that all of the absolute magnitude information encoded in [Fe/H] is already contained in the period, and so metallicity need not be added as a covariate in the model.

Finally, we derive an empirical M_V-[Fe/H] relationship using the posterior mean μ values from our Bayesian fitting to the *WISE* data. From this data, our best fit relationship is $M_V = (0.10 \pm 0.02)([\text{Fe/H}] + 1.6) + (0.59 \pm 0.10)$, which differs significantly in its slope, but not in its intercept value, to the Chaboyer (1999) relationship—in equation 3.3—that was used to compute the original distance priors. Fig. 3.8 shows a scatterplot of our estimated M_V as a function of metallicity; there is significant scatter around the empirical relationship, with a handful of large outliers. We also overplot the Chaboyer (1999) relation to demonstrate that both relations fit the data reasonably well. We qualify our new M_V-[Fe/H] relation by noting that the relatively constrained metallicity range of our sample RR Lyrae variables limits the relation's applicability at other metallicities. As RR Lyrae metallicity deviates from ~ -1.5 the uncertainty in the slope of the relation rises steeply.

At a glance, the nontrivial difference between the Chaboyer (1999) M_V-[Fe/H] relationship used to calculate our distance priors and the new M_V-[Fe/H] relationship we derive using our distance posteriors could indicate an inconsistency in the Bayesian approach to our period–luminosity relation fits. In particular, this discrepancy may suggest that the large spread in the prior distance distributions has allowed the Bayesian fitting technique too much freedom in computing posterior distances. To test this, we run a simple weighted least squares regression to fit each of the period–luminosity relations, fixing the distances at the exact values from the Chaboyer (1999) M_V-[Fe/H] relationship (without using a Bayesian fitting method to update the distance estimates). This simpler fitting method re-

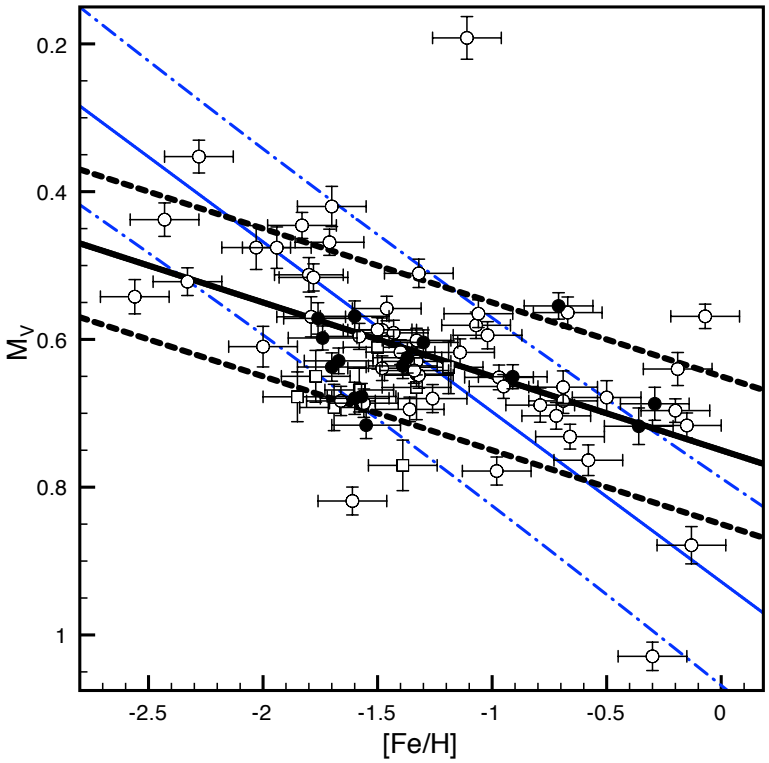

Figure 3.8: M_V-[Fe/H] relation as derived from our new, *WISE*-constrained RR Lyrae distances. In the figure, RRab are plotted as circles and RRc as squares. Blazhko-affected RR Lyrae stars are indicated by filled points. The black thick lines depict our fit of the relation, $M_V = 0.10([\mathrm{Fe/H}] + 1.6) + 0.59$, while the amount of intrinsic scatter about the fit is ± 0.10 mag, represented by the black dashed lines. The blue thinner lines depict the relation from Chaboyer (1999), $M_V = (0.23\pm0.04)([\mathrm{Fe/H}]+1.6)+(0.56\pm0.12)$, with dash-dot lines showing the $\pm 1\sigma$ bounds of the relation.

sults in statistically identical slope and zero point parameters for all three *WISE* bands. The scatter about the least squares fit, however, increases to 0.12 mag in W1 and W2, and 0.15 mag in W3 (from 0.016, and 0.076 from the Bayesian method). This increased scatter is expected, since the primary purpose of applying the Bayesian fitting technique is to reduce this scatter by simultaneously finding more accurate distances through the posterior distribution (i.e., updating the distance estimates given the *WISE* data). We can thus state confidently that the discrepancy between the Chaboyer (1999) M_V-[Fe/H] relationship and the new M_V-[Fe/H] relationship that we derive does not affect the period–luminosity relation fits.

3.6 Conclusions

We have presented the first calibration of the RR Lyrae period-luminosity relations at three mid-infrared wavelengths. Our estimated period–luminosity relations, tied to the Vega magnitude system, are:

$$M_{W1} = (-0.421 \pm 0.014) - (1.681 \pm 0.147)\log_{10}(P/0.50118\text{ d}) \quad (3.11)$$
$$M_{W2} = (-0.423 \pm 0.014) - (1.715 \pm 0.147)\log_{10}(P/0.50118\text{ d}) \quad (3.12)$$
$$M_{W3} = (-0.493 \pm 0.015) - (1.688 \pm 0.150)\log_{10}(P/0.50118\text{ d}). \quad (3.13)$$

These relations achieve an absolute magnitude prediction error as low as ± 0.016 mag in *WISE* bands W1 and W2 (rising to 0.076 mag in W3) near the mean period value $P_0 = 0.50118$ day. Using these relations we calculated new distances to our sample of RR Lyrae stars with a mean fractional distance error of 0.97% (statistical) and 1.17% (systematic).

We further demonstrated that the posterior distances resulting from the newly-derived period–luminosity relations are consistent with the prior distance distributions. An attempt to find an independent, statistically significant metallicity dependence in the mid-infrared period–luminosity relations confirmed the mid-infrared relations' independence from metallicity effects. Additionally, we applied our posterior distance estimates of our 76 RR Lyrae star sample to fit a new absolute V-band luminosity-metallicity relation.

Perhaps the most significant contribution possible of the RR Lyrae period–luminosity relation is a well-constrained measurement of the LMC distance. The distance modulus of the LMC is a hugely consequential value in the extension of the distance ladder out to cosmological scales, and the the subsequent calculation of the Hubble constant, H_0 (Schaefer 2008). The mid-infrared period–luminosity relations presented here will allow future studies of LMC RR Lyrae variables conducted with *Spitzer* (warm) or possibly the *James Webb Space Telescope* to measure reliable LMC distances with error at the $\sim$2% level or lower.[8] It is conceivable that a comprehensive mid-infrared survey of LMC RR Lyrae variables would enable the three-dimensional stellar structure mapping of the LMC with $\sim$1 kpc resolution.

The accuracy of any estimate of the period–luminosity relation is influenced by the accuracy of the *a priori* distances for the RR Lyrae sample used. Soon the *HST* parallax measurements (Benedict 2008) of V*RZCep, V*UVOct, V*SUDra and V*XZCyg will be published. Our results in Table 3.2 serve as predictions of what will be found for the first three of those sources (once the *WISE* data on V*XZCyg is released, equations 3.13 could be used to postdict the *HST* result). The *Gaia* satellite of the European Space Agency, a 5-year astrometry mission to be launched in mid-2013, promises trigonometric parallax measurements of all field RR Lyrae variables within 3 kpc with individual accuracy $\sigma(\pi) < 3\%$ (Cacciari 2009b). Although these measurements will not be available for many years to

[8]Note that the current absolute calibration uncertainty of *WISE* relative to *Spitzer* is 2.4, 2.8, 4.5% (W1,W2,W3, respectively), as provided in the Explanatory Supplement to the *WISE* Preliminary Data Release Products — http://wise2.ipac.caltech.edu/docs/release/prelim/expsup/sec4_3g.html. This would dominate over the errors in our *WISE*-determined distance measure.

come, they have tremendous potential to further constrain the period–luminosity relations presented herein. In doing so, we can hope to study Galactic substructure well into the optically-obscured Galactic plane and further improve the resulting distance estimates for the LMC and beyond.

3.7 Appendix: *WISE* Period Recovery

There are two primary concerns with using *WISE* data to discover short-period variable stars. First, the number of observations on any given patch of sky is small (minimum 16 in the final *WISE* dataset) and determined primarily by the ecliptic latitude. Secondly, the peak-to-trough amplitude of pulsating variables is significantly decreased at mid-infrared wavelengths as compared to optical wavelengths ($\sim$0.2 mag in W1 compared to $\sim$1 mag in V for RR Lyrae variables). Our analysis shows that even with these disadvantageous factors, the *WISE* light curves can yield accurate periods quite often. Peaks in the periodogram are expected to have frequency widths $\sim 1/T$, where T is the time spanned by the observations. We note that our best-fit frequencies, determined on a grid of frequency steps $0.01/T$, agree with well with those of Fernley et al. (1998) (to better than $0.2/T$ typically). We plot an example periodogram using the W2 light curve of an RR Lyrae star with the median number of *WISE* observations (14) in Fig. 3.9.

For the fitting of period–luminosity relations, it is important to have accurate log-Period estimates or, equivalently, accurate fractional period estimates. We describe the (in)accuracy of a recovered period by the simple fractional error as compared to the known, true period.

$$\text{Recovered Period Fract. Error} = \left|\mathrm{P_m} - \mathrm{P_t}\right| / \mathrm{P_t} \tag{3.14}$$

with $\mathrm{P_m}$ the period measured solely from the *WISE* light curve and $\mathrm{P_t}$ the true period as measured from the *Hipparcos* light curve.

Fig. 3.10 shows histograms of the period recovery accuracy for each *WISE* band relative to *Hipparcos* and illustrates that nearly all *WISE* light curves produce accurate periods in the shorter wavelength bands W1 and W2.

To explore how the number of epochs in a light curve affects period recovery, we plot in Fig. 3.11 recovered period fractional error as a function of the number of observations for band W2. Because of the survey strategy of *WISE*, a larger number of observations typically indicates both increased temporal resolution (increased frequency of observation) and increased total light curve timespan (duration between first and last observation). As expected, there is a general trend of reduced recovered period fractional error with increasing number of observations. Beyond 20 observations, the typical period error is $\lesssim 2\%$.

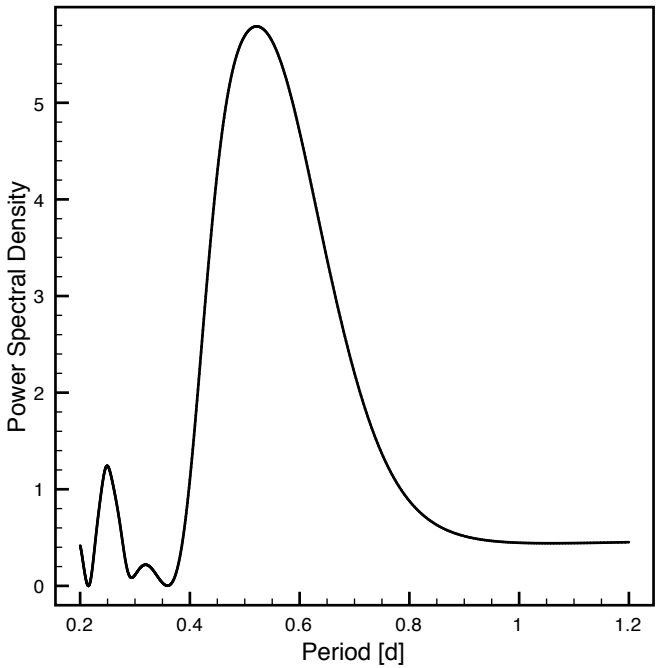

Figure 3.9: Periodogram generated from the 14 epochs of W2 data for V*MSAra. To envelope the reasonable period range of RR Lyrae stars we plot from 0.2 to 1.2 day. The archival *Hipparcos* period of 0.525 day is well recovered from the *WISE* data (peak at 0.522 day).

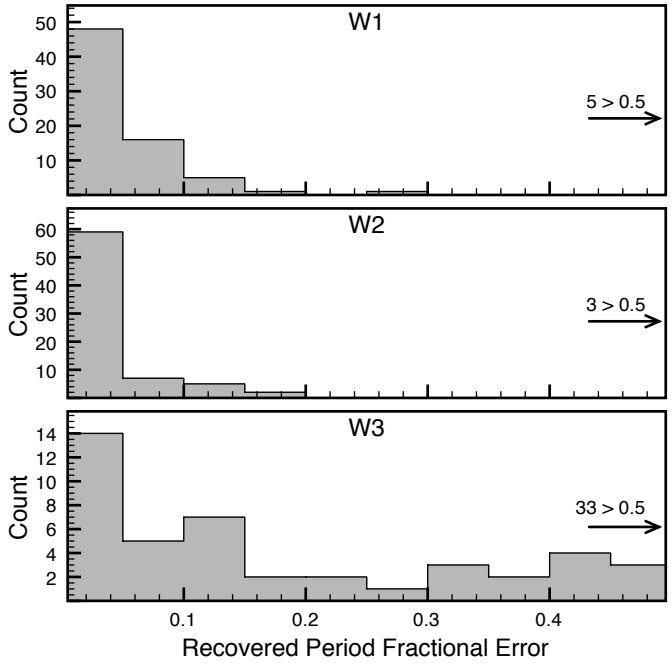

Figure 3.10: Distribution of recovered period fractional error across the three *WISE* bands. The plots are cropped to a maximum fractional error of 0.5 and the resultant number of excluded light curves is noted in each plot.

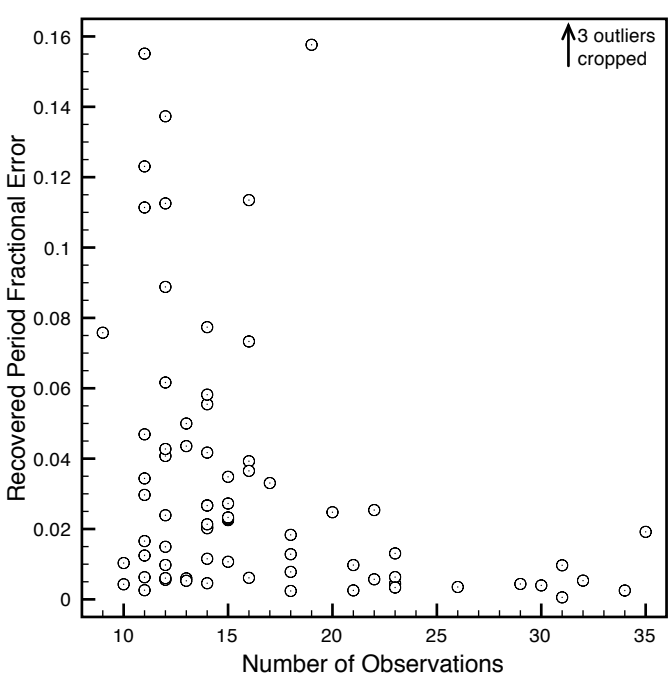

Figure 3.11: Recovered period fractional error plotted as a function of number of *WISE* observations for band W2. As expected, there is a general trend of reduced recovered period fractional error with increasing number of observations. Beyond 20 observations, the typical period error is $\lesssim 2\%$.

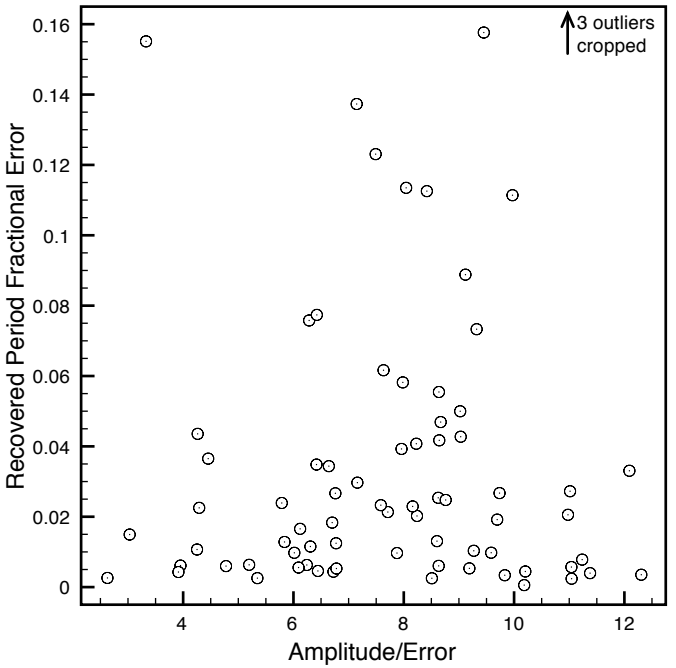

Figure 3.12: Recovered period fractional error plotted as a function of light curve amplitude/$\langle$mag error$\rangle$ for band W2. Although we would expect reduced recovered period fractional error with increasing amplitude/$\langle$mag error$\rangle$, this trend is not obvious in the plot. "Vertical light curve smudging" is not a significant source of error in the recovered period for our dataset.

Any period-finding algorithm must distinguish a shape for the light curve. That is, a phased light curve must be smoothly varying in that the uncertainty in the brightness at any phase point is considerably smaller than the amplitude of the light curve. As the photometric uncertainty increases relative to the amplitude, there is an effect of "vertical smudging" in which the light curve shape becomes less distinguishable. The flux amplitudes of RR Lyrae variables are about two times smaller in the mid-infrared as compared to the visual band. To investigate if this plays a factor in period recovery with *WISE* light curve data, Fig. 3.12 plots recovered period fractional error as a function of light curve amplitude/⟨mag error⟩ for band W2. Although we would expect to observe decreased period error with increased amplitude/⟨mag error⟩, this is not observed. We can conclude that "vertical smudging" is at most a non-dominant source of error in the recovered periods.

Acknowledgments

We thank D. Hoffman, R. Cutri, P. Eisenhardt, and N. Wright for valuable conversations about *WISE* and the *WISE* data. We thank the entire *WISE* team for having produced a wonderful mid-IR dataset. The authors acknowledge the generous support of a CDI grant (#0941742) from the National Science Foundation. JSB and CRK were also partially supported by grant NSF/AST-100991. NRB is supported through the Einstein Fellowship Program (NASA Cooperative Agreement: NNG06DO90A). This research has made use of the NASA/IPAC Infrared Science Archive, which is operated by the Jet Propulsion Laboratory, California Institute of Technology, under contract with the National Aeronautics and Space Administration. This publication makes use of data products from the Wide-field Infrared Survey Explorer, which is a joint project of the University of California, Los Angeles, and the Jet Propulsion Laboratory/California Institute of Technology, funded by the National Aeronautics and Space Administration. This research has made use of NASA's Astrophysics Data System.

Chapter 4

A Bayesian Approach to Calibrating Period–Luminosity Relations of RR Lyrae Stars in the Mid-infrared

An earlier version of this chapter was previously published as Ap&SS 341, 83 with coauthors Joseph W. Richards, Nathaniel R. Butler, and Joshua S. Bloom.[1]

Abstract

A Bayesian approach to calibrating period–luminosity relations has substantial benefits over generic least squares fits. In particular, the Bayesian approach takes into account the full prior distribution of the model parameters, such as the *a priori* distances, and refits these parameters as part of the process of settling on the most highly-constrained final fit. Additionally, the Bayesian approach can naturally ingest data from multiple wavebands and simultaneously fit the parameters of period–luminosity relations for each waveband in a procedure that constrains the parameter posterior distributions so as to minimize the scatter of the final fits appropriately in all wavebands. Here we describe the generalized approach to Bayesian model fitting and then specialize to a detailed description of applying Bayesian linear model fitting to the mid-infrared period–luminosity relations of RR Lyrae variable stars. For this example application we quantify the improvement afforded by using a Bayesian model fit. We also compare distances previously predicted in our example application to recently published parallax distances measured with the *Hubble Space Telescope* and find their agreement to be a vindication of our methodology. Our intent with this article is to spread awareness of the benefits and applicability of this Bayesian approach and encourage future period–luminosity relation investigations to consider employing this analysis method.

4.1 Introduction

The period–luminosity relations of pulsating variable stars — typically variables of types RR Lyrae, Cepheid, and Mira — are invaluable tools for constructing the rung of the distance ladder that connects the Milky Way to other nearby galaxies, extending to ~ 5 Mpc. Recent applications of this distance measurement technique using Cepheids have successfully mated Cepheid distances to SNe Ia host galaxies and constrained the Hubble Constant, H_0, to 3.3% (Riess et al. 2011). The authors have recently derived mid-infrared period–luminosity relations for RR Lyrae variables (Klein et al. 2011), and demonstrated their potential to serve as important distance indicators for the Large Magellanic Cloud. Additionally, continuing studies of Miras (Whitelock et al. 2008) confirm their potential to provide accurate distances even beyond the reach of Cepheids.

The accuracy and precision of any distance measurement made using the period–luminosity relation of a variable star, or any population of variable stars within a distant system, is dominated by the uncertainty of the locally calibrated period–luminosity relation. The general method is to fit a period–luminosity relation to the variables for which trigonometric parallax measurements are available (Feast & Catchpole 1997). For more than the past decade only *Hipparcos* (original catalog published as Perryman & ESA (1997), and improved reduction by van Leeuwen (2007)) could provide these required local distance measurements to a significantly large sample of local stars with the accuracy necessary. More recently, the *Hubble Space Telescope* Fine Guidance Sensor has been used to provide higher accuracy parallax measurements for nine Cepheids (Benedict et al. 2007) and five RR Lyrae variables (Benedict et al. 2011). In the coming decade, with the launch of the ESA's astrometry mission *Gaia*, the sample size of potential period–luminosity relation calibrators and the accuracy of their parallax distances will be significantly augmented (Cacciari 2009a).

Period–luminosity relations are typically calibrated using straightforward, simple, frequentist statistical techniques (see, for example, Sollima et al. (2006) fitting RR Lyrae variables, Matsunaga et al. (2006) fitting type II Cepheids, Feast & Catchpole (1997) fitting classical Cepheids, and Glass & Evans (2003) fitting Miras). At the basic level, a period–luminosity relation is an equation of the form $M = \alpha \log P + \beta$, where M is the absolute magnitude (in a given waveband), α is the slope, P is the period (in days), and β is the zero point magnitude (which itself may be a function of metallicity). This simple linear equation can be reliably fit with the method of least squares, and the accuracy of the fit can be assessed with the standard deviation of the residuals, a metric commonly referred to as the scatter.

A significant limitation of the least squares regression method is that it does not make use of the full prior probability distribution of the parallax distances. Allowing the distances more flexibility to move within their prior distributions translates into posterior distances that are more consistent with the fitted period–luminosity relation and therefore more accurate (on average) than the prior distance mean. A second limitation is that this traditional method is not easily adapted to fitting period–luminosity relations of the same variables in different wavebands simultaneously. Intelligently combining data from multiple wavebands

has the potential to produce better final period–luminosity relation fits.

A Bayesian approach for fitting the period–luminosity relation parameters overcomes these traditional limitations. Barnes et al. (2003) discusses in substantial depth the application of a Bayesian approach to the Cepheid distance scale, using physical pulsational models and radial velocity data. In the present work we confine our examination to the application of Bayesian methods in calibrating, purely phenomenologically, the period–luminosity relations of pulsating variable stars. We use as our example the calibration performed by Klein et al. (2011). In Section 4.2 we describe the generalized Bayesian modeling approach. In Section 4.3 we work through the application of this Bayesian approach to mid-infrared period–luminosity relations of RR Lyrae variables, as first demonstrated by the authors in Klein et al. (2011). We perform a traditional, least squares fit to the RR Lyrae period–luminosity relations and compare with the fits from our Bayesian approach in Section 4.4. Finally, in Section 4.5 we draw conclusions and discuss future applications.

4.2 Technical Explanation of Bayesian Period–Luminosity Relation Fitting

An excellent and thorough description of Bayesian fitting of linear models is provided in Gelman et al. (2003). Barnes et al. (2003) applies Bayesian analysis to the Cepheid distance scale, but does not use linear Bayesian model fitting for deriving the Cepheid period–luminosity relation. Here we review the foundation of the Bayesian approach.

If we assume that our data, denoted by y, follows some pattern or rule or model, as in common in nature, and denote the model parameter(s) by θ, then we may write the probability of the model being true as $p(\theta)$ and the posterior probability that the model is true given our observed data y as $p(\theta|y)$. The probability $p(\theta)$ is the prior distribution on the model, it is what we know before making observations. We can also define the likelihood as the probability $p(y|\theta)$ of observing the particular data y conditioned on the model θ. Thus, we have the unnormalized Bayes' theorem

$$p(\theta|y) \propto p(\theta)p(y|\theta), \tag{4.1}$$

the probability of the model being true given the data is proportional to the prior probability of the model times the likelihood.[2]

To fit observed data y to a model with parameters θ we simply evaluate equation 4.1 throughout a fine grid of values for θ to create the posterior distribution of the model. We

[2]The exact (normalized) form of Bayes' theorem is

$$p(\theta|y) = \frac{p(\theta)p(y|\theta)}{p(y)}, \tag{4.2}$$

but for our purposes we implement equation 4.1 by Monte Carlo computer simulation and thus the analytical normalization can be ignored.

can examine this posterior distribution (through analysis of repeated random draws from the distribution) to find the most likely fit parameters, as well as uncertainty in these parameters. Furthermore, this posterior distribution reveals the most likely true values for the data y, which is of course conditional on the prior distributions of the data.

4.3 Application to Mid-infrared RR Lyrae Variables

In Klein et al. (2011) we apply Bayesian model fitting to a sample of 76 RR Lyrae light curves observed with the Wide-Field Infrared Survey Explorer (*WISE*) (Wright et al. 2010). Each of the RR Lyrae variables was well-observed in three *WISE* bands (W1 at 3.4, W2 at 4.6, and W3 at 12 μm) and their prior distance distributions are generated by applying the RR Lyrae M_V–[Fe/H] relation given in Chaboyer (1999) to their *Hipparcos* mean flux V-band magnitudes, correcting for dust extinction.

Using the nomenclature of Section 4.2 we define our observed data for each RR Lyrae star as $y = (m, P)$, the apparent magnitude and period. The unknown fit parameters are then $\theta = (\mu, M_0, \alpha, \sigma)$, the distance modulus, absolute magnitude zero point, period–luminosity relation slope, and scatter. We can also define $\beta = (\mu, M_0, \alpha)$ so that then $\theta = (\beta, \sigma)$. We put an informative normal prior on each μ (from the V-band distance estimates) and we put a flat prior on everything else.

We then write our statistical model of the period–luminosity relationship as

$$m_{ij} = \mu_i + M_{0,j} + \alpha_j \log_{10}(P_i/P_0) + \epsilon_{ij}, \tag{4.3}$$

where μ_i is the distance modulus for ith RR Lyrae star, $M_{0,j}$ is the absolute magnitude zero point for the jth *WISE* band at $P = P_0$, where $P_0 = 0.50118$ day is the mean period of the sample, and α_j is the slope of the period–luminosity relationship in the jth band. We assume that any extinction is negligible in these bands. The error terms ϵ_{ij} are independent zero-mean Gaussian random deviates with variance $(\sigma\sigma_{m_{ij}})^2$, which describe the intrinsic scatter in the m_{ij} about the model, where σ is a free parameter which is an unknown scale factor on the known measurement errors, $\sigma_{m_{ij}}$.[3] We fit the model (equation 4.3) using a Bayesian procedure, outlined below and explicitly described in Section 4 of Klein et al. (2011).

First, we assume a normal (Gaussian) prior distribution on each of the distance moduli with mean $\mu_{0,i}$ and standard deviation $\sigma_{\mu_{0,i}}$, as described above. For the other parameters in our model (equation 4.3), we assume a flat, noninformative prior distribution.

Our likelihood is normal:

$$p(m, P|\beta, \sigma) \propto p(m|\beta, \sigma) = N(\mathbf{X}\beta, \sigma^2 \mathrm{diag}(\sigma_m^2)), \tag{4.4}$$

where N denotes the multivariate normal distribution. Note that $p(m, P|\theta) \propto p(m|\theta)$ since P is independent of m and doesn't depend on any of the parameters θ.

[3]The average measurement error, σ_m, is 0.013, 0.013, and 0.045 mag in W1, W2, and W3, respectively.

In the nomenclature of Section 4.2 we are solving for

$$p(\theta|y) = p(\beta, \sigma|m, P) = p(\beta|m, P, \sigma)p(\sigma|m, P). \tag{4.5}$$

The joint posterior distribution, $p(\beta, \sigma|m, P)$, can be sampled by first drawing from $p(\sigma|m, P)$ and then, conditional on that draw, selecting from $p(\beta|m, P, \sigma)$. The posterior distribution for β, conditional on the value of σ, follows the multivariate normal distribution,

$$\beta|m, P, \sigma \sim N(\widehat{\beta}, (\mathbf{X}'_*\Sigma_*^{-1}\mathbf{X}_*)^{-1}), \tag{4.6}$$

where $\widehat{\beta}$ is the standard maximum likelihood (weighted least squares) solution, $\widehat{\beta} = (\mathbf{X}'_*\Sigma_*^{-1}\mathbf{X}_*)^{-1}\mathbf{X}'_*\Sigma_*^{-1}m_*$. Unlike the posterior distribution of β (given σ), the posterior distribution of σ, $p(\sigma^2|m, P)$, does not follow a simple conjugate distribution. Instead, the distribution follows the form

$$p(\sigma^2|m, P) \propto \frac{p(\beta)p(\sigma^2)L(m|P, \beta, \sigma)}{p(\beta|m, P, \sigma)}, \tag{4.7}$$

where the prior on β is proportional to the informative prior on μ, the flat prior on σ is $p(\sigma^2) \propto \sigma^{-2}$, and the data likelihood L is the product, over all observed magnitudes, of the Gaussian likelihood of the data given the model (equation 4.3) with all parameters specified.

We draw samples from our joint posterior distribution $p(\beta, \sigma|m, P)$ using equations 4.6 and 4.7 in conjunction. In practice, we compute[4] $p(\sigma^2|m, P)$ over a fine grid of σ values using equation 4.7, and then draw a sample of σ from this density. For each sampled σ, we subsequently draw a β from equation 4.6, conditional on the drawn σ value. We repeat this process 10,000 times to characterize the joint posterior distribution. Using a large sample from this joint posterior distribution, we can compute quantities of interest such as the maximum *a posteriori* slopes and zero points of the period–luminosity relationship of each *WISE* band, the intrinsic scatter of the data around the period–luminosity relationship in each band, and the spread in the *a posteriori* distribution of the period–luminosity relation parameters.

4.4 Comparison with Traditional Fit

To demonstrate the improvement in the fit from the Bayesian approach, which in turn means an improvement in the predicted distances resulting from the calibrated period–luminosity relation, we compare it to a traditional least squares regression fit. Using the same prior distances (technically, the expectation value of the prior distance distributions), period measurements, and observed *WISE* mean flux magnitudes we perform a least squares fit for the slope α and zero point β of the period–luminosity relation. We calculate the scatter

[4] Assuming that $\beta = \widehat{\beta}$. Several iterations show that the posterior distribution of σ is insensitive to the assumed choice of β.

(1σ) as the standard deviation of the residuals to the fit. The fit parameters and scatter are presented in Table 4.1. In Fig. 4.1 we overplot in red the least squares period–luminosity relation fits into Fig. 5 from Klein et al. (2011).

Table 4.1: Comparison of least squares (subscript LS) and Bayesian (subscript B) fits to the *WISE* RR Lyrae period–luminosity relations. We calculate the scatter (1σ) as the standard deviation of the residuals to each fit.

Band	$\alpha_{\rm LS}$	$\beta_{\rm LS}$	$1\sigma_{\rm LS}$	$\alpha_{\rm B}$	$\beta_{\rm B}$	$1\sigma_{\rm B}$
W1	−0.420	−1.675	0.124	−0.421	−1.681	0.007
W2	−0.425	−1.713	0.124	−0.423	−1.715	0.007
W3	−0.503	−1.763	0.149	−0.493	−1.688	0.074

As expected, the actual parameters of the period–luminosity relations, zero point and slope, are statistically consistent. Comparison of their 1σ scatter, however, illustrates that the Bayesian approach produces a set of period–luminosity relations with nearly eighteen times lower scatter in *WISE* bands W1 and W2 and two times lower scatter in W3. The Bayesian fit's significant reduction in scatter primarily results from allowing the posterior distances to be fit from within the prior distances' distributions. Thus, the scatter of the Bayesian fit more closely approaches the true intrinsic scatter.

4.5 Conclusions

Table 4.1 and Fig. 4.1 clearly demonstrate the Bayesian modeling approach's ability to produce a set of more tightly constrained period–luminosity relations. This benefit of the approach primarily arrises from its taking into account the full prior distribution on the distances and allowing the fit to refine these distance distributions. The traditional least squares fitting method instead utilizes only the expectation value of these prior distances and leaves them unchanged during the fitting procedure, hence producing a fit with significantly larger scatter.

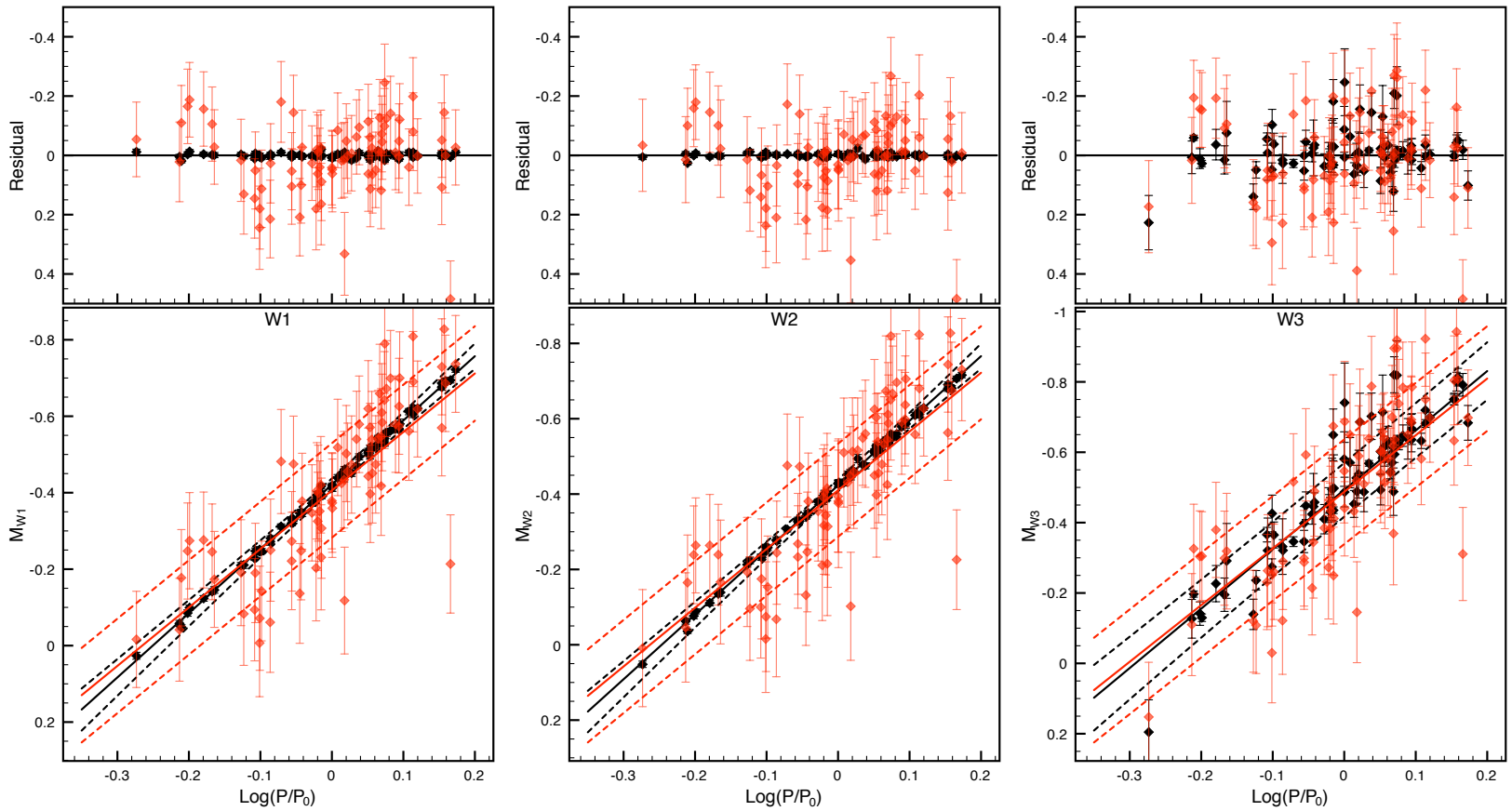

Figure 4.1: Period-luminosity relations for W1, W2, and W3 (left to right). Results of the Bayesian fitting procedure are shown in black, and the results of the least squares fit are overplotted in red. In each figure, the solid lines show the models' predictions of the RR Lyrae absolute magnitude, as a function of RR Lyrae period. The dashed lines show the $\pm 1\sigma$ scatter. The top panel of each plot shows the residual spread around the best fit model of each fit procedure. The error bars of the Bayesian fit for W1 and W2 are smaller than the diamond markers.

It is natural to inquire as to whether the Bayesian model is overly constrained. That is, one must be careful not to allow the posterior distance distributions to diverge significantly from the prior distributions. To evaluate this property of the Bayesian fit it is reasonable to compute and examine the prior, posterior, and prediction probability densities, as shown for four examples in Fig. 7 of Klein et al. (2011). Finally, we note that the the newest *HST* parallax measurements for the four RR Lyrae variables V*RRLyr, V*RZCep, V*SUDra, and V*UVOct (Benedict et al. 2011) were not yet available for use as distance priors in the Bayesian fit performed in Klein et al. (2011), however the distance posteriors produced in that work compare quite well with these newly published parallax distances (see Table 4.2). We interpret these predictions of the parallax distances as a strong vindication of our methodology.

Table 4.2: Recently published RR Lyrae *HST* parallax distances (Benedict et al. 2011) compared with the values which Klein et al. (2011) previously predicted through Bayesian linear model fitting of the mid-infrared period–luminosity relations. All distances are given in parsecs.

Name	*HST* d	PL Fit d	Bayesian Prior d
V*RRLyr	265±9	253±2	262±15
V*RZCep	394±30	381±6	405±23
V*SUDra	704±80	696±7	696±40
V*UVOct	585±34	536±4	553±32

While it is true that the Bayesian modeling method described in this article is not strictly applicable to all situations (for example, when fitting data which share a common distance prior as is standard for studies of pulsating variables in the Large Magellanic Cloud), it is nevertheless an invaluable tool for calibrating the Galactic period–luminosity relations of RR Lyrae, Cepheid, and Mira variables. This approach also has the potential to improve the model fits of other phenomena, such as the calibration of other distance indicators (SNe Ia, planetary nebulae, tip of the red giant branch, etc). Our intent with this article is to spread awareness of the benefits and applicability of this Bayesian approach and encourage future period–luminosity relation investigations to consider employing this powerful analysis method.

Acknowledgments

The authors acknowledge the generous support of a CDI grant (#0941742) from the National Science Foundation. JSB and CRK were also partially supported by grant NSF/AST-100991. This research has made use of NASA's Astrophysics Data System.

Chapter 5

Mid-infrared Period–Luminosity Relations of RR Lyrae Stars Derived from the AllWISE Data Release

An earlier version of this chapter was previously published as MNRAS 440, L96 with coauthors Joseph W. Richards, Nathaniel R. Butler, and Joshua S. Bloom.[1]

Abstract

We use photometry from the recent AllWISE Data Release of the *Wide-field Infrared Survey Explorer* (*WISE*) of 129 calibration stars, combined with prior distances obtained from the established M_V–[Fe/H] relation and *Hubble Space Telescope* trigonometric parallax, to derive mid-infrared period–luminosity relations for RR Lyrae pulsating variable stars. We derive relations in the $W1$, $W2$, and $W3$ wavebands (3.4, 4.6, and 12 μm, respectively), and for each of the two main RR Lyrae sub-types (RRab and RRc). We report an error on the period–luminosity relation slope for RRab stars of 0.2. We also fit posterior distances for the calibration catalog and find a median fractional distance error of 0.8 per cent.

5.1 Introduction

As calibratable standard candles, RR Lyrae pulsating variable stars provide a means to obtain highly precise (1-2 per cent error) distance measurements within the range of 1-100 kpc. These old (age $\gtrsim 10 \times 10^9$ yr) Population II objects permeate the Milky Way Halo and Bulge, and many reside in the Disc. Preston (1964) and Smith (1995) both provide excellent reviews of this class of variable stars. We refer the reader to Section 5 of Sandage

[1] Klein et al. (2014b): Copyright 2014, The Authors. Published by Oxford University Press on behalf of the Royal Astronomical Society.

& Tammann (2006) for a review of optical (V-band) implementations of RR Lyrae stars as distance indicators.

It is well known that in optical wavebands the RR Lyrae period–luminosity relation is negligible (nearly no slope in the linear relation), but that at near- and mid-infrared wavebands the slope steepens and the relation is quite constrained. Figure 4 of Madore et al. (2013) illustrates this phenomenon, and indicates an expected asymptote in the RRab period–luminosity relation slope of around -2.4 to -2.8. Additionally, since much of the Milky Way RR Lyrae population resides behind significant interstellar dust, the markedly reduced extinction at infrared wavelengths (demonstrated in Figure 8 of Fritz et al. 2011) is often lower than photometric errors. Thus, at mid-infrared wavelengths, the need for dust extinction corrections to set mid-infrared luminosity vanishes.

In the present work we calibrate mid-infrared period–luminosity relations for RR Lyrae stars using the AllWISE Data Release of the *Wide-field Infrared Survey Explorer* (*WISE*) and *NEOWISE* missions (Wright et al. 2010; Mainzer et al. 2011). Much of this work is a continuation of the methodology developed in Klein et al. (2011), which performed a similar analysis using the *WISE* Preliminary Data Release. The earlier Preliminary Data Release included only the first 105 days of the *WISE* mission, covering 57 per cent of the sky. The AllWISE Data Release (made public 2013 November 13) covers the entire sky and combines all the *WISE* survey data from 2010 January 7 to 2011 February 1. By using this more comprehensive dataset the present analysis incorporates 129 RR Lyrae calibration stars, whereas Klein et al. (2011) made use of only 76 RR Lyrae period–luminosity relation calibrators. Furthermore, the longer temporal baseline and improved photometric accuracy of the AllWISE Data Release provides for more accurate mean-flux magnitude measurements of the calibration stars.

A similar investigation into the mid-infrared period–luminosity relations of RR Lyrae stars is presented in Dambis et al. (2014). The calibrations performed in Dambis et al. (2014) use RR Lyrae stars in 15 Galactic globular clusters, with distances extending beyond 15 kpc.[2] It is encouraging to note that the period–luminosity relation slopes reported in Dambis et al. (2014), modulo a slight metallically dependance, agree so well with the calibrations published in the present work.

The applications for RR Lyrae stars as distance indicators are diverse and fundamental to many areas of astronomical inquiry. They are found throughout the Milky Way Halo and Bulge, pervade the Disc, and are still shining in neighboring dwarf galaxies.

This paper is outlined as follows. We present a brief description of the *WISE* and ancillary data in Section 5.2. In Section 5.3 we review the employed light curve analysis methodology. In Section 5.4 we present the derived period–luminosity relations, and in Section 5.5 we discuss the conclusions and future implications of this work.

[2]The calibration sample used in the present work, described in Section 5.2, is comprised of nearby ($\leqslant 2.5$ kpc) stars with well-detected *WISE* light curves.

5.2 Data Description

WISE provides imaging data in four mid-infrared wavebands: $W1$ centered at 3.4 μm, $W2$ centered at 4.6 μm, $W3$ centered at 12 μm, and $W4$ centered at 22 μm. Although the original *WISE* mission was designed for static science goals, the orbit and survey strategy of the *WISE* spacecraft (described in Wright et al. 2010) are conducive to recovering light curves of periodic variables with periods $\lesssim$ 1.5 day, which is well-matched to RR Lyrae variables.

In this analysis we make use of the most recent *WISE* data release, AllWISE. The AllWISE Data Release (made public 2013 November 13) combines the 4-Band Cryogenic Survey (main *WISE* mission covering the full sky 1.2 times from 2010 January 7 to 2010 August 6), the 3-Band Cryogenic survey (first three wavebands, 30 per cent of the sky from 2010 August 6 to 2010 September 29), and the *NEOWISE* post-cryogenic survey (first two wavebands, covering 70 per cent of the sky from 2010 September 20 to 2011 February 1). The individual photometry epochs were retrieved from the AllWISE Multiepoch Photometry Database.

As in Klein et al. (2011) we employ the catalog of 144 relatively local ($\leqslant$ 2.5 kpc) RR Lyrae variables developed by Fernley et al. (1998). Fifteen of these stars are excluded from our present analysis because they were not well-detected by *WISE*. *WISE* photometry data with any quality flags were rejected for the period–luminosity relation fits (most common cause was confusion with neighbouring sources, in part due to the $\sim$ 6.3 arcsec PSF of *WISE*).

Also as in Klein et al. (2011), *Hipparcos* photometry (Perryman & ESA 1997) is transformed into V-band (Gould & Popowski 1998), corrected for dust extinction (using the line-of-sight extinction from Schlegel et al. 1998 and the R factor from Schultz & Wiemer 1975), and combined with the Chaboyer (1999) M_V–[Fe/H] relation to yield prior distance moduli, $\mu_{\rm prior}$. Precise trigonometric parallax angles for four of the stars (RRLyr, UVOct, XZCyg, and SUDra; all of the RRab subclass) have been previously measured with the *Hubble Space Telescope* and published in Benedict et al. (2011).[3] For these four stars the more precise, parallax-derived distance moduli are used in the period–luminosity relation fits. We note that the the distance moduli derived from the metallicity–luminosity relation for these four stars is in statistical agreement (within 2σ) with the parallax-derived distances.

A significant difference between the present work and that of Klein et al. (2011) is that the two primary RR Lyrae subclasses (RRab and RRc stars) are now treated independently. Previously, in Klein et al. (2011) all the RR Lyrae stars were fit together, which (as noted by Madore et al. 2013) is physically inappropriate because they follow different period–luminosity relations (RRab stars oscillate in the fundamental mode, whereas RRc stars do so in the first overtone). It is common practice to "fundamentalize" the periods of the RRc stars, as in Dall'Ora et al. (2004), and use them to supplement the RRab period–luminosity fit. In the present analysis we instead treat the two subclasses independently, so as to calibrate both the RRab and RRc period–luminosity relations.

[3]RRc star RZCep also has an HST-measured parallax, but this star was rejected from the fit following the procedure described in Section 5.3.

5.3 Light Curve Analysis Methods

The light curve analysis methods employed in the present work are an evolution of those described in Klein et al. (2011). Mean-flux magnitudes are measured from harmonic model fits to the phase-folded *WISE* photometry. To more accurately assess the uncertainty associated with the measured mean-flux magnitude for each star, a parametric bootstrapping procedure was performed. The *WISE* photometry was resampled (assuming a normal distribution) and refit with a harmonic model 5,000 times to generate a distribution of mean-flux magnitude measurements. The standard deviation of this bootstrapped mean-flux magnitude distribution was taken to be the uncertainty used later in the period–luminosity relation fits.

The 5,000 harmonic models generated by the bootstrapping procedure were averaged to produce a mean harmonic model. This mean harmonic model yields a robust light curve amplitude. Furthermore, the standard deviation of the 5,000 harmonic models at each phase value provides a metric of how well the shape of the true light curve is recovered in the *WISE* photometry (if there is a lot of spread in the distribution of harmonic models, then the photometry is not accurate enough to reveal the shape of the true brightness oscillation). To improve the quality of the dataset used in the period–luminosity relation fits, any *WISE* light curve with a bootstrapped harmonic model maximum standard deviation larger than its robust amplitude measurement was excluded. This procedure serves to ensure that only stars with *WISE* light curves well-fit by the harmonic model (i.e., those exhibiting clear sinusoidal-like oscillation) are used in the period–luminosity relation fits.

One final step before performing the period–luminosity relation derivations described in Section 5.4 was to conduct a traditional least-squares linear regression for each relation independently. The resultant fitted zero points and slopes were incorporated into the full simultaneous Bayesian derivation as the starting values for the MCMC traces. Additionally, this procedure allowed for the identification and rejection of anomalous ($> 2\sigma$) outliers.

The final dataset used in the period–luminosity relation fits is comprised of 104 RRab stars with $W1$ photometry, 104 RRab stars with $W2$ photometry, 66 RRab stars with $W3$ photometry, 19 RRc stars with $W1$ photometry, 19 RRc stars with $W2$ photometry, and 9 RRc stars with $W3$ photometry. Table 5.1 presents all of the apparent magnitude photometry used in the period–luminosity relation fits, as well as the prior distances and the resultant posterior distances calculated during the fitting.

5.4 Period–Luminosity Relations

The present derivation of period–luminosity relations is very similar to the Bayesian approach first described in Klein et al. (2011) and later formalised in Klein et al. (2012a). In brief, our statistical model of the period–luminosity relationship is

$$m_{ij} = \mu_i + M_{0,j} + \alpha_j \log_{10}(P_i/P_0) + \epsilon_{ij} \tag{5.1}$$

where m_{ij} is the observed apparent magnitude of the ith RR Lyrae star in the jth *WISE* waveband, μ_i is the distance modulus for the ith RR Lyrae star, $M_{0,j}$ is the absolute magnitude zero point for the jth waveband, α_j is the slope in the jth waveband, P_i is the period of the ith RR Lyrae star in days, P_0 is a period normalization factor (we use $P_{0,\mathrm{RRab}} = 0.55$ day and $P_{0,\mathrm{RRc}} = 0.32$ day), and the ϵ_{ij} error terms are independent zero-mean Gaussian random deviates with variance $\left(\sigma\sigma_{m_{ij}}\right)^2$. The error terms describe the intrinsic scatter in m_{ij} about the model, where σ is a free parameter which is an unknown scale factor on the known measurement errors, $\sigma_{m_{ij}}$. We initialize σ with a flat prior and find that its posterior distribution is approximately normally distributed with mean 1.42 (1.16) and standard deviation 0.08 (0.18) for the RRab (RRc) fit.

We fit the three linear relationships simultaneously using a Bayesian MCMC method. After the fit converges we draw 150,000 samples of the posterior model parameters. The posterior distributions are well-represented as Gaussian, so we report the traditional distribution mean and standard deviation in the zero points, slopes, and posterior distance moduli. The calibrated period–luminosity relations for RRab stars are:

$$M_{W1} = -0.495\,(\pm0.013) - 2.38\,(\pm0.20) \times \log\left(P/0.55\text{ d}\right) \tag{5.2}$$
$$M_{W2} = -0.490\,(\pm0.013) - 2.39\,(\pm0.20) \times \log\left(P/0.55\text{ d}\right) \tag{5.3}$$
$$M_{W3} = -0.537\,(\pm0.013) - 2.42\,(\pm0.20) \times \log\left(P/0.55\text{ d}\right) \tag{5.4}$$

The calibrated period–luminosity relations for RRc stars are:

$$M_{W1} = -0.231\,(\pm0.031) - 1.64\,(\pm0.62) \times \log\left(P/0.32\text{ d}\right) \tag{5.5}$$
$$M_{W2} = -0.216\,(\pm0.031) - 1.70\,(\pm0.62) \times \log\left(P/0.32\text{ d}\right) \tag{5.6}$$
$$M_{W3} = -0.232\,(\pm0.032) - 1.71\,(\pm0.65) \times \log\left(P/0.32\text{ d}\right) \tag{5.7}$$

The calibrated period–luminosity relations are plotted in Fig. 5.1. In each panel the solid black line denotes the best-fit period–luminosity relation, which corresponds to the above listed equations. The dashed lines indicate the 1-σ prediction uncertainty for application of the best-fit period–luminosity relation to a new star with known period. The plotted points are the predictions for each star produced from jackknife fits (produced by withholding that star from input to a new fit, then using that new fit to predict the "jackkniffed" star's absolute magnitude). The absolute magnitude error on each datapoint is dominated by the prediction error of the fit (which is why it generally tracks with the 1-σ prediction uncertainty envelope shown in dashed black lines). Note that these error bars do not correspond with the scatter of the data about the best fit line, nor should there be such a theoretical expectation. The minimum 1-σ prediction uncertainty is given in the upper left of each panel. Blazhko-affected stars are indicated with diamond symbols, but they were not found to deviate from the fits. This is likely because the amplitude modulation at mid-infrared wavelengths is significantly reduced, but further study is needed to investigate this issue.

As a check on the fitted period–luminosity relations we compare the prior distance moduli, μ_{prior}, with the posterior distance moduli that were produced during the fitting, μ_{post}. Fig. 5.2

confirms that there is no obvious discrepancy between the distributions of the prior and posterior distances. The residual panel demonstrates that the posterior distances are in very good statistical agreement with the prior distances. The error bars here, in contrast with the prediction uncertainty error bars used in Fig. 5.1, are derived from the $\mu_{\rm prior}$ and $\mu_{\rm post}$ distributions and should correspond with the scatter observed in the residual panel. In fact, 112 of 129 (87 per cent) of the residual data points are within one error bar length of zero, indicating that the errors are slightly overestimated.

The prediction uncertainties illustrated in Fig. 5.1 are intrinsic to the waveband-specific period–luminosity relations. The posterior distances produced through the simultaneous Bayesian linear regression, presented in Table 5.1 and plotted in Fig. 5.2, are improved beyond the single-waveband prediction by using all three wavebands. This is representative of the advantages of employing a simultaneous fitting method.

5.5 Conclusions

We have presented derivations of the period–luminosity relations at 3.4, 4.6, and 12 μm (first three wavebands of *WISE*) using AllWISE photometry for 129 calibrating stars. The employed Bayesian simultaneous linear regression fitting method yielded improved distances for these 129 calibrators with a median fractional error of 0.8 per cent.

Although the presented relations are intrinsic to the *WISE* photometric system, we expect that similarly well-constrained mid-infrared period–luminosity relations particular to the *Spitzer Space Telescope* or, eventually, the *James Webb Space Telescope*, can be constructed following the same methodology. Translating the *WISE* relations into other instrumental photometric systems is possible, but introduces significant systematic uncertainty.

The *WISE* spacecraft has recently been reactivated to observe with its $W1$ and $W2$ wavebands for the period 2014–2016. This will allow for continued observations of a few thousand nearby RR Lyrae stars (within about 6 kpc), most of which have yet to be discovered and classified. The tightly-constrained mid-infrared period–luminosity relations will enable these stars to serve as very well-localized "test particles" in the Galactic Disc and Halo.

Acknowledgments

The authors acknowledge the generous support of a CDI grant (#0941742) from the National Science Foundation. J.S.B. and C.R.K. were also partially supported by grant NSF/AST-100991. This publication makes use of data products from the *Wide-field Infrared Survey Explorer*, which is a joint project of the University of California, Los Angeles, and the Jet Propulsion Laboratory/California Institute of Technology, funded by the National Aeronautics and Space Administration. This publication also makes use of data products from *NEOWISE*, which is a project of the Jet Propulsion Laboratory/California Institute of Technology, funded by the Planetary Science Division of the National Aeronautics and Space Administration. This research has made use of NASA's Astrophysics Data System.

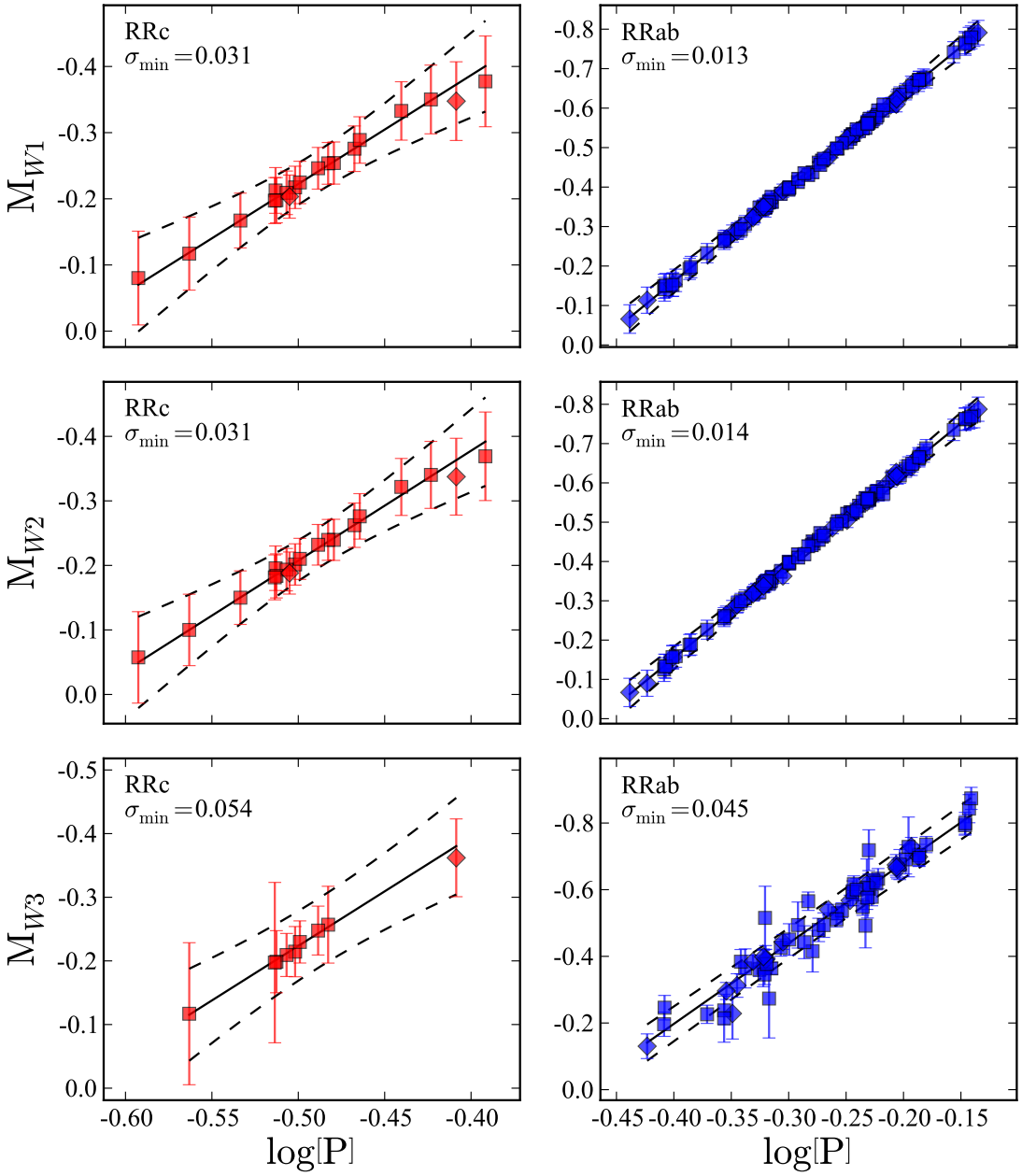

Figure 5.1: Period–Luminosity relations derived for each *WISE* waveband. Blazhko-affected stars, as identified via http://www.univie.ac.at/tops/blazhko/Blazhkolist.html, are denoted with diamonds, stars not known to exhibit the Blazhko effect are denoted with squares. The solid black line in each panel denotes the best-fit period–luminosity relation. The dashed lines indicate the 1-σ prediction uncertainty for application of the best-fit period–luminosity relation to a new star with known period. See Section 5.4 for further explanation, particularly with respect to the seemingly overestimated error bars.

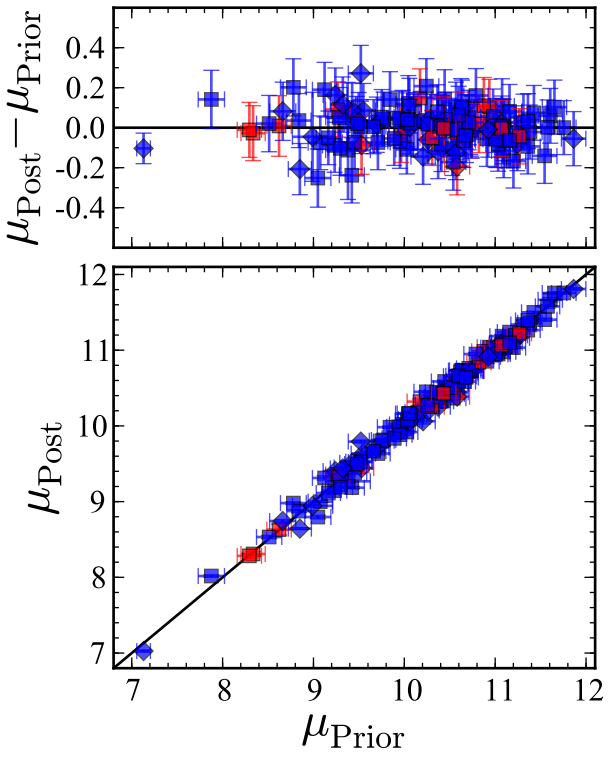

Figure 5.2: Prior vs posterior distance moduli. RRab stars are in blue, RRc stars in red. Blazhko-affected stars are denoted with diamonds, stars not known to exhibit the Blazhko effect are denoted with squares.

Table 5.1: Catalog of calibration RR Lyrae stars.

Name	Type	Blazhko Affected?	Period (d)	*WISE* Apparent Magnitudes $W1$	$W2$	$W3$	Model Amplitudes $W1$	$W2$	$W3$	Prior Distance $\mu_{\rm prior}$	Posterior Distance $\mu_{\rm post}$	d (pc)
AACMi	RRab	False	0.4763	10.238±0.006	10.249±0.005	10.222±0.054	0.286	0.260	0.113	10.444±0.146	10.587±0.017	1310±10.3
ABUMa	RRab	False	0.5996	9.570±0.005	9.592±0.004	9.530±0.026	0.173	0.136	0.070	10.044±0.141	10.163±0.016	1078±8.2
AEBoo	RRc	False	0.3149	9.713±0.004	9.721±0.004	9.665±0.023	0.099	0.099	0.083	9.965±0.134	9.928±0.032	967±14.1
AFVir	RRab	False	0.4837	10.698±0.006	10.712±0.009	··· ± ···	0.266	0.203	···	11.093±0.134	11.063±0.017	1632±12.6
AMTuc	RRc	False	0.4058	10.569±0.004	10.578±0.004	··· ± ···	0.104	0.103	···	11.019±0.133	10.970±0.068	1563±49.3
AMVir	RRab	True	0.6151	10.096±0.005	10.097±0.005	··· ± ···	0.218	0.206	···	10.676±0.134	10.705±0.018	1383±11.4
APSer	RRc	False	0.3408	10.162±0.005	10.170±0.005	··· ± ···	0.105	0.090	···	10.418±0.133	10.435±0.034	1222±19.2
ARHer	RRab	True	0.4700	··· ± ···	10.270±0.004	··· ± ···	···	0.184	···	10.600±0.134	10.596±0.018	1316±10.7
ARPer	RRab	False	0.4255	8.564±0.005	8.570±0.004	8.570±0.013	0.220	0.248	0.242	9.048±0.144	8.796±0.024	574±6.3
ATAnd	RRab	False	0.6169	9.027±0.006	9.021±0.005	··· ± ···	0.147	0.175	···	9.709±0.135	9.635±0.018	845±7.1
ATVir	RRab	False	0.5258	10.217±0.006	10.204±0.005	10.239±0.061	0.212	0.247	0.249	10.670±0.120	10.655±0.014	1352±8.6
AUVir	RRc	False	0.3432	10.759±0.004	10.773±0.005	··· ± ···	0.095	0.078	···	10.936±0.133	11.040±0.035	1614±25.9
AVPeg	RRab	False	0.3904	9.303±0.005	9.326±0.004	9.255±0.020	0.206	0.250	0.087	9.376±0.148	9.451±0.030	777±10.8
AVVir	RRab	False	0.6569	10.508±0.004	10.510±0.005	··· ± ···	0.264	0.238	···	11.076±0.134	11.185±0.022	1726±17.5
AXLeo	RRab	False	0.7268	10.879±0.006	10.895±0.008	··· ± ···	0.186	0.154	···	11.606±0.134	11.666±0.030	2153±29.5
BBEri	RRab	False	0.5699	10.194±0.004	10.205±0.003	10.139±0.034	0.216	0.242	0.078	10.736±0.134	10.729±0.014	1399±9.1
BCDra	RRab	False	0.7196	10.077±0.003	10.088±0.003	10.010±0.031	0.206	0.183	0.059	10.909±0.135	10.853±0.028	1481±19.3
BHPeg	RRab	True	0.6410	8.975±0.005	8.994±0.005	8.905±0.018	0.205	0.180	0.034	9.549±0.134	9.635±0.020	845±8.0
BKDra	RRab	False	0.5921	10.003±0.003	9.997±0.003	9.991±0.022	0.257	0.271	0.151	10.566±0.134	10.569±0.016	1300±9.3
BNPav	RRab	False	0.5672	11.233±0.006	11.230±0.006	··· ± ···	0.319	0.297	···	11.652±0.134	11.755±0.015	2244±15.1
BNVul	RRab	False	0.5941	8.611±0.006	··· ± ···	8.557±0.012	0.256	···	0.291	9.422±0.138	9.184±0.017	687±5.4
BPPav	RRab	False	0.5271	··· ± ···	11.311±0.005	··· ± ···	···	0.320	···	11.756±0.134	11.756±0.014	2245±14.8
BRAqr	RRab	False	0.4819	10.294±0.006	10.313±0.007	··· ± ···	0.308	0.315	···	10.569±0.138	10.657±0.017	1354±10.4
BTDra	RRab	False	0.5887	10.410±0.003	10.420±0.004	10.375±0.041	0.270	0.250	0.195	11.094±0.133	10.978±0.015	1569±11.1
BVAqr	RRab	True	0.3644	9.996±0.005	9.995±0.005	··· ± ···	0.056	0.087	···	10.206±0.134	10.062±0.036	1029±16.9
BXLeo	RRc	False	0.3628	10.663±0.006	10.679±0.006	··· ± ···	0.109	0.081	···	10.876±0.134	10.986±0.044	1575±31.7
CGLib	RRc	False	0.3068	10.129±0.005	10.128±0.005	··· ± ···	0.091	0.096	···	10.173±0.142	10.321±0.034	1159±18.2
CGPeg	RRab	False	0.4671	9.853±0.005	9.862±0.005	··· ± ···	0.216	0.238	···	10.148±0.140	10.181±0.018	1087±8.9
CIAnd	RRab	False	0.4847	10.976±0.004	10.979±0.005	··· ± ···	0.266	0.301	···	11.311±0.139	11.339±0.016	1853±13.5
CSEri	RRc	False	0.3113	8.098±0.004	8.111±0.004	8.096±0.009	0.063	0.076	0.114	8.335±0.133	8.308±0.033	459±6.9
DDHya	RRab	False	0.5018	11.101±0.006	11.105±0.007	··· ± ···	0.223	0.170	···	11.426±0.136	11.500±0.015	1996±13.9
DHPeg	RRc	False	0.2555	8.563±0.005	8.577±0.005	··· ± ···	0.058	0.067	···	8.621±0.134	8.630±0.071	532±17.3
DNAqr	RRab	False	0.6338	9.912±0.005	9.918±0.008	9.863±0.039	0.212	0.186	0.072	10.576±0.133	10.554±0.020	1290±12.0
DXDel	RRab	False	0.4726	8.633±0.004	8.658±0.005	8.620±0.013	0.245	0.217	0.150	8.779±0.142	8.981±0.017	625±4.9
FWLup	RRab	False	0.4842	7.643±0.005	7.658±0.004	7.654±0.008	0.093	0.148	0.103	7.876±0.145	8.017±0.016	401±2.9
HHPup	RRab	False	0.3907	9.879±0.003	9.886±0.003	9.774±0.021	0.301	0.301	0.067	9.978±0.141	10.020±0.030	1009±13.9
IKHya	RRab	True	0.6503	8.739±0.005	8.735±0.005	8.705±0.015	0.152	0.160	0.118	9.240±0.134	9.403±0.021	760±7.5
IOLyr	RRab	False	0.5771	10.492±0.004	10.492±0.004	··· ± ···	0.279	0.273	···	10.977±0.135	11.034±0.015	1610±10.9
MSAra	RRab	False	0.5250	··· ± ···	10.601±0.005	··· ± ···	···	0.230	···	11.088±0.134	11.043±0.015	1616±10.9
MTTel	RRc	False	0.3169	8.053±0.006	8.077±0.004	8.065±0.010	0.110	0.096	0.109	8.295±0.134	8.284±0.031	454±6.6
RRCet	RRab	False	0.5530	8.502±0.005	8.497±0.006	8.470±0.013	0.226	0.237	0.176	9.075±0.134	8.999±0.014	631±4.0
RRGem	RRab	True	0.3973	10.227±0.007	10.224±0.006	··· ± ···	0.294	0.274	···	10.363±0.143	10.380±0.029	1191±16.0

Continued on Next Page...

Table 5.1 – Continued

Name	Type	Blazhko Affected?	Period (d)	*WISE* Apparent Magnitudes $W1$	$W2$	$W3$	Model Amplitudes $W1$	$W2$	$W3$	Prior Distance $\mu_{\rm prior}$	Posterior Distance $\mu_{\rm post}$	d (pc)
RRLeo	RRab	False	0.4524	9.630±0.005	9.628±0.006	··· ± ···	0.262	0.303	···	10.028±0.121	9.919±0.020	963±8.9
RRLyr	RRab	True	0.5668	6.498±0.007	··· ± ···	6.459±0.005	0.192	0.196	0.192	7.130±0.075	7.027±0.015	254±1.7
RSBoo	RRab	True	0.3773	9.414±0.005	9.438±0.005	9.397±0.017	0.251	0.288	0.233	9.498±0.142	9.528±0.033	805±12.2
RUCet	RRab	True	0.5863	10.531±0.006	10.544±0.008	10.479±0.074	0.236	0.196	0.235	11.071±0.134	11.095±0.016	1656±12.3
RUPsc	RRc	True	0.3903	9.070±0.004	9.078±0.004	9.062±0.015	0.089	0.109	0.073	9.529±0.133	9.443±0.059	774±21.1
RUScl	RRab	False	0.4933	9.141±0.005	9.149±0.008	9.097±0.020	0.285	0.292	0.215	9.518±0.134	9.524±0.016	803±5.8
RVCap	RRab	True	0.4477	9.971±0.006	9.975±0.008	10.025±0.074	0.188	0.170	0.257	10.372±0.134	10.253±0.021	1124±10.8
RVCet	RRab	True	0.6234	9.574±0.004	9.587±0.004	9.541±0.022	0.209	0.203	0.223	10.263±0.120	10.202±0.018	1098±9.3
RVCrB	RRc	False	0.3316	10.476±0.004	10.481±0.004	··· ± ···	0.068	0.078	···	10.742±0.133	10.728±0.032	1398±20.3
RVOct	RRab	False	0.5711	9.451±0.004	··· ± ···	9.367±0.020	0.238	···	0.082	9.842±0.139	9.983±0.015	992±6.8
RVUMa	RRab	True	0.4681	9.735±0.004	9.739±0.005	··· ± ···	0.211	0.215	···	10.059±0.134	10.063±0.018	1029±8.3
RWCnc	RRab	True	0.5472	10.675±0.005	10.679±0.005	··· ± ···	0.249	0.220	···	11.244±0.134	11.164±0.014	1709±10.8
RXCet	RRab	True	0.5737	10.183±0.006	10.190±0.005	··· ± ···	0.197	0.216	···	10.740±0.134	10.722±0.015	1395±9.6
RXCol	RRab	True	0.5937	11.233±0.005	11.241±0.005	··· ± ···	0.175	0.190	0.469	11.863±0.134	11.809±0.016	2300±17.2
RXEri	RRab	False	0.5872	··· ± ···	··· ± ···	8.270±0.009	···	···	0.152	8.840±0.134	8.875±0.019	596±5.3
RYCol	RRab	True	0.4789	9.788±0.003	9.790±0.003	9.744±0.022	0.249	0.234	0.192	10.109±0.136	10.138±0.016	1066±7.9
RYOct	RRab	False	0.5635	10.725±0.005	10.718±0.005	··· ± ···	0.184	0.173	···	11.158±0.134	11.239±0.014	1769±11.6
RZCVn	RRab	False	0.5674	10.420±0.005	10.428±0.005	··· ± ···	0.292	0.251	···	11.032±0.134	10.949±0.014	1548±10.3
RZCet	RRab	False	0.5106	10.621±0.004	10.615±0.004	10.540±0.068	0.223	0.213	0.351	11.201±0.134	11.034±0.014	1610±10.4
SAra	RRab	True	0.4519	9.505±0.006	9.503±0.006	9.481±0.029	0.274	0.254	0.189	9.521±0.138	9.793±0.020	909±8.3
SCom	RRab	False	0.5866	10.539±0.006	10.546±0.008	··· ± ···	0.273	0.282	···	11.094±0.134	11.101±0.016	1660±12.5
SSCVn	RRab	False	0.4785	10.847±0.006	10.850±0.006	··· ± ···	0.181	0.168	···	11.222±0.134	11.196±0.017	1735±13.5
SSFor	RRab	True	0.4954	9.122±0.006	9.149±0.010	9.069±0.016	0.270	0.233	0.194	9.426±0.136	9.512±0.016	799±5.8
SSLeo	RRab	False	0.6263	9.864±0.005	9.879±0.006	9.823±0.041	0.208	0.242	0.184	10.456±0.134	10.498±0.019	1258±11.1
SSOct	RRab	True	0.6218	9.721±0.005	9.703±0.004	9.656±0.025	0.284	0.229	0.137	10.287±0.122	10.330±0.018	1164±9.9
STBoo	RRab	True	0.6223	9.816±0.004	9.822±0.004	9.772±0.023	0.240	0.277	0.173	10.413±0.133	10.439±0.018	1224±10.4
STCVn	RRc	False	0.3291	10.414±0.004	10.428±0.005	10.482±0.052	0.089	0.069	0.171	10.626±0.135	10.665±0.031	1358±19.6
STCom	RRab	False	0.5989	10.145±0.005	10.149±0.005	··· ± ···	0.189	0.226	···	10.725±0.135	10.728±0.017	1398±10.7
STLeo	RRab	False	0.4780	10.412±0.015	10.417±0.009	10.245±0.093	0.295	0.248	0.425	10.709±0.135	10.760±0.019	1419±12.6
STVir	RRab	False	0.4108	10.536±0.005	10.542±0.005	··· ± ···	0.270	0.235	···	10.625±0.139	10.729±0.026	1399±17.0
SUDra	RRab	False	0.6604	8.594±0.004	8.580±0.004	8.532±0.010	0.272	0.280	0.224	9.380±0.246	9.268±0.022	714±7.3
SVEri	RRab	False	0.7139	8.546±0.004	8.551±0.004	8.519±0.010	0.183	0.190	0.182	9.122±0.134	9.312±0.028	729±9.4
SVHya	RRab	True	0.4785	··· ± ···	··· ± ···	9.323±0.024	···	···	0.065	9.697±0.134	9.712±0.036	876±14.4
SVScl	RRc	False	0.3774	10.489±0.005	10.503±0.005	··· ± ···	0.088	0.084	···	10.821±0.133	10.840±0.052	1472±35.1
SWAnd	RRab	True	0.4423	8.475±0.005	8.479±0.004	8.448±0.014	0.245	0.261	0.179	8.662±0.144	8.744±0.021	561±5.5
SWAqr	RRab	False	0.4593	10.018±0.006	10.019±0.009	9.961±0.055	0.232	0.227	0.185	10.408±0.134	10.325±0.020	1161±10.4
SWDra	RRab	False	0.5697	9.284±0.004	9.290±0.004	9.221±0.016	0.275	0.245	0.183	9.772±0.135	9.815±0.014	918±6.0
SXAqr	RRab	False	0.5357	10.580±0.005	10.584±0.006	··· ± ···	0.232	0.214	···	11.112±0.134	11.047±0.014	1620±10.3
SXFor	RRab	False	0.6053	9.830±0.004	9.836±0.004	··· ± ···	0.212	0.201	···	10.528±0.133	10.424±0.017	1216±9.4
SXUMa	RRc	False	0.3072	10.046±0.004	10.076±0.004	10.045±0.035	0.110	0.084	0.145	10.306±0.134	10.254±0.034	1124±17.6
SZGem	RRab	False	0.5011	10.626±0.006	10.621±0.007	··· ± ···	0.214	0.250	···	11.009±0.134	11.020±0.015	1600±11.4
TSex	RRc	False	0.3247	9.116±0.005	9.134±0.005	9.109±0.023	0.062	0.066	0.087	9.268±0.134	9.359±0.031	744±10.6
TTCnc	RRab	True	0.5635	9.920±0.006	9.939±0.010	··· ± ···	0.197	0.183	···	10.570±0.134	10.444±0.015	1227±8.6
TTLyn	RRab	False	0.5974	8.567±0.007	8.566±0.005	8.523±0.014	0.174	0.205	0.075	9.233±0.133	9.144±0.017	674±5.1

Continued on Next Page...

Table 5.1 – Continued

Name	Type	Blazhko Affected?	Period (d)	*WISE* Apparent Magnitudes $W1$	$W2$	$W3$	Model Amplitudes $W1$	$W2$	$W3$	Prior Distance $\mu_{\rm prior}$	Posterior Distance $\mu_{\rm post}$	d (pc)
TUUMa	RRab	False	0.5577	8.602±0.005	8.610±0.005	8.575±0.018	0.235	0.238	0.119	9.164±0.133	9.113±0.014	665±4.2
TVBoo	RRc	True	0.3126	10.171±0.004	10.189±0.004	··· ± ···	0.111	0.083	···	10.581±0.137	10.386±0.032	1195±17.8
TVCrB	RRab	False	0.5846	10.715±0.004	10.704±0.004	10.773±0.065	0.199	0.207	0.195	11.359±0.137	11.265±0.015	1791±12.6
TWBoo	RRab	False	0.5323	10.123±0.004	10.131±0.005	10.106±0.032	0.288	0.293	0.084	10.650±0.133	10.586±0.013	1310±8.0
TWHer	RRab	False	0.3996	10.216±0.004	10.220±0.003	··· ± ···	0.274	0.314	···	10.373±0.138	10.379±0.028	1191±15.5
TWLyn	RRab	False	0.4819	10.721±0.005	10.733±0.005	10.809±0.117	0.233	0.213	0.363	11.076±0.139	11.082±0.016	1646±12.5
TYAps	RRab	False	0.5017	10.337±0.005	10.337±0.005	10.283±0.045	0.284	0.277	0.109	10.634±0.137	10.734±0.015	1402±9.5
TZAur	RRab	False	0.3917	10.794±0.006	10.812±0.005	··· ± ···	0.263	0.291	···	11.003±0.138	10.945±0.030	1545±21.4
UCom	RRc	False	0.2927	10.897±0.005	10.913±0.006	··· ± ···	0.103	0.086	···	11.068±0.134	11.064±0.041	1632±30.9
ULep	RRab	False	0.5815	9.438±0.003	9.435±0.003	9.439±0.020	0.255	0.247	0.279	9.939±0.134	9.987±0.015	994±6.8
UPic	RRab	False	0.4404	10.325±0.004	10.338±0.004	10.356±0.037	0.287	0.272	0.112	10.597±0.138	10.594±0.021	1314±12.9
UUCet	RRab	False	0.6061	10.753±0.005	10.787±0.006	··· ± ···	0.166	0.220	···	11.382±0.134	11.361±0.017	1871±15.0
UUVir	RRab	False	0.4756	9.460±0.006	9.465±0.006	··· ± ···	0.258	0.229	···	9.751±0.137	9.804±0.017	914±7.3
UVOct	RRab	True	0.5426	8.169±0.004	··· ± ···	8.103±0.007	0.234	···	0.207	8.850±0.127	8.643±0.014	535±3.4
UYBoo	RRab	False	0.6508	9.696±0.004	9.705±0.005	9.664±0.025	0.250	0.258	0.205	10.539±0.139	10.367±0.021	1184±11.6
UZCVn	RRab	False	0.6978	10.837±0.005	10.844±0.006	··· ± ···	0.200	0.194	···	11.576±0.134	11.579±0.026	2069±25.1
V413CrA	RRab	False	0.5893	9.095±0.006	9.110±0.005	··· ± ···	0.272	0.210	···	9.662±0.134	9.668±0.016	858±6.3
V440Sgr	RRab	False	0.4775	9.030±0.005	9.035±0.005	9.034±0.025	0.261	0.271	0.316	9.452±0.134	9.379±0.017	751±5.8
V445Oph	RRab	False	0.3970	9.181±0.005	9.177±0.005	··· ± ···	0.253	0.243	···	9.282±0.147	9.333±0.029	736±9.8
V499Cen	RRab	False	0.5212	9.845±0.005	9.837±0.005	9.710±0.024	0.241	0.219	0.205	10.256±0.134	10.276±0.014	1135±7.2
VInd	RRab	False	0.4796	8.838±0.006	8.842±0.007	8.815±0.017	0.269	0.262	0.268	9.296±0.133	9.192±0.017	689±5.3
VWScl	RRab	False	0.5109	10.030±0.005	10.040±0.005	··· ± ···	0.357	0.314	···	10.243±0.137	10.450±0.014	1230±8.0
VXHer	RRab	False	0.4554	9.590±0.005	9.584±0.005	9.499±0.031	0.331	0.355	0.093	9.952±0.133	9.883±0.019	948±8.4
VXScl	RRab	False	0.6373	··· ± ···	10.760±0.007	10.675±0.087	···	0.125	0.355	11.544±0.136	11.403±0.022	1908±19.3
VYLib	RRab	False	0.5339	10.048±0.006	10.032±0.008	··· ± ···	0.280	0.252	···	10.513±0.135	10.504±0.014	1262±8.3
VYSer	RRab	False	0.7141	8.734±0.005	8.733±0.005	8.697±0.017	0.226	0.213	0.126	9.477±0.134	9.496±0.028	793±10.2
VZHer	RRab	False	0.4403	10.470±0.004	10.473±0.004	10.519±0.069	0.316	0.299	0.163	10.707±0.135	10.734±0.021	1402±13.8
VZPeg	RRc	False	0.3065	11.022±0.006	11.040±0.006	11.004±0.121	0.058	0.058	0.229	11.266±0.134	11.223±0.034	1756±27.7
WCVn	RRab	False	0.5518	9.337±0.004	9.340±0.005	9.324±0.018	0.243	0.225	0.115	9.889±0.134	9.835±0.014	927±5.8
WCrt	RRab	False	0.4120	10.464±0.006	10.472±0.006	··· ± ···	0.207	0.226	···	10.597±0.140	10.661±0.026	1356±16.5
WTuc	RRab	False	0.6422	10.293±0.004	10.300±0.005	··· ± ···	0.270	0.230	···	10.788±0.133	10.949±0.020	1548±14.5
WYAnt	RRab	False	0.5743	9.544±0.005	9.561±0.005	9.490±0.029	0.240	0.214	0.100	10.069±0.133	10.090±0.015	1042±7.1
WYPav	RRab	False	0.5886	10.535±0.005	10.537±0.005	10.380±0.059	0.217	0.182	0.308	11.161±0.136	11.098±0.016	1658±12.1
WZHya	RRab	False	0.5377	9.601±0.005	9.606±0.005	9.579±0.034	0.181	0.214	0.137	10.033±0.134	10.073±0.014	1034±6.5
XAri	RRab	False	0.6511	7.861±0.005	7.867±0.004	7.837±0.011	0.255	0.248	0.107	8.512±0.139	8.533±0.021	509±5.0
XCrt	RRab	True	0.7328	10.122±0.007	10.126±0.005	··· ± ···	0.192	0.201	···	10.923±0.134	10.913±0.030	1523±21.3
XXAnd	RRab	False	0.7227	9.386±0.004	9.397±0.004	9.291±0.016	0.262	0.248	0.233	10.055±0.134	10.165±0.029	1079±14.3
XXPup	RRab	False	0.5172	10.010±0.005	10.026±0.008	10.002±0.047	0.274	0.241	0.442	10.365±0.134	10.445±0.014	1227±8.1
XZAps	RRab	False	0.5873	10.832±0.004	10.834±0.005	··· ± ···	0.283	0.269	···	11.360±0.136	11.394±0.016	1900±13.6
XZCyg	RRab	True	0.4666	8.622±0.003	8.627±0.003	8.560±0.006	0.231	0.186	0.162	8.990±0.222	8.944±0.017	615±4.9
XZDra	RRab	True	0.4765	9.088±0.003	9.101±0.003	9.040±0.009	0.248	0.253	0.235	9.323±0.137	9.438±0.016	772±5.8
YZCap	RRc	False	0.2735	10.306±0.006	10.339±0.007	10.416±0.097	0.069	0.129	0.552	10.433±0.135	10.430±0.055	1219±30.8
ZMic	RRab	False	0.5869	10.080±0.005	10.082±0.005	10.065±0.059	0.198	0.224	0.241	10.679±0.135	10.641±0.016	1343±9.7

Chapter 6

Towards Precision Distances and 3D Dust Maps Using Broadband Period–Magnitude Relations of RR Lyrae Stars

An earlier version of this chapter has been submitted for publication in MNRAS with coauthor Joshua S. Bloom.[1]

Abstract

We determine the period-magnitude relations of RR Lyrae stars in 13 photometric bandpasses from 0.4 to 12 μm using timeseries observations of 134 stars with prior parallax measurements from *Hipparcos* and the *Hubble Space Telescope* (*HST*). The Bayesian formalism, extended from our previous work to include the effects of line-of-sight dust extinction, allows for the simultaneous inference of the posterior distribution of the mean absolute magnitude, slope of the period-magnitude power-law, and intrinsic scatter about a perfect power-law for each bandpass. In addition, the distance modulus and line-of-sight dust extinction to each RR Lyrae star in the calibration sample is determined, yielding a sample median fractional distance error of 0.66 per cent. The intrinsic scatter in all bands appears to be larger than the photometric errors, except in *WISE* $W1$ (3.4 μm) and *WISE* $W2$ (4.6 μm) where the photometric error ($\sigma \approx 0.05\,\mathrm{mag}$) appears to be comparable or larger than the intrinsic scatter. This suggests that additional observations at these wavelengths could improve the inferred distances to these sources further. With $\sim 100,000$ RR Lyrae stars expected throughout the Galaxy, the precision dust extinction measurements towards 134 lines-of-sight offer a proof of concept for using such sources to make 3D tomographic maps of dust throughout the Milky

[1] Klein & Bloom (2014).

Way. We find a small but significant increase (3 per cent) in the effective extinction towards sources far from the Galactic plane relative to the expectation from recent dust maps and we suggest several explanations. As an application of the methodology, we infer the distance to the RRc-type star RZCep at low Galactic latitude ($b = 5.5°$) to be $\mu = 8.0397 \pm 0.0123$ mag (405.4 ± 2.3 pc) with color excess $E(B-V) = 0.2461 \pm 0.0089$ mag. This distance, equivalent to a parallax of 2467 ± 14 microarcsec, is consistent with the published *HST* parallax measurement but with an uncertainty that is 13 times smaller than the *HST* measurement. If our measurements (and methodology) hold up to scrutiny, the distances to these stars have been determined to an accuracy comparable to those expected with *Gaia*. As RR Lyrae are one of the primary components of the cosmic distance ladder, the achievement of sub-1 per cent distance errors within a formalism that accounts for dust extinction may be considered a strong buttressing of the path to eventual 1 per cent uncertainties in Hubble's constant.

6.1 Introduction

RR Lyrae stars are old (age $\gtrsim 10 \times 10^9$ yr) Population II pulsating stars that exist throughout the Milky Way Bulge, Disc, and Halo. At optical wavebands they are variable with peak-to-peak amplitudes up to about 1 mag. This amplitude generally diminishes with increasing wavelength to around 0.3 mag in the mid-infrared ($\lambda \sim 4\mu$m). The heat generation and gravitational support of RR Lyrae stars comes from the fusion of helium in the core and hydrogen in a shell surrounding the core. RR Lyrae stars have specific values of temperature, luminosity, and radius such that they exist in the instability strip of the Hertzsprung–Russell diagram. In this slice of stellar parameter-space stars are unstable to radial oscillation, and RR Lyrae stars oscillate with periods ranging from about 0.2 to 0.9 d.[2] This, and oscillating temperature changes, leads to periodic luminosity variability. Preston (1964) and Smith (1995) both provide excellent reviews of RR Lyrae pulsating variable stars.

RR Lyrae (and other pulsational variables, namely Cepheids) have inspired more than a century's worth of close attention because of the correlation of their fundamental oscillation period and luminosity. This empirical relation, supported by theoretical modelling (e.g., Catelan et al. 2004), has led to their use as primary distance indicators within the Milky Way and to the nearest neighbouring galaxies. With an effective range of ~ 100 kpc (for a limiting AB mag of ~ 20), they bridge the gap in the cosmic distance ladder between trigonometric parallax and the Tip of the Red Giant Branch (TRGB) method. RR Lyrae stars can also serve to calibrate Cepheid distances, most significantly by precisely measuring the distance and morphology of the Magellanic Clouds.

Distance determinations are achieved by leveraging empirical RR Lyrae period–magnitude relations to infer an RR Lyrae star's intrinsic luminosity in a given waveband (absolute magnitude, M) from its measured oscillation period. In prior work this relation is commonly called the "period–luminosity" relation, but here we prefer to use the term "period–

[2] On weeks-long periods, some stars exhibit peak-amplitude variations called the Blazhko effect (cf. subsection 6.4.3 for an additional description).

magnitude" relation to distinguish that it is not a predictor of bolometric luminosity, but instead of absolute magnitude in a given waveband.

With absolute magnitude for a given waveband in hand, the distance modulus, μ, is then calculated after observing the mean-flux apparent magnitude of the star in the same waveband, m,[3] and using the color excess, $E\,(B-V)$, to correct for extinction due to light scattering by interstellar dust grains. For waveband j, the equation for distance modulus, which is common for all bands, is

$$\mu = m_j - M_j - E\,(B-V) \times (a_j R_V + b_j)\,, \tag{6.1}$$

where a_j and b_j are the wavelength-specific parameters for the interstellar extinction law defined in Cardelli et al. (1989) and R_V is the extinction law factor ($R_V = A_V/E[B-V]$) with value equal to 3.1 for the diffuse interstellar medium adopted from Schultz & Wiemer (1975).

The period–magnitude relations of RR Lyrae stars have previously been primarily studied in the near-infrared K-band (Sollima et al. 2006) and mid-infrared bands of the *Wide-field Infrared Survey Explorer* (*WISE*) all-sky satellite survey mission (Klein et al. 2011; Madore et al. 2013; Dambis et al. 2014; Klein et al. 2014b). The slope of the period–magnitude relation at the shorter-wavelength optical bands is shallower, and a stronger correlation has been found between metallicity, [Fe/H], and optical (generally V-band) absolute magnitude. However, shorter-wavelength observations exhibit large scatter about a linear relation and there is no clear consensus on the necessity of the inclusion of secondary and/or nonlinear terms. The interested reader is referred to Section 5 of Sandage & Tammann (2006) for a review of optical (V-band) implementations of RR Lyrae stars as distance indicators.

In this analysis for the first time empirical RR Lyrae period–magnitude relations are simultaneously derived for 13 wavebands between the ultraviolet and mid-infrared. The calibration dataset is comprised of 134 RR Lyrae stars with photometry data combined from four astronomical observing facilities (two ground-based telescopes and the space-based *Hipparcos* and *WISE* satellites). Distances for the calibration RR Lyrae stars are determined with median fractional error of 0.66 per cent, and the multi-wavelength data are also used to solve for the color excess to each calibration star.

The improved waveband-specific period–magnitude relations presented here, as well as the Bayesian methodology for simultaneously calibrating or applying any subset of the 13 relations, represent a significant advancement in the use of RR Lyrae stars to measure distance. The claimed level of precision compares to (and even rivals) the expected astrometric precision of *Gaia*, the space-based, parallax/astrometry mission launched by the European Space Agency in December 2013 (Clark & Quartz 2012).

This paper is outlined as follows. We present a description of the ground-based optical, *Hipparcos*, ground-based near-infrared, and *WISE* datasets in Section 6.2. In Section 6.3 we review our light curve analysis methodology, describing how mean-flux magnitudes are measured for the sample. In Section 6.4 we present our Bayesian simultaneous linear regression

[3]Mean-flux magnitude is derived from a star's phase-folded light curve; the specifics are described in Section 6.3.

formalism, extended from our prior work, and the resultant period–magnitude relations. In Section 6.5 we relate additional findings of note resulting from the period–magnitude relation fits. In Section 6.6 we demonstrate how the multi-band period–magnitude relations are applied to estimate the distance to RZCep, which had been excluded from the period–magnitude relation fits owing to high, and poorly constrained, interstellar extinction. Finally, in Section 6.7 we discuss the conclusions and future implications of this work.

6.2 Data Description

The RR Lyrae calibration sample used in this work is based upon the catalog of 144 relatively local ($\leqslant$ 2.5 kpc) RR Lyrae variables developed by Fernley et al. (1998). Six of these stars are excluded from our present analysis because of minimal light curve data and poor harmonic model fits determined via the procedure described in Section 6.3. Another three stars (ARPer, RZCep, and BNVul) are excluded because of their large and poorly constrained color excess values (these stars lie too close to the Galactic Plane for the Schlegel et al. 1998 and Schlafly & Finkbeiner 2011 dust maps to provide accurate color excess measurements). And, one additional star, ATSer, was excluded because only *Hipparcos* and $W3$ photometry was available for this star, and the $W3$ magnitude was a significant outlier in prior period–magnitude relation fits.

In total, the calibration sample is 134 stars, with 637 band-specific light curves composed of 33,630 epochs. Table A.1 provides complete observable prior and fitted posterior data for the calibration sample.

The calibration sample contains RR Lyrae stars belonging to both of the two most common subtypes: RRab (115) and RRc (19). RRab stars oscillate at their fundamental period, P_f, and RRc stars oscillate at their first overtone period, P_{fo}. The RRc stars' periods must be "fundamentalised" before deriving the period–magnitude relations. As in Dall'Ora et al. (2004), an RRc star's fundamentalised period is given by

$$\log_{10}(P_f) = \log_{10}(P_{fo}) + 0.127. \tag{6.2}$$

6.2.1 Color Excess and Distance Modulus Priors

Line-of-sight $E(B-V)$ color excess values published in Schlegel et al. (1998) and Schlafly & Finkbeiner (2011) were retrieved from the NASA/IPAC Infrared Science Archive. These color excess values estimate the total cumulative interstellar extinction due to dust. In practice, the calibration stars are embedded in the Galaxy and the dust maps, which were derived from far-infrared imaging, are averaged over large (tens of arcminute) scales. The former means that the true color excess can be significantly less than the published value for that line of sight (even approaching zero if the star is close enough) and the latter implies that the published values should be considered to have significantly larger uncertainty bounds when applied to precise lines of sight terminating at unresolved point sources.

In order to begin the Markov Chain Monte Carlo (MCMC) regression traces (Section 6.4.1) and ultimately fit for color excess posteriors, the Schlafly & Finkbeiner (2011) values were adapted into prior color excess distributions according to the following procedure. If $E(B-V)_{\rm SF} > 0.125$, then the prior distribution was set to be uniform $\mathcal{U}(0, 2.5 \times E(B-V)_{\rm SF})$. Otherwise, if $E(B-V)_{\rm SF} \leq 0.125$, then the prior distribution was set to be $\mathcal{U}(0, 0.125)$.

Prior distributions for the calibrator distance moduli were derived as in Klein et al. (2011) and Klein et al. (2014b). *Hipparcos* photometry (Perryman & ESA 1997) were transformed into V-band (Gould & Popowski 1998), corrected for dust extinction (using the line-of-sight extinction from Schlafly & Finkbeiner 2011 and the R factor from Schultz & Wiemer 1975), and combined with the Chaboyer (1999) M_V–[Fe/H] relation to yield prior distance moduli, $\mu_{\rm Prior}$. Precise trigonometric parallax angles for four of the stars (RRLyr, UVOct, XZCyg, and SUDra; all of the RRab subclass) have been previously measured with the *Hubble Space Telescope* (*HST*) and published (Benedict et al. 2011).[4] For these four stars the more precise, parallax-derived distance moduli were used in the period–magnitude relation fits. We note that the the distance moduli derived from the metallicity–magnitude relation for these four stars is in statistical agreement (within 2σ) with the parallax-derived distances.

6.2.2 *Hipparcos* Photometry

The European Space Agency *Hipparcos* astrometry satellite was launched in August 1989 and operated until March 1993, ultimately producing a catalog of photometry, parallax, and, in the case of variable stars, light curves, published in Perryman & ESA (1997). *Hipparcos* obtained light curves for 186 RR Lyrae stars, 134 of which serve as the calibration sample for the period–magnitude relations derived in this work.

Since *Hipparcos* was primarily an astrometry mission, its imaging detector used a broadband visible light passband, defined primarily by the response function of the detector, an unfiltered S20 image dissector scanner. Bessell (2000) characterizes the *Hipparcos* waveband, commonly referred to as H_P. Throughout this work, to reduce potential confusion with the near-infrared H-band, the *Hipparcos* waveband is referred to as *hipp*. The effective wavelength of the *hipp* waveband is taken to be 0.517 μm, and the bandpass itself is substantially broader than V-band (see Fig. 2 of Bessell 2000).

Hipparcos was a temporally dense all-sky survey, and thus it provides the most complete and numerous light curve data for the RR Lyrae calibration sample. All 134 calibrator stars have *hipp* light curves, which are composed of 11,822 epochs.

6.2.3 Optical Photometry

Ground-based optical light curves were obtained with the Nickel 1-m telescope and Direct Imaging Camera at Lick Observatory in California. Imaging data was collected in the U, B,

[4]The RRc star RZCep also has an *HST*-measured parallax, but this star was rejected from our fit because of low galactic latitude and, consequently, a poorly constrained prior color excess value.

V, R, I, and Sloan Digital Sky Survey (SDSS) z wavebands during 26 nights between 2010 May 4 and 2013 February 4. Standard image reduction was conducted using common Python scientific computing modules [using PyFITS (Barrett & Bridgman 1999) for image reading and writing] and aperture photometry was measured with SExtractor (Bertin & Arnouts 1996). Photometric calibration was performed using observations of Landolt standards in the U, B, V, R, and I wavebands (Landolt 1992, updated by Landolt 2009), and SDSS standards for the z waveband (Smith et al. 2002).

The Direct Imaging Camera filter wheel could only accommodate four filters at one time, and so preference was given to U, B, V, and R for the first 21 nights (before 2012). The I and z filters replaced the U and B filters in the 5 observing nights after and including 2012 November 6. The targets for these last 5 nights were repeats of stars already observed during the first 21 nights, and the primary purpose was to supplement the calibration waveband coverage of the sample.

In the U-band 22 light curves were obtained, consisting of 1409 epochs. In the B-band 24 light curves were obtained, consisting of 1599 epochs. In the V-band 25 light curves were obtained, consisting of 1991 epochs. In the R-band 25 light curves were obtained, consisting of 2031 epochs. In the I-band 9 light curves were obtained, consisting of 410 epochs. And, in the z-band 9 light curves were obtained, consisting of 400 epochs.

6.2.4 Near-infrared Photometry

Observations in the J, H, and $K_{\rm short}$ (herein abbreviated simply as K) wavebands were conducted between 2009 April 14 and 2011 May 18 with the 1.3-m Peters Automated Infrared Telescope (PAIRITEL; Bloom et al. 2006) at Fred Lawrence Whipple Observatory in Arizona. PAIRITEL was the robotized *2MASS* North telescope mated with the repurposed *2MASS* South camera. As such, the near-infrared wavebands used in the present work are identical to the *2MASS* photometric system, and photometric calibration was conducted using reference stars contained within the same $8.53' \times 8.53'$ field of view. The near-infrared images were reduced and coadded with the software pipeline described in the following subsection. Aperture photometry was measured with SExtractor.

In the J-band 18 light curves were obtained, consisting of 1293 epochs. In the H-band 17 light curves were obtained, consisting of 1247 epochs. And, in the K-band 22 light curves were obtained, consisting of 1512 epochs.

PAIRITEL Reduction Pipeline

Because PAIRITEL reused the *2MASS* camera and unaltered readout electronics, each epoch consisted of multiple exposure triplets separated by ∼dozen seconds during which a small dither offset was enforced. Each single exposure in the triplet had an exposure time of 7.8 s. A single epoch generally consisted of 8 or 9 triplets, making for a total integration time of $\sim$ 3–3.5 minutes.

In support of this work on RR Lyrae period–magnitude relations, as well as the prime

science goal of PAIRITEL to followup gamma-ray burst (GRB) afterglows, a new image reduction and co-addition pipeline was developed for the robotic telescope and deployed for near-real time operation. This software was the third and final reduction pipeline developed for PAIRITEL.[5] It operated autonomously in concert with the telescope as new data was gathered each night, often providing reduced and coadded images within a few minutes of the end of an observation. This was particularly beneficial for quickly reacting to GRBs and issuing GCN circulars. The reduction pipeline also provided invaluable near-real time diagnostic information for the telescope supervisors when troubleshooting mechanical, technical, or telescope control system-related faults.

The *2MASS* camera uses two dichroics and three near-infrared detectors to simultaneously record the J, H, and K exposures. For the most part, the reduction pipeline operates on each waveband independently. However, because the images are taken simultaneously in each band, the relative and absolute astrometric solutions for the images need only be solved for J and can then be applied to the two longer-wavelength (and less sensitive) H and K exposures.

The constrained image readout mode of PAIRITEL dictated much of how the reduction pipeline operated. Each 7.8 s integration of a triplet exposure (called a "long read") was preceded by a "short read" of 0.051 s. The short read served as a bias read for the long read, and was subtracted from the long read as the first step in the reduction process. The short reads themselves were also processed to produce final coadded images with very short total exposure times. The advantage of processing the short reads is recovery of extremely bright sources that otherwise saturate in the long reads. This was the intended avenue for photometering the nearby bright RR Lyrae stars, such as RRLyr itself, but ultimately the photometric precision recoverable from the reduced and coadded short reads was found to be unacceptable.

In the near-infrared, the brightness of the atmosphere is significant and must be subtracted to improve the signal-to-noise ratio of astrophysical sources. The reduction pipeline creates median sky background images by masking pixels suspected to fall on sources and stacking temporally-adjacent images. The sky brightness fluctuates on 5- to 10-minute timescales, so for a given "target" exposure the pipeline uses the images recorded within ± 5 minutes to create this median sky flux image. (Of course, if the target exposure is within 5 minutes of the beginning or end of the observation period, then fewer adjacent images contribute to its sky flux image.)

It was found that the detector response varied significantly, and in a correlated manner, with the read-cycle position of the long reads in the triplet exposures. To account for this, a different sky flux image is produced for each of the three long reads in a triplet exposure, wherein only the first long read of each contributing triplet exposure is combined into the sky flux image corresponding to the first long read of the target triplet exposure, and so on for the second and third reads in the cycle.

The accuracy of this sky brightness subtraction procedure relies heavily upon correctly

[5]The PAIRITEL reduction software repository is hosted at https://github.com/ckleinastro/pairitel_reduction_pipeline.

masking pixels containing flux from astrophysical sources from contributing to the median sky flux image. The reduction pipeline runs this sky subtraction procedure twice, first with a preliminary source pixel mask and then with a more refined, and conservative, source pixel mask constructed from the images resulting from summing long reads of each triplet exposure after subtracting the first iteration of the sky flux images. The source pixel masks were generated by employing a median absolute deviation outlier detection algorithm in combination with the objects check image output from SExtractor. The raw source pixel masks were then Gaussian smoothed (blurred) to expand the masked pixel area and account for diffuse emission from extended sources and the telescope's PSF. The dither steps between each triplet exposure were large enough to "step over" the footprints of unsaturated (and most saturated) point sources, as well as most galaxies with radii $\lesssim 30''$.

After the sky flux subtraction, each triplet exposure is divided by archival flat frames for each detector (the autonomous software did not automatically acquire twilight flats during normal operations). Then each triplet exposure is directly pixel-wise summed to create a "triplestack". Each pixel is $2'' \times 2''$, and the telescope jitter was far smaller, so this does not result in any significant smearing. The final step in the reduction process is to coadd the images and produce mosaics, but before this can be done the relative dither offsets must be measured from the pixel data and written into the FITS header WCS keywords. Note that an absolute astrometric solution is not necessary at this step, only a WCS solution that incorporates precisely correct relative offsets between the triplestacks. To accomplish this, the reduction pipeline runs SExtractor on each J-band triplestack and analyes the resultant catalogs to identify the deepest triplestack image. This deep triplestack, generally the image with the most well-detected sources, serves as the reference image from which the pixel offsets of the other images in the sequence are measured. The relative sky position offsets and rotations between the J, H, and K detectors are well known and constant, so it is only necessary to measure the offsets in the J-band triplestack sequence.

A normalized cross-correlation image-alignment program (specially developed by E. Rosten) is used to measure the pixel offsets between the reference triplestack and all other images in the sequence. In addition to the image pair, the alignment program also requires an approximate pixel offset (derived from the telescope control system's imprecise pointing data) and a search box width (default width is 9 pixels, but this can be adjusted as necessary for specific reduction requests). The computed pixel offsets are accurate at the sub-pixel level.

With relative pixel offsets in hand, the reduction pipeline writes appropriate WCS information into the FITS headers of the J, H, and K triplestack sequences and then uses Swarp (Bertin et al. 2002) to median-combine and mosaic the reduced imaging data. Right before the final triplestack list is generated for Swarp, though, triplestack images with suspected bad WCS alignments or unreasonably few point sources are rejected (the most often cause of rejection at this point is variable poor sky conditions). In the mosaicing process the pixel resolution is changed from $2''$ to $1''$. Additionally, archival and dynamically-generated bad pixel masks are provided to Swarp for application in the coaddition process. The final astrometry is solved using astrometry.net (Lang et al. 2010), although sometimes the pipeline falls back on Scamp (Bertin 2006) and then, if Scamp also fails, a specifically-developed

pattern-matching Python program is employed.

6.2.5 *WISE* Photometry

Mid-infrared light curve photometry data were obtained from the AllWISE Data Release of the *Wide-field Infrared Survey Explorer* (*WISE*) and its extended *NEOWISE* mission (Wright et al. 2010; Mainzer et al. 2011). *WISE* provides imaging data in four mid-infrared wavebands: $W1$ centered at 3.4 μm, $W2$ centered at 4.6 μm, $W3$ centered at 12 μm, and $W4$ centered at 22 μm. Although the original *WISE* mission was designed for static science goals, the orbit and survey strategy of the *WISE* spacecraft (described in Wright et al. 2010) are highly conducive to recovering light curves of periodic variables with periods $\lesssim 1.5$ d, which is well-matched to RR Lyrae variables.

The AllWISE Data Release (made public 2013 November 13) combines the 4-Band Cryogenic Survey (main *WISE* mission covering the full sky 1.2 times from 2010 January 7 to 2010 August 6), the 3-Band Cryogenic survey (first three wavebands, 30 per cent of the sky from 2010 August 6 to 2010 September 29), and the *NEOWISE* post-cryogenic survey (first two wavebands, covering 70 per cent of the sky from 2010 September 20 to 2011 February 1). The individual photometry epochs were retrieved from the AllWISE Multiepoch Photometry Database.

WISE, like *Hipparcos*, was an all-sky survey and thus the AllWISE Data Release provides very good coverage of the calibration sample. In the $W1$-band 126 light curves were obtained, consisting of 4202 epochs. In the $W2$-band 127 light curves were obtained, consisting of 4204 epochs. And, in the $W3$-band 79 light curves were obtained, consisting of 1510 epochs. Significantly fewer stars were detected and provided light curves accepted into the calibration sample in $W3$ because the $W3$ detector was not as sensitive and was not operating for the *NEOWISE* period. Additionally, all $W4$ data are rejected from the present work because only the few brightest calibration RR Lyrae stars were detected in that bandpass.

6.3 Light Curve Analysis Methods

The light curve analysis methods employed in this work are an evolution of those described in Klein et al. (2011) and Klein et al. (2014b). Each band-specific light curve is parametrically resampled (assuming a normal distribution) 500 times to fit 500 harmonic models using the adopted pulsation period from Fernley et al. (1998). Thus, 500 realizations of the mean-flux magnitude are measured, and the standard deviation of this distribution is taken to be the uncertainty on the mean-flux magnitude. These are the observed mean-flux magnitudes reported in Table A.1 and are not corrected for interstellar extinction.

The 500 harmonic models generated by the bootstrapping procedure were averaged to produce a mean harmonic model. Fig. 6.1 shows the phase-folded light curve data and mean harmonic models for ABUMa (which was specifically selected to show a well-observed RR Lyrae calibration star with complete 13-waveband data). Plots of all of the observed light

curves for all of the RR Lyrae stars in the calibration sample are provided in Appendix B.

The mean harmonic model yields a robust light curve amplitude. Furthermore, the standard deviation of the 500 harmonic models at each phase value provides a metric of how well the shape of the true light curve is recovered in the photometry data (if there is a lot of spread in the distribution of harmonic models, then the photometry is not accurate enough to reveal the shape of the true brightness oscillation). To improve the quality of the dataset used in the period–magnitude relation fits, any light curve with a bootstrapped harmonic model maximum standard deviation larger than its robust amplitude measurement was excluded. This procedure serves to ensure that only stars with light curves well-fit by the harmonic model (i.e., those exhibiting clear sinusoidal-like oscillation) are used in the period–magnitude relation fits.

The summary information given above in Section 6.2 for the number of light curves obtained in each waveband has already taken into account the results of this quality selection process. For example, most of the diminution in the number of $W3$ light curves (79) as compared to $W1$ (126) or $W2$ (127) is due to this requirement that the model uncertainty be less than the light curve amplitude.

6.4 Period–Magnitude Relations

The present derivation of period–magnitude relations is similar to the Bayesian approach first described in Klein et al. (2011) and later formalised in Klein et al. (2012a). A significant advancement over previous implementations is the inclusion of color excess as a model parameter. Our statistical model of the period–magnitude relationship is

$$m_{ij} = \mu_i + M_{0,j} + \alpha_j \log_{10}(P_i/P_0) + E(B-V)_i\,(a_j R_V + b_j) + \epsilon_{ij}, \tag{6.3}$$

where m_{ij} is the observed apparent magnitude of the ith RR Lyrae star in the jth waveband, μ_i is the distance modulus for the ith RR Lyrae star, $M_{0,j}$ is the absolute magnitude zero point for the jth waveband, α_j is the slope in the jth waveband, P_i is the fundamentalised period of the ith RR Lyrae star in days, P_0 is a period normalisation factor (we use the mean fundamentalised period of the calibration sample, $P_0 = 0.52854$ d), $E(B-V)_i$ is the color excess of the ith RR Lyrae star, a_j and b_j are the wavelength-specific parameters for the interstellar extinction law defined in Cardelli et al. (1989), R_V is the extinction law factor ($R_V = A_V/E[B-V]$) with value equal to 3.1 for the diffuse interstellar medium adopted from Schultz & Wiemer (1975), and the ϵ_{ij} error terms are independent zero-mean Gaussian random deviates with variance $(\sigma^2_{\mathrm{intrinsic},j} + \sigma^2_{m_{ij}})$. We note that the ϵ_{ij} error terms are defined differently than in previous work to allow for the model to fit wavelength-dependent intrinsic period–magnitude relation scatter ($\sigma_{\mathrm{intrinsic},j}$). This additive error term, which we call the intrinsic scatter, describes the residual about the best-fit period–magnitude relation in each waveband which cannot be accounted for by instrumental photometric error. Such scatter would naturally be expected if there are unmodelled wavelength-sensitive dependencies (such as with metallicity) on the period–magnitude relation.

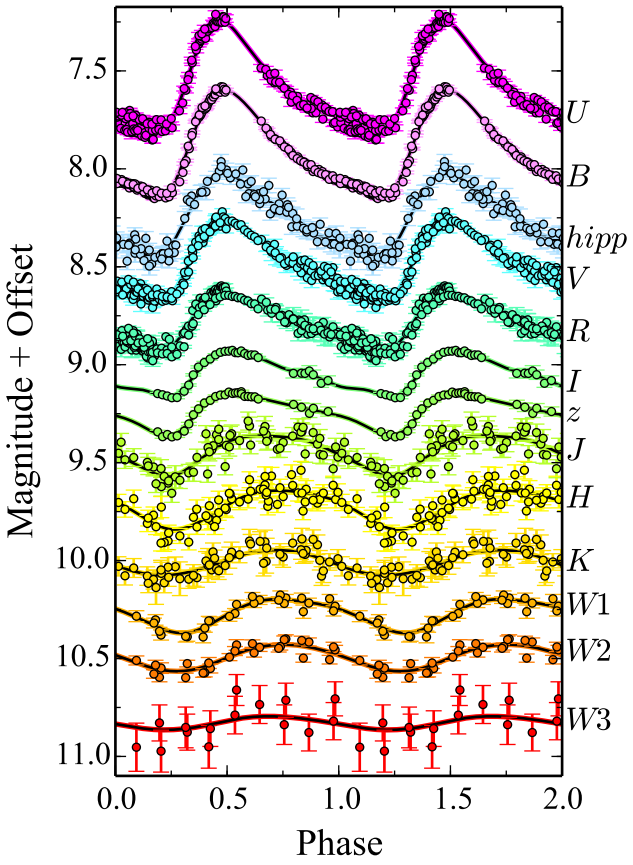

Figure 6.1: Light curves of RR Lyrae star ABUMa with period 0.6 d. The black solid curves are the mean of 500 bootstrapped harmonic models fitted to the light curve data in each waveband. The phase migration of the light curve peak brightness is real. An arbitrary relative phase offset was applied to the *Hipparcos* light curve because those data were observed between 1989 and 1993 (whereas the rest of the data were acquired between 2009 and 2013). Nearly 10,000 cycles occurred between the last *Hipparcos* observation and the first PAIRITEL observation, and this expanse was too large to accurately phase match.

To perform the Bayesian regression a design matrix $\mathbf{X}$ is constructed for the model expressed in Equation 6.3. $\mathbf{X}$ has dimensions 637×294. Each of the 637 light curves produced one mean-flux magnitude measurement which is represented by a row in $\mathbf{X}$. The terms in Equation 6.3 with i-dependence (μ_i and $E[B-V]_i$, where each RR Lyrae star is fit with one value) each require 134 columns. And, the terms in Equation 6.3 with j-dependence ($M_{0,j}$ and α_j, where each waveband is fit with one value) each require 13 columns.

We define the vector of model parameters, $\mathbf{b}$, which contains the 134 values of μ_i, the 13 values of $M_{0,j}$, the 13 values of α_j, and the 134 values of $E(B-V)_i$. The vector of observed mean-flux magnitudes, $\mathbf{m}_{\rm obs}$, is then given by the dot product of the design matrix and the vector of model parameters,

$$\mathbf{m}_{\rm obs} = \mathbf{X} \cdot \mathbf{b}. \tag{6.4}$$

The model parameters are fit by an implementation of MCMC sampling (6.4.1) that iteratively refines the distributions of the model parameters until a converged steady-state is achieved. The fitting algorithm is run with the PyMC (Patil et al. 2010) Python module, which leverages the distribution of the observed data vector $\mathbf{m}_{\rm obs}$ with variance given by $(\sigma^2_{{\rm intrinsic},j} + \sigma^2_{m_{ij}})$, as well as the model parameter vector $\mathbf{b}$ and the associated variance on each model parameter.

Initially $\mathbf{b}$ is populated with prior distributions and the MCMC sampling traces are run until convergence, after which 50,000 additional samples are drawn to record the fitted model parameter distributions (also called the posteriors). To avoid inappropriate biasing of the posterior distributions for the slope and intercepts, a wide normal distribution is adopted:

$$M_{0,j,{\rm Prior}} = \mathcal{N}(0, 2^2), \tag{6.5}$$

$$\alpha_{j,{\rm Prior}} = \mathcal{N}(0, 5^2). \tag{6.6}$$

The prior distributions for distance modulus and color excess are star-dependent and given in subsection 6.2.1.

The summary results for the simultaneous 13-waveband period–magnitude relation fits are provided in Table 6.1. In the ensuing subsections more detail is provided for the execution of the MCMC fitting procedure, the posterior joint distributions for the 13 (zero point, intercept) pairs are illustrated and explained, and the comprehensive $\log_{10}(P) - M$ plot and a validation $\mu_{\rm Prior} - \mu_{\rm Post}$ plot are furnished.

Table 6.1: Period–magnitude relation parameters and 1-σ uncertainties. The band-specific form of the period–magnitude equation is $M = M_0 + \alpha \log_{10}(P/P_0)$, where $P_0 = 0.52854$ d. $\sigma_{\rm instrumental}$ is the average photometric uncertainty for the mean-flux magnitudes in each band and is dominated by the quality of the light curve data (although individual light curve consistency of each star does contribute). Note that $\sigma_{\rm instrumental}$ is not a model parameter, but is provided in the table for direct comparison with $\sigma_{\rm intrinsic}$, which is the fitted intrinsic scatter of the period–magnitude relation in each waveband. Fig. 6.23 plots both $\sigma_{\rm intrinsic}$ and $\sigma_{\rm instrumental}$ as a function of wavelength.

band	M_0 (intercept)	α (slope)	$\sigma_{\rm intrinsic}$	$\sigma_{\rm instrumental}$
U	0.9304 ± 0.0584	-0.3823 ± 0.7130	0.2358 ± 0.0438	0.0232 ± 0.0175
B	0.7099 ± 0.0237	0.0129 ± 0.3104	0.0553 ± 0.0126	0.0145 ± 0.0118
hipp	0.5726 ± 0.0174	-0.4625 ± 0.2246	0.0474 ± 0.0079	0.0098 ± 0.0085
V	0.4319 ± 0.0184	-0.4091 ± 0.2370	0.0320 ± 0.0079	0.0106 ± 0.0085
R	0.2638 ± 0.0164	-0.7461 ± 0.2108	0.0274 ± 0.0072	0.0091 ± 0.0067
I	0.1065 ± 0.0380	-1.0456 ± 0.4285	0.0713 ± 0.0264	0.0188 ± 0.0170
z	0.5406 ± 0.0539	-0.8770 ± 0.6547	0.1153 ± 0.0432	0.0175 ± 0.0184
J	-0.1490 ± 0.0153	-1.7138 ± 0.1834	0.0385 ± 0.0081	0.0058 ± 0.0017
H	-0.3509 ± 0.0148	-2.1936 ± 0.1752	0.0312 ± 0.0068	0.0060 ± 0.0015
K	-0.3472 ± 0.0160	-2.4599 ± 0.1849	0.0498 ± 0.0089	0.0071 ± 0.0019
$W1$	-0.4703 ± 0.0112	-2.1968 ± 0.1252	0.0032 ± 0.0020	0.0050 ± 0.0013
$W2$	-0.4583 ± 0.0112	-2.2337 ± 0.1249	0.0055 ± 0.0018	0.0053 ± 0.0016
$W3$	-0.4924 ± 0.0119	-2.3026 ± 0.1342	0.0227 ± 0.0036	0.0350 ± 0.0291

6.4.1 MCMC Fitting Details

Seven MCMC sampling traces of the model fit were produced, each iterating 25,200,000 steps and thinned by a factor of 252 to result in traces with 100,000 iterations. As an illustrative example, Figs. 6.2, 6.3, and 6.4 show trace plots for the H-band $\sigma_{\rm intrinsic}$, M_0, and α, respectively. Additionally, trace plots for the μ and $E(B-V)$ of ABUMa are shown respectively in Figs. 6.5 and 6.6.

The traces are considered to be converged after 50,000 iterations, and these converged portions of each of the seven traces are combined to form a posterior distribution for each model parameter of 350,000 samples. Convergence is verified by computing the Gelman-Rubin multiple sequence convergence diagnostic, $\hat{R}$ (Gelman & Rubin 1992), and ensuring $\hat{R} \lesssim 1.1$ in the portion of the chains considered to be converged. The Gelman-Rubin diagnostic factor is the square root of the weighted sum of the within chain variance, W, and between chain variance, B, divided by the within chain variance. Here,

$$\hat{R} = \sqrt{\frac{\left(1 - \frac{1}{n}\right) W + \left(\frac{1}{n}\right) B}{W}}, \tag{6.7}$$

where n is the of length each chain. In Figs. 6.2 through 6.6 the Gelman-Rubin diagnostic is displayed for the first 10,000 iterations (demonstrating the lack of convergence early in the MCMC sampling chain) and also for the final 50,000 iterations (where the traces are considered to be converged).

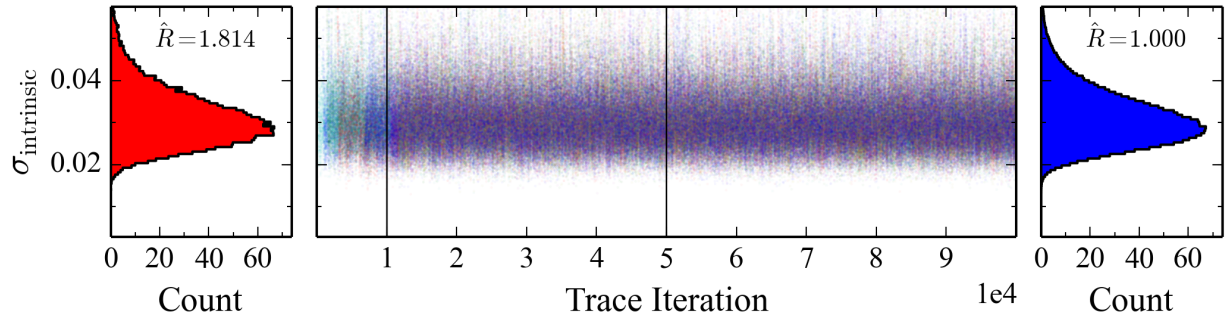

Figure 6.2: MCMC traces of intrinsic scatter, $\sigma_{\rm intrinsic}$, for the H waveband. All seven traces of 100,000 samples each are plotted simultaneously, colored by trace. The left panel shows the normalized histogram of the first 10,000 samples from each trace and the right panel shows the normalised histogram of the last 50,000 samples from each trace. In each histogram panel the Gelman-Rubin convergence diagnostic, $\hat{R}$ (Gelman & Rubin 1992), is given. $\hat{R}$ should converge to 1 and traces are generally considered converged when $\hat{R} \lesssim 1.1$. The first 50,000 samples are rejected as burn-in and the last 50,000 samples are considered to be drawn from the converged posterior distribution.

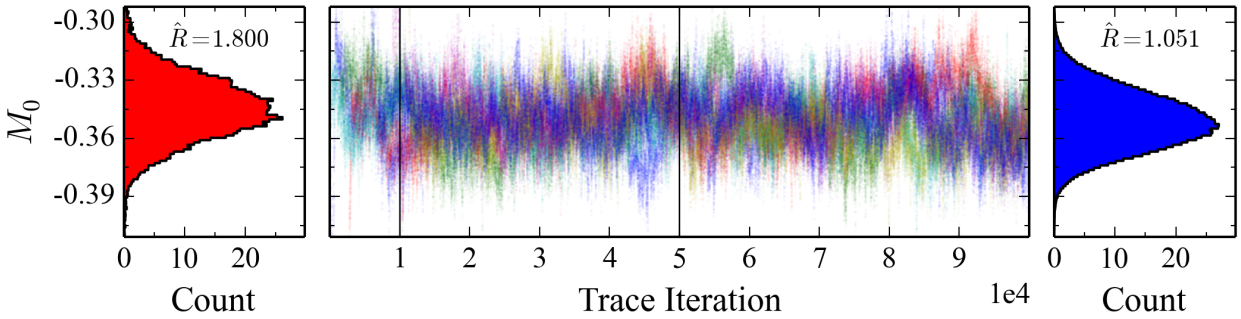

Figure 6.3: MCMC traces of M_0 for the H waveband. Panels formatted as in Fig. 6.2.

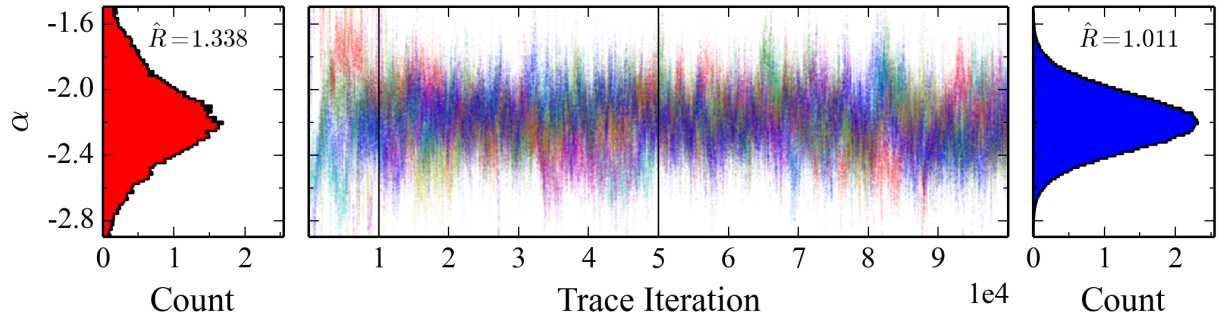

Figure 6.4: MCMC traces of α for the H waveband. Panels formatted as in Fig. 6.2.

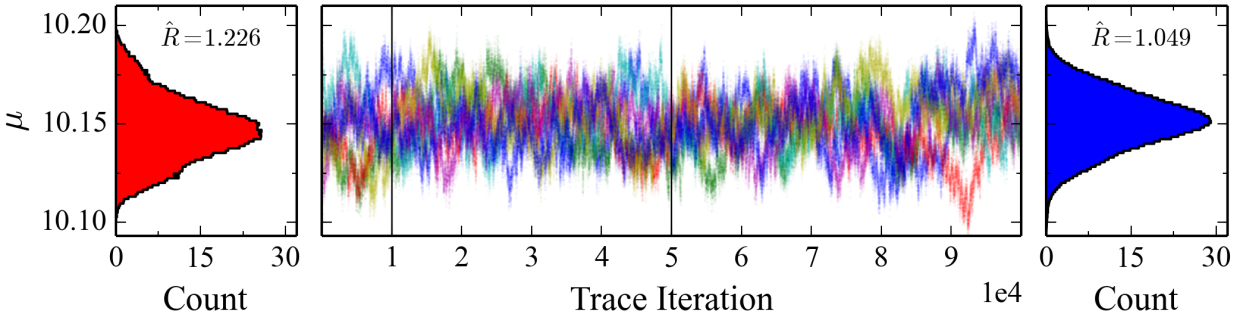

Figure 6.5: MCMC traces of μ for ABUMa. Panels formatted as in Fig. 6.2.

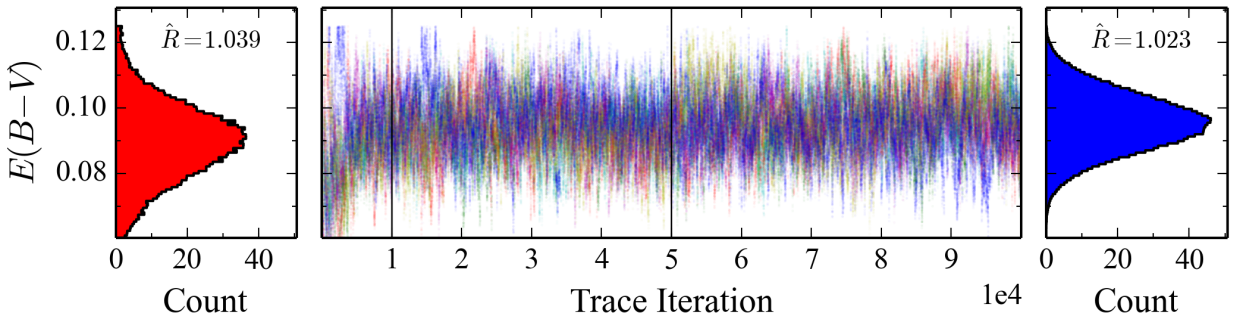

Figure 6.6: MCMC traces of $E(B-V)$ for ABUMa. Panels formatted as in Fig. 6.2.

6.4.2 Zero Point and Slope Joint Distributions

One significant advantage of a Bayesian approach to linear regression over frequentist methods is that the posterior model parameters are sampled from final joint distributions. Thus, any covariance in the distributions is accurately recorded and the traditional assumption of Gaussian behaviour is not necessary, but can instead be tested. Indeed, the posterior M_0 and α distributions are generally well-approximated by Gaussians, but some waveband-specific pairs exhibit covariance. Figs. 6.7–6.19 display the posterior contour density plots and histograms for the zero point and slope of the 13 waveband-specific period–magnitude relations.

The pronounced covariance between M_0 and α observed for the I and z wavebands is primarily caused by the lop-sided distribution of the periods of the RR Lyrae stars for which I- and z-band data were obtained. Only three of the nine stars observed in these wavebands have $P < P_0$, and thus the covariance between the linear regression intercept and slope was not well-removed.

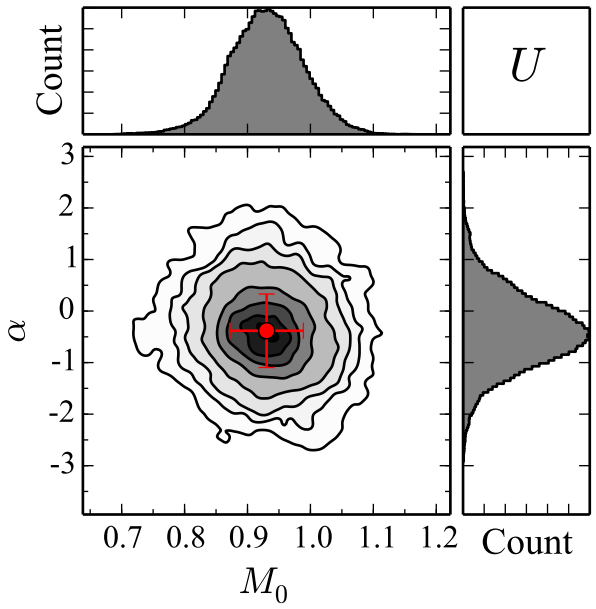

Figure 6.7: Contour density plot and histograms for the U band period–magnitude relation magnitude intercept (M_0) and slope (α). The red circle with associated error bars shows the means and standard deviations of the posterior M_0 and α distributions.

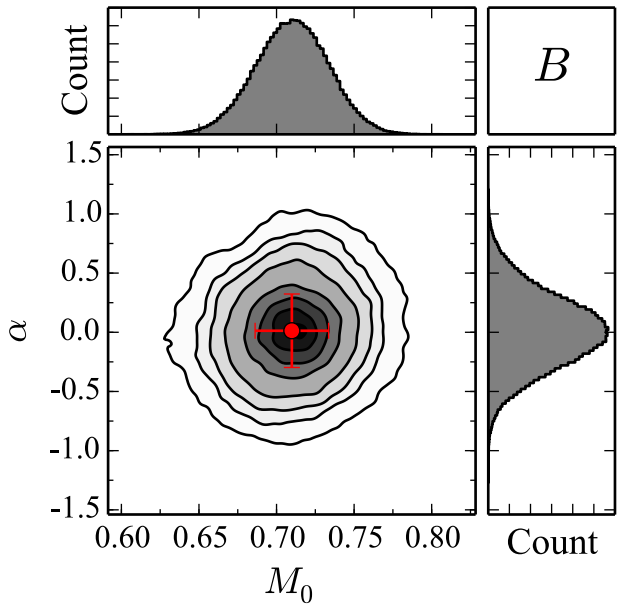

Figure 6.8: Contour density plot and histograms for the B band period–magnitude relation magnitude intercept (M_0) and slope (α). The red circle with associated error bars shows the means and standard deviations of the posterior M_0 and α distributions.

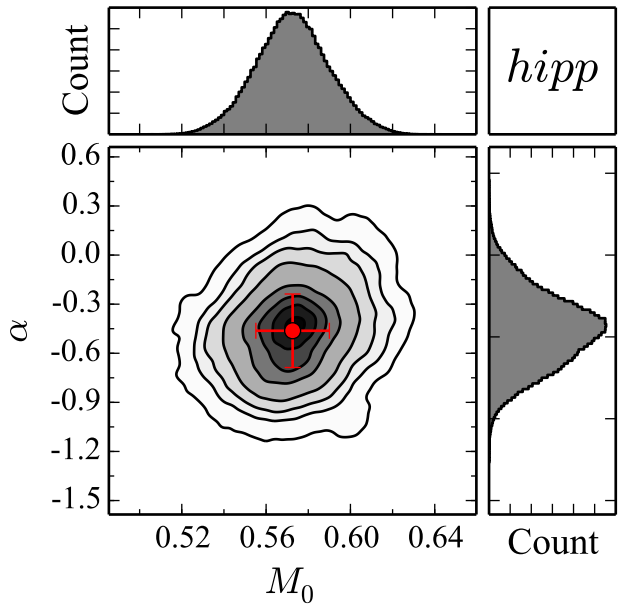

Figure 6.9: Contour density plot and histograms for the *hipp* band period–magnitude relation magnitude intercept (M_0) and slope (α). The red circle with associated error bars shows the means and standard deviations of the posterior M_0 and α distributions.

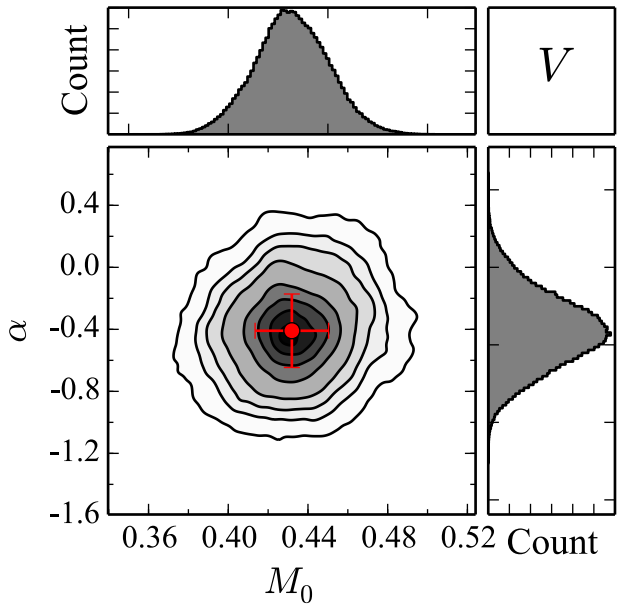

Figure 6.10: Contour density plot and histograms for the V band period–magnitude relation magnitude intercept (M_0) and slope (α). The red circle with associated error bars shows the means and standard deviations of the posterior M_0 and α distributions.

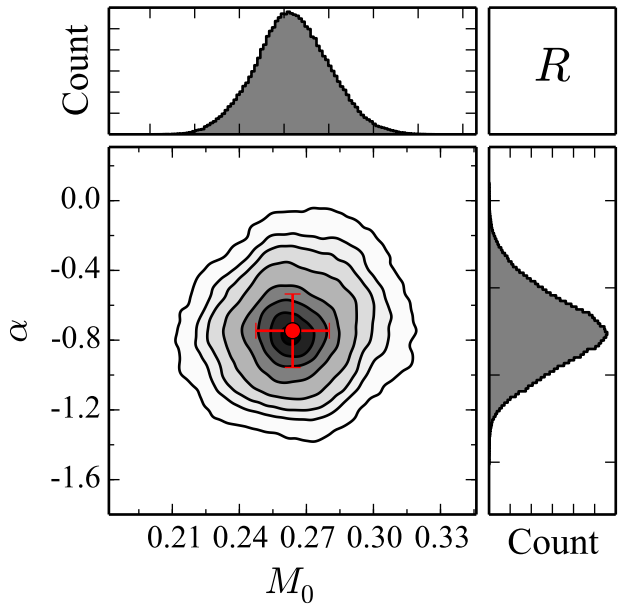

Figure 6.11: Contour density plot and histograms for the R band period–magnitude relation magnitude intercept (M_0) and slope (α). The red circle with associated error bars shows the means and standard deviations of the posterior M_0 and α distributions.

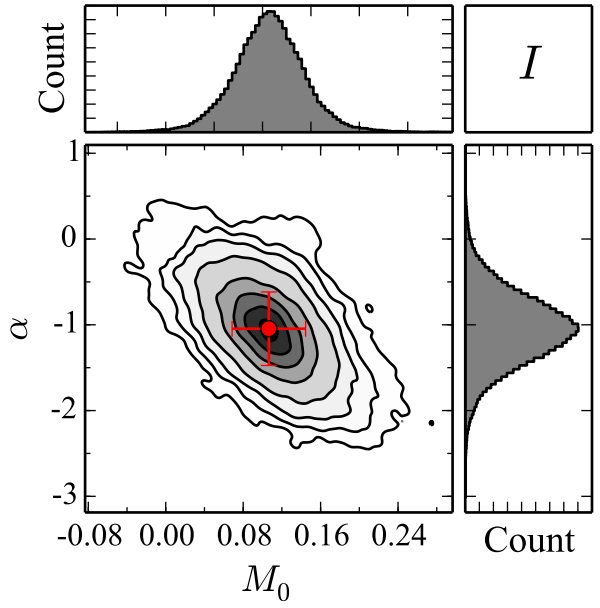

Figure 6.12: Contour density plot and histograms for the I band period–magnitude relation magnitude intercept (M_0) and slope (α). The red circle with associated error bars shows the means and standard deviations of the posterior M_0 and α distributions. The exhibited correlation in these parameters for I band is caused by the lopsided period distribution of the RR Lyrae variables for which I band data was obtained (c.f. Fig. 6.20, only three of nine stars have $P < P_0$).

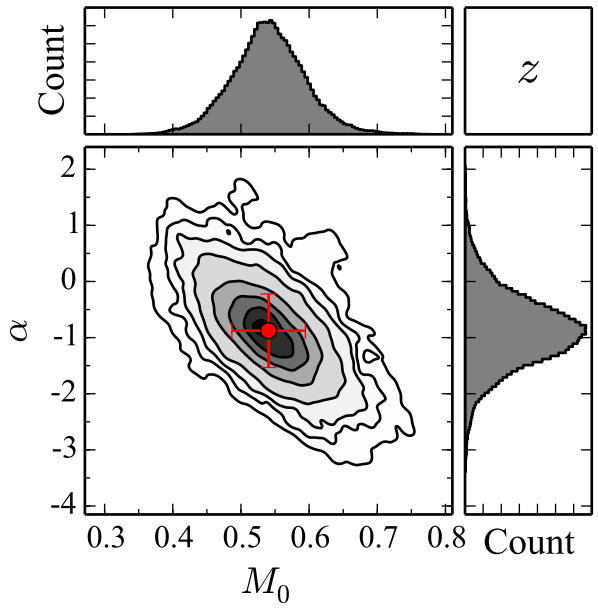

Figure 6.13: Contour density plot and histograms for the z band period–magnitude relation magnitude intercept (M_0) and slope (α). The red circle with associated error bars shows the means and standard deviations of the posterior M_0 and α distributions. As in Fig. 6.12, a correlation in these parameters is obvious. The explanation, an uneven period distribution about P_0 in the subset of RR Lyrae stars for which z band data was obtained, is the same as for I band (Fig. 6.12).

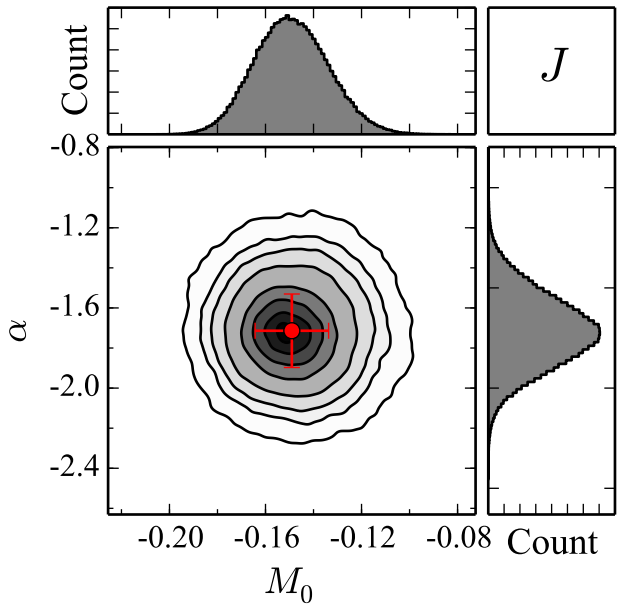

Figure 6.14: Contour density plot and histograms for the J band period–magnitude relation magnitude intercept (M_0) and slope (α). The red circle with associated error bars shows the means and standard deviations of the posterior M_0 and α distributions.

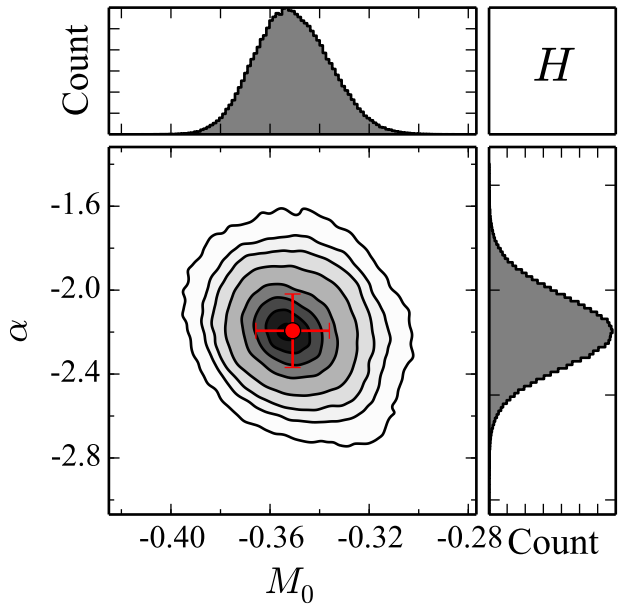

Figure 6.15: Contour density plot and histograms for the H band period–magnitude relation magnitude intercept (M_0) and slope (α). The red circle with associated error bars shows the means and standard deviations of the posterior M_0 and α distributions.

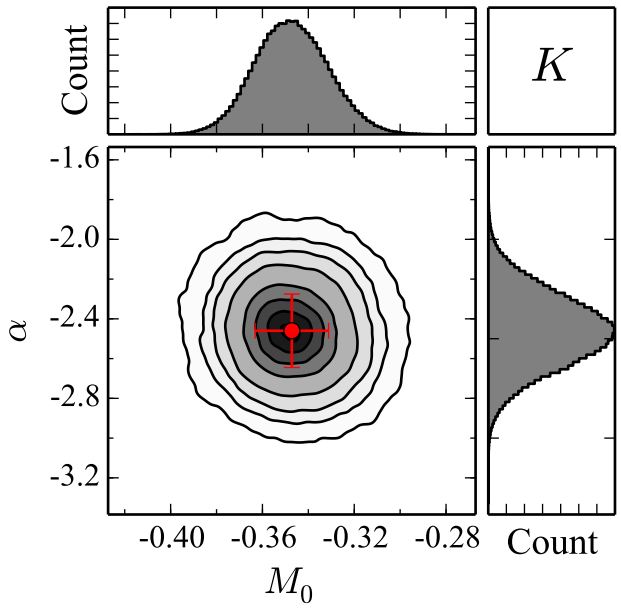

Figure 6.16: Contour density plot and histograms for the K band period–magnitude relation magnitude intercept (M_0) and slope (α). The red circle with associated error bars shows the means and standard deviations of the posterior M_0 and α distributions.

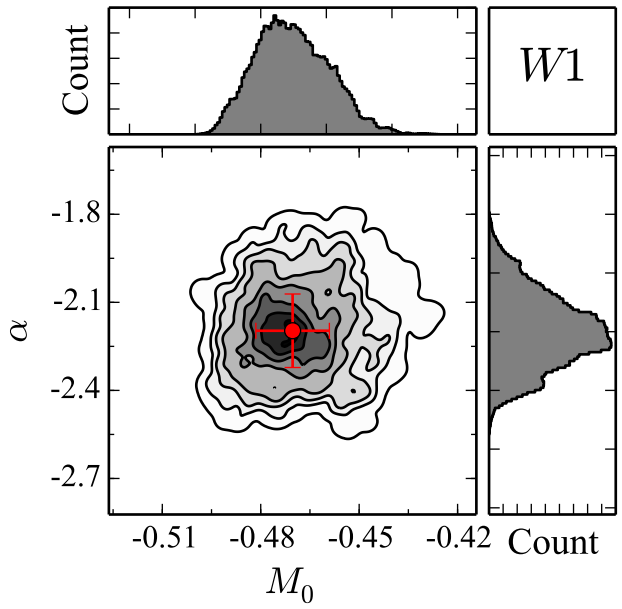

Figure 6.17: Contour density plot and histograms for the $W1$ band period–magnitude relation magnitude intercept (M_0) and slope (α). The red circle with associated error bars shows the means and standard deviations of the posterior M_0 and α distributions.

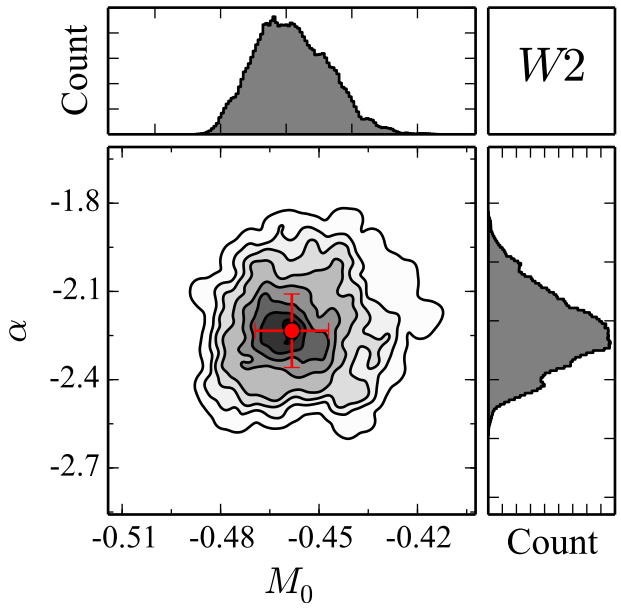

Figure 6.18: Contour density plot and histograms for the $W2$ band period–magnitude relation magnitude intercept (M_0) and slope (α). The red circle with associated error bars shows the means and standard deviations of the posterior M_0 and α distributions.

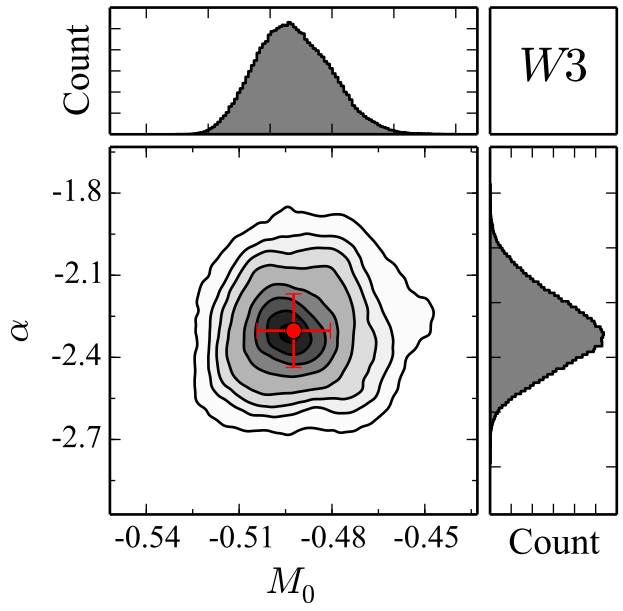

Figure 6.19: Contour density plot and histograms for the $W3$ band period–magnitude relation magnitude intercept (M_0) and slope (α). The red circle with associated error bars shows the means and standard deviations of the posterior M_0 and α distributions.

6.4.3 Period–Magnitude Relation Plot

Fig. 6.20 depicts the 13 period–magnitude relations in one large plot. The zero points of the relations are shifted vertically in the plot, as noted with the offsets given on the right hand side, to separate out the relations as displayed graphically. The solid black lines denote the best-fitting period–magnitude relations, and the dashed lines indicate the 1σ prediction uncertainty for application of the best-fitting period–magnitude relation to a new star with known period. Also noted on the right hand side is the minimum prediction uncertainty, here given simply as σ, which provides a sense for how accurately a single new RR Lyrae star's absolute magnitude can be predicted from a given band-specific period–magnitude relation. This value is the minimum vertical distance between the solid and dashed lines for each relation (which usually occurs around P_0). RRab stars are denoted with blue markers and RRc stars are shows in red. The plot contains 637 markers, one for each RR Lyrae light curve.

In addition to illustrating the 13 period–magnitude relations, this plot can also be interpreted to show the waveband distribution of the 637 light curves in the calibration dataset. For example, it is evident that the space-based *Hipparcos* and *WISE* missions provide light curve data in their wavebands for most of the calibration sample, and also that only nine stars were observed in I and z (and that those nine are biased towards longer periods). The plot also provides a graphical display of the proportion of RRab versus RRc stars (blue versus red markers) in the sample, broken down by waveband.

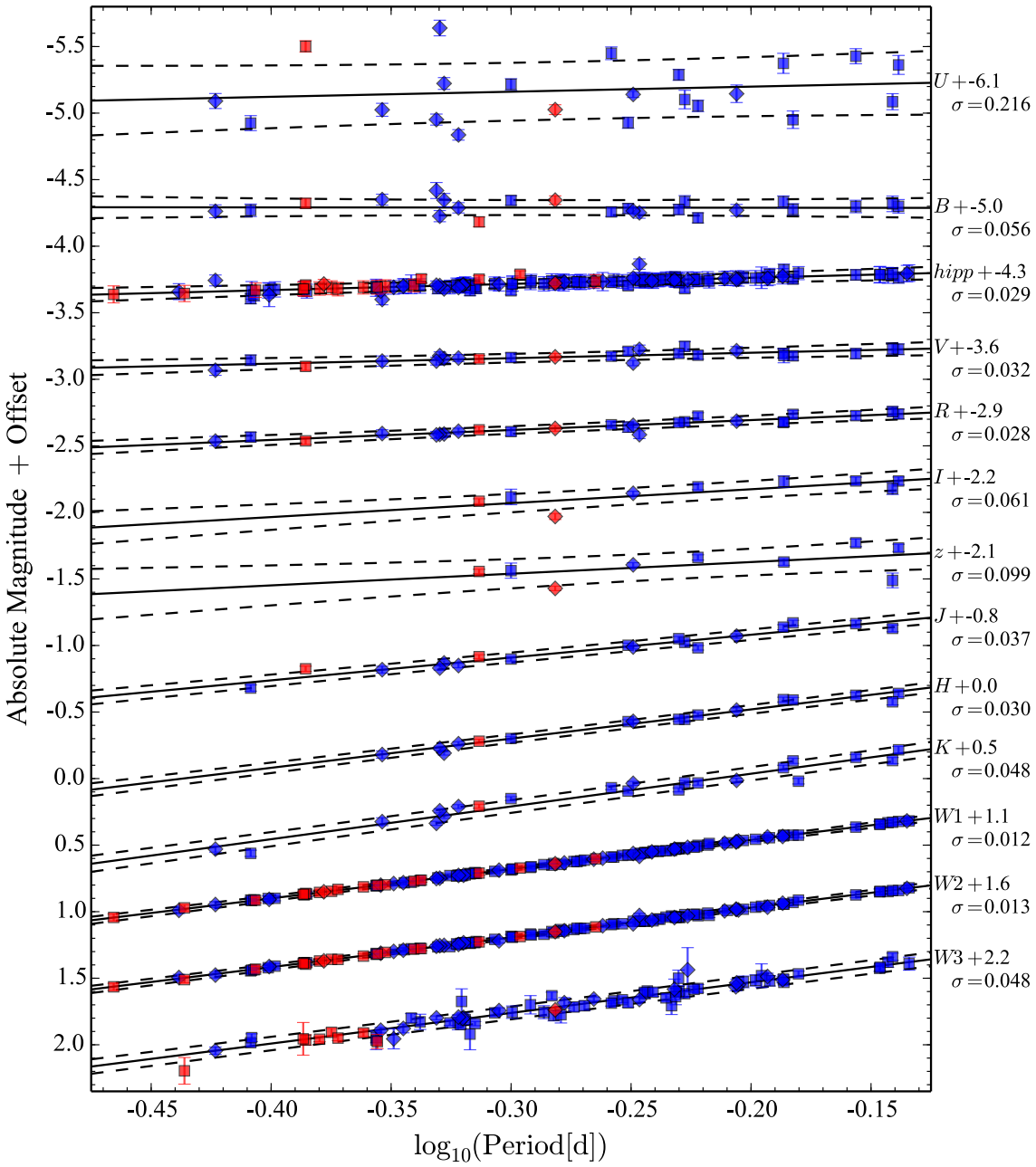

Figure 6.20: Multi-band period–magnitude relations. RRab stars are in blue, RRc stars in red. Blazhko-affected stars are denoted with diamonds, stars not known to exhibit the Blazhko effect are denoted with squares. Solid black lines are the best-fitting period–magnitude relations in each waveband and dashed lines indicate the 1-σ prediction uncertainty for application of the best-fitting period–magnitude relation to a new star with known period. The noted scatter, σ associated with each band in the figure, is the minimum prediction uncertainty, which is where the dashed line "bowtie pinch" around $P_0 = 0.52854$ d.

A large fraction of RR Lyrae stars (at least 20 per cent, and likely significantly more) are affected by an amplitude modulation called the Blazhko effect. This effect manifests as a slow cyclic evolution of the light curve shape, with a period ranging from weeks to months (Smith 1995, chapter 5.2). The nature of the Blazhko effect, a second-order amplitude modulation, does not result in a significant impact on a star's mean-flux magnitude. In Fig. 6.20 Blazhko-affected stars, as identified via `http://www.univie.ac.at/tops/blazhko/Blazhkolist.html`, are shown with diamonds and stars without confirmed evidence of the Blazhko effect are shown with squares.

Because of the longer-period nature of the effect, observational investigations of the RR Lyrae Blazhko effect require considerable telescope resources. To our knowledge, no such investigations have been carried out in near- or mid-infrared wavebands. That the amplitude distribution of RR Lyrae stars is significantly reduced in the near- and mid-infrared, as compared to optical bands, suggests that the magnitude of the Blazkho effect will also be diminished in the infrared (Gavrilchenko et al. 2013). However, observational studies are required to test this hypothesis. In the present analysis, and as indicated in Fig. 6.20, there is no significant impact on the period–magnitude relation by the inclusion of Blazhko-affected stars in the fit.

As a commonsense check on the period–magnitude relations of Fig. 6.20 and the applied simultaneous Bayesian linear regression fitting method, a plot of the prior distance moduli versus the posterior distance moduli for the calibration sample is provided in Fig. 6.21. Any bias or a strongly non-normal distribution of the $\mu_{\rm Post} - \mu_{\rm Prior}$ residuals would indicate overfitting. Since the distance modulus is treated as a model parameter to be fit, it is very important that the fitting method respects the original prior distance modulus values.

Fig. 6.21 shows that the prior and posterior distances are in very good agreement. Specifically, 112 out of the 134 calibrators (84 per cent) have $\mu_{\rm Post} - \mu_{\rm Prior}$ residuals that lie within one-errorbar length of zero. The errors on the posterior distance moduli may thus be slightly overestimated. The null hypothesis that the posterior-prior distance modulus residuals are drawn from a standard normal distribution is accepted by a Kolmogorov-Smirnov test with $p = 0.2$.

In Fig. 6.21 RRLyr itself is the star with the lowest distance modulus. The fitted posterior distance modulus of RRLyr is $\mu_{\rm Post} = 6.9962 \pm 0.0143$ with a prior distance modulus, derived from the measured *HST* parallax, of $\mu_{\rm Prior} = 7.130 \pm 0.075$. For RRLyr, the residual significance is -1.75σ.

6.5 Further Discussion of the Fits

The complex model used in the period–magnitude relation fits (described above in Section 6.4), which newly incorporates color excess and intrinsic scatter, allows for a deeper analysis of the results. In the following subsections we present the fit results as spectral energy distributions (SEDs), compare the fitted period–magnitude relation intrinsic scatter and mean photometric error as a function of wavelength, analyze the color excess results

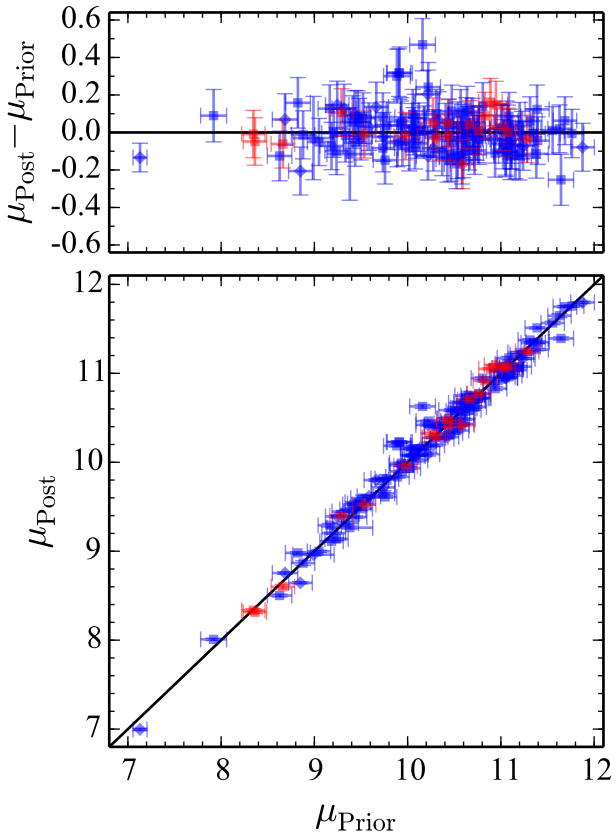

Figure 6.21: Prior versus posterior distance moduli, with residual plot in upper panel. Colors and symbols as in Fig. 6.20. 112 out of the 134 (84 per cent) of the residual data points are within one error bar length of zero, indicating that the errors are slightly overestimated.

more closely, and discuss the evolution of period–magnitude relation slope with wavelength.

6.5.1 RR Lyrae Spectral Energy Distributions

The period–magnitude relation fits provide the absolute magnitudes (at time of mean-magnitude) of the typical RR Lyrae star in 13 wavebands as a function of period. Another way to present, and think about, this result is by converting the fits to SEDs for RR Lyrae stars at selected periods. This is demonstrated in Fig. 6.22, along with two model stellar spectra (light grey lines) selected with temperatures and radii to bracket the ranges of these parameters inferred in the RR Lyrae population.

This plot of SEDs for RR Lyrae stars of various fundamental periods illustrates why the period–magnitude relations at optical wavebands (near the SED peak) have a shallower slope than at infrared wavebands (along the Rayleigh-Jeans tail). The vertical distance between two SEDs tracks with the slope of the period–magnitude relation. This vertical distance

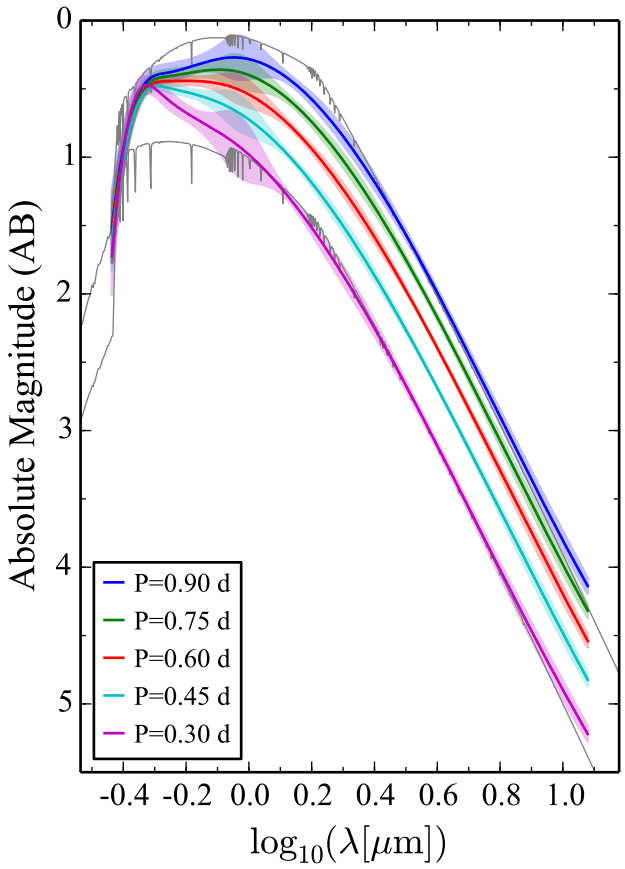

Figure 6.22: Spectral energy distributions of RR Lyrae stars with assorted fundamental oscillation periods, derived from the period–magnitude relations of Fig. 6.20. The individual data points are omitted to permit clearer perception of the spline interpolation curves. Note the large width around 1 μm, which is caused by the less tightly constrained I- and z-band period–magnitude relations. The light gray lines are model stellar spectra from Castelli and Kurucz Atlas 2004 accessed from Space Telescope Science Institute FTP (`http://www.stsci.edu/ftp/cdbs/grid/ck04models`). The models are meant to bracket the RR Lyrae parameter space in radius and effective temperature. The brighter model spectrum corresponds to $T_{\rm eff} = 6250$ K and $R = 7$ R$_\odot$, and the dimmer spectrum to $T_{\rm eff} = 7000$ K and $R = 4$ R$_\odot$. Both models are for $\log g = 2.5$ and $\log Z = -2.5$. This temperature and radius range is consistent with previous work: c.f. Smith (1995).

between the brightest SED (longest period RR Lyrae star) and the dimmest SED (shortest period) is effectively zero shortward R-band, and then this distance increases with increasing wavelength until the SEDs become nearly parallel in the Rayleigh-Jeans tail. This near-parallel property of the SEDs in the infrared graphically explains why the period–magnitude relation slope approaches an asymptote with increasing wavelength.

6.5.2 Intrinsic Scatter and Photometric Error

As described in Section 6.4 the model used in the period–magnitude relation fits allows for investigation of the intrinsic scatter, and of particular importance is the comparison between intrinsic scatter and the photometric error on the mean-flux magnitude measurements. Fig. 6.23 shows both intrinsic scatter and mean photometric error as a function of wavelength. At any given wavelength, the maximum of the intrinsic scatter and mean photometric error provides a floor to how tightly the resultant period–magnitude relation can be constrained (and, in effect, sets the precision limit of distance measurements).

If the photometric error dominates over the intrinsic scatter, then a tighter period–magnitude relation can be derived by collecting better light curve data (i.e., with more sensitive instruments and/or more observation epochs). However, if the intrinsic scatter exceeds the mean photometric error already achieved, then the path towards a tighter period–magnitude relation is not as direct. In this latter case, the period–magnitude relation scatter can be reduced slowly via the augmentation of the calibration sample, but the intrinsic scatter will always dictate the minimum absolute magnitude uncertainty when applying the relation to new stars. The inclusion of a spectroscopically derived metallicity as an additional model parameter could, of course, serve to reduce the intrinsic scatter (e.g., Sandage & Tammann 2006) but we expressly have used a model based upon photometry alone.

Fig. 6.23 shows that the intrinsic scatter exceeds the photometric error for all wavebands except $W1$ and $W2$. This explains why the minimum prediction uncertainty given in Fig. 6.20, σ along the right hand side, is lowest for these wavebands. Furthermore, this finding indicates that continued development and application of RR Lyrae period–magnitude relations at wavebands between 3 and 5 μm will produce the tightest absolute magnitude constraints.

6.5.3 Color Excess Results

A major improvement to the model fit in the present multi-band period–magnitude relations derivation is simultaneously fitting for color excess to each of the calibration stars. This is not feasible with light curve data for only one wavelength regime (such as the work published in Klein et al. 2011 and Klein et al. 2014b). However, the present investigation spans the optical, near-infrared, and mid-infrared wavelength regimes, and this enables color excess to be treated as a model parameter.

An all-sky visualization in Galactic coordinates of the fitted color excess values, as well as the distance modulus, is shown in Fig. 6.24. The colorbar is purposefully asymmetric

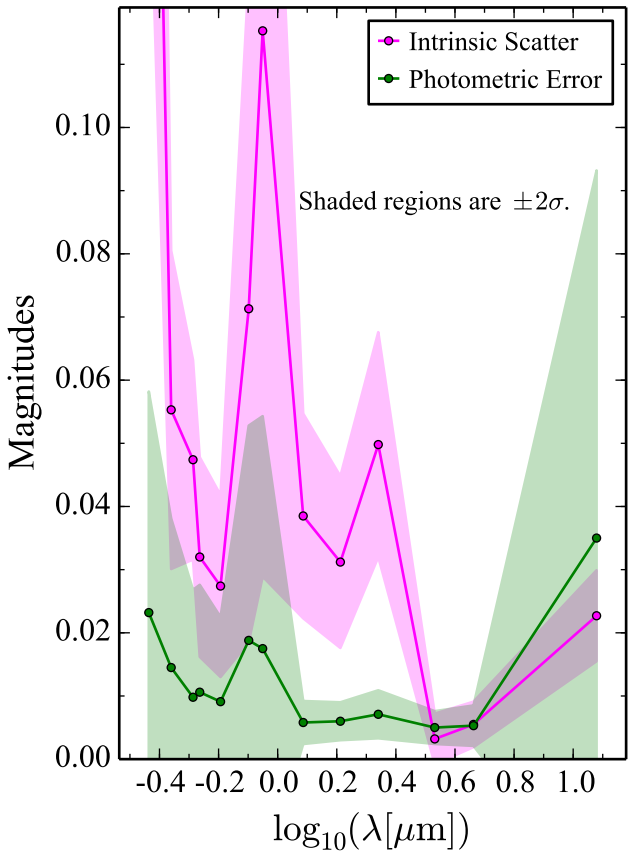

Figure 6.23: Photometric uncertainty and fitted intrinsic scatter as a function of wavelength. Note that the intrinsic scatter at the mid-infrared wavebands ($W1$, $W2$, and $W3$) is of similar value to the average photometric errors, whereas at shorter wavelengths the intrinsic scatter dominates and is the primary source of distance prediction uncertainty in those waveband-specific period–magnitude relations.

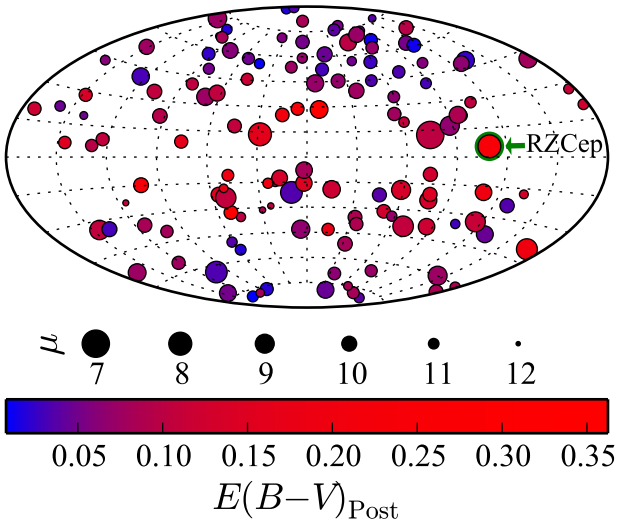

Figure 6.24: Aitoff projection in galactic coordinates of the RR Lyrae stars with symbols colored by posterior fitted color excess, $E(B-V)_{\rm Post}$, and sized by posterior fitted distance modulus, μ. The center of the figure is directed towards the Galactic Center. The distance and color excess of RZCep, a star rejected from the calibration sample and used as an example application in Section 6.6 of the period–magnitude relations, is represented by the marker outlined in green and indicated by the label and green arrow.

to better conform to the dynamic range of the color excess values (most of the values are near 0.08 mag, and very few fall between 0.2 mag and 0.35 mag). An obvious feature of this skymap is the lack of RR Lyrae stars near the Galactic plane. This was enforced by the sample selection criteria discussed in Section 6.2. A second visual trend is that the stars closer to the plane generally have higher color excess values than those nearer the poles due to higher concentrations of interstellar dust near the Galactic plane.

To further explore the fitted color excess values, Fig. 6.25 shows the residual $E(B-V)$ as a function of the absolute value of Galactic latitude, b. It is expected that the prior $E(B-V)_{\rm SF}$ values at low Galactic latitude are greater than the fitted posterior values, since the prior values represent the full color excess expected along a line of sight to infinite distance whereas the posterior values follow a line of sight that terminates at the star (which presumably lies in front of much of the dust that contributes to the prior color excess value). This expectation is indeed seen to hold in Fig. 6.25 for galactic latitudes less than about 15 deg.

An unexpected feature of Fig. 6.25 is that the mean residual color excess does not settle around zero at high galactic latitude. At high latitude a calibrator RR Lyrae star should be behind most of the interstellar dust, and thus the posterior value should approach the prior $E(B-V)_{\rm SF}$ value. However, the mean residual at $b > 30^\circ$ is 0.033 ± 0.001 (with scatter about the mean of 0.024), indicating that either the $E(B-V)_{\rm SF}$ values have a systematic bias, the calibrator RR Lyrae stars are more likely to lie behind more dust than nearby

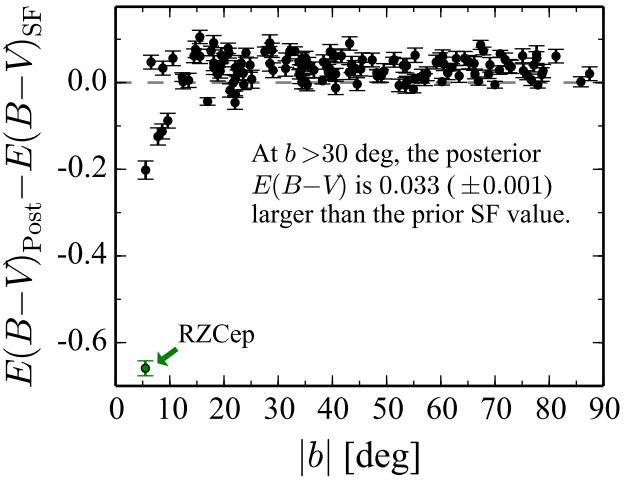

Figure 6.25: Change in color excess, $E(B-V)$, as a function of Galactic latitude, b. RZCep, a star rejected from the calibration sample and used as an example application in Section 6.6 of the period–magnitude relations, is represented by the green marker. The large color excess residual of RZCep indicates that most of the dust contributing to the $E(B-V)_{\rm SF} = 0.9054$ value along its line of sight actually resides behind the star, as expected for a nearby ($d = 405.4 \pm 2.3$ pc) star at a galactic latitude of 5.5°.

lines of sight as measured in the Schlegel et al. (1998) dust map, the value of $R_V = 3.1$ is systematically incorrect, or some combination of all three.

6.5.4 Period–Magnitude Relation Slope

Fig. 6.26 depicts the period–magnitude relation slope as a function of wavelength for the results from this work and other recent studies. In particular, Catelan et al. (2004) produced theoretical calibrations of the period–magnitude relation at I, J, H, and K. Sollima et al. (2006) provides a K-band relation derived from observations of globular clusters. Madore et al. (2013) and Dambis et al. (2014) both derive mid-infrared relations using *WISE* data, the former using four calibrators with *HST* parallax measurements and the latter using RR Lyrae stars detected by *WISE* in globular clusters.

As indicated by the RR Lyrae SEDs (c.f. Fig. 6.22), the period–magnitude relation slope is observed to asymptote with increasing wavelength to a value around −2.3. Note that the slope (α) axis is plotted with lower (steeper) values nearer to the top of the figure. The figure also shows a turnover in the slope in the B-band, but the uncertainty in the U-band slope is too large to rule out the monotonic trend of increasing slope (decreasing in absolute value) with decreasing wavelength. There is a qualitative concordance of our results with other observational and theoretical work.

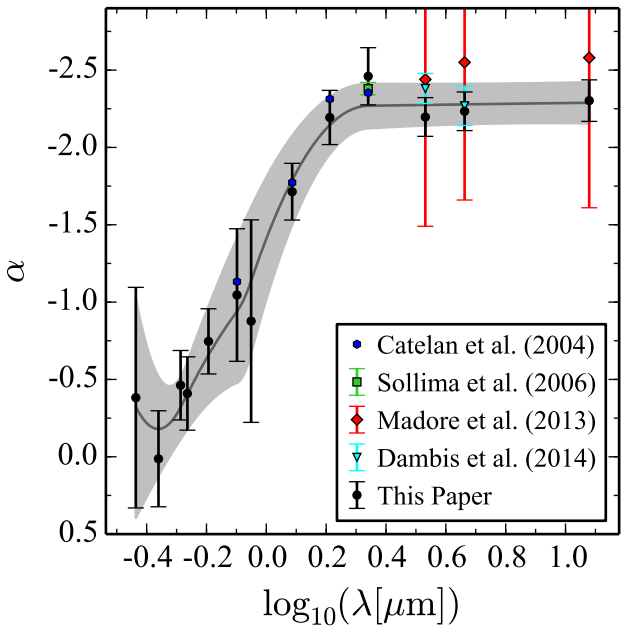

Figure 6.26: Period–magnitude relation slope (α) as a function of wavelength. Gray band is a spline interpolation of the new calibrations presented in this paper.

6.6 Example Application

Light curve data were obtained for RZCep (RRc star with period 0.308645 d, or fundamentalised period 0.413484 d) in the U, B, $hipp$, V, R, I, z, $W1$, $W2$, and $W3$ wavebands (see Table 6.2). However, due to low galactic latitude ($b = 5.5°$) and high $E(B-V)_{\rm SF} = 0.9054 \pm 0.0148$ mag, this star was excluded from the period–magnitude relation fits presented in Section 6.4.

Table 6.2: Mean-flux magnitude data for RZCep.

U	10.4516 ± 0.0052
B	9.7888 ± 0.0047
$hipp$	9.4727 ± 0.0075
V	9.2304 ± 0.0123
R	9.0369 ± 0.0090
I	8.8288 ± 0.0166
z	9.1478 ± 0.0260
$W1$	7.8482 ± 0.0035
$W2$	7.8634 ± 0.0028
$W3$	7.7455 ± 0.0047

Estimating the distance to RZCep using the period–magnitude relations is an excellent test of the results because an *HST* parallax measurement, $\mu_{HST} = 8.02 \pm 0.17$, was published as part of Benedict et al. (2011).

To apply the period–magnitude relations and fit for a distance modulus to RZCep, Equation 6.3 can be rearranged to place the new likelihood information (now including the period–magnitude relation zero point and slope terms) on the left hand side and the formula can be simplified to apply only to RZCep (i subscripts are dropped). The form of the model used for estimating the distance to a single star is thus

$$m_j - M_{0,j} - \alpha_j \log_{10}(P/P_0) = \mu + E(B-V)(a_j R_V + b_j) + \epsilon_j, \tag{6.8}$$

where now ϵ_j is a zero-mean Gaussian random deviate with variance

$$\sigma^2_{m_j} + \sigma^2_{M_{0,j}} + \left[\sigma_{\alpha_j} \log_{10}(P/P_0)\right]^2 + \sigma^2_{j,\mathrm{intrinsic}}.$$

A Bayesian linear regression is fit to solve for the two unknowns, μ and $E(B-V)$, and $R_V = 3.1$ is again used as the extinction law factor (c.f. Section 6.4). The prior distributions should be uninformative and wide [for example, $\mu \sim \mathcal{U}(0, 14)$ and $E(B-V) \sim \mathcal{U}(0, 2)$]. The fit can proceed with mean-flux magnitude measurements in only two bands, but obviously additional waveband data will improve the distance prediction accuracy.

For RZCep, applying the period–magnitude relations derived in Section 6.4 with this Bayesian prediction procedure results in a distance modulus estimate of $\mu_{\mathrm{PLR}} = 8.0397 \pm 0.0123$ (or 405.4 ± 2.3 pc). This is a fractional prediction distance error of 0.57 per cent, an improvement of ∼13 times the reported *HST* parallax distance precision (Benedict et al. 2011) and nearly equal to the 14 microarcsec parallax precision (0.57 per cent fractional distance error) *Gaia* is expected to achieve for bright stellar sources in its end-of-mission analysis (de Bruijne 2012).

In solving for the distance prediction, the fit also produces a posterior color excess value for RZCep, $E(B-V)_{\mathrm{RZCep}} = 0.2461 \pm 0.0089$. This is significantly less than the line of sight to infinite distance color excess of $E(B-V)_{\mathrm{SF}} = 0.9054$, and is very much consistent with RZCep lying only about 400 pc away, even if it is only 5.5° off the Galactic plane. This example demonstrates that the multi-band period–magnitude relation can be used to accurately simultaneously fit for an RR Lyrae star's color excess and distance modulus using only its period and mean-flux magnitude measurements. Fig. 6.28 is the contour density plot for the predicted color excess and distance modulus for RZCep. The anti-correlation is as expected; for a given brightness, a larger color excess value requires that the star be closer, and vice versa.

In theory, the fitted model of Equation 6.8 can be modified to also fit for the extinction law factor, R_V. Such a model was constructed and fit, with the prior distribution of $R_V = \mathcal{N}(3.1, 1)$. The posterior distance is essentially unchanged: $\mu_{\mathrm{PLR}} = 8.0394 \pm 0.0128$ (or 405.4 ± 2.4 pc). The posterior color excess is similar, but substantially wider: $E(B-V)_{\mathrm{RZCep}} = 0.2398 \pm 0.0399$. And, the posterior R_V is highly covariant with color excess and very wide: $R_{V,\mathrm{RZCep}} = 3.2768 \pm 0.5820$. Fig. 6.29 shows the contour density plots for these posterior distributions. Unlike in Fig. 6.28, the color excess and distance modulus are not apparently anti-correlated, suggesting that it is effectively the overall magnitude of the bandpass-dependent extinction (set by the combination of $E[B-V]$ and R_V) which is most directly constrained by the data.

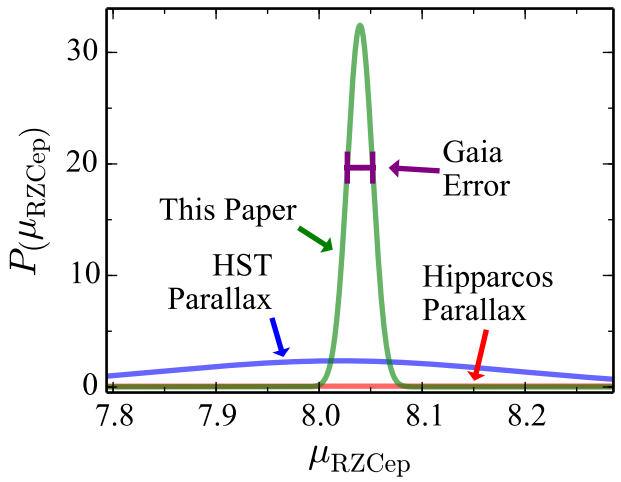

Figure 6.27: Probability density for the distance modulus of RZCep as determined by various methods. The *Hubble Space Telescope* (*HST*) parallax measurement is from Benedict et al. (2011), the *Hipparcos* parallax measurement is from van Leeuwen (2007), and the *Gaia* distance prediction error is 14 microarcsec (de Bruijne 2012), which is very similar to the uncertainty on $\mu_{\rm PLR}$ derived in Section 6.6.

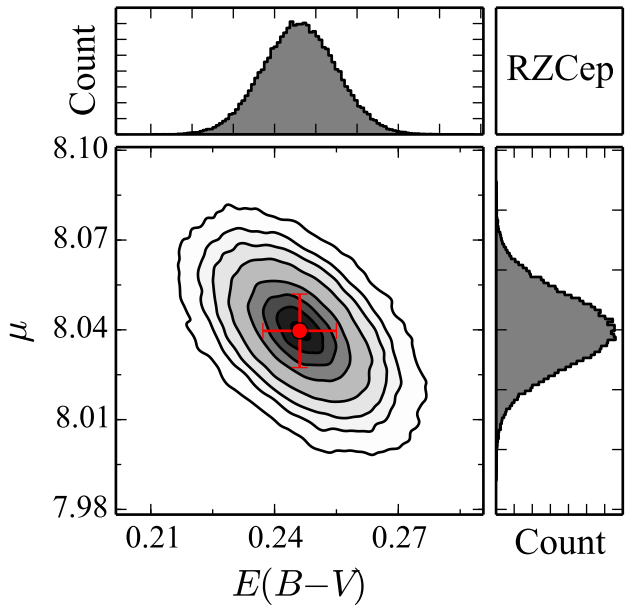

Figure 6.28: Contour density plot and histograms for the predicted color excess, $E(B-V)$, and distance modulus, μ, of RZCep from the multi-band period–magnitude relation. 100,000 samples were generated after the MCMC chain converged. The red circle with associated error bars shows the means and standard deviations of the $E(B-V)$ and μ distributions. Here we fix $R_V = 3.1$.

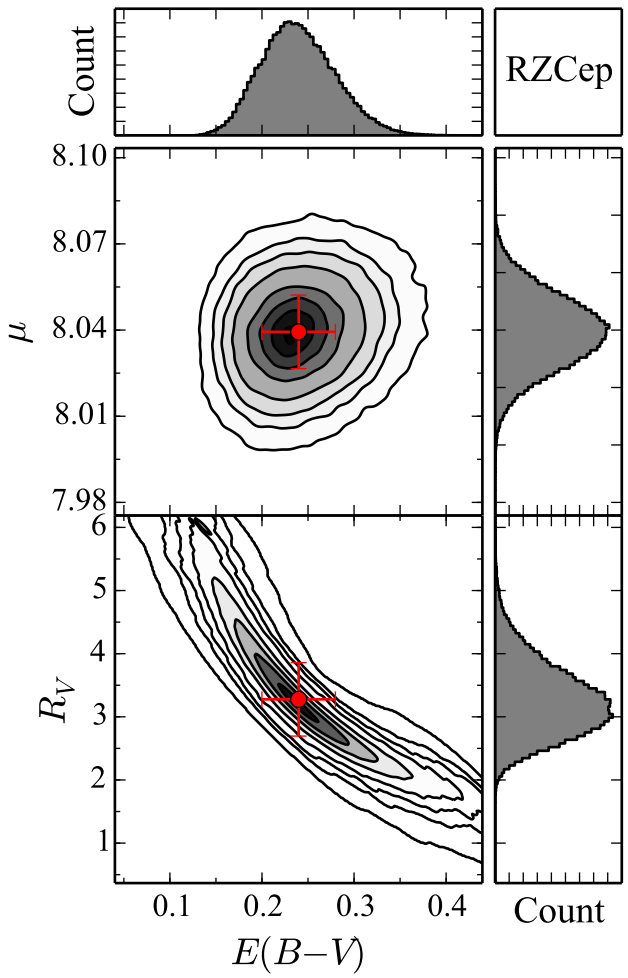

Figure 6.29: Contour density plot and histograms for the predicted color excess, $E(B-V)$, extinction law factor, R_V, and distance modulus, μ, of RZCep from the multi-band period–magnitude relation with R_V fitted as a model parameter (instead of adopting $R_V = 3.1$, as was done for the model that produced Fig. 6.28). 100,000 samples were generated after the MCMC chain converged. The red circle with associated error bars shows the means and standard deviations of the $E(B-V)$, R_V, and μ distributions.

6.7 Discussion and Conclusions

We have applied a simultaneous Bayesian linear regression methodology to 637 mean-flux magnitude measurements of a calibration sample of 134 RR Lyrae stars to derive new, tightly-constrained RR Lyrae period–magnitude relations in 13 wavebands. As part of the regression model, the color excess, $E(B-V)$, for each star was also determined. The final result is that the distances to the 134 calibration stars are measured with median fractional error of 0.66 per cent. We showed how the period–magnitude relations can be used singly or in combination through the methodology described in Section 6.6 to derive distances to other observed RR Lyrae stars achieving a similar level of precision.

As part of the multi-band fit, the intrinsic scatter, $\sigma_{\rm intrinsic}$, for each period–magnitude relation was constrained. Intrinsic scatter is the residual about the best-fit period–magnitude relation in each waveband which cannot be accounted for by instrumental photometric error. It was found that $\sigma_{\rm intrinsic}$ is minimised for the mid-infrared $W1$ and $W2$ wavebands, indicating that this wavelength regime provides the most accurate absolute magnitude predictions via its period–magnitude relations. The overall principle of the simultaneous multi-band fitting methodology is that additional wavelength data for a star is always useful in improving the absolute magnitude (and thus distance) estimate accuracy. However, the $\sigma_{\rm intrinsic}$ analysis suggests that the most valuable wavebands for this purpose are around 3-5 μm.

Also of note are the specific results pertaining to fitted color excess for each calibration RR Lyrae star. The regression found that tighter period–magnitude relation fits were possible by preferring a systematic increase in posterior color excess, as compared to the $E(B-V)_{\rm SF}$ values (c.f. Fig. 6.25). While this could be explained by a systematic error in the Schlegel et al. (1998) dust map or an R_V value significantly different from 3.1, a possible physical explanation is that RR Lyrae stars are often enshrouded in a local dust envelope. Stellar evolution models require the progenitors of RR Lyrae stars to shed about 0.1 $M_\odot$ of material within a few hundred million years as the stars evolve to the horizontal branch (Smith 1995). This material, blown off the stars via stellar wind, may cool to form dust. Strict conclusions should not be drawn from the findings of these period–magnitude relation fits, but further investigation of this hypothesis is encouraged.

As an alternative method for presenting the results, the period–magnitude relations were used to calculate the mean-flux SEDs of RR Lyrae stars as a function of period, as presented in Fig. 6.22. The derived SEDs coincide with model stellar spectra calculated at bounding values of RR Lyrae effective temperature and radius. This perspective view of the period–magnitude relations makes clear why the relation slope, α, is observed to asymptote at longer wavelengths, as shown in Fig. 6.26.

There are some possible extensions to the formalism we have presented. First, in the analysis presented we fixed $R_V = 3.1$ but R_V could be left as a free parameter either globally or for every line of sight. In our initial work for this paper we left R_V to be free for every line of sight and found that the MCMC chains did not converge. This is understandable given the degeneracies between μ, R_V and $E(B-V)$ in the formulation and the fact that many stars in the sample had only a few bandpasses in which mean magnitudes were measured.

Nevertheless, we believe that $\sigma_{\rm intrinsic}$ serves to capture any of the potential systematic errors that might be induced by a variable or globally different value of R_V. There is some validation on this point in that when we allowed R_V to vary for RZCep, traces in R_V and $E(B-V)$ are strongly anti-correlated but the inferred distance posterior is essentially unchanged (see Fig. 6.29). By adding UV data (say from the Swift satellite), in a future work, the degeneracy between R_V and $E(B-V)$ may be broken. Second, we did not include in the formalism any term related to a possible effect on metallcity, lacking a physically motivated parametrization for doing so. If such a theoretical formalism is found, it could be easily incorporated. Note that we found no correlation of deviations from period-magnitude relations with metallicity, again offering $\sigma_{\rm intrinsic}$ as the likely capturer of any systematic errors of unmodelled metallicity dependencies.

The future applications of the derived RR Lyrae period–magnitude relations range from nearby Milky Way structure studies to distance measurements at truly cosmic scales (pushing into the Hubble Flow at $d > 100$ Mpc). Ground-based optical surveys (PanSTARRS, iPTF, Catalina Sky Survey, OGLE IV, LSST, etc.) and the proliferation of near-infrared followup facilities (RATIR, NEWFIRM, UKIRT, etc.) are now enabling studies of Milky Way Field and Halo RR Lyrae stars to produce highly accurate distance measurements. Mid-infrared facilities and surveys (SOFIA, *Spitzer Space Telescope*, MaxWISE, and in the near future, JWST) can also be leveraged to significantly improve RR Lyrae distance measurement precision. These studies will use the RR Lyrae period–magnitude relations to map Milky Way stellar density, measure the morphology of remnant tidal streams in the Halo, and probe the depth structure of the Magellanic Clouds.

Additionally, as demonstrated in the present work, combining optical and infrared light curve data for an RR Lyrae star can provide a fit for both distance and color excess along that line of sight to that distance. Given enough RR Lyrae targets (Eyer et al. 2012 predicts ∼100,000 RR Lyrae stars in the Milky Way), a 3D dust map can be constructed to better understand the distribution of Milky Way dust grains and to also aide in estimating line-of-sight extinction for studies of other objects within the Milky Way. As a cross check and calibrator, we see precision 3D line-of-sight dust measurements (Bailer-Jones 2011) as complementary to the ongoing all-sky efforts using aggregate stellar populations (Sale 2012; Berry et al. 2012; Hanson & Bailer-Jones 2014; Green et al. 2014), which offer aggregate dust measures over arcminute scales and in wide distance bins. With a significantly larger sample, it will also be possible to test how universal the power-law fits are for different subpopulations of RR Lyrae: there may very well be measurable differences in relations as a function of metallicity, environment and/or population origin (e.g., thick disk vs. bulge).

RR Lyrae stars serve as primary distance indicators in the Cosmic Distance Ladder via their period–magnitude relations. As such, RR Lyrae stars are vital to calibrating the relations used for secondary distance indicators that extend out well beyond the Local Group. Error in distance measurement methods propagates up the distance ladder, and thus minimisation of error at the local end can significantly improve the accuracy of secondary indicators and the derived higher-level measurements, such as H_0. This effect, as applied through improving the Cepheid Leavitt Law to better constrain Type Ia supernovae luminosity, has

recently been very well utilised by both Riess et al. (2011) and Freedman et al. (2012) in their measurements of H_0 with ~ 3 per cent precision.

RR Lyrae stars, in combination with the TRGB method to reach distant supernova host galaxies, offer a systematically separate and competitive means for Type Ia supernova luminosity calibration. Additional physical distance measurement methods such as this are necessary to help resolve the conflict between the H_0 values found by the distance ladder methods of Riess et al. (2011) (73.8 ± 2.4 km s^{-1} Mpc^{-1}) and Freedman et al. (2012) (74.3 ± 2.1 km s^{-1} Mpc^{-1}), and the statistically significantly lower measurement derived by Planck Collaboration et al. (2013) with Cosmic Microwave Background data from the Planck satellite (67.3 ± 1.2 km s^{-1} Mpc^{-1}). If our methodology holds up to scrutiny the achievement of sub-1 per cent fractional distance errors (herein, 0.66 per cent for the calibration sample) within a formalism that accounts for dust extinction may be considered a strong buttressing of the path to eventual 1 per cent uncertainties in Hubble's constant.

Acknowledgments

The authors acknowledge the generous support of grants (#0941742 and #1009991) from the National Science Foundation. The authors acknowledge and thank Ed Rosten for providing the normalized cross correlation image-alignment program utilized as part of the PAIRITEL reduction pipeline. PAIRITEL was operated by the Smithsonian Astrophysical Observatory (SAO) and was made possible by a grant from the Harvard University Milton Fund, a camera loan from the University of Virginia, and continued support of the SAO and UC Berkeley. The research with PAIRITEL was also support by NASA guest investigator grants NNX12AE67G and NNX13AC58G. We are grateful for the assistance of the staffs at all of the observatories used to obtain the data. This research has made use of the NASA/IPAC Infrared Science Archive, which is operated by the Jet Propulsion Laboratory, California Institute of Technology, under contract with the National Aeronautics and Space Administration. This publication makes use of data products from the Two Micron All Sky Survey, which is a joint project of the University of Massachusetts and the Infrared Processing and Analysis Center/California Institute of Technology, funded by the National Aeronautics and Space Administration and the National Science Foundation. This publication makes use of data products from the *Wide-field Infrared Survey Explorer*, which is a joint project of the University of California, Los Angeles, and the Jet Propulsion Laboratory/California Institute of Technology, funded by the National Aeronautics and Space Administration. This publication also makes use of data products from *NEOWISE*, which is a project of the Jet Propulsion Laboratory/California Institute of Technology, funded by the Planetary Science Division of the National Aeronautics and Space Administration. This research has made use of NASA's Astrophysics Data System.

Chapter 7

Probing the Distance and Morphology of the Large Magellanic Cloud with RR Lyrae stars

An earlier version of this chapter has been submitted for publication in MNRAS with coauthors S. B. Cenko, Adam A. Miller, Dara J. Norman, and Joshua S. Bloom.[1]

Abstract

We present a Bayesian analysis of the distances to 15,040 Large Magellanic Cloud (LMC) RR Lyrae stars using V- and I-band light curves from the Optical Gravitational Lensing Experiment, in combination with new z-band observations from the Dark Energy Camera. Our median individual RR Lyrae distance statistical error is 1.89 kpc (fractional distance error of 3.76 per cent). We present three-dimensional contour plots of the number density of LMC RR Lyrae stars and measure a distance to the core LMC RR Lyrae center of

$$\begin{aligned} d_{\rm LMC} &= 50.2482 \pm 0.0546 \text{ (statistical) } \pm 0.4628 \text{ (systematic) kpc} \\ \mu_{\rm LMC} &= 18.5056 \pm 0.0024 \text{ (statistical) } \pm 0.02 \text{ (systematic).} \end{aligned}$$

This finding is statistically consistent with and four times more precise than the canonical value determined by a recent meta-analysis of 233 separate LMC distance determinations. We also measure a maximum tilt angle of $11.84^\circ \pm 0.80^\circ$ at a position angle of 62°, and report highly precise constraints on the V, I, and z RR Lyrae period–magnitude relations. The full dataset of observed mean-flux magnitudes, derived color excess $E(V-I)$ values, and fitted RR Lyrae distances produced through this work is made available through the publication's associated online data.

[1] Klein et al. (2014a).

7.1 Introduction

At a distance of roughly 50 kpc, the Large Magellanic Cloud (LMC) is the closest galaxy to the Milky Way with mass $\gtrsim 10^{10}$ $M_\odot$. As such, it serves as an essential anchor point for the cosmic distance ladder. A precisely measured distance to the LMC allows for accurate luminosity calibrations of primary distance indicators such as pulsating variables (PVs; e.g., Cepheids and RR Lyrae stars). These calibrations enable precise distance measurements to galaxies well beyond the LMC (c.f. Freedman et al. 2001 and Riess et al. 2011, both of which use Cepheids to measure host galaxy distances of > 15 Mpc), which can, in turn, calibrate secondary distance indicators such as Type Ia supernovae. de Grijs et al. (2014) provides an excellent and comprehensive review of LMC distance measurements published between 1990 and the end of 2013, and recommends a canonical distance modulus of $\mu_{\rm LMC} = 18.49 \pm 0.09$ mag ($d_{\rm LMC} = 49.888 \pm 2.068$ kpc). Pietrzyński et al. (2013) recently used eight long-period, late-type eclipsing systems in the LMC to measure a distance of 49.97 ± 0.19 (statistical) $\pm$ 1.11 (systematic) kpc, and this result was used in the meta-analysis as the standard by which other, less accurate findings were assessed. Precisely pinning down the LMC's distance is a necessary step in the continuing improvement of the cosmic distance ladder as progress is made towards a 1 per cent error measurement of the Hubble constant, H_0.

The bulk identification and study of thousands of LMC PVs also enables investigation of the three-dimensional structure of the LMC. Through their individual distance measurements, the many thousands of RR Lyrae stars in the LMC can serve as test particles tracing the old (> 10 Gyr) stellar population, revealing its three-dimensional morphology. While there are $\sim$10 times fewer Cepheids, these higher-mass variables can be employed to reveal the structure of the younger LMC stellar population (e.g., Alcock et al. 1999). With adequate precision this line of inquiry can inform our understanding of the LMC, its formation, and the nature of its gravitational interaction with the Milky Way.

In the present study the individual distances to 15,040 RR Lyrae stars in the LMC identified in the catalogue of variable stars produced by the third phase of the Optical Gravitational Lensing Experiment (OGLE III, Udalski et al. 2008b and Soszyński et al. 2009) are measured and used to infer a distance to the central core of the LMC RR Lyrae population, as well as to recover the three-dimensional density structure of the population. More than a century of research has been conducted on RR Lyrae stars, much of it in pursuit of improving their utility as distance indicators, and an adequate treatment of this topic cannot be provided here. The interested reader is directed towards Preston (1964) and Smith (1995) which both provide excellent overviews of RR Lyrae pulsating variable stars, and towards Sandage & Tammann (2006) for a review of RR Lyrae stars as distance indicators.

This investigation is similar to the recent studies (Haschke et al. 2012; Wagner-Kaiser & Sarajedini 2013; Deb & Singh 2014), which all used the V- and I-band OGLE III data as the basis for their LMC distance and structure measurements. Our study leverages new z-band mean-flux photometry for the LMC RR Lyrae stars obtained with the Dark Energy Camera (DECam, first described in Wester & Dark Energy Survey Collaboration 2005 with

recent status update given by Flaugher et al. 2012) in combination with the OGLE III V- and I-band light curves to simultaneously calibrate the three period–magnitude relations and fit for extinction. From these relations we determine the posterior distance moduli to each RR Lyrae star. This simultaneous period–magnitude relation calibration and distance fitting methodology was first described in Klein et al. (2011, 2012a, 2014b), and expanded to include simultaneous color excess fitting in Klein & Bloom (2014), hereafter KB14.[2]

This paper is outlined as follows: the OGLE III and DECam data, as well as the calculation of mean-flux magnitudes, are described in Section 7.2. The method by which the individual RR Lyrae star distances are determined is detailed in Section 7.3. In Section 7.4 these distances are used to describe and analyse the distance to and morphology of the LMC RR Lyrae population. Finally, in Section 7.5 we compare the present work to other similar studies and discuss the implications of our results.

7.2 Data Description

The OGLE III catalogue of LMC RR Lyrae stars (overview of LMC photometry: Udalski et al. 2008b, characterisation of LMC RR Lyrae stars: Soszyński et al. 2009) was used as the input target list for the present work. This is supplemented with z-band observations of the LMC acquired with DECam during its science verification period in 2012 November. The OGLE III catalogue provided V- and I-band light curves for 22,247 stars. Requiring that each star also have DECam z-band data results in a sample of 17,629 stars. This is further reduced by median absolute deviation clipping and sigma-clipping from a least squares linear regression, described in detail in subection 7.3.2, to a final sample of 15,040 RR Lyrae stars (11,846 RRab and 3,194 RRc).

The sky coverage of both the OGLE III survey and the DECam observing program, along with the scatter plot map of the final RR Lyrae sample, is shown in Fig. 7.1. The OGLE III coverage is quite uniform and complete within its combined footprint, but the DECam coverage has multiple gaps resulting from the observing strategy and instrumental deficiencies which are further discussed in subsection 7.2.2.

7.2.1 OGLE III Mean-flux Magnitudes

OGLE III V- and I-band light curves and measured periods for the RR Lyrae stars (RRab and RRc subtypes) were downloaded from the catalogue published in Soszyński et al. (2009). Mean-flux magnitudes for each light curve were measured following the procedure described in Section 3 of KB14. In short, the raw data is parametrically resampled 500 times to fit 500 harmonic models and derive 500 mean-flux magnitude measurements for each light curve. The standard deviation of these bootstrapped mean-flux magnitude measurements is taken to be the measurement error. This procedure resulted in 22,125 V-band and 22,188

[2]In the present work, however, we do not fit the color excess as part of the model, in part because this makes the solution, now involving 10^2 times more stars, computationally intractable.

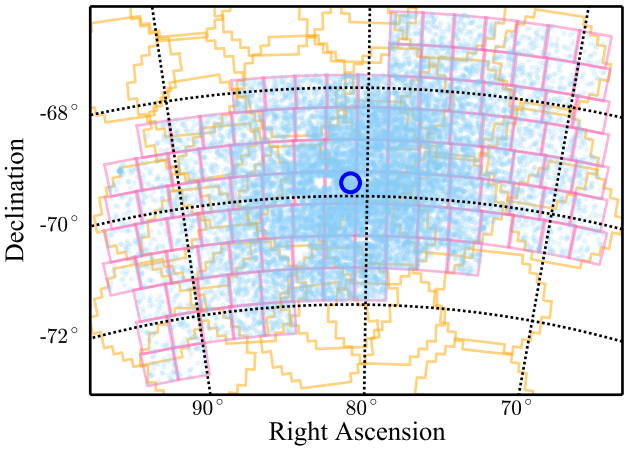

Figure 7.1: Map of the LMC RR Lyrae stars (blue points) superimposed upon OGLE III (pink) and DECam (gold) field-of-view outlines. The central blue circle shows the optical center of the LMC at RA: 80.8942°, Dec: −69.7561° (J2000).

I-band RR Lyrae mean-flux magnitudes. This is less than the starting OGLE III dataset of 22,247 light curves in each band because light curves which produce highly discrepant bootstrapped harmonic models are rejected. The mean error in V is 0.006 mag and the mean error in I is 0.0024 mag.

7.2.2 DECam Observations and Reduction

As part of the DECam Science Verification program (Program ID: 2012B-3002; PI: Bloom), we obtained a single epoch of z-band exposures of $30 \times 3.0\,\mathrm{deg}^2$ fields on 16 nights from 2012 November 1–18 UT. The fields were selected to maximize coverage of the OGLE III LMC footprint, with small offsets applied to cover chip gaps and minimize bleed trails from extremely bright stars (Fig. 7.1). For each exposure, 61 of the 62 individual science CCDs[3] were processed using standard reduction algorithms (bias subtraction, flat-fielding, etc.) using the computational resources at the National Energy Research Scientific Computing Center (NERSC[4]).

Astrometry on individual frames was calibrated with respect to reference sources from the Two Micron All Sky Survey (2MASS; Skrutskie et al. 2006) using the astrometry.net software package (Lang et al. 2010). Photometric calibration was performed using same-night observations of sources in the Sloan Digital Sky Survey Stripe 82 Standard Star Catalogue (Ivezić et al. 2007). Applying standard calibration methodology (e.g., Ofek et al. 2012), we find that we can achieve a robust scatter in our absolute photometric calibration of $\lesssim 0.02$ mag on clear nights ($\gtrsim 50$ per cent of the observing time from the Science Verification run). While this calibration can be improved with more advanced modeling of instrumental

[3]One chip, C61, was not fully operable during the Science Verification run.
[4]See http://www.nersc.gov.

signatures (e.g., Tucker et al. 2014), we find that 2 per cent precision is sufficient for our scientific objectives.[5]

The DECam observing program produced on average one 1-second exposure for each of the 30 fields each night. This sub-optimal exposure depth and cadence was necessitated by the oversubscription of DECam and the desire to test the instrument performance in unusual or extreme modes of operation during the science verification period. Most of the RR Lyrae targets are marginally detected in single exposures, but this was not sufficient to produce the traditional phase-folded light curves that provide mean-flux measurements through harmonic modeling. To recover z-band mean-flux magnitudes the individual epochs of each CCD were flux-scaled using relative photometric zero points measured with PSFex (Bertin 2011) and SExtractor (Bertin & Arnouts 1996), and then average combined with Swarp (Bertin et al. 2002). This procedure resulted in a mean error on the z-band mean-flux magnitude measurements for the final RR Lyrae sample of 0.0387 mag, which includes the errors introduced by absolute photometric calibration and the relative epoch-to-epoch flux-scaling.

7.3 RR Lyrae Distance Measurements

Distances for the individual RR Lyrae stars are measured using the observed, extinction-corrected V, I, and z magnitudes in combination with the period–magnitude relations. The method employed is similar to the simultaneous Bayesian linear regression methodology described in KB14. A significant difference is that in the present analysis the color excess is considered part of the observed data, not as a prior to which a posterior distribution is fit. The following two subsections detail the derivation of individual RR Lyrae color excess and provide more description of the specific period–magnitude relations fitting procedure.

7.3.1 Color Excess

The $E(V-I)$ color excess for each RR Lyrae star is derived from the observed OGLE III mean-flux magnitudes and the previously-calibrated V and I period–magnitude relations published in KB14. This approach is conceptually similar to that of Haschke et al. (2011), with the main difference being that the earlier study used the theoretical V-band metallicity–luminosity and I-band period–metallicity–luminosity relations of Catelan et al. (2004). In the present work, color excess is given by the subtraction of the absolute color (from the period–magnitude relations) from the observed color,

$$E(V-I) = (m_V - m_I) - [M_V(P) - M_I(P)]. \tag{7.1}$$

The dominant source of error in the color excess calculation is the intrinsic scatter of the period–magnitude relations. The median color excess for the LMC RR Lyrae population is

[5]Error in the color excess, itself dominated by intrinsic scatter in the previously-derived period–magnitude relations of KB14, dominates over photometry errors when calculating individual RR Lyrae star distances.

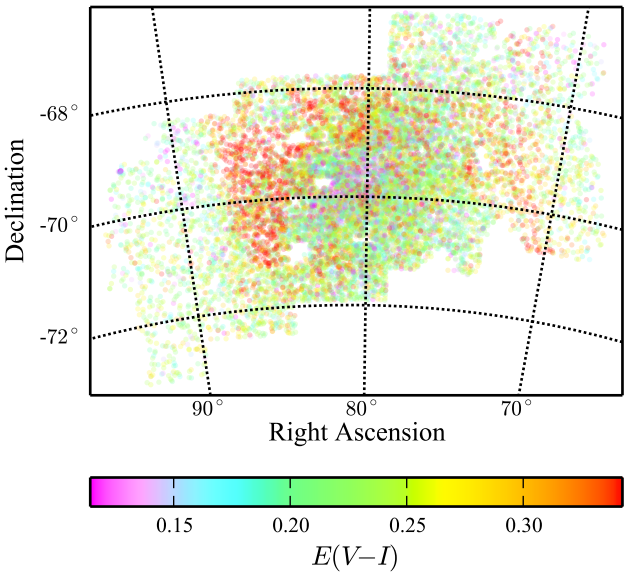

Figure 7.2: Map of the LMC RR Lyrae stars colored by color excess value, $E(V-I)$. Median RR Lyrae color excess value is 0.228 mag, and the median error per star is 0.093 mag.

found to be 0.228 mag, with a median error of 0.093 mag. This is significantly greater than the median value of 0.11 mag (with standard deviation of 0.06 mag) found by Haschke et al. (2011). Fig. 7.2 is a map of the RR Lyrae distribution colored by color excess. Two prominent regions of large extinction are apparent, one shaped like a downward-pointing wedge located at a right ascension $\approx 87°$, and the other a band running north-south centered at right ascension $\approx 73°$. Both of these features are also noted by Haschke et al. (2011) and depicted in their Fig. 10.

The band-specific extinction for each star was derived from the measured color excess value using the extinction curve data given in Table 6 of Schlegel et al. (1998). We apply a conversion factor of 1.62 to transform $E(V-I)$ to the conventional $E(B-V)$ (see Johnson 1968, Schultz & Wiemer 1975, and Rieke & Lebofsky 1985). The corrected mean-flux magnitudes are thus given by

$$m_V = m_{V,\mathrm{obs}} - 3.240 \times [E\,(V-I)\,/1.62] \tag{7.2}$$
$$m_I = m_{I,\mathrm{obs}} - 1.962 \times [E\,(V-I)\,/1.62] \tag{7.3}$$
$$m_z = m_{z,\mathrm{obs}} - 1.479 \times [E\,(V-I)\,/1.62]\,. \tag{7.4}$$

7.3.2 Period–Magnitude Relations

The V, I, and z extinction-corrected mean-flux magnitudes were used to calibrate period–magnitude relations through a method similar to the Bayesian simultaneous linear regression formalism employed for 13 simultaneous fits in KB14. The primary difference in this application is that the color excess is not fitted as a model parameter, and is instead incorporated

into the likelihood (observed data). The framework easily accommodates the extra model parameters, but the augmented processing time, which goes roughly as $\mathcal{O}(n^2)$, is unreasonable for fitting a model with 15,040 stars (compared to the calibration sample size of 134 for KB14).

Before the Bayesian MCMC fitting procedure was performed, the dataset of 17,629 stars was cleaned to reject outliers. These are most likely foreground stars or stars with poorly measured photometry resulting from crowding effects. All stars with a median absolute deviation in magnitude greater than 5σ for any of the three wavebands were removed, and then a simple least squares linear regression was performed to fit preliminary period–magnitude relations and all stars more than 4σ from the best fitted line for any waveband's relation were also removed. 15,040 RR Lyrae stars survived the cuts and made it into the calibration sample.

The calibration sample is composed of 11,846 RRab stars (fundamental mode pulsators, period P_f) and 3,194 RRc stars (first overtone pulsators, periods P_{fo}). The RRc stars' periods must be "fundamentalized" before deriving the period–magnitude relations. As in Dall'Ora et al. (2004), an RRc star's fundamentalized period is given by

$$\log_{10}(P_f) = \log_{10}(P_{fo}) + 0.127. \tag{7.5}$$

The general form of the period–magnitude relation is then

$$m_{ij} = \mu_i + M_{0,j} + \alpha_j \log_{10}(P_i/P_0) + \epsilon_{ij}, \tag{7.6}$$

where m_{ij} is the observed apparent, extinction-corrected mean-flux magnitude of the ith RR Lyrae star in the jth waveband, μ_i is the distance modulus for the ith RR Lyrae star, $M_{0,j}$ is the absolute magnitude zero point for the jth waveband, α_j is the slope in the jth waveband, P_i is the fundamentalized period of the ith RR Lyrae star in days, P_0 is a period normalisation factor (for consistency with KB14 we use $P_0 = 0.52854$ d), and the ϵ_{ij} error terms are independent zero-mean Gaussian random deviates with variance $(\sigma^2_{\text{intrinsic},j} + \sigma^2_{m_{ij}})$.

The error on the extinction-corrected mean-flux magnitudes, $\sigma_{m_{ij}}$, was derived by propagating the error from the contributing observed apparent magnitudes and color excess terms (see equations 7.2–7.4). The intrinsic scatter of the period–magnitude relations, $\sigma_{\text{intrinsic},j}$, which is added in quadrature with $\sigma^2_{m_{ij}}$ to calculate the standard deviation of the likelihood, is adopted from the findings of KB14: $\sigma_{\text{intrinsic},V} = 0.0320$, $\sigma_{\text{intrinsic},I} = 0.0713$, and $\sigma_{\text{intrinsic},z} = 0.1153$.

The prior distributions for $M_{0,j}$ and α_j were normal distributions centered at the fitted values for the V, I, and z period–magnitude relations found by KB14, with standard deviations expanded to 0.2 for M_0 and 1.5 for α (to allow the MCMC traces freedom to explore a wider parameter-space). The same prior, $\mathcal{N}(18.5, 0.2163^2)$, was used for all of the μ_i. This standard deviation was selected to be a fractional distance error of 10 per cent (≈ 5 kpc), which is much larger than the depth of the LMC and significantly larger than (> 2 times) the median posterior σ_{μ_i}.

To fit the model given by equation 7.6 ten identical MCMC traces were run, each generating 3.5 million iterations. The first 0.5 million were discarded as burn-in and the remaining

3 million were thinned by 300 to result in ten traces of 10,000 iterations each. The Gelman-Rubin convergence diagnostic, $\hat{R}$ (Gelman & Rubin 1992), was computed for each posterior model parameter (3 zero points, 3 slopes, and 15,040 distance moduli) and all are found to be well-converged ($\hat{R} < 1.1$).

The best fitted period–magnitude relations and a scatter plot of the RR Lyrae posteriors (M computed using $\mu_{\rm Post}$) is presented in Fig. 7.3. The equations for the period–magnitude relations are

$$M_V = (0.448 \pm 0.003) - (0.999 \pm 0.038) \times \log_{10}(P/P_0) \tag{7.7}$$
$$M_I = (0.073 \pm 0.002) - (1.701 \pm 0.034) \times \log_{10}(P/P_0) \tag{7.8}$$
$$M_z = (0.483 \pm 0.002) - (1.774 \pm 0.034) \times \log_{10}(P/P_0)\,. \tag{7.9}$$

These results are consistent (within 2σ) with the findings published in KB14 (also Chapter 6). The new slopes are systematically lower, although the previous constraints are considerably wider. The extremely tight distributions for the posterior M_0 and α are due to the very large number of RR Lyrae stars in the calibration dataset, as compared to previous studies that have used calibration samples of a few dozen to slightly more than one hundred stars collated from the local Milky Way field RR Lyrae population.

7.4 LMC Distance and Morphology

The individual distance moduli fitted via the Bayesian simultaneous linear regression method described in subsection 7.3.2 have a median error of 0.0816 mag (a fractional distance error of 3.76 per cent, or 1.89 kpc). The standard deviation of the distances is 2.2 kpc, which is a proxy for the physical extent of the LMC along the line of sight. Thus, the individual RR Lyrae distances serve as a probe of the LMC depth structure, and can be analysed as a population to reveal structure at even smaller physical scales. The following subsections present an analysis of the spatial distribution of the LMC core RR Lyrae population and the overall tilt of the LMC in the plane of the sky. Fig. 7.4 shows a map of the RR Lyrae stars colored by distance, with the strip exhibiting maximum tilt outlined in blue.

7.4.1 RR Lyrae Density Structure

To investigate the density structure of RR Lyrae stars in the LMC, the spherical sky coordinates (right ascension, declination, and distance from Earth) for each star were transformed into a local, LMC-centered cartesian coordinate frame. Then, the local number density was computed for each star by counting the number of neighboring stars within a sphere of $V = 1$ kpc^3. This generated 15,040 local number density data points which were then interpolated onto a grid of $401 \times 401 \times 401$ voxels in a cube of side length 6 kpc to produce the three-dimensional contour plots presented in Figs. 7.5, 7.6, and 7.7.

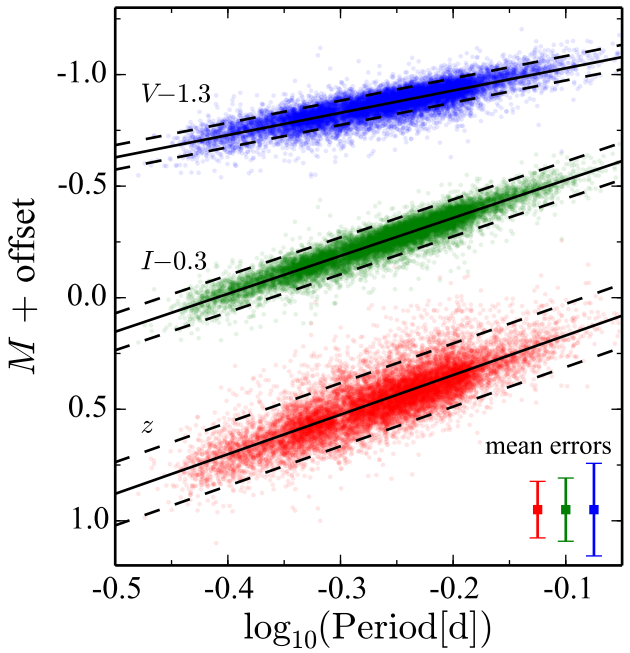

Figure 7.3: V-, I-, and z-band period–magnitude relations (solid lines) derived for the LMC RR Lyrae population, superimposed on scatter plots of the RR Lyrae posteriors (M computed using $\mu_{\rm Post}$). The dashed lines denote the 1σ prediction intervals for a new RR Lyrae star with known period.

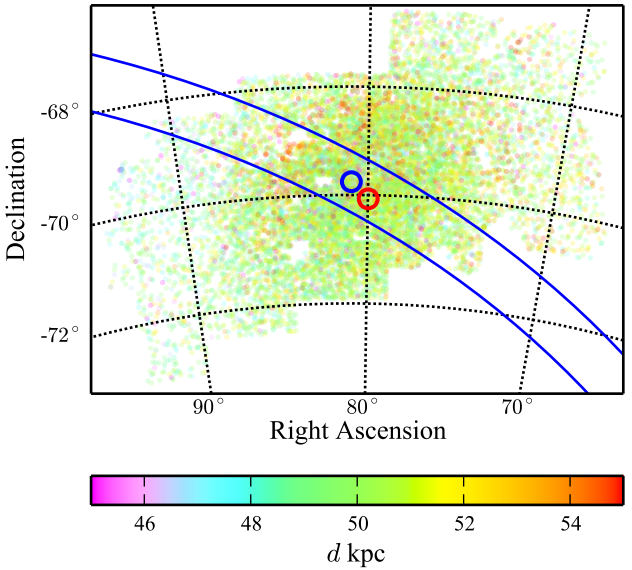

Figure 7.4: Map of the LMC RR Lyrae stars colored by distance. The strip outlined in blue is centered at the LMC optical center (blue circle), and has a width of 1 kpc and a position angle of 62°. Along this strip the distance slope angle (the tilt of the LMC in the plane of the sky) is measured to be $11.84° \pm 0.80°$, with the eastern side (left-hand-side on the page) being closer to Earth. The red circle denotes our measured central position for the core RR Lyrae population at right ascension 79.9855° and declination −70.0697°.

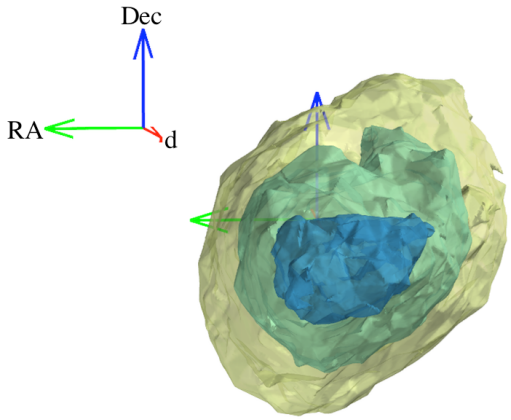

Figure 7.5: Three-dimensional contour plot of RR Lyrae number density in the core of the LMC. The view is projected along the vector pointing away from Earth (red arrow pointing into the page). The green arrow points along the direction of increasing right ascension and the blue arrow points along the direction of increasing declination. The origin of the arrow vectors inside the density contours is at the optical center of the LMC, at the central distance of the RR Lyrae population. Each arrow is 1 kpc in length. The contour surfaces are at RR Lyrae number densities of 200, 250, and 300 kpc^{-3}.

These three-dimensional plots clearly show that the core, highest-density concentration of RR Lyrae stars lies southward and somewhat westward of the optical center. Additionally, the depth of the core appears significantly larger than its extent in right ascension or declination. The much larger individual RR Lyrae position error in depth ($\sim$ 1.9 kpc vs effectively 0 for right ascension and declination) can lead to apparent elongation along that axis in these results, which must be taken into account when interpreting the plots.

A distance to the center of the core LMC RR Lyrae population was determined by parametric resampling of the mean distance measurement for the 1,231 stars that lie within the 250 kpc^{-3} density contour. This resulting distance measurement is 50.2482 ± 0.0546 kpc ($\mu_{\rm LMC} = 18.5056 \pm 0.0024$), where the given error is statistical. Due to the 0.02 mag absolute photometric calibration of the DECam z-band mean-flux magnitudes [which dominates over the OGLE III photometric calibration error (Udalski et al. 2008a)], an additional systematic LMC distance error of 0.4628 kpc (0.02 mag for distance modulus) is appropriate. The right ascension of the core center was found to be 79.9855° and the declination was found to be $-70.0697°$.

7.4.2 Tilt of the LMC RR Lyrae Population

The tilt angle of the LMC in the plane of the sky (derived from the depth slope) was measured by rotating 1 kpc-wide strips about the optical center through all position angles (0° through 180°). The general schematic for this approach is provided in Fig. 7.4. All of the

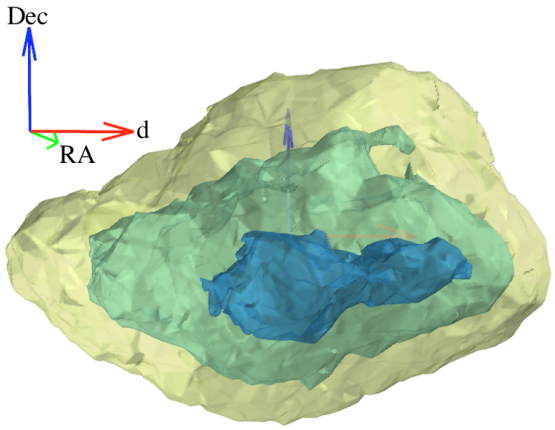

Figure 7.6: Three-dimensional contour plot of RR Lyrae number density in the core of the LMC, now rotated so that the view is projected along the vector of increasing right ascension (right ascension increases into the page). Axis arrows and contours same as Fig. 7.5.

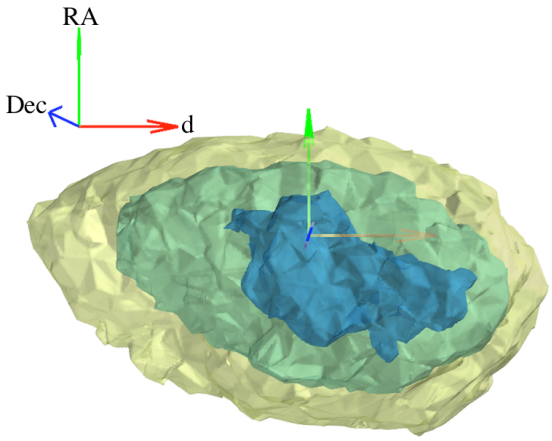

Figure 7.7: Three-dimensional contour plot of RR Lyrae number density in the core of the LMC, now rotated so that the view is projected along the vector of decreasing declination (declination increases out of the page). Axis arrows and contours same as Fig. 7.5. This view illustrates the tilt of the LMC in the plane of the sky. We see here that eastern side (larger right ascension) is generally closer to Earth.

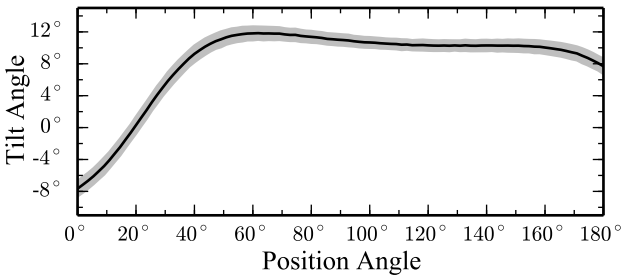

Figure 7.8: LMC tilt angle measured along 1 kpc wide strips centered at the LMC optical center. The gray shaded band is the standard deviation found by parametrically resampling the RR Lyrae distance data 1000 times. Maximum tilt angle of $11.84° \pm 0.80°$ is measured at a position angle of 62°. This strip is superimposed on the LMC RR Lyrae map shown in Fig. 7.4.

stars within a strip were projected onto the strip center line to provide a consistent metric for distance along the strip, akin to radial distance from the LMC center. Then, 1000 least squares linear regressions were performed with parametric resampling to measure the slope of the mean LMC depth along each strip. This procedure was conducted at 100 position angles to produce the results shown in Fig. 7.8. The maximum LMC tilt angle of $11.84° \pm 0.80°$ is measured at a position angle of 62°. It is also important to note that a wide plateau of tilt angle $> 8°$ is observed between position angles of 40° and 180°, quite consistent with an overall LMC position angle $\approx 110°$.

The tilt angle found through this method is in significant disagreement with the much larger inclination angle values found by recent studies, 24.20° (no error given) and $32° \pm 4°$ by Deb & Singh 2014 and Haschke et al. 2012, respectively. The full dataset of RR Lyrae distances found through the present work is available in the publication's associated online data, and we encourage interested researchers to apply their favored spatial modeling technique to our data to corroborate or disprove the results of this analysis.

7.5 Discussion and Conclusions

We have combined the OGLE III V- and I-band LMC RR Lyrae light curve data with new z-band observations from DECam to measure the distance to 15,040 LMC RR Lyrae stars and simultaneously fit the V, I, and z period–magnitude relations. Our primary findings are much tighter constraints on the period–magnitude relation zero points and slopes, as well as a new, precise distance measurement to the center of the core LMC RR Lyrae population of 50.2482 ± 0.0546 (statistical) ± 0.4628 (systematic) kpc [$\mu_{\rm LMC} = 18.5056 \pm 0.0024$ (statistical) ± 0.02 (systematic)]. This finding is statistically consistent with and four times more precise than the canonical value determined by de Grijs et al. (2014) through a meta-analysis of 233 separate LMC distance determinations published between 1990 and 2013.

We additionally provide three-dimensional contour plots of the RR Lyrae number density distribution in Figs. 7.5, 7.6, and 7.7 which aide in visualising the location of the center of the RR Lyrae population with respect to the LMC optical center and the tilt of the LMC in the plane of the sky (particularly apparent in Fig. 7.7). We conducted an analysis to measure the tilt angle of the LMC in the plane of the sky and found the maximum tilt to be $11.84° \pm 0.80°$ at a position angle of $62°$.

The full dataset of 15,040 RR Lyrae stars with mean-flux magnitude measurements in V, I, and z, along with derived color excess $E(V-I)$ values and fitted distances are provided in this publication's associated online data. We encourage other researchers to conduct independent analyses of LMC RR Lyrae morphology and overall distance using our dataset.

We caution against future studies that use a singular, highly precise LMC distance measurement as the basis for calibrating distance indicators. While the center point of the LMC can be well-defined by distances to a few thousand stars, the uncertainty to any one star is still about 3-4 per cent. Thus the distance to individual calibrators (i.e., Cepheids) in the LMC system cannot be determined as precisely as our reported distance to the core LMC RR Lyrae center. At worst, the distance to any single member of the LMC can be inferred with error equal to the spread in the LMC depth, which we find to be 2.22 kpc.

The best way to improve RR Lyrae-based LMC distance measurements is to incorporate longer-wavelength photometry, either ground-based near-infrared or space-based mid-infrared (the latter being even more beneficial). This will enable the use of the higher-precision period–magnitude relations applicable for $\lambda > 1$ μm derived in KB14. Additionally, these data would require lower extinction correction values, further reducing the error on the RR Lyrae absolute magnitudes. Finally, longer-wavelength and multi-waveband data, in combination with continued development of the MCMC sampling algorithms and augmented computational resources, can allow for simultaneous fitting of absolute magnitude and color excess for the tens of thousands of LMC RR Lyrae stars.

Acknowledgments

Authors Klein and Bloom acknowledge the generous support of National Science Foundation grants #0941742, #1009991, and #1251274. A.A.M. acknowledges support for this work by NASA from a Hubble Fellowship grant HST-HF-51325.01, awarded by STScI, operated by AURA, Inc., for NASA, under contract NAS 5-26555. Part of the research was carried out at JPL, operated by Caltech under a contract with NASA. The authors thank Rollin Thomas and Peter Nugent for developing and adapting the DECam data processing systems used in the course of this work. This project used data obtained with the Dark Energy Camera, which was constructed by the Dark Energy Survey collaborating institutions. The National Energy Research Scientific Computing Center, supported by the Office of Science of the U.S. Department of Energy, provided staff, computational resources, and data storage for this project. This research has made use of the SIMBAD database, operated at CDS, Strasbourg, France. This research has made use of NASA's Astrophysics Data System.

Chapter 8

Conclusions

8.1 Summary of Primary Results

In this dissertation I have presented multiple projects and investigations aimed at improving RR Lyrae distance indicators. The primary results of this research are the derivation of 13 band-specific RR Lyrae period–magnitude relations applicable between 0.3 and 12 μm, precise distance and line of sight color excess measurements for a local calibration sample of 134 RR Lyrae stars, and a new distance to and three-dimensional morphological description of the Large Magellanic Cloud (LMC) RR Lyrae population. These findings make use of a novel Bayesian simultaneous linear regression methodology, the development of which should also be considered as a significant product of the research.

These findings demonstrate the benefits of using infrared data in calibrations of RR Lyrae period–magnitude relations. The near-infrared and (especially) mid-infrared photometry enabled my Bayesian model to take advantage of the tighter intrinsic scatter and overall steeper slope of the RR Lyrae period–magnitude relations in these wavebands. Since the model simultaneously fits for the other wavebands, these longer-wavelength data contributed substantially to the improved precision of the derived optical RR Lyrae period–magnitude relations. Additionally, the wide waveband coverage of the calibration sample dataset, from near-ultraviolet to mid-infrared, facilitated the fit of posterior color excess distributions. This is largely helped by the drastic decrement in interstellar extinction as one moves from the optical to mid-infrared.

8.2 Future Directions

This dissertation work should be considered as a step towards expanded use of RR Lyrae stars as distance indicators, with a particular emphasis on applications using infrared data and simultaneously combining observations from multiple wavebands. I have demonstrated this approach's considerable merit by producing very tightly-constrained period–magnitude relations and, in measuring a new distance to the LMC, I have provided an example applica-

tion of using the Bayesian methodology to combine observations from multiple wavebands. In the past two to three years this subfield has been actively acquiring new mid-infrared data with the *Spitzer Space Telescope* (Carnegie RR Lyrae Program and *Spitzer* Merger History and Shape of the Galactic Halo program), as well as independent and supplemental projects utilizing ground-based near-infrared observing facilities. We are well on our way to developing a precise, RR Lyrae-based alternative to the traditional Cepheid-based Cosmic Distance Ladder.

In the near future the field of RR Lyrae stars will explode with new voluminous and complementary datasets and improved instrumental capabilities. Firstly, *Gaia* will provide very precise (1 per cent error) distances to all RR Lyrae stars within 3 kpc and distances with 10 per cent fractional error for all other detectable Milky Way RR Lyrae stars (Cacciari 2009a). This will serve as the foundation for a new RR Lyrae period–luminosity calibration sample and will result in ultra-precise period–magnitude relation parameters. The subsequent studies will be able to more closely probe the intrinsic scatter of RR Lyrae stars about their period–luminosity relation, potentially exposing new avenues for additional subclassification and morsels of data that may inform our theoretical understanding of RR Lyrae stellar interiors and the pulsation mechanism.

The Large Synoptic Survey Telescope (LSST) will identify hundreds of thousands of new RR Lyrae stars that have been previously missed due to the attenuating effects of interstellar extinction in the Milky Way Plane or because of the technical difficulty of large scale time-domain surveys (LSST Science Collaboration et al. 2009). LSST's long-term, frequent monitoring will finally provide the data needed for large-scale, statistically significant studies of Blazhko-affected RR Lyrae stars. Additionally, LSST will serve as the discovery engine that can point the way for targeted followup in infrared wavebands. With an optical light curve in hand from LSST, complementary near- and mid-infrared observations can be designed to acquire mean-flux magnitude measurements using a fraction of the combined exposure time traditionally needed to fully sample light curve phase.

Finally, the *Wide-Field Infrared Survey Telescope* (*WFIRST*, Spergel et al. 2013c,b) will combine the calibration sample from *Gaia* with the more distant Milky Way and Magellanic Cloud RR Lyrae stars identified by LSST to measure highly-precise distances and line of sight color excess values for hundreds of thousands of RR Lyrae variable stars. The resulting three-dimensional Milky Way, LMC, and SMC maps will represent a leap forward for Galactic structure mapping and produce a substantial distance measurement error decrement that will radiate up the Cosmic Distance Ladder. In the near future, this confluence of large scale projects promises to more thoroughly and precisely describe our physical location within the Galaxy and in the Universe, and it is my hope that through this greater understanding of humanity's context and our relative insignificance to the Universe, that we can all gain a deeper appreciation for our significance to each other and of the privilege of possessing the intelligence and technology requisite for the reflection.

Appendix A

Multi-band Light Curve and Period–Magnitude Relation Fitting Summary Table

The following table provides complete observable prior and fitted posterior data for the RR Lyrae calibration sample used in the study presented in Chapter 6.

Table A.1: Catalog of calibration RR Lyrae stars (transposed into columns to fit on the page). Observed values, measured priors, and inferred posterior variables are shown.

Measurements and Priors							
Name	AACMi	ABUMa	AEBoo	AFVel	AFVir	AMTuc	AMVir
Type	RRab	RRab	RRc	RRab	RRab	RRc	RRab
Blazhko Affected?	False	False	False	True	False	False	True
Period (d)	0.4763	0.5996	0.3149	0.5274	0.4837	0.4058	0.6151
[Fe/H]	-0.15	-0.49	-1.39	-1.49	-1.33	-1.49	-1.37
$\mu_{\rm prior}$	10.4730 ± 0.1384	10.0551 ± 0.1326	9.9779 ± 0.1252	10.2164 ± 0.1282	11.1113 ± 0.1258	11.0296 ± 0.1250	10.7082 ± 0.1254
$E(B-V)_{\rm SF}$	0.0997 ± 0.0029	0.0226 ± 0.0012	0.0230 ± 0.0012	0.2783 ± 0.0068	0.0208 ± 0.0010	0.0205 ± 0.0005	0.0628 ± 0.0015
m_U	···	11.6575 ± 0.0026	···	···	···	···	···
m_B	···	11.3352 ± 0.0017	···	···	···	···	···
m_{hipp}	11.6734 ± 0.0059	11.0349 ± 0.0038	10.7220 ± 0.0034	11.5419 ± 0.0059	11.8920 ± 0.0104	11.7425 ± 0.0047	11.6182 ± 0.0053
m_V	···	10.8694 ± 0.0016	···	···	···	···	···
m_R	···	10.5775 ± 0.0018	···	···	···	···	···
m_I	···	10.3370 ± 0.0075	···	···	···	···	···
m_z	···	10.7343 ± 0.0066	···	···	···	···	···
m_J	···	10.0556 ± 0.0065	···	···	···	···	···
m_H	···	9.7284 ± 0.0059	···	···	···	···	···
m_K	···	9.7181 ± 0.0072	···	···	···	···	···
m_{W1}	10.2375 ± 0.0057	9.5697 ± 0.0047	9.7129 ± 0.0042	9.9828 ± 0.0067	10.6980 ± 0.0062	10.5692 ± 0.0041	10.0964 ± 0.0046
m_{W2}	10.2493 ± 0.0053	9.5920 ± 0.0043	9.7212 ± 0.0041	9.9809 ± 0.0114	10.7121 ± 0.0085	10.5782 ± 0.0040	10.0968 ± 0.0048
m_{W3}	10.2216 ± 0.0539	9.5304 ± 0.0259	9.6652 ± 0.0235	9.9081 ± 0.0361	···	···	···
Posterior Inferences							
$\mu_{\rm post}$	10.5864 ± 0.0135	10.1514 ± 0.0146	9.9580 ± 0.0167	10.4202 ± 0.0132	11.0736 ± 0.0136	11.0600 ± 0.0123	10.6906 ± 0.0151
$E(B-V)_{\rm post}$	0.1469 ± 0.0157	0.0955 ± 0.0088	0.0456 ± 0.0157	0.1656 ± 0.0159	0.0682 ± 0.0158	0.0359 ± 0.0148	0.1155 ± 0.0158
M_U	···	1.0458 ± 0.0433	···	···	···	···	···
M_B	···	0.7872 ± 0.0377	···	···	···	···	···
M_{hipp}	0.5973 ± 0.0517	0.5649 ± 0.0314	0.6120 ± 0.0522	0.5697 ± 0.0517	0.5908 ± 0.0522	0.5627 ± 0.0488	0.5426 ± 0.0531
M_V	···	0.4189 ± 0.0297	···	···	···	···	···
M_R	···	0.1768 ± 0.0258	···	···	···	···	···
M_I	···	0.0077 ± 0.0220	···	···	···	···	···
M_z	···	0.4383 ± 0.0197	···	···	···	···	···
M_J	···	-0.1827 ± 0.0171	···	···	···	···	···
M_H	···	-0.4775 ± 0.0160	···	···	···	···	···
M_K	···	-0.4672 ± 0.0163	···	···	···	···	···
M_{W1}	-0.3746 ± 0.0144	-0.5984 ± 0.0153	-0.2530 ± 0.0170	-0.4663 ± 0.0145	-0.3875 ± 0.0146	-0.4970 ± 0.0127	-0.6144 ± 0.0157
M_{W2}	-0.3529 ± 0.0143	-0.5697 ± 0.0151	-0.2418 ± 0.0170	-0.4570 ± 0.0172	-0.3688 ± 0.0158	-0.4856 ± 0.0127	-0.6063 ± 0.0157
M_{W3}	-0.3681 ± 0.0555	-0.6232 ± 0.0297	-0.2938 ± 0.0288	-0.5158 ± 0.0385	···	···	···

Continued on Next Page...

Table A.1 – Continued

Measurements and Priors							
Name	ANSer	APSer	ARHer	ATAnd	ATVir	AUVir	AVPeg
Type	RRab	RRc	RRab	RRab	RRab	RRc	RRab
Blazhko Affected?	False	False	True	False	False	False	False
Period (d)	0.5221	0.3408	0.4700	0.6169	0.5258	0.3432	0.3904
[Fe/H]	−0.07	−1.58	−1.30	−1.18	−1.60	−1.50	−0.08
$\mu_{\rm prior}$	9.9119 ± 0.1392	10.4358 ± 0.1249	10.5896 ± 0.1267	9.7576 ± 0.1264	10.6467 ± 0.1204	10.9470 ± 0.1251	9.4122 ± 0.1390
$E(B-V)_{\rm SF}$	0.0364 ± 0.0006	0.0362 ± 0.0008	0.0106 ± 0.0004	0.1037 ± 0.0034	0.0270 ± 0.0010	0.0251 ± 0.0004	0.0615 ± 0.0007
m_U	···	···	11.6492 ± 0.0208	···	···	···	11.2715 ± 0.0212
m_B	···	···	11.4039 ± 0.0369	···	···	···	10.7393 ± 0.0085
m_{hipp}	11.0333 ± 0.0066	11.1798 ± 0.0042	11.3436 ± 0.0176	10.8035 ± 0.0032	11.3858 ± 0.0093	11.6728 ± 0.0063	10.5961 ± 0.0058
m_V	···	···	11.1605 ± 0.0120	···	···	···	10.3325 ± 0.0136
m_R	···	···	11.0098 ± 0.0058	···	···	···	10.1416 ± 0.0143
m_I	···	···	···	···	···	···	···
m_z	···	···	···	···	···	···	···
m_J	···	···	10.5740 ± 0.0043	···	···	···	9.7057 ± 0.0089
m_H	···	···	10.4404 ± 0.0043	···	···	···	···
m_K	···	···	10.4081 ± 0.0049	···	···	···	9.5753 ± 0.0118
m_{W1}	9.7778 ± 0.0046	10.1622 ± 0.0047	···	9.0272 ± 0.0055	10.2172 ± 0.0059	10.7590 ± 0.0044	9.3025 ± 0.0046
m_{W2}	9.7940 ± 0.0047	10.1704 ± 0.0045	10.2697 ± 0.0038	9.0215 ± 0.0051	10.2036 ± 0.0049	10.7727 ± 0.0052	9.3259 ± 0.0045
m_{W3}	9.8092 ± 0.0394	···	···	···	10.2392 ± 0.0608	···	9.2549 ± 0.0203
Posterior Inferences							
$\mu_{\rm post}$	10.2282 ± 0.0124	10.4858 ± 0.0141	10.6129 ± 0.0141	9.6101 ± 0.0154	10.6641 ± 0.0128	11.0940 ± 0.0138	9.4673 ± 0.0199
$E(B-V)_{\rm post}$	0.0675 ± 0.0157	0.0297 ± 0.0144	0.0330 ± 0.0079	0.1956 ± 0.0163	0.0473 ± 0.0159	0.0100 ± 0.0085	0.1305 ± 0.0103
M_U	···	···	0.8773 ± 0.0442	···	···	···	1.1753 ± 0.0565
M_B	···	···	0.6540 ± 0.0503	···	···	···	0.7302 ± 0.0469
M_{hipp}	0.5800 ± 0.0516	0.5949 ± 0.0479	0.6206 ± 0.0333	0.5413 ± 0.0540	0.5641 ± 0.0523	0.5454 ± 0.0311	0.6936 ± 0.0392
M_V	···	···	0.4443 ± 0.0295	···	···	···	0.4566 ± 0.0394
M_R	···	···	0.3107 ± 0.0242	···	···	···	0.3337 ± 0.0356
M_I	···	···	···	···	···	···	···
M_z	···	···	···	···	···	···	···
M_J	···	···	-0.0689 ± 0.0156	···	···	···	0.1197 ± 0.0234
M_H	···	···	-0.1913 ± 0.0149	···	···	···	···
M_K	···	···	-0.2165 ± 0.0149	···	···	···	0.0617 ± 0.0233
M_{W1}	-0.4622 ± 0.0130	-0.3288 ± 0.0147	···	-0.6171 ± 0.0162	-0.4551 ± 0.0138	-0.3368 ± 0.0145	-0.1876 ± 0.0204
M_{W2}	-0.4415 ± 0.0130	-0.3186 ± 0.0146	-0.3467 ± 0.0145	-0.6096 ± 0.0161	-0.4656 ± 0.0134	-0.3224 ± 0.0147	-0.1554 ± 0.0204
M_{W3}	-0.4205 ± 0.0412	···	···	···	-0.4259 ± 0.0622	···	-0.2155 ± 0.0285

Continued on Next Page...

Table A.1 – Continued

Measurements and Priors							
Name	AVVir	AXLeo	BBEri	BCDra	BHPeg	BKDra	BNPav
Type	RRab	RRab	RRab	RRab	RRab	RRab	RRab
Blazhko Affected?	False	False	False	False	True	False	False
Period (d)	0.6569	0.7268	0.5699	0.7196	0.6410	0.5921	0.5672
[Fe/H]	−1.25	−1.72	−1.32	−2.00	−1.22	−1.95	−1.32
$\mu_{\rm prior}$	11.0864 ± 0.1259	11.6287 ± 0.1253	10.7566 ± 0.1256	10.9380 ± 0.1263	9.5845 ± 0.1258	10.5386 ± 0.1261	11.6869 ± 0.1268
$E(B-V)_{\rm SF}$	0.0273 ± 0.0007	0.0314 ± 0.0007	0.0427 ± 0.0015	0.0584 ± 0.0030	0.0714 ± 0.0008	0.0376 ± 0.0013	0.0722 ± 0.0019
m_U	12.5931 ± 0.0445	12.6331 ± 0.0426	···	···	···	11.6247 ± 0.0592	···
m_B	12.1289 ± 0.0049	12.5612 ± 0.0067	···	···	···	11.2840 ± 0.0309	···
m_{hipp}	11.9070 ± 0.0075	12.3547 ± 0.0086	11.6116 ± 0.0058	11.6880 ± 0.0049	10.5529 ± 0.0029	11.2293 ± 0.0094	12.6395 ± 0.0179
m_V	11.7724 ± 0.0062	12.1832 ± 0.0047	···	···	···	10.9613 ± 0.0260	···
m_R	11.4829 ± 0.0037	11.9429 ± 0.0035	···	···	···	10.8216 ± 0.0184	···
m_I	···	11.7078 ± 0.0046	···	···	···	···	···
m_z	···	12.0931 ± 0.0063	···	···	···	···	···
m_J	10.8540 ± 0.0046	···	···	···	···	10.3610 ± 0.0040	···
m_H	10.6143 ± 0.0059	11.0378 ± 0.0099	···	···	···	10.1354 ± 0.0044	···
m_K	10.5599 ± 0.0069	10.9501 ± 0.0117	···	···	···	10.1089 ± 0.0052	···
m_{W1}	10.5080 ± 0.0044	10.8789 ± 0.0057	10.1940 ± 0.0037	10.0772 ± 0.0028	8.9745 ± 0.0053	10.0026 ± 0.0030	11.2329 ± 0.0056
m_{W2}	10.5097 ± 0.0046	10.8946 ± 0.0079	10.2047 ± 0.0034	10.0882 ± 0.0026	8.9943 ± 0.0049	9.9974 ± 0.0032	11.2298 ± 0.0056
m_{W3}	···	···	10.1395 ± 0.0344	10.0102 ± 0.0313	8.9051 ± 0.0183	9.9908 ± 0.0218	···
Posterior Inferences							
$\mu_{\rm post}$	11.1728 ± 0.0174	11.6483 ± 0.0220	10.7216 ± 0.0131	10.8278 ± 0.0213	9.6155 ± 0.0169	10.5744 ± 0.0139	11.7497 ± 0.0133
$E(B-V)_{\rm post}$	0.0562 ± 0.0097	0.0513 ± 0.0112	0.0970 ± 0.0144	0.1024 ± 0.0173	0.1189 ± 0.0165	0.0108 ± 0.0073	0.1006 ± 0.0170
M_U	1.1495 ± 0.0658	0.7378 ± 0.0712	···	···	···	0.9980 ± 0.0697	···
M_B	0.7228 ± 0.0428	0.7001 ± 0.0508	···	···	···	0.6646 ± 0.0448	···
M_{hipp}	0.5468 ± 0.0362	0.5355 ± 0.0432	0.5664 ± 0.0477	0.5188 ± 0.0598	0.5411 ± 0.0557	0.6188 ± 0.0286	0.5544 ± 0.0584
M_V	0.4236 ± 0.0343	0.3744 ± 0.0406	···	···	···	0.3529 ± 0.0365	···
M_R	0.1634 ± 0.0298	0.1608 ± 0.0358	···	···	···	0.2189 ± 0.0291	···
M_I	···	-0.0359 ± 0.0298	···	···	···	···	···
M_z	···	0.3672 ± 0.0277	···	···	···	···	···
M_J	-0.3699 ± 0.0194	···	···	···	···	-0.2233 ± 0.0153	···
M_H	-0.5906 ± 0.0188	-0.6398 ± 0.0247	···	···	···	-0.4452 ± 0.0148	···
M_K	-0.6328 ± 0.0188	-0.7164 ± 0.0251	···	···	···	-0.4693 ± 0.0148	···
M_{W1}	-0.6746 ± 0.0179	-0.7784 ± 0.0227	-0.5445 ± 0.0134	-0.7685 ± 0.0214	-0.6617 ± 0.0176	-0.5737 ± 0.0141	-0.5344 ± 0.0142
M_{W2}	-0.6692 ± 0.0180	-0.7592 ± 0.0234	-0.5274 ± 0.0133	-0.7506 ± 0.0214	-0.6339 ± 0.0174	-0.5782 ± 0.0142	-0.5307 ± 0.0142
M_{W3}	···	···	-0.5844 ± 0.0367	-0.8199 ± 0.0378	-0.7131 ± 0.0248	-0.5839 ± 0.0259	···

Continued on Next Page...

Table A.1 – Continued

Measurements and Priors							
Name	BPPav	BRAqr	BTDra	BVAqr	BXLeo	CGLib	CGPeg
Type	RRab	RRab	RRab	RRab	RRc	RRc	RRab
Blazhko Affected?	False	False	False	True	False	False	False
Period (d)	0.5271	0.4819	0.5887	0.3644	0.3628	0.3068	0.4671
[Fe/H]	−1.48	−0.74	−1.75	−1.42	−1.28	−1.19	−0.50
$\mu_{\rm prior}$	11.7622 ± 0.1282	10.5687 ± 0.1297	11.1006 ± 0.1252	10.2180 ± 0.1254	10.8883 ± 0.1258	10.2718 ± 0.1320	10.1743 ± 0.1325
$E(B-V)_{\rm SF}$	0.0561 ± 0.0023	0.0238 ± 0.0003	0.0086 ± 0.0006	0.0286 ± 0.0006	0.0235 ± 0.0015	0.1934 ± 0.0128	0.0647 ± 0.0009
m_U	···	···	12.0710 ± 0.0111	···	···	···	···
m_B	···	···	11.9436 ± 0.0156	···	11.9440 ± 0.0170	···	···
m_{hipp}	12.6249 ± 0.0278	11.4950 ± 0.0072	11.7445 ± 0.0069	11.0037 ± 0.0083	11.6594 ± 0.0067	11.6143 ± 0.0058	11.2793 ± 0.0049
m_V	···	···	11.5652 ± 0.0109	···	11.5547 ± 0.0048	···	···
m_R	···	···	11.3541 ± 0.0080	···	11.3781 ± 0.0051	···	···
m_I	···	···	···	···	11.2008 ± 0.0055	···	···
m_z	···	···	···	···	11.6218 ± 0.0043	···	···
m_J	···	···	10.7770 ± 0.0063	···	10.9511 ± 0.0053	···	···
m_H	···	···	10.5630 ± 0.0062	···	10.7800 ± 0.0059	···	···
m_K	···	···	10.5806 ± 0.0061	···	10.7644 ± 0.0071	···	···
m_{W1}	···	10.2939 ± 0.0058	10.4103 ± 0.0034	9.9959 ± 0.0054	10.6633 ± 0.0057	10.1293 ± 0.0052	9.8530 ± 0.0047
m_{W2}	11.3106 ± 0.0047	10.3130 ± 0.0071	10.4202 ± 0.0037	9.9948 ± 0.0051	10.6793 ± 0.0057	10.1279 ± 0.0049	9.8623 ± 0.0049
m_{W3}	···	···	10.3753 ± 0.0413	···	···	···	···
Posterior Inferences							
$\mu_{\rm post}$	11.7567 ± 0.0137	10.6673 ± 0.0135	10.9747 ± 0.0135	10.0916 ± 0.0229	11.0502 ± 0.0130	10.3228 ± 0.0177	10.1825 ± 0.0136
$E(B-V)_{\rm post}$	0.0886 ± 0.0176	0.0708 ± 0.0155	0.0590 ± 0.0080	0.0812 ± 0.0170	0.0185 ± 0.0077	0.2012 ± 0.0164	0.1438 ± 0.0120
M_U	···	···	0.8123 ± 0.0415	···	···	···	···
M_B	···	···	0.7242 ± 0.0383	···	0.8173 ± 0.0366	···	···
M_{hipp}	0.5727 ± 0.0639	0.5915 ± 0.0510	0.5733 ± 0.0299	0.6415 ± 0.0600	0.5477 ± 0.0277	0.6208 ± 0.0556	0.6173 ± 0.0407
M_V	···	···	0.4060 ± 0.0298	···	0.4467 ± 0.0259	···	···
M_R	···	···	0.2255 ± 0.0254	···	0.2798 ± 0.0226	···	···
M_I	···	···	···	···	0.1162 ± 0.0185	···	···
M_z	···	···	···	···	0.5437 ± 0.0165	···	···
M_J	···	···	-0.2513 ± 0.0162	···	-0.1159 ± 0.0147	···	···
M_H	···	···	-0.4453 ± 0.0153	···	-0.2807 ± 0.0143	···	···
M_K	···	···	-0.4150 ± 0.0149	···	-0.2923 ± 0.0147	···	···
M_{W1}	···	-0.3857 ± 0.0144	-0.5747 ± 0.0139	-0.1099 ± 0.0234	-0.3901 ± 0.0140	-0.2286 ± 0.0184	-0.3546 ± 0.0143
M_{W2}	-0.4557 ± 0.0142	-0.3619 ± 0.0150	-0.5608 ± 0.0140	-0.1055 ± 0.0234	-0.3728 ± 0.0141	-0.2164 ± 0.0183	-0.3356 ± 0.0143
M_{W3}	···	···	-0.6007 ± 0.0435	···	···	···	···

Continued on Next Page...

Table A.1 – Continued

Measurements and Priors							
Name	CIAnd	CSEri	DDHya	DHPeg	DNAqr	DXDel	FWLup
Type	RRab	RRc	RRab	RRc	RRab	RRab	RRab
Blazhko Affected?	False	False	False	False	False	False	False
Period (d)	0.4847	0.3113	0.5018	0.2555	0.6338	0.4726	0.4842
[Fe/H]	−0.69	−1.41	−0.97	−1.24	−1.66	−0.39	−0.20
$\mu_{\rm prior}$	11.3465 ± 0.1305	8.3455 ± 0.1251	11.3880 ± 0.1291	8.6623 ± 0.1258	10.5845 ± 0.1250	8.8231 ± 0.1341	7.9191 ± 0.1390
$E(B-V)_{\rm SF}$	0.0585 ± 0.0019	0.0182 ± 0.0004	0.0210 ± 0.0004	0.0822 ± 0.0016	0.0219 ± 0.0007	0.1145 ± 0.0018	0.1552 ± 0.0047
m_U	···	···	···	···	···	···	···
m_B	···	···	···	···	···	···	···
m_{hipp}	12.3960 ± 0.0089	9.0667 ± 0.0019	12.2517 ± 0.0212	9.6165 ± 0.0025	11.2930 ± 0.0053	10.0346 ± 0.0028	9.1470 ± 0.0020
m_V	···	···	···	···	···	···	···
m_R	···	···	···	···	···	···	···
m_I	···	···	···	···	···	···	···
m_z	···	···	···	···	···	···	···
m_J	···	···	···	···	···	···	···
m_H	···	···	···	···	···	···	···
m_K	···	···	···	···	···	···	···
m_{W1}	10.9765 ± 0.0043	8.0984 ± 0.0045	11.1008 ± 0.0060	8.5625 ± 0.0052	9.9119 ± 0.0052	8.6332 ± 0.0045	7.6428 ± 0.0052
m_{W2}	10.9789 ± 0.0046	8.1113 ± 0.0040	11.1053 ± 0.0070	8.5768 ± 0.0055	9.9178 ± 0.0080	8.6582 ± 0.0052	7.6578 ± 0.0042
m_{W3}	···	8.0960 ± 0.0091	···	···	9.8626 ± 0.0387	8.6200 ± 0.0125	7.6535 ± 0.0084
Posterior Inferences							
$\mu_{\rm post}$	11.3406 ± 0.0126	8.3370 ± 0.0171	11.5111 ± 0.0128	8.6008 ± 0.0258	10.5447 ± 0.0166	8.9812 ± 0.0138	8.0088 ± 0.0131
$E(B-V)_{\rm post}$	0.1315 ± 0.0108	0.0336 ± 0.0149	0.0480 ± 0.0166	0.1061 ± 0.0180	0.0629 ± 0.0168	0.1340 ± 0.0157	0.1603 ± 0.0157
M_U	···	···	···	···	···	···	···
M_B	···	···	···	···	···	···	···
M_{hipp}	0.6168 ± 0.0378	0.6176 ± 0.0506	0.5805 ± 0.0582	0.6617 ± 0.0638	0.5387 ± 0.0558	0.6067 ± 0.0516	0.6036 ± 0.0514
M_V	···	···	···	···	···	···	···
M_R	···	···	···	···	···	···	···
M_I	···	···	···	···	···	···	···
M_z	···	···	···	···	···	···	···
M_J	···	···	···	···	···	···	···
M_H	···	···	···	···	···	···	···
M_K	···	···	···	···	···	···	···
M_{W1}	-0.3871 ± 0.0132	-0.2445 ± 0.0175	-0.4186 ± 0.0139	-0.0568 ± 0.0263	-0.6438 ± 0.0171	-0.3714 ± 0.0142	-0.3940 ± 0.0139
M_{W2}	-0.3758 ± 0.0133	-0.2294 ± 0.0174	-0.4109 ± 0.0144	-0.0355 ± 0.0263	-0.6337 ± 0.0182	-0.3374 ± 0.0145	-0.3682 ± 0.0136
M_{W3}	···	-0.2418 ± 0.0193	···	···	-0.6835 ± 0.0421	-0.3643 ± 0.0185	-0.3590 ± 0.0155

Continued on Next Page...

Table A.1 – Continued

Measurements and Priors							
Name	HHPup	HKPup	IKHya	IOLyr	MSAra	MTTel	RRCet
Type	RRab	RRab	RRab	RRab	RRab	RRc	RRab
Blazhko Affected?	False	False	True	False	False	False	False
Period (d)	0.3907	0.7343	0.6503	0.5771	0.5250	0.3169	0.5530
[Fe/H]	−0.50	−1.11	−1.24	−1.14	−1.48	−1.85	−1.45
$\mu_{\rm prior}$	10.0797 ± 0.1357	10.1600 ± 0.1377	9.2449 ± 0.1260	11.0029 ± 0.1269	11.1554 ± 0.1254	8.3624 ± 0.1257	9.0495 ± 0.1251
$E(B-V)_{\rm SF}$	0.1522 ± 0.0054	0.2979 ± 0.0109	0.0580 ± 0.0009	0.0580 ± 0.0039	0.1067 ± 0.0017	0.0526 ± 0.0026	0.0203 ± 0.0003
m_U	···	···	···	···	···	···	···
m_B	···	···	···	···	···	···	···
m_{hipp}	11.4170 ± 0.0248	11.4502 ± 0.0045	10.1603 ± 0.0079	11.9471 ± 0.0057	12.1712 ± 0.0090	9.0515 ± 0.0019	9.8001 ± 0.0047
m_V	···	···	···	···	···	···	···
m_R	···	···	···	···	···	···	···
m_I	···	···	···	···	···	···	···
m_z	···	···	···	···	···	···	···
m_J	···	···	···	···	···	···	···
m_H	···	···	···	···	···	···	···
m_K	···	···	···	···	···	···	···
m_{W1}	9.8786 ± 0.0032	9.8629 ± 0.0046	8.7387 ± 0.0051	10.4924 ± 0.0040	···	8.0528 ± 0.0060	8.5019 ± 0.0046
m_{W2}	9.8857 ± 0.0030	9.8591 ± 0.0043	8.7354 ± 0.0050	10.4921 ± 0.0039	10.6012 ± 0.0053	8.0770 ± 0.0045	8.4967 ± 0.0057
m_{W3}	9.7739 ± 0.0214	9.8207 ± 0.0437	8.7046 ± 0.0150	···	···	8.0650 ± 0.0102	8.4702 ± 0.0132
Posterior Inferences							
$\mu_{\rm post}$	10.0220 ± 0.0197	10.6280 ± 0.0222	9.3912 ± 0.0172	11.0260 ± 0.0133	11.0353 ± 0.0138	8.3145 ± 0.0167	8.9987 ± 0.0128
$E(B-V)_{\rm post}$	0.2289 ± 0.0182	0.0960 ± 0.0180	0.0729 ± 0.0171	0.1098 ± 0.0150	0.1685 ± 0.0158	0.0345 ± 0.0151	0.0732 ± 0.0157
M_U	···	···	···	···	···	···	···
M_B	···	···	···	···	···	···	···
M_{hipp}	0.6317 ± 0.0664	0.5021 ± 0.0622	0.5259 ± 0.0578	0.5549 ± 0.0498	0.5742 ± 0.0525	0.6221 ± 0.0510	0.5572 ± 0.0511
M_V	···	···	···	···	···	···	···
M_R	···	···	···	···	···	···	···
M_I	···	···	···	···	···	···	···
M_z	···	···	···	···	···	···	···
M_J	···	···	···	···	···	···	···
M_H	···	···	···	···	···	···	···
M_K	···	···	···	···	···	···	···
M_{W1}	-0.1834 ± 0.0198	-0.7819 ± 0.0226	-0.6652 ± 0.0178	-0.5528 ± 0.0137	···	-0.2677 ± 0.0176	-0.5097 ± 0.0133
M_{W2}	-0.1609 ± 0.0198	-0.7792 ± 0.0225	-0.6637 ± 0.0178	-0.5457 ± 0.0137	-0.4521 ± 0.0145	-0.2412 ± 0.0171	-0.5099 ± 0.0138
M_{W3}	-0.2534 ± 0.0290	-0.8095 ± 0.0490	-0.6883 ± 0.0228	···	···	-0.2503 ± 0.0195	-0.5302 ± 0.0183

Continued on Next Page...

Table A.1 – Continued

Measurements and Priors							
Name	RRGem	RRLeo	RRLyr	RSBoo	RUCet	RUPsc	RUScl
Type	RRab	RRab	RRab	RRab	RRab	RRc	RRab
Blazhko Affected?	True	False	True	True	True	True	False
Period (d)	0.3973	0.4524	0.5668	0.3773	0.5863	0.3903	0.4933
[Fe/H]	−0.29	−1.60	−1.39	−0.36	−1.66	−1.75	−1.27
$\mu_{\rm prior}$	10.3327 ± 0.1505	10.0176 ± 0.1207	7.1300 ± 0.0749	9.4632 ± 0.1345	11.0754 ± 0.1252	9.5342 ± 0.1251	9.4811 ± 0.1260
$E(B-V)_{\rm SF}$	0.0581 ± 0.0009	0.0346 ± 0.0035	0.0884 ± 0.0029	0.0122 ± 0.0009	0.0204 ± 0.0006	0.0405 ± 0.0002	0.0174 ± 0.0004
m_U	···	···	···	11.0377 ± 0.0161	···	10.8122 ± 0.0055	···
m_B	···	···	8.1640 ± 0.0102	10.6999 ± 0.0076	···	10.3626 ± 0.0048	···
m_{hipp}	11.4682 ± 0.0656	10.7816 ± 0.0067	7.7671 ± 0.0216	10.4385 ± 0.0067	11.7789 ± 0.0086	10.2505 ± 0.0040	10.2643 ± 0.0100
m_V	···	···	7.6874 ± 0.0095	10.3927 ± 0.0053	···	10.0942 ± 0.0058	···
m_R	···	···	7.5756 ± 0.0134	10.1735 ± 0.0084	···	9.9088 ± 0.0027	···
m_I	···	···	···	···	···	9.8370 ± 0.0148	···
m_z	···	···	···	···	···	10.2620 ± 0.0068	···
m_J	···	···	···	···	···	···	···
m_H	···	···	···	···	···	···	···
m_K	···	···	···	9.6157 ± 0.0073	···	···	···
m_{W1}	10.2269 ± 0.0067	9.6300 ± 0.0055	6.4979 ± 0.0072	9.4144 ± 0.0045	10.5314 ± 0.0062	9.0705 ± 0.0041	9.1405 ± 0.0051
m_{W2}	10.2236 ± 0.0056	9.6277 ± 0.0056	6.4361 ± 0.0089	9.4376 ± 0.0051	10.5438 ± 0.0077	9.0784 ± 0.0044	9.1488 ± 0.0085
m_{W3}	···	···	6.4588 ± 0.0051	9.3974 ± 0.0172	10.4786 ± 0.0739	9.0624 ± 0.0148	9.0974 ± 0.0203
Posterior Inferences							
$\mu_{\rm post}$	10.3982 ± 0.0194	9.9342 ± 0.0146	6.9962 ± 0.0143	9.5506 ± 0.0213	11.0953 ± 0.0143	9.5232 ± 0.0120	9.5362 ± 0.0130
$E(B-V)_{\rm post}$	0.1212 ± 0.0175	0.0745 ± 0.0158	0.1010 ± 0.0096	0.0992 ± 0.0104	0.0390 ± 0.0157	0.0447 ± 0.0074	0.0440 ± 0.0153
M_U	···	···	···	1.0091 ± 0.0563	···	1.0738 ± 0.0367	···
M_B	···	···	0.7487 ± 0.0409	0.7375 ± 0.0482	···	0.6539 ± 0.0320	···
M_{hipp}	0.6658 ± 0.0881	0.5989 ± 0.0525	0.4342 ± 0.0389	0.5570 ± 0.0408	0.5534 ± 0.0524	0.5783 ± 0.0264	0.5814 ± 0.0506
M_V	···	···	0.3751 ± 0.0321	0.5314 ± 0.0388	···	0.4312 ± 0.0254	···
M_R	···	···	0.3159 ± 0.0295	0.3640 ± 0.0351	···	0.2690 ± 0.0216	···
M_I	···	···	···	···	···	0.2306 ± 0.0226	···
M_z	···	···	···	···	···	0.6712 ± 0.0168	···
M_J	···	···	···	···	···	···	···
M_H	···	···	···	···	···	···	···
M_K	···	···	···	0.0299 ± 0.0227	···	···	···
M_{W1}	-0.1925 ± 0.0204	-0.3172 ± 0.0154	-0.5159 ± 0.0157	-0.1535 ± 0.0218	-0.5707 ± 0.0153	-0.4606 ± 0.0126	-0.4033 ± 0.0136
M_{W2}	-0.1876 ± 0.0201	-0.3144 ± 0.0155	-0.5709 ± 0.0167	-0.1236 ± 0.0219	-0.5557 ± 0.0161	-0.4496 ± 0.0127	-0.3920 ± 0.0153
M_{W3}	···	···	-0.5397 ± 0.0151	-0.1554 ± 0.0274	-0.6178 ± 0.0753	-0.4619 ± 0.0190	-0.4398 ± 0.0241

Continued on Next Page...

Table A.1 – Continued

Measurements and Priors							
Name	RVCap	RVCet	RVCrB	RVOct	RVUMa	RWCnc	RWDra
Type	RRab	RRab	RRc	RRab	RRab	RRab	RRab
Blazhko Affected?	True	True	False	False	True	True	True
Period (d)	0.4477	0.6234	0.3316	0.5711	0.4681	0.5472	0.4429
[Fe/H]	−1.61	−1.60	−1.69	−1.71	−1.20	−1.67	−1.55
$\mu_{\rm prior}$	10.3711 ± 0.1253	10.2752 ± 0.1201	10.7633 ± 0.1251	9.9290 ± 0.1288	10.0507 ± 0.1261	11.2381 ± 0.1293	11.0533 ± 0.1270
$E(B-V)_{\rm SF}$	0.0451 ± 0.0023	0.0270 ± 0.0006	0.0371 ± 0.0014	0.1540 ± 0.0104	0.0160 ± 0.0010	0.0186 ± 0.0008	0.0111 ± 0.0005
m_U	···	···	···	···	10.7862 ± 0.0431	···	12.1720 ± 0.0102
m_B	···	···	···	···	11.0654 ± 0.0237	···	11.7263 ± 0.0075
m_{hipp}	11.1668 ± 0.0053	11.0143 ± 0.0039	11.4850 ± 0.0038	11.0300 ± 0.0077	10.8455 ± 0.0058	11.9334 ± 0.0332	11.7514 ± 0.0231
m_V	···	···	···	···	10.6617 ± 0.0099	···	11.5082 ± 0.0239
m_R	···	···	···	···	10.5260 ± 0.0094	···	11.3365 ± 0.0109
m_I	···	···	···	···	···	···	···
m_z	···	···	···	···	···	···	···
m_J	···	···	···	···	10.0945 ± 0.0057	···	10.9582 ± 0.0045
m_H	···	···	···	···	9.8792 ± 0.0063	···	10.7856 ± 0.0053
m_K	···	···	···	···	9.8387 ± 0.0080	···	10.7831 ± 0.0062
m_{W1}	9.9708 ± 0.0055	9.5740 ± 0.0037	10.4759 ± 0.0041	9.4510 ± 0.0040	9.7355 ± 0.0041	10.6749 ± 0.0051	···
m_{W2}	9.9747 ± 0.0085	9.5869 ± 0.0037	10.4815 ± 0.0042	···	9.7391 ± 0.0045	10.6785 ± 0.0053	···
m_{W3}	10.0247 ± 0.0736	9.5412 ± 0.0224	···	9.3666 ± 0.0201	···	···	···
Posterior Inferences							
$\mu_{\rm post}$	10.2668 ± 0.0152	10.1910 ± 0.0158	10.7718 ± 0.0149	9.9671 ± 0.0137	10.0784 ± 0.0133	11.1663 ± 0.0129	10.9485 ± 0.0316
$E(B-V)_{\rm post}$	0.0873 ± 0.0157	0.0828 ± 0.0160	0.0335 ± 0.0148	0.1531 ± 0.0162	0.0513 ± 0.0082	0.0603 ± 0.0187	0.0308 ± 0.0131
M_U	···	···	···	···	0.4606 ± 0.0586	···	1.0752 ± 0.0488
M_B	···	···	···	···	0.7740 ± 0.0419	···	0.6500 ± 0.0410
M_{hipp}	0.6089 ± 0.0517	0.5471 ± 0.0526	0.6014 ± 0.0492	0.5523 ± 0.0533	0.5960 ± 0.0291	0.5659 ± 0.0684	0.7003 ± 0.0396
M_V	···	···	···	···	0.4227 ± 0.0288	···	0.4633 ± 0.0387
M_R	···	···	···	···	0.3136 ± 0.0253	···	0.3077 ± 0.0287
M_I	···	···	···	···	···	···	···
M_z	···	···	···	···	···	···	···
M_J	···	···	···	···	-0.0305 ± 0.0154	···	-0.0183 ± 0.0255
M_H	···	···	···	···	-0.2284 ± 0.0149	···	-0.1805 ± 0.0276
M_K	···	···	···	···	-0.2579 ± 0.0155	···	-0.1763 ± 0.0293
M_{W1}	-0.3112 ± 0.0159	-0.6314 ± 0.0159	-0.3017 ± 0.0152	-0.5429 ± 0.0139	-0.3519 ± 0.0138	-0.5020 ± 0.0134	···
M_{W2}	-0.3015 ± 0.0171	-0.6130 ± 0.0159	-0.2940 ± 0.0153	···	-0.3448 ± 0.0140	-0.4943 ± 0.0136	···
M_{W3}	-0.2444 ± 0.0752	-0.6515 ± 0.0274	···	-0.6041 ± 0.0243	···	···	···

Continued on Next Page...

Table A.1 – Continued

Measurements and Priors							
Name	RXCet	RXCol	RXEri	RYCol	RYOct	RZCet	RZCVn
Type	RRab	RRab	RRab	RRab	RRab	RRab	RRab
Blazhko Affected?	True	True	False	True	False	False	False
Period (d)	0.5737	0.5937	0.5872	0.4789	0.5635	0.5106	0.5674
[Fe/H]	−1.28	−1.70	−1.33	−0.91	−1.83	−1.36	−1.84
$\mu_{\rm prior}$	10.7399 ± 0.1257	11.8760 ± 0.1269	8.8788 ± 0.1254	10.1189 ± 0.1284	11.2008 ± 0.1260	11.1082 ± 0.1258	11.0505 ± 0.1257
$E(B-V)_{\rm SF}$	0.0245 ± 0.0007	0.0674 ± 0.0016	0.0585 ± 0.0018	0.0253 ± 0.0011	0.0983 ± 0.0028	0.0267 ± 0.0009	0.0131 ± 0.0004
m_U	···	···	···	···	···	···	···
m_B	···	···	···	···	···	···	···
m_{hipp}	11.5443 ± 0.0057	12.7253 ± 0.0214	9.7687 ± 0.0022	11.0103 ± 0.0109	12.1221 ± 0.0108	11.9015 ± 0.0113	11.6885 ± 0.0110
m_V	···	···	···	···	···	···	···
m_R	···	···	···	···	···	···	···
m_I	···	···	···	···	···	···	···
m_z	···	···	···	···	···	···	···
m_J	···	···	···	···	···	···	···
m_H	···	···	···	···	···	···	···
m_K	···	···	···	···	···	···	···
m_{W1}	10.1826 ± 0.0061	11.2333 ± 0.0050	···	9.7882 ± 0.0034	10.7254 ± 0.0051	10.6211 ± 0.0044	10.4203 ± 0.0053
m_{W2}	10.1895 ± 0.0053	11.2411 ± 0.0051	···	9.7900 ± 0.0034	10.7175 ± 0.0054	10.6154 ± 0.0045	10.4283 ± 0.0052
m_{W3}	···	11.0361 ± 0.1660	8.2701 ± 0.0086	9.7438 ± 0.0216	···	10.5399 ± 0.0677	···
Posterior Inferences							
$\mu_{\rm post}$	10.7179 ± 0.0135	11.7971 ± 0.0143	8.8661 ± 0.0265	10.1474 ± 0.0128	11.2344 ± 0.0131	11.0384 ± 0.0123	10.9494 ± 0.0134
$E(B-V)_{\rm post}$	0.0801 ± 0.0157	0.1124 ± 0.0174	0.1050 ± 0.0165	0.0819 ± 0.0156	0.1001 ± 0.0161	0.0866 ± 0.0155	0.0536 ± 0.0159
M_U	···	···	···	···	···	···	···
M_B	···	···	···	···	···	···	···
M_{hipp}	0.5594 ± 0.0522	0.5532 ± 0.0609	0.5526 ± 0.0515	0.5897 ± 0.0526	0.5538 ± 0.0536	0.5743 ± 0.0524	0.5603 ± 0.0526
M_V	···	···	···	···	···	···	···
M_R	···	···	···	···	···	···	···
M_I	···	···	···	···	···	···	···
M_z	···	···	···	···	···	···	···
M_J	···	···	···	···	···	···	···
M_H	···	···	···	···	···	···	···
M_K	···	···	···	···	···	···	···
M_{W1}	-0.5493 ± 0.0146	-0.5834 ± 0.0149	···	-0.3736 ± 0.0131	-0.5265 ± 0.0138	-0.4324 ± 0.0128	-0.5384 ± 0.0141
M_{W2}	-0.5370 ± 0.0143	-0.5680 ± 0.0149	···	-0.3662 ± 0.0130	-0.5277 ± 0.0140	-0.4323 ± 0.0129	-0.5269 ± 0.0141
M_{W3}	···	-0.7631 ± 0.1667	-0.5984 ± 0.0278	-0.4055 ± 0.0251	···	-0.5005 ± 0.0689	···

Continued on Next Page...

Table A.1 – Continued

Measurements and Priors							
Name	SAra	SCom	SSCVn	SSFor	SSLeo	SSOct	STBoo
Type	RRab	RRab	RRab	RRab	RRab	RRab	RRab
Blazhko Affected?	True	False	False	True	False	True	True
Period (d)	0.4519	0.5866	0.4785	0.4954	0.6263	0.6218	0.6223
[Fe/H]	−0.71	−1.91	−1.37	−0.94	−1.79	−1.60	−1.76
$\mu_{\rm prior}$	9.6640 ± 0.1313	11.0639 ± 0.1259	11.2257 ± 0.1264	9.4306 ± 0.1278	10.4427 ± 0.1253	10.4262 ± 0.1216	10.4079 ± 0.1254
$E(B-V)_{\rm SF}$	0.1286 ± 0.0027	0.0156 ± 0.0008	0.0063 ± 0.0008	0.0133 ± 0.0002	0.0172 ± 0.0004	0.2798 ± 0.0054	0.0173 ± 0.0002
m_U	···	···	···	···	···	···	11.5212 ± 0.0492
m_B	···	···	···	···	···	···	11.2783 ± 0.0199
m_{hipp}	10.8368 ± 0.0164	11.6941 ± 0.0095	11.9494 ± 0.0172	10.2761 ± 0.0073	11.1057 ± 0.0077	11.9985 ± 0.0099	11.0782 ± 0.0098
m_V	···	···	···	···	···	···	10.9063 ± 0.0071
m_R	···	···	···	···	···	···	10.7212 ± 0.0067
m_I	···	···	···	···	···	···	···
m_z	···	···	···	···	···	···	···
m_J	···	···	···	···	···	···	10.1901 ± 0.0039
m_H	···	···	···	···	···	···	9.9373 ± 0.0046
m_K	···	···	···	···	···	···	9.9594 ± 0.0050
m_{W1}	9.5053 ± 0.0057	10.5392 ± 0.0062	10.8471 ± 0.0062	9.1215 ± 0.0058	9.8640 ± 0.0054	9.7206 ± 0.0045	9.8162 ± 0.0044
m_{W2}	9.5035 ± 0.0057	10.5460 ± 0.0077	10.8497 ± 0.0058	9.1495 ± 0.0099	9.8790 ± 0.0055	9.7032 ± 0.0042	9.8218 ± 0.0038
m_{W3}	9.4806 ± 0.0291	···	···	9.0691 ± 0.0160	9.8228 ± 0.0409	9.6558 ± 0.0250	9.7721 ± 0.0234
Posterior Inferences							
$\mu_{\rm post}$	9.8001 ± 0.0146	11.1046 ± 0.0142	11.2113 ± 0.0134	9.5248 ± 0.0132	10.4948 ± 0.0159	10.2837 ± 0.0155	10.4366 ± 0.0153
$E(B-V)_{\rm post}$	0.1308 ± 0.0165	0.0174 ± 0.0116	0.0442 ± 0.0153	0.0497 ± 0.0154	0.0240 ± 0.0137	0.3521 ± 0.0166	0.0270 ± 0.0088
M_U	···	···	···	···	···	···	0.9545 ± 0.0660
M_B	···	···	···	···	···	···	0.7296 ± 0.0433
M_{hipp}	0.6004 ± 0.0570	0.5316 ± 0.0405	0.5908 ± 0.0531	0.5855 ± 0.0512	0.5310 ± 0.0471	0.5407 ± 0.0560	0.5516 ± 0.0335
M_V	···	···	···	···	···	···	0.3852 ± 0.0313
M_R	···	···	···	···	···	···	0.2142 ± 0.0274
M_I	···	···	···	···	···	···	···
M_z	···	···	···	···	···	···	···
M_J	···	···	···	···	···	···	-0.2711 ± 0.0172
M_H	···	···	···	···	···	···	-0.5147 ± 0.0164
M_K	···	···	···	···	···	···	-0.4868 ± 0.0162
M_{W1}	-0.3177 ± 0.0155	-0.5685 ± 0.0154	-0.3719 ± 0.0146	-0.4119 ± 0.0142	-0.6350 ± 0.0167	-0.6246 ± 0.0160	-0.6252 ± 0.0159
M_{W2}	-0.3107 ± 0.0156	-0.5605 ± 0.0160	-0.3663 ± 0.0144	-0.3806 ± 0.0163	-0.6184 ± 0.0167	-0.6183 ± 0.0159	-0.6177 ± 0.0158
M_{W3}	-0.3225 ± 0.0326	···	···	-0.4568 ± 0.0207	-0.6725 ± 0.0439	-0.6359 ± 0.0294	-0.6650 ± 0.0280

Continued on Next Page...

Table A.1 – Continued

Measurements and Priors							
Name	STCom	STCVn	STLeo	STVir	SUDra	SVEri	SVHya
Type	RRab	RRc	RRab	RRab	RRab	RRab	RRab
Blazhko Affected?	False	False	False	False	False	False	True
Period (d)	0.5989	0.3291	0.4780	0.4108	0.6604	0.7139	0.4785
[Fe/H]	−1.10	−1.07	−1.17	−0.67	−1.80	−1.70	−1.50
$\mu_{\rm prior}$	10.7061 ± 0.1266	10.6632 ± 0.1267	10.7609 ± 0.1263	10.6371 ± 0.1310	9.3800 ± 0.2457	9.1648 ± 0.1251	9.7408 ± 0.1254
$E(B-V)_{\rm SF}$	0.0218 ± 0.0007	0.0122 ± 0.0004	0.0377 ± 0.0010	0.0357 ± 0.0005	0.0085 ± 0.0004	0.0794 ± 0.0022	0.0745 ± 0.0003
m_U	···	···	···	···	···	···	···
m_B	···	···	···	···	···	···	···
m_{hipp}	11.5430 ± 0.0049	11.4454 ± 0.0046	11.6342 ± 0.0078	11.6188 ± 0.0133	9.8461 ± 0.0036	10.0497 ± 0.0028	10.6548 ± 0.0114
m_V	···	···	···	···	···	···	···
m_R	···	···	···	···	···	···	···
m_I	···	···	···	···	···	···	···
m_z	···	···	···	···	···	···	···
m_J	···	···	···	···	···	···	···
m_H	···	···	···	···	···	···	···
m_K	···	···	···	···	8.7928 ± 0.0102	···	···
m_{W1}	10.1454 ± 0.0050	10.4141 ± 0.0043	10.4122 ± 0.0146	10.5364 ± 0.0048	8.5941 ± 0.0039	8.5463 ± 0.0043	···
m_{W2}	10.1491 ± 0.0051	10.4283 ± 0.0048	10.4167 ± 0.0092	10.5417 ± 0.0050	8.5800 ± 0.0037	8.5507 ± 0.0042	···
m_{W3}	···	10.4820 ± 0.0516	10.2447 ± 0.0931	···	8.5324 ± 0.0097	8.5192 ± 0.0096	9.3226 ± 0.0237
Posterior Inferences							
$\mu_{\rm post}$	10.7202 ± 0.0143	10.7055 ± 0.0153	10.7688 ± 0.0150	10.7509 ± 0.0177	9.2648 ± 0.0179	9.2919 ± 0.0209	9.7172 ± 0.0354
$E(B-V)_{\rm post}$	0.0828 ± 0.0157	0.0395 ± 0.0159	0.0817 ± 0.0158	0.0744 ± 0.0166	0.0237 ± 0.0142	0.0728 ± 0.0177	0.1036 ± 0.0184
M_U	···	···	···	···	···	···	···
M_B	···	···	···	···	···	···	···
M_{hipp}	0.5467 ± 0.0526	0.6081 ± 0.0524	0.5930 ± 0.0524	0.6199 ± 0.0573	0.5023 ± 0.0492	0.5151 ± 0.0610	0.5921 ± 0.0540
M_V	···	···	···	···	···	···	···
M_R	···	···	···	···	···	···	···
M_I	···	···	···	···	···	···	···
M_z	···	···	···	···	···	···	···
M_J	···	···	···	···	···	···	···
M_H	···	···	···	···	···	···	···
M_K	···	···	···	···	-0.4803 ± 0.0208	···	···
M_{W1}	-0.5892 ± 0.0151	-0.2983 ± 0.0156	-0.3708 ± 0.0207	-0.2275 ± 0.0182	-0.6748 ± 0.0182	-0.7583 ± 0.0213	···
M_{W2}	-0.5799 ± 0.0151	-0.2815 ± 0.0158	-0.3609 ± 0.0174	-0.2172 ± 0.0183	-0.6873 ± 0.0182	-0.7490 ± 0.0212	···
M_{W3}	···	-0.2244 ± 0.0538	-0.5256 ± 0.0945	···	-0.7329 ± 0.0203	-0.7743 ± 0.0229	-0.3969 ± 0.0423

Continued on Next Page...

Table A.1 – Continued

Measurements and Priors							
Name	SVScl	SWAnd	SWAqr	SWDra	SXAqr	SXFor	SXUMa
Type	RRc	RRab	RRab	RRab	RRab	RRab	RRc
Blazhko Affected?	False	True	False	False	False	False	False
Period (d)	0.3774	0.4423	0.4593	0.5697	0.5357	0.6053	0.3072
[Fe/H]	−1.77	−0.24	−1.63	−1.12	−1.87	−1.66	−1.81
$\mu_{\rm prior}$	10.8271 ± 0.1251	8.6851 ± 0.1364	10.4640 ± 0.1260	9.7775 ± 0.1264	11.1155 ± 0.1272	10.5371 ± 0.1250	10.3073 ± 0.1253
$E(B-V)_{\rm SF}$	0.0133 ± 0.0004	0.0391 ± 0.0011	0.0733 ± 0.0040	0.0126 ± 0.0001	0.0455 ± 0.0009	0.0122 ± 0.0009	0.0103 ± 0.0007
m_U	···	···	···	···	···	···	10.9381 ± 0.0130
m_B	···	···	···	···	···	···	11.0094 ± 0.0057
m_{hipp}	11.4519 ± 0.0034	9.7641 ± 0.0070	11.3469 ± 0.0110	10.5792 ± 0.0036	11.8534 ± 0.0217	11.2135 ± 0.0037	10.9130 ± 0.0051
m_V	···	···	···	···	···	···	10.8223 ± 0.0040
m_R	···	···	···	···	···	···	10.6751 ± 0.0034
m_I	···	···	···	···	···	···	···
m_z	···	···	···	···	···	···	···
m_J	···	···	···	···	···	···	10.2669 ± 0.0057
m_H	···	···	···	···	···	···	···
m_K	···	···	···	···	···	···	···
m_{W1}	10.4889 ± 0.0048	8.4746 ± 0.0050	10.0175 ± 0.0061	9.2835 ± 0.0041	10.5804 ± 0.0055	9.8295 ± 0.0037	10.0456 ± 0.0039
m_{W2}	10.5032 ± 0.0045	8.4788 ± 0.0044	10.0187 ± 0.0091	9.2899 ± 0.0038	10.5842 ± 0.0058	9.8357 ± 0.0041	10.0764 ± 0.0041
m_{W3}	···	8.4476 ± 0.0144	9.9611 ± 0.0553	9.2208 ± 0.0162	···	···	10.0449 ± 0.0351
Posterior Inferences							
$\mu_{\rm post}$	10.9155 ± 0.0122	8.7544 ± 0.0150	10.3306 ± 0.0145	9.8133 ± 0.0130	11.0501 ± 0.0126	10.4167 ± 0.0147	10.2805 ± 0.0177
$E(B-V)_{\rm post}$	0.0077 ± 0.0070	0.1116 ± 0.0099	0.1250 ± 0.0161	0.0647 ± 0.0159	0.0704 ± 0.0165	0.0753 ± 0.0166	0.0123 ± 0.0077
M_U	···	···	···	···	···	···	0.5984 ± 0.0427
M_B	···	···	···	···	···	···	0.6779 ± 0.0365
M_{hipp}	0.5107 ± 0.0255	0.6375 ± 0.0355	0.5995 ± 0.0543	0.5501 ± 0.0527	0.5686 ± 0.0579	0.5455 ± 0.0542	0.5915 ± 0.0312
M_V	···	···	···	···	···	···	0.5033 ± 0.0298
M_R	···	···	···	···	···	···	0.3625 ± 0.0266
M_I	···	···	···	···	···	···	···
M_z	···	···	···	···	···	···	···
M_J	···	···	···	···	···	···	-0.0248 ± 0.0197
M_H	···	···	···	···	···	···	···
M_K	···	···	···	···	···	···	···
M_{W1}	-0.4280 ± 0.0131	-0.2993 ± 0.0158	-0.3350 ± 0.0155	-0.5411 ± 0.0135	-0.4820 ± 0.0135	-0.6003 ± 0.0148	-0.2370 ± 0.0181
M_{W2}	-0.4131 ± 0.0130	-0.2876 ± 0.0156	-0.3254 ± 0.0169	-0.5303 ± 0.0134	-0.4734 ± 0.0136	-0.5891 ± 0.0150	-0.2055 ± 0.0182
M_{W3}	···	-0.3093 ± 0.0208	-0.3723 ± 0.0572	-0.5939 ± 0.0208	···	···	-0.2358 ± 0.0392

Continued on Next Page...

Table A.1 – Continued

Measurements and Priors							
Name	SZGem	TSex	TTCnc	TTLyn	TUUMa	TVBoo	TVCrB
Type	RRab	RRc	RRab	RRab	RRab	RRc	RRab
Blazhko Affected?	False	False	True	False	False	True	False
Period (d)	0.5011	0.3247	0.5635	0.5974	0.5577	0.3126	0.5846
[Fe/H]	−1.46	−1.34	−1.57	−1.56	−1.51	−2.44	−2.33
$\mu_{\rm prior}$	11.0131 ± 0.1257	9.2908 ± 0.1257	10.5829 ± 0.1252	9.2373 ± 0.1249	9.1837 ± 0.1255	10.5871 ± 0.1294	11.3804 ± 0.1286
$E(B-V)_{\rm SF}$	0.0380 ± 0.0004	0.0435 ± 0.0032	0.0558 ± 0.0016	0.0156 ± 0.0005	0.0200 ± 0.0001	0.0083 ± 0.0006	0.0337 ± 0.0010
m_U	12.1369 ± 0.0145	···	12.0422 ± 0.0025	···	···	···	···
m_B	11.8787 ± 0.0083	···	11.7278 ± 0.0019	···	···	···	···
m_{hipp}	11.8195 ± 0.0135	10.1100 ± 0.0032	11.4224 ± 0.0074	9.9466 ± 0.0033	9.9200 ± 0.0126	11.0413 ± 0.0034	11.9737 ± 0.0085
m_V	11.6121 ± 0.0218	···	11.3335 ± 0.0085	···	···	···	···
m_R	11.4445 ± 0.0209	···	11.0313 ± 0.0025	···	···	···	···
m_I	11.2010 ± 0.0555	···	10.7409 ± 0.0044	···	···	···	···
m_z	11.6385 ± 0.0546	···	11.1316 ± 0.0077	···	···	···	···
m_J	10.9750 ± 0.0065	···	10.3672 ± 0.0049	···	···	···	···
m_H	10.7564 ± 0.0064	···	10.0807 ± 0.0048	···	···	···	···
m_K	10.6980 ± 0.0065	···	10.0173 ± 0.0055	···	···	···	···
m_{W1}	10.6263 ± 0.0064	9.1159 ± 0.0053	9.9200 ± 0.0061	8.5672 ± 0.0068	8.6018 ± 0.0046	10.1707 ± 0.0044	10.7152 ± 0.0044
m_{W2}	10.6213 ± 0.0071	9.1343 ± 0.0051	9.9395 ± 0.0100	8.5663 ± 0.0050	8.6102 ± 0.0048	10.1888 ± 0.0045	10.7040 ± 0.0043
m_{W3}	···	9.1085 ± 0.0226	···	8.5234 ± 0.0139	8.5749 ± 0.0176	···	10.7734 ± 0.0646
Posterior Inferences							
$\mu_{\rm post}$	11.0313 ± 0.0128	9.3972 ± 0.0157	10.4338 ± 0.0134	9.1381 ± 0.0145	9.1116 ± 0.0127	10.4179 ± 0.0169	11.2664 ± 0.0140
$E(B-V)_{\rm post}$	0.0461 ± 0.0083	0.0310 ± 0.0148	0.1347 ± 0.0041	0.0773 ± 0.0160	0.0731 ± 0.0152	0.0118 ± 0.0094	0.0485 ± 0.0159
M_U	0.8836 ± 0.0422	···	0.9595 ± 0.0229	···	···	···	···
M_B	0.6562 ± 0.0354	···	0.7349 ± 0.0208	···	···	···	···
M_{hipp}	0.6346 ± 0.0313	0.6093 ± 0.0500	0.5395 ± 0.0197	0.5507 ± 0.0533	0.5646 ± 0.0518	0.5841 ± 0.0349	0.5455 ± 0.0524
M_V	0.4365 ± 0.0345	···	0.4781 ± 0.0196	···	···	···	···
M_R	0.2929 ± 0.0311	···	0.2460 ± 0.0166	···	···	···	···
M_I	0.0840 ± 0.0583	···	0.0565 ± 0.0155	···	···	···	···
M_z	0.5376 ± 0.0570	···	0.4940 ± 0.0162	···	···	···	···
M_J	-0.0982 ± 0.0151	···	-0.1890 ± 0.0145	···	···	···	···
M_H	-0.3012 ± 0.0143	···	-0.4299 ± 0.0143	···	···	···	···
M_K	-0.3496 ± 0.0142	···	-0.4642 ± 0.0145	···	···	···	···
M_{W1}	-0.4130 ± 0.0141	-0.2867 ± 0.0164	-0.5373 ± 0.0147	-0.5843 ± 0.0159	-0.5226 ± 0.0134	-0.2493 ± 0.0174	-0.5597 ± 0.0143
M_{W2}	-0.4149 ± 0.0145	-0.2662 ± 0.0164	-0.5087 ± 0.0167	-0.5801 ± 0.0152	-0.5093 ± 0.0134	-0.2303 ± 0.0174	-0.5677 ± 0.0144
M_{W3}	···	-0.2893 ± 0.0274	···	-0.6164 ± 0.0200	-0.5383 ± 0.0217	···	-0.4937 ± 0.0662

Continued on Next Page...

Table A.1 – Continued

Measurements and Priors							
Name	TWBoo	TWHer	TWLyn	TYAps	TZAur	UCom	ULep
Type	RRab	RRab	RRab	RRab	RRab	RRc	RRab
Blazhko Affected?	False	False	False	False	False	False	False
Period (d)	0.5323	0.3996	0.4819	0.5017	0.3917	0.2927	0.5815
[Fe/H]	−1.46	−0.69	−0.66	−0.95	−0.79	−1.25	−1.78
$\mu_{\rm prior}$	10.6626 ± 0.1252	10.3065 ± 0.1307	11.0950 ± 0.1315	10.7642 ± 0.1293	11.0244 ± 0.1298	11.0761 ± 0.1258	9.9314 ± 0.1258
$E(B-V)_{\rm SF}$	0.0128 ± 0.0004	0.0371 ± 0.0012	0.0399 ± 0.0006	0.1344 ± 0.0060	0.0553 ± 0.0008	0.0134 ± 0.0004	0.0290 ± 0.0015
m_U	···	···	···	···	···	···	···
m_B	···	···	···	···	···	···	···
m_{hipp}	11.3870 ± 0.0069	11.2856 ± 0.0127	12.0925 ± 0.0166	11.9424 ± 0.0087	12.0407 ± 0.0139	11.8208 ± 0.0058	10.6343 ± 0.0123
m_V	···	···	···	···	···	···	···
m_R	···	···	···	···	···	···	···
m_I	···	···	···	···	···	···	···
m_z	···	···	···	···	···	···	···
m_J	···	···	···	···	···	···	···
m_H	···	···	···	···	···	···	···
m_K	···	···	···	···	···	···	···
m_{W1}	10.1234 ± 0.0040	10.2158 ± 0.0037	10.7208 ± 0.0052	10.3365 ± 0.0046	10.7941 ± 0.0065	10.8974 ± 0.0050	9.4383 ± 0.0034
m_{W2}	10.1307 ± 0.0048	10.2202 ± 0.0033	10.7329 ± 0.0054	10.3371 ± 0.0051	10.8117 ± 0.0053	10.9133 ± 0.0056	9.4346 ± 0.0035
m_{W3}	10.1063 ± 0.0323	···	10.8089 ± 0.1170	10.2834 ± 0.0449	···	···	9.4387 ± 0.0203
Posterior Inferences							
$\mu_{\rm post}$	10.5887 ± 0.0122	10.4029 ± 0.0187	11.0864 ± 0.0131	10.7241 ± 0.0125	10.9618 ± 0.0199	11.0775 ± 0.0199	9.9904 ± 0.0134
$E(B-V)_{\rm post}$	0.0684 ± 0.0163	0.0775 ± 0.0165	0.1117 ± 0.0102	0.1904 ± 0.0158	0.1233 ± 0.0114	0.0338 ± 0.0159	0.0297 ± 0.0151
M_U	···	···	···	···	···	···	···
M_B	···	···	···	···	···	···	···
M_{hipp}	0.5703 ± 0.0536	0.6243 ± 0.0574	0.6337 ± 0.0383	0.5835 ± 0.0525	0.6678 ± 0.0439	0.6304 ± 0.0539	0.5447 ± 0.0518
M_V	···	···	···	···	···	···	···
M_R	···	···	···	···	···	···	···
M_I	···	···	···	···	···	···	···
M_z	···	···	···	···	···	···	···
M_J	···	···	···	···	···	···	···
M_H	···	···	···	···	···	···	···
M_K	···	···	···	···	···	···	···
M_{W1}	-0.4772 ± 0.0126	-0.2007 ± 0.0190	-0.3851 ± 0.0139	-0.4208 ± 0.0130	-0.1892 ± 0.0209	-0.1861 ± 0.0202	-0.5573 ± 0.0137
M_{W2}	-0.4654 ± 0.0129	-0.1910 ± 0.0189	-0.3655 ± 0.0140	-0.4074 ± 0.0132	-0.1633 ± 0.0205	-0.1678 ± 0.0204	-0.5590 ± 0.0137
M_{W3}	-0.4839 ± 0.0346	···	-0.2802 ± 0.1176	-0.4450 ± 0.0466	···	···	-0.5524 ± 0.0243

Continued on Next Page...

Table A.1 – Continued

Measurements and Priors							
Name	UPic	UUCet	UUVir	UVOct	UYBoo	UYCyg	UZCVn
Type	RRab	RRab	RRab	RRab	RRab	RRab	RRab
Blazhko Affected?	False	False	False	True	False	False	False
Period (d)	0.4404	0.6061	0.4756	0.5426	0.6508	0.5607	0.6978
[Fe/H]	−0.72	−1.28	−0.87	−1.74	−2.56	−0.80	−1.89
$\mu_{\rm prior}$	10.6122 ± 0.1309	11.3944 ± 0.1256	9.7347 ± 0.1284	8.8500 ± 0.1271	10.5241 ± 0.1310	9.8849 ± 0.1433	11.5551 ± 0.1256
$E(B-V)_{\rm SF}$	0.0085 ± 0.0002	0.0199 ± 0.0006	0.0166 ± 0.0004	0.0851 ± 0.0008	0.0312 ± 0.0012	0.2134 ± 0.0147	0.0202 ± 0.0011
m_U	···	···	···	···	11.3250 ± 0.0583	11.9622 ± 0.0071	12.4177 ± 0.0204
m_B	···	···	···	···	11.2323 ± 0.0155	11.4233 ± 0.0090	12.4218 ± 0.0061
m_{hipp}	11.4926 ± 0.0178	12.1837 ± 0.0055	10.6073 ± 0.0070	9.5646 ± 0.0099	11.0562 ± 0.0086	11.2010 ± 0.0033	12.2051 ± 0.0069
m_V	···	···	···	···	10.9193 ± 0.0102	10.9679 ± 0.0096	12.0891 ± 0.0063
m_R	···	···	···	···	10.7131 ± 0.0103	10.7718 ± 0.0311	11.8361 ± 0.0040
m_I	···	···	···	···	···	···	11.5987 ± 0.0096
m_z	···	···	···	···	···	···	11.9510 ± 0.0141
m_J	···	···	···	···	10.0649 ± 0.0042	10.0977 ± 0.0056	11.2357 ± 0.0047
m_H	···	···	···	···	9.7919 ± 0.0046	9.8288 ± 0.0055	10.9612 ± 0.0055
m_K	···	···	···	···	9.7926 ± 0.0066	9.8238 ± 0.0059	10.9193 ± 0.0048
m_{W1}	10.3249 ± 0.0035	10.7526 ± 0.0052	9.4599 ± 0.0060	8.1686 ± 0.0044	9.6960 ± 0.0042	9.6813 ± 0.0064	10.8371 ± 0.0046
m_{W2}	10.3377 ± 0.0036	10.7874 ± 0.0061	9.4651 ± 0.0059	···	9.7046 ± 0.0048	···	10.8437 ± 0.0063
m_{W3}	10.3558 ± 0.0375	···	···	8.1028 ± 0.0070	9.6642 ± 0.0254	9.6733 ± 0.0292	···
Posterior Inferences							
$\mu_{\rm post}$	10.6088 ± 0.0151	11.3508 ± 0.0155	9.8170 ± 0.0134	8.6442 ± 0.0130	10.3566 ± 0.0171	10.1853 ± 0.0139	11.5659 ± 0.0199
$E(B-V)_{\rm post}$	0.0796 ± 0.0167	0.0817 ± 0.0162	0.0598 ± 0.0155	0.1068 ± 0.0161	0.0503 ± 0.0096	0.1255 ± 0.0087	0.0372 ± 0.0104
M_U	···	···	···	···	0.7260 ± 0.0754	1.1722 ± 0.0420	0.6726 ± 0.0567
M_B	···	···	···	···	0.6669 ± 0.0447	0.7169 ± 0.0370	0.7016 ± 0.0470
M_{hipp}	0.6183 ± 0.0583	0.5606 ± 0.0534	0.5910 ± 0.0519	0.5644 ± 0.0531	0.5318 ± 0.0359	0.5971 ± 0.0296	0.5152 ± 0.0397
M_V	···	···	···	···	0.4052 ± 0.0348	0.3895 ± 0.0295	0.4068 ± 0.0378
M_R	···	···	···	···	0.2252 ± 0.0308	0.2590 ± 0.0393	0.1731 ± 0.0331
M_I	···	···	···	···	···	···	-0.0364 ± 0.0288
M_z	···	···	···	···	···	···	0.3288 ± 0.0285
M_J	···	···	···	···	-0.3375 ± 0.0190	-0.2018 ± 0.0155	-0.3640 ± 0.0221
M_H	···	···	···	···	-0.5934 ± 0.0181	-0.4281 ± 0.0147	-0.6258 ± 0.0212
M_K	···	···	···	···	-0.5819 ± 0.0183	-0.4061 ± 0.0148	-0.6597 ± 0.0206
M_{W1}	-0.2978 ± 0.0153	-0.6124 ± 0.0161	-0.3676 ± 0.0145	-0.4942 ± 0.0134	-0.6694 ± 0.0175	-0.5259 ± 0.0151	-0.7353 ± 0.0204
M_{W2}	-0.2797 ± 0.0154	-0.5722 ± 0.0165	-0.3583 ± 0.0144	···	-0.6574 ± 0.0177	···	-0.7261 ± 0.0208
M_{W3}	-0.2548 ± 0.0404	···	···	-0.5438 ± 0.0147	-0.6936 ± 0.0306	-0.5149 ± 0.0323	···

Continued on Next Page...

Table A.1 – Continued

Measurements and Priors							
Name	V341Aql	V413CrA	V440Sgr	V445Oph	V499Cen	V675Sgr	VInd
Type	RRab	RRab	RRab	RRab	RRab	RRab	RRab
Blazhko Affected?	False	False	False	False	False	False	False
Period (d)	0.5780	0.5893	0.4775	0.3970	0.5212	0.6423	0.4796
[Fe/H]	-1.22	-1.26	-1.40	-0.19	-1.43	-2.28	-1.50
$\mu_{\rm prior}$	9.9077 ± 0.1263	9.7342 ± 0.1261	9.4373 ± 0.1254	9.3336 ± 0.1393	10.2820 ± 0.1258	9.5211 ± 0.1309	9.2069 ± 0.1277
$E(B-V)_{\rm SF}$	0.0831 ± 0.0021	0.0864 ± 0.0033	0.0844 ± 0.0020	0.2708 ± 0.0079	0.0716 ± 0.0021	0.2058 ± 0.0055	0.0419 ± 0.0009
m_U	...	...	...	...	...	...	...
m_B	...	...	...	...	...	...	...
m_{hipp}	10.9021 ± 0.0102	10.6989 ± 0.0040	10.3741 ± 0.0068	11.1570 ± 0.0090	11.1914 ± 0.0125	10.4024 ± 0.0093	10.0147 ± 0.0265
m_V	...	...	...	...	...	...	...
m_R	...	...	...	...	...	...	...
m_I	...	...	...	...	...	...	...
m_z	...	...	...	...	...	...	...
m_J	...	...	...	...	...	...	...
m_H	...	...	...	...	...	...	...
m_K	...	...	...	...	...	...	...
m_{W1}	9.6770 ± 0.0048	9.0952 ± 0.0059	9.0303 ± 0.0055	9.1812 ± 0.0052	9.8454 ± 0.0052	...	8.8385 ± 0.0056
m_{W2}	9.6871 ± 0.0048	9.1103 ± 0.0047	9.0346 ± 0.0050	9.1768 ± 0.0048	9.8370 ± 0.0053	...	8.8425 ± 0.0070
m_{W3}	...	...	9.0338 ± 0.0252	...	9.7105 ± 0.0238	8.9183 ± 0.0206	8.8154 ± 0.0166
Posterior Inferences							
$\mu_{\rm post}$	10.2266 ± 0.0135	9.6509 ± 0.0144	9.3833 ± 0.0132	9.3167 ± 0.0192	10.2763 ± 0.0124	9.5973 ± 0.0336	9.2029 ± 0.0135
$E(B-V)_{\rm post}$	0.0370 ± 0.0155	0.1469 ± 0.0162	0.1184 ± 0.0157	0.3624 ± 0.0168	0.1063 ± 0.0159	0.0815 ± 0.0190	0.0661 ± 0.0171
M_U	...	...	...	...	...	...	...
M_B	...	...	...	...	...	...	...
M_{hipp}	0.5520 ± 0.0519	0.5582 ± 0.0533	0.5959 ± 0.0520	0.6319 ± 0.0579	0.5606 ± 0.0534	0.5335 ± 0.0574	0.5913 ± 0.0618
M_V	...	...	...	...	...	...	...
M_R	...	...	...	...	...	...	...
M_I	...	...	...	...	...	...	...
M_z	...	...	...	...	...	...	...
M_J	...	...	...	...	...	...	...
M_H	...	...	...	...	...	...	...
M_K	...	...	...	...	...	...	...
M_{W1}	-0.5560 ± 0.0142	-0.5814 ± 0.0153	-0.3736 ± 0.0140	-0.1988 ± 0.0198	-0.4495 ± 0.0132	...	-0.3760 ± 0.0143
M_{W2}	-0.5435 ± 0.0141	-0.5564 ± 0.0149	-0.3614 ± 0.0139	-0.1788 ± 0.0196	-0.4507 ± 0.0133	...	-0.3675 ± 0.0149
M_{W3}	...	...	-0.3521 ± 0.0285	...	-0.5682 ± 0.0268	-0.6808 ± 0.0393	-0.3890 ± 0.0213

Continued on Next Page...

Table A.1 – Continued

Measurements and Priors							
Name	VWScl	VXHer	VXScl	VYLib	VYSer	VZHer	VZPeg
Type	RRab	RRab	RRab	RRab	RRab	RRab	RRc
Blazhko Affected?	False	False	False	False	False	False	False
Period (d)	0.5109	0.4554	0.6373	0.5339	0.7141	0.4403	0.3065
[Fe/H]	−0.84	−1.58	−2.25	−1.34	−1.79	−1.02	−1.80
$\mu_{\rm prior}$	10.2214 ± 0.1308	9.9443 ± 0.1296	11.6447 ± 0.1350	10.5978 ± 0.1264	9.4979 ± 0.1251	10.6984 ± 0.1276	11.2823 ± 0.1253
$E(B-V)_{\rm SF}$	0.0142 ± 0.0011	0.0421 ± 0.0015	0.0151 ± 0.0005	0.1566 ± 0.0049	0.0364 ± 0.0004	0.0266 ± 0.0007	0.0329 ± 0.0016
m_U	···	···	···	···	···	···	···
m_B	···	···	···	···	···	···	···
m_{hipp}	11.0930 ± 0.0241	10.7367 ± 0.0346	12.1950 ± 0.0443	11.8212 ± 0.0066	10.2226 ± 0.0033	11.5694 ± 0.0118	11.9648 ± 0.0057
m_V	···	···	···	···	···	···	···
m_R	···	···	···	···	···	···	···
m_I	···	···	···	···	···	···	···
m_z	···	···	···	···	···	···	···
m_J	···	···	···	···	···	···	···
m_H	···	···	···	···	···	···	···
m_K	···	···	···	···	···	···	···
m_{W1}	10.0296 ± 0.0048	9.5902 ± 0.0054	···	10.0482 ± 0.0061	8.7341 ± 0.0050	10.4700 ± 0.0042	11.0216 ± 0.0057
m_{W2}	10.0404 ± 0.0053	9.5844 ± 0.0052	10.7601 ± 0.0072	10.0325 ± 0.0078	8.7334 ± 0.0045	10.4727 ± 0.0043	11.0396 ± 0.0059
m_{W3}	···	9.4993 ± 0.0310	10.6749 ± 0.0869	···	8.6972 ± 0.0166	10.5192 ± 0.0687	11.0036 ± 0.1213
Posterior Inferences							
$\mu_{\rm post}$	10.4633 ± 0.0122	9.8978 ± 0.0144	11.3923 ± 0.0184	10.4837 ± 0.0129	9.4782 ± 0.0210	10.7519 ± 0.0151	11.2476 ± 0.0179
$E(B-V)_{\rm post}$	0.0206 ± 0.0131	0.0758 ± 0.0186	0.0797 ± 0.0204	0.2311 ± 0.0158	0.0698 ± 0.0175	0.0643 ± 0.0161	0.0288 ± 0.0148
M_U	···	···	···	···	···	···	···
M_B	···	···	···	···	···	···	···
M_{hipp}	0.5610 ± 0.0499	0.5862 ± 0.0704	0.5369 ± 0.0809	0.5668 ± 0.0518	0.5117 ± 0.0600	0.6030 ± 0.0550	0.6210 ± 0.0508
M_V	···	···	···	···	···	···	···
M_R	···	···	···	···	···	···	···
M_I	···	···	···	···	···	···	···
M_z	···	···	···	···	···	···	···
M_J	···	···	···	···	···	···	···
M_H	···	···	···	···	···	···	···
M_K	···	···	···	···	···	···	···
M_{W1}	-0.4374 ± 0.0130	-0.3209 ± 0.0152	···	-0.4759 ± 0.0140	-0.7563 ± 0.0215	-0.2932 ± 0.0155	-0.2310 ± 0.0187
M_{W2}	-0.4251 ± 0.0132	-0.3215 ± 0.0151	-0.6408 ± 0.0195	-0.4761 ± 0.0149	-0.7523 ± 0.0213	-0.2861 ± 0.0155	-0.2111 ± 0.0188
M_{W3}	···	-0.4003 ± 0.0342	-0.7192 ± 0.0888	···	-0.7827 ± 0.0267	-0.2343 ± 0.0703	-0.2446 ± 0.1226

Continued on Next Page...

Table A.1 – Continued

Measurements and Priors							
Name	WCrt	WCVn	WTuc	WYAnt	WYPav	WZHya	XAri
Type	RRab	RRab	RRab	RRab	RRab	RRab	RRab
Blazhko Affected?	False	False	False	False	False	False	False
Period (d)	0.4120	0.5518	0.6422	0.5743	0.5886	0.5377	0.6511
[Fe/H]	−0.54	−1.22	−1.57	−1.48	−0.98	−1.39	−2.43
$\mu_{\rm prior}$	10.6282 ± 0.1339	9.8910 ± 0.1258	10.8059 ± 0.1250	10.0935 ± 0.1257	11.2003 ± 0.1276	10.0638 ± 0.1253	8.6270 ± 0.1314
$E(B-V)_{\rm SF}$	0.0420 ± 0.0027	0.0045 ± 0.0005	0.0180 ± 0.0002	0.0584 ± 0.0009	0.0932 ± 0.0009	0.0700 ± 0.0011	0.1816 ± 0.0053
m_U	···	10.8266 ± 0.0271	···	···	···	···	···
m_B	···	10.8711 ± 0.0064	···	···	···	···	···
m_{hipp}	11.6604 ± 0.0214	10.6432 ± 0.0027	11.5222 ± 0.0059	10.9542 ± 0.0135	12.2915 ± 0.0087	10.9904 ± 0.0047	9.6448 ± 0.0185
m_V	···	10.4831 ± 0.0052	···	···	···	···	9.5478 ± 0.0397
m_R	···	10.2615 ± 0.0053	···	···	···	···	9.2420 ± 0.0128
m_I	···	···	···	···	···	···	8.8414 ± 0.0342
m_z	···	···	···	···	···	···	9.2763 ± 0.0087
m_J	···	···	···	···	···	···	···
m_H	···	···	···	···	···	···	···
m_K	···	9.4288 ± 0.0076	···	···	···	···	···
m_{W1}	10.4641 ± 0.0064	9.3375 ± 0.0042	10.2932 ± 0.0042	9.5439 ± 0.0053	10.5348 ± 0.0053	9.6012 ± 0.0054	7.8611 ± 0.0049
m_{W2}	10.4724 ± 0.0058	9.3399 ± 0.0046	10.3003 ± 0.0049	9.5613 ± 0.0047	10.5373 ± 0.0054	9.6064 ± 0.0051	7.8673 ± 0.0041
m_{W3}	···	9.3240 ± 0.0184	···	9.4897 ± 0.0290	10.3797 ± 0.0591	9.5793 ± 0.0342	7.8374 ± 0.0112
Posterior Inferences							
$\mu_{\rm post}$	10.6785 ± 0.0179	9.8352 ± 0.0123	10.9455 ± 0.0165	10.0826 ± 0.0136	11.0750 ± 0.0141	10.0701 ± 0.0125	8.5017 ± 0.0171
$E(B-V)_{\rm post}$	0.1032 ± 0.0139	0.0708 ± 0.0080	0.0193 ± 0.0132	0.0928 ± 0.0163	0.1985 ± 0.0153	0.1049 ± 0.0155	0.1996 ± 0.0111
M_U	···	0.6505 ± 0.0479	···	···	···	···	···
M_B	···	0.7421 ± 0.0349	···	···	···	···	···
M_{hipp}	0.6378 ± 0.0520	0.5720 ± 0.0284	0.5124 ± 0.0461	0.5622 ± 0.0551	0.5547 ± 0.0512	0.5706 ± 0.0508	0.4776 ± 0.0435
M_V	···	0.4263 ± 0.0274	···	···	···	···	0.4212 ± 0.0544
M_R	···	0.2416 ± 0.0238	···	···	···	···	0.2195 ± 0.0348
M_I	···	···	···	···	···	···	-0.0317 ± 0.0428
M_z	···	···	···	···	···	···	0.4726 ± 0.0246
M_J	···	···	···	···	···	···	···
M_H	···	···	···	···	···	···	···
M_K	···	-0.4315 ± 0.0145	···	···	···	···	···
M_{W1}	-0.2324 ± 0.0188	-0.5101 ± 0.0130	-0.6557 ± 0.0171	-0.5549 ± 0.0144	-0.5749 ± 0.0149	-0.4873 ± 0.0134	-0.6754 ± 0.0178
M_{W2}	-0.2171 ± 0.0187	-0.5029 ± 0.0131	-0.6473 ± 0.0172	-0.5313 ± 0.0142	-0.5590 ± 0.0149	-0.4750 ± 0.0133	-0.6558 ± 0.0176
M_{W3}	···	-0.5128 ± 0.0221	···	-0.5950 ± 0.0321	-0.7000 ± 0.0607	-0.4932 ± 0.0363	-0.6689 ± 0.0205

Continued on Next Page...

Table A.1 – Continued

Measurements and Priors							
Name	XCrt	XXAnd	XXPup	XZAps	XZCyg	XZDra	YZCap
Type	RRab	RRab	RRab	RRab	RRab	RRab	RRc
Blazhko Affected?	True	False	False	False	True	True	False
Period (d)	0.7328	0.7227	0.5172	0.5873	0.4666	0.4765	0.2735
[Fe/H]	−2.00	−1.94	−1.33	−1.06	−1.44	−0.79	−1.06
$\mu_{\rm prior}$	10.9310 ± 0.1260	10.0755 ± 0.1257	10.4890 ± 0.1259	11.3132 ± 0.1285	8.9900 ± 0.2218	9.3182 ± 0.1293	10.4375 ± 0.1269
$E(B-V)_{\rm SF}$	0.0235 ± 0.0011	0.0400 ± 0.0006	0.0727 ± 0.0010	0.1255 ± 0.0063	0.1096 ± 0.0024	0.0653 ± 0.0016	0.0562 ± 0.0015
m_U	···	11.3344 ± 0.0187	···	···	10.4268 ± 0.0102	11.1269 ± 0.0119	···
m_B	···	10.9785 ± 0.0294	···	···	9.8155 ± 0.0492	10.5170 ± 0.0205	···
m_{hipp}	11.5665 ± 0.0053	10.7737 ± 0.0041	11.3809 ± 0.0117	12.4955 ± 0.0090	9.7733 ± 0.0130	10.3450 ± 0.0083	11.3667 ± 0.0052
m_V	···	10.6322 ± 0.0057	···	···	9.6300 ± 0.0101	10.1573 ± 0.0032	···
m_R	···	10.3853 ± 0.0096	···	···	9.4501 ± 0.0114	9.9620 ± 0.0047	···
m_I	···	10.2381 ± 0.0332	···	···	···	···	···
m_z	···	10.8157 ± 0.0483	···	···	···	···	···
m_J	···	9.8546 ± 0.0103	···	···	···	9.4753 ± 0.0085	···
m_H	···	9.5945 ± 0.0082	···	···	···	9.2333 ± 0.0081	···
m_K	···	9.5284 ± 0.0076	···	···	8.8196 ± 0.0071	9.1867 ± 0.0071	···
m_{W1}	10.1221 ± 0.0068	9.3857 ± 0.0039	10.0098 ± 0.0053	10.8324 ± 0.0042	8.6225 ± 0.0029	9.0883 ± 0.0030	10.3057 ± 0.0057
m_{W2}	10.1258 ± 0.0054	9.3966 ± 0.0036	10.0262 ± 0.0076	10.8339 ± 0.0049	8.6271 ± 0.0032	9.1010 ± 0.0026	10.3386 ± 0.0073
m_{W3}	···	9.2910 ± 0.0164	10.0025 ± 0.0471	···	8.5596 ± 0.0064	9.0397 ± 0.0094	10.4164 ± 0.0972
Posterior Inferences							
$\mu_{\rm post}$	10.8957 ± 0.0224	10.1516 ± 0.0213	10.4448 ± 0.0127	11.3743 ± 0.0138	8.9601 ± 0.0132	9.4457 ± 0.0128	10.4188 ± 0.0230
$E(B-V)_{\rm post}$	0.0496 ± 0.0177	0.0350 ± 0.0112	0.1060 ± 0.0161	0.1705 ± 0.0162	0.0660 ± 0.0082	0.0867 ± 0.0076	0.0877 ± 0.0176
M_U	···	1.0143 ± 0.0603	···	···	1.1487 ± 0.0415	1.2636 ± 0.0394	···
M_B	···	0.6818 ± 0.0584	···	···	0.5816 ± 0.0603	0.7115 ± 0.0387	···
M_{hipp}	0.5055 ± 0.0614	0.5055 ± 0.0426	0.5827 ± 0.0536	0.5525 ± 0.0540	0.5930 ± 0.0319	0.6102 ± 0.0285	0.6553 ± 0.0610
M_V	···	0.3711 ± 0.0409	···	···	0.4633 ± 0.0294	0.4403 ± 0.0261	···
M_R	···	0.1425 ± 0.0369	···	···	0.3177 ± 0.0265	0.2901 ± 0.0230	···
M_I	···	0.0215 ± 0.0444	···	···	···	···	···
M_z	···	0.6111 ± 0.0553	···	···	···	···	···
M_J	···	-0.3288 ± 0.0256	···	···	···	-0.0492 ± 0.0163	···
M_H	···	-0.5770 ± 0.0236	···	···	···	-0.2618 ± 0.0154	···
M_K	···	-0.6355 ± 0.0229	···	···	-0.1638 ± 0.0150	-0.2897 ± 0.0146	···
M_{W1}	-0.7823 ± 0.0234	-0.7720 ± 0.0217	-0.4536 ± 0.0135	-0.5717 ± 0.0143	-0.3491 ± 0.0134	-0.3725 ± 0.0131	-0.1284 ± 0.0236
M_{W2}	-0.7752 ± 0.0230	-0.7587 ± 0.0217	-0.4300 ± 0.0146	-0.5587 ± 0.0145	-0.3401 ± 0.0135	-0.3539 ± 0.0130	-0.0897 ± 0.0240
M_{W3}	···	-0.8614 ± 0.0269	-0.4447 ± 0.0488	···	-0.4020 ± 0.0146	-0.4080 ± 0.0159	-0.0042 ± 0.0999

Continued on Next Page...

Table A.1 – Continued

Measurements and Priors	
Name	ZMic
Type	RRab
Blazhko Affected?	False
Period (d)	0.5869
[Fe/H]	−1.10
$\mu_{\rm prior}$	10.7181 ± 0.1269
$E(B-V)_{\rm SF}$	0.0818 ± 0.0028
m_U	···
m_B	···
m_{hipp}	11.7528 ± 0.0060
m_V	···
m_R	···
m_I	···
m_z	···
m_J	···
m_H	···
m_K	···
m_{W1}	10.0802 ± 0.0051
m_{W2}	10.0819 ± 0.0053
m_{W3}	10.0647 ± 0.0589
Posterior Inferences	
$\mu_{\rm post}$	10.6220 ± 0.0139
$E(B-V)_{\rm post}$	0.1720 ± 0.0152
M_U	···
M_B	···
M_{hipp}	0.5574 ± 0.0506
M_V	···
M_R	···
M_I	···
M_z	···
M_J	···
M_H	···
M_K	···
M_{W1}	-0.5719 ± 0.0146
M_{W2}	-0.5585 ± 0.0147
M_{W3}	-0.5613 ± 0.0605

Appendix B

Multi-band Light Curve Plots

The following 134 plots show all of the observed light curves (637 total, comprised of 33,630 epochs) that contributed to the RR Lyrae calibration sample used in the study presented in Chapter 6. Note that the *hipp*-band light curves often seem out of phase with the other data. This is a result of the *Hipparcos* observations being nearly 10,000 cycles older than the newer data; *Hipparcos* operated between 1989 and 1993 and all of the newer data were acquired between 2009 and 2013. The periods are not determined with sufficient accuracy to correctly phase-align light curve data with a temporal gap this large. Additionally, a minority of light curves are fitted with models that exhibit poor agreement with the data. This is often due to the Blazhko effect (stars known to be affected are identified in Table A.1) and sometimes simply a poor model fit (not enough Fourier terms). However, even in cases of obvious model failure, the inferred mean-flux magnitude is quite robust.

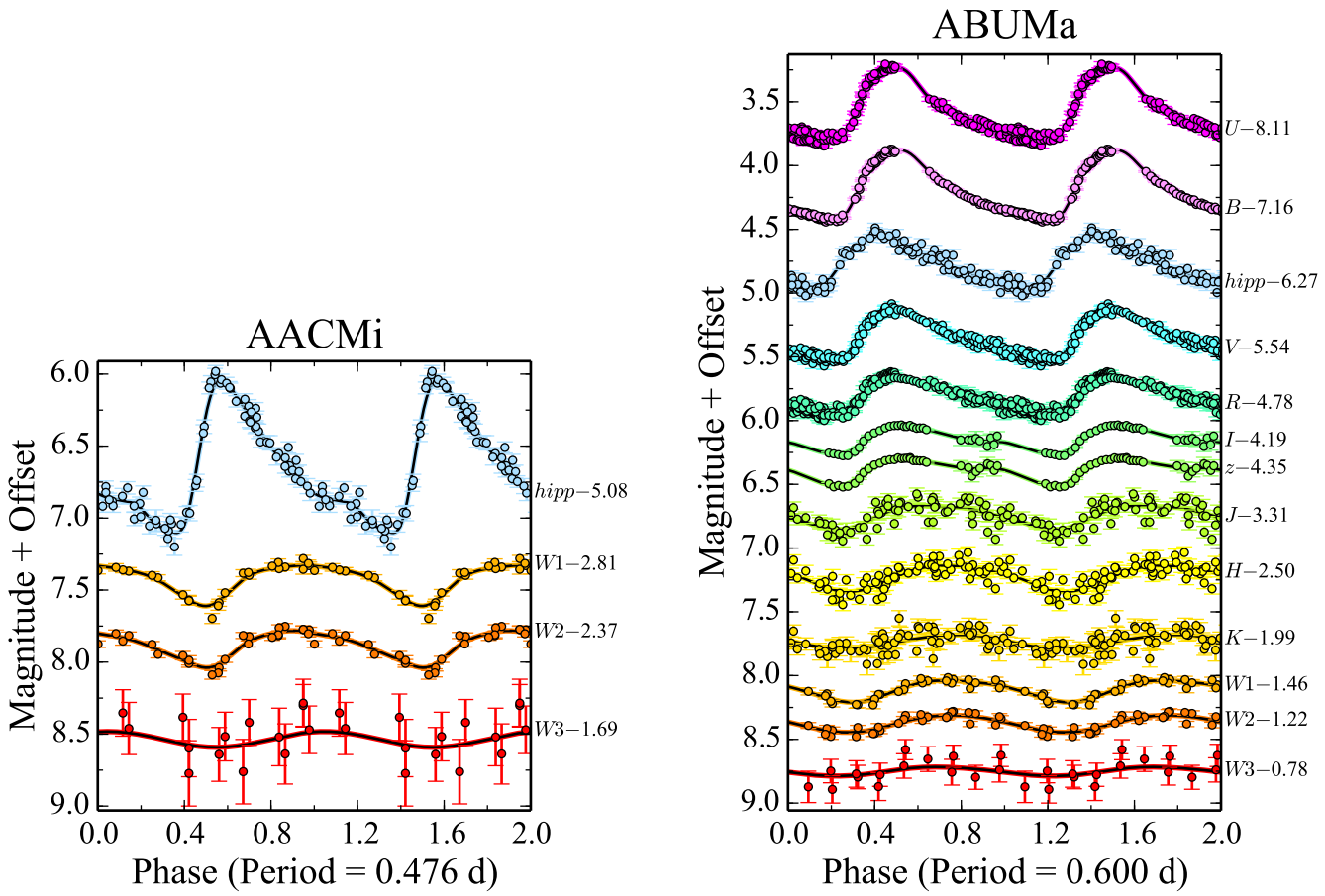

Figure B.1: Observed light curves for AACMi and ABUMa.

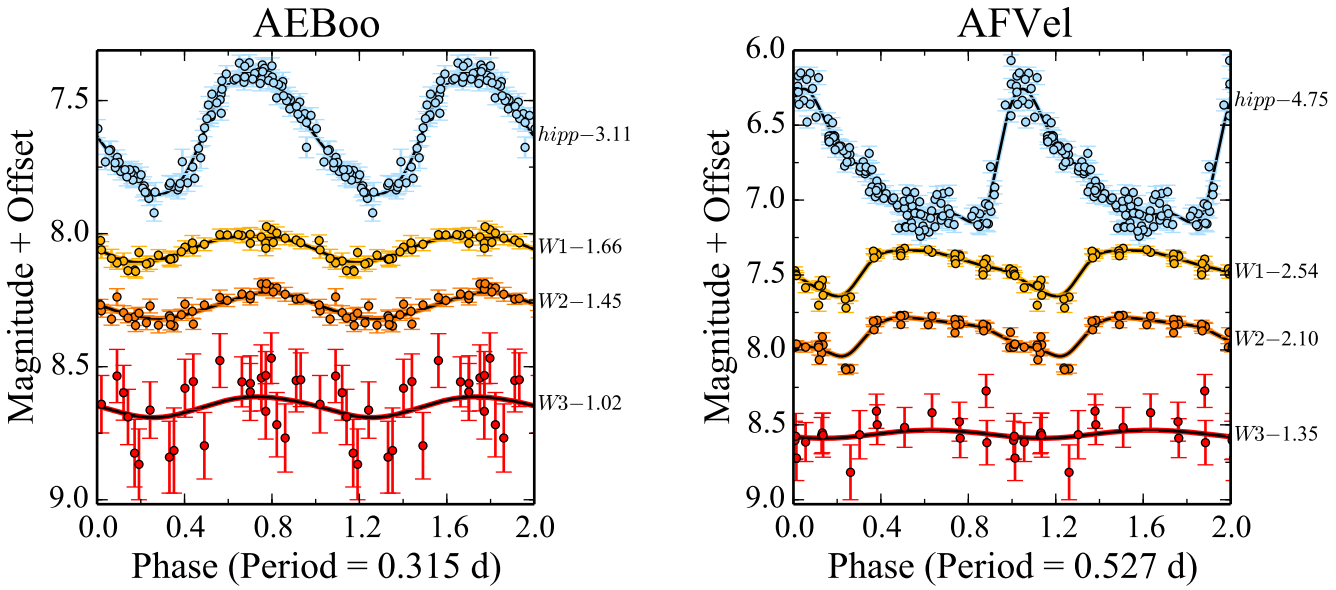

Figure B.2: Observed light curves for AEBoo and AFVel.

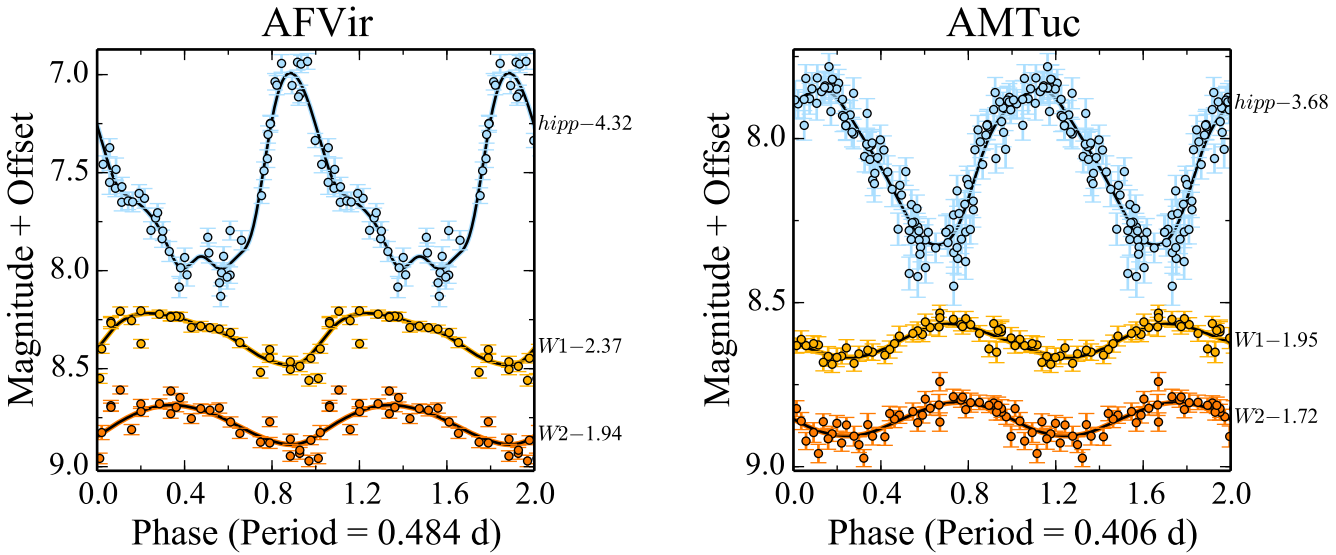

Figure B.3: Observed light curves for AFVir and AMTuc.

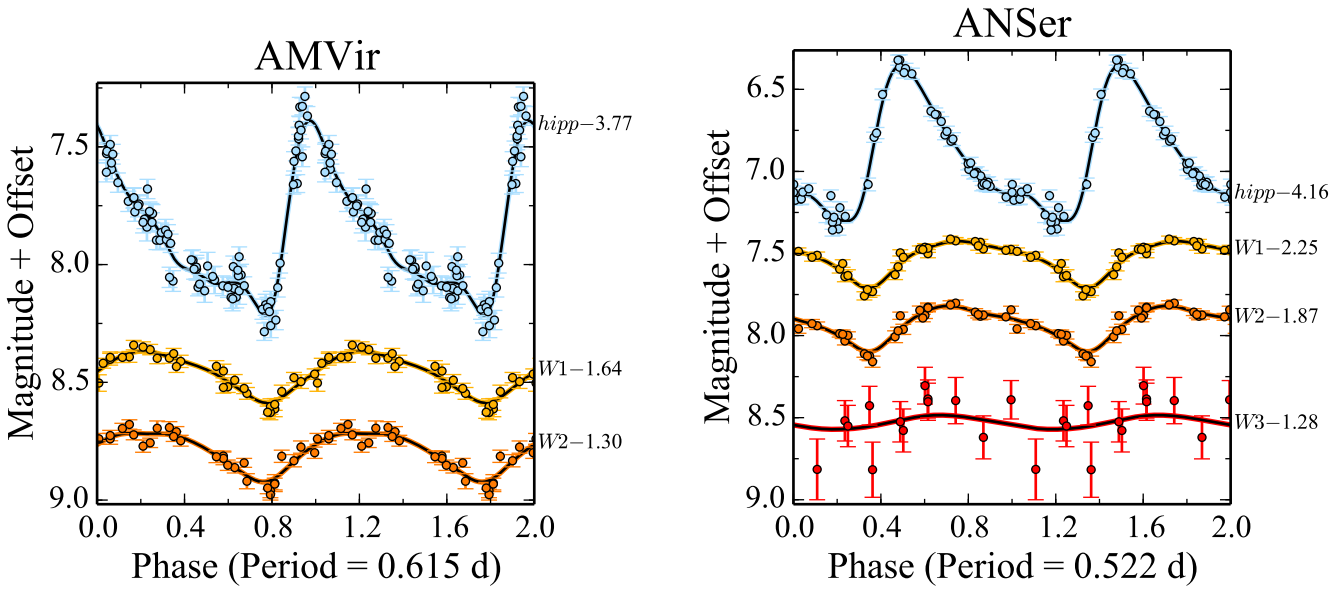

Figure B.4: Observed light curves for AMVir and ANSer.

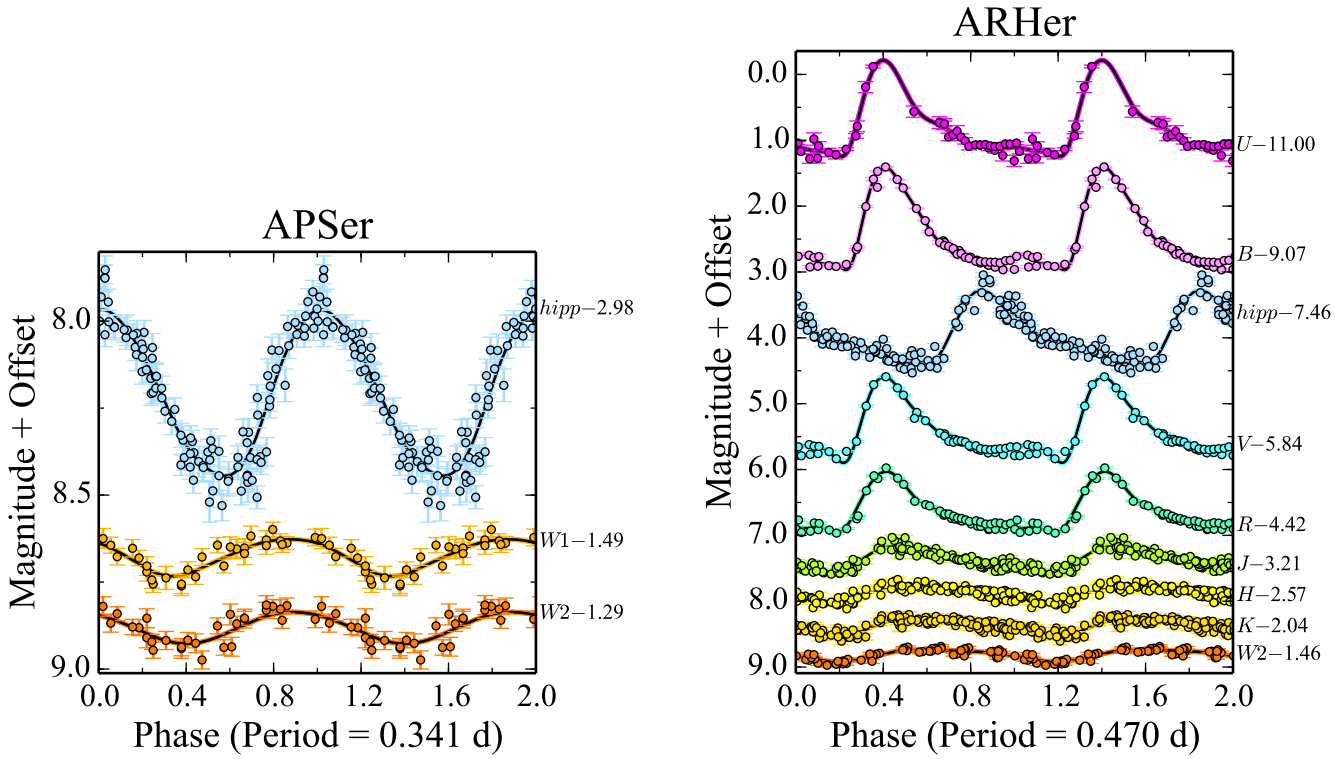

Figure B.5: Observed light curves for APSer and ARHer.

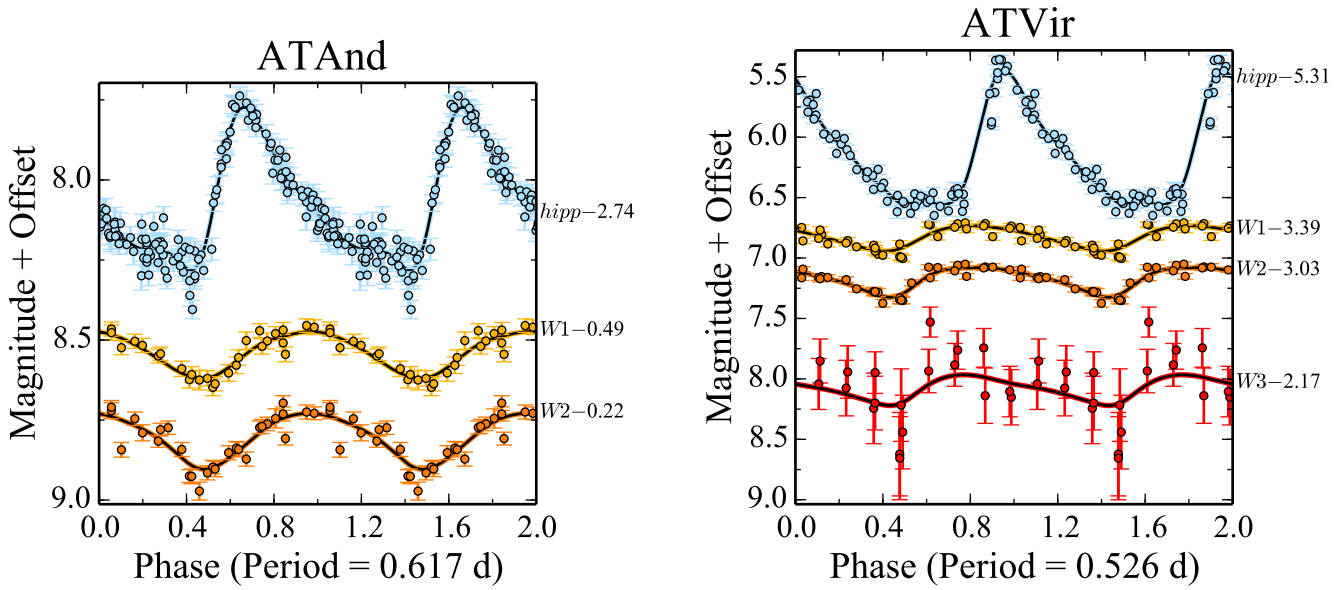

Figure B.6: Observed light curves for ATAnd and ATVir.

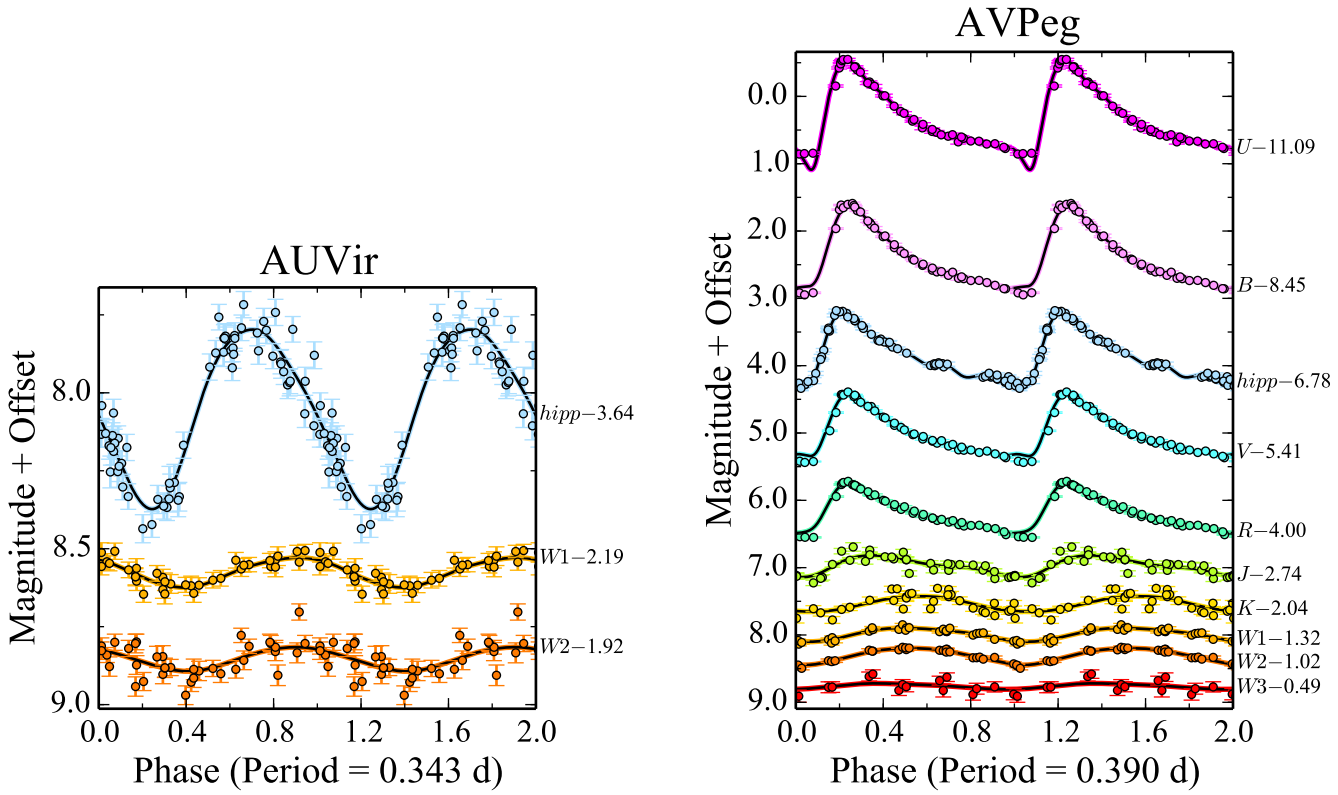

Figure B.7: Observed light curves for AUVir and AVPeg.

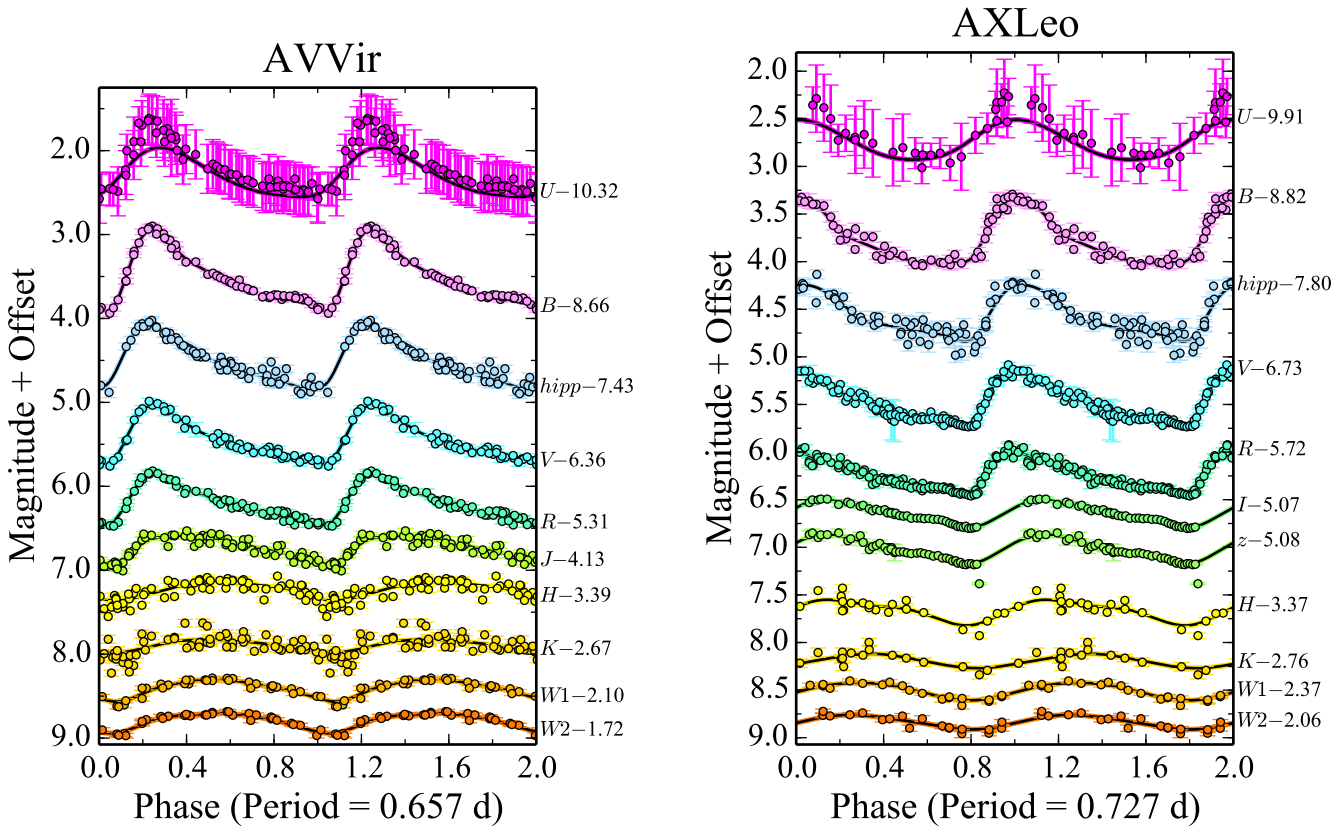

Figure B.8: Observed light curves for AVVir and AXLeo.

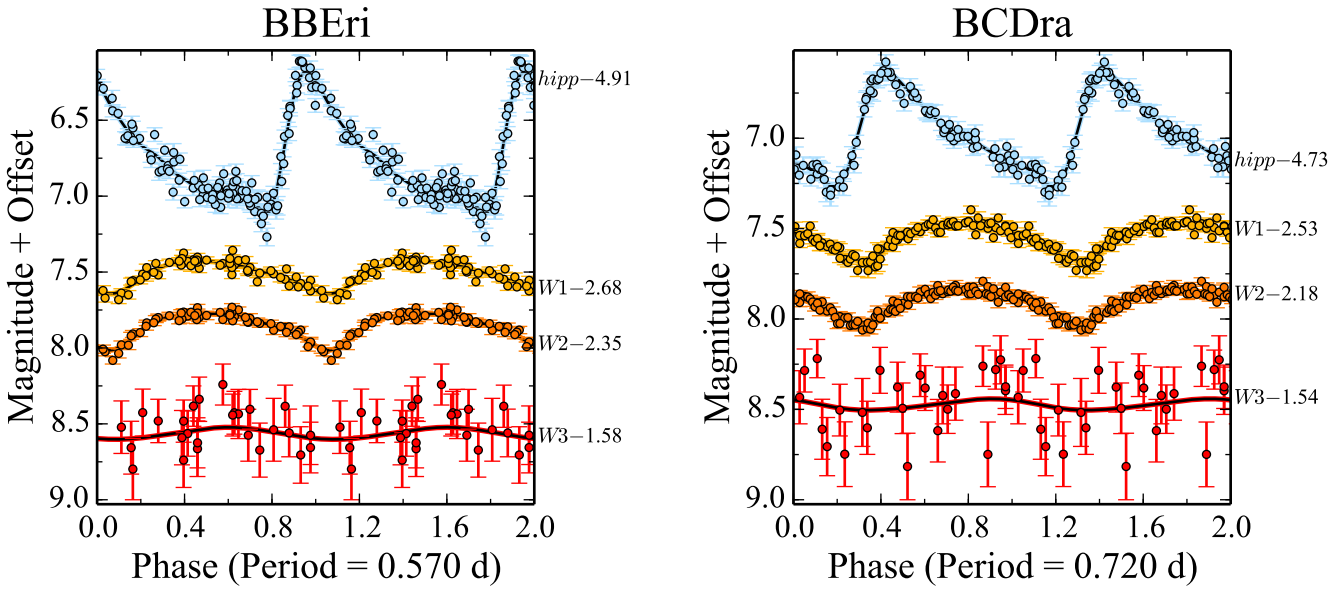

Figure B.9: Observed light curves for BBEri and BCDra.

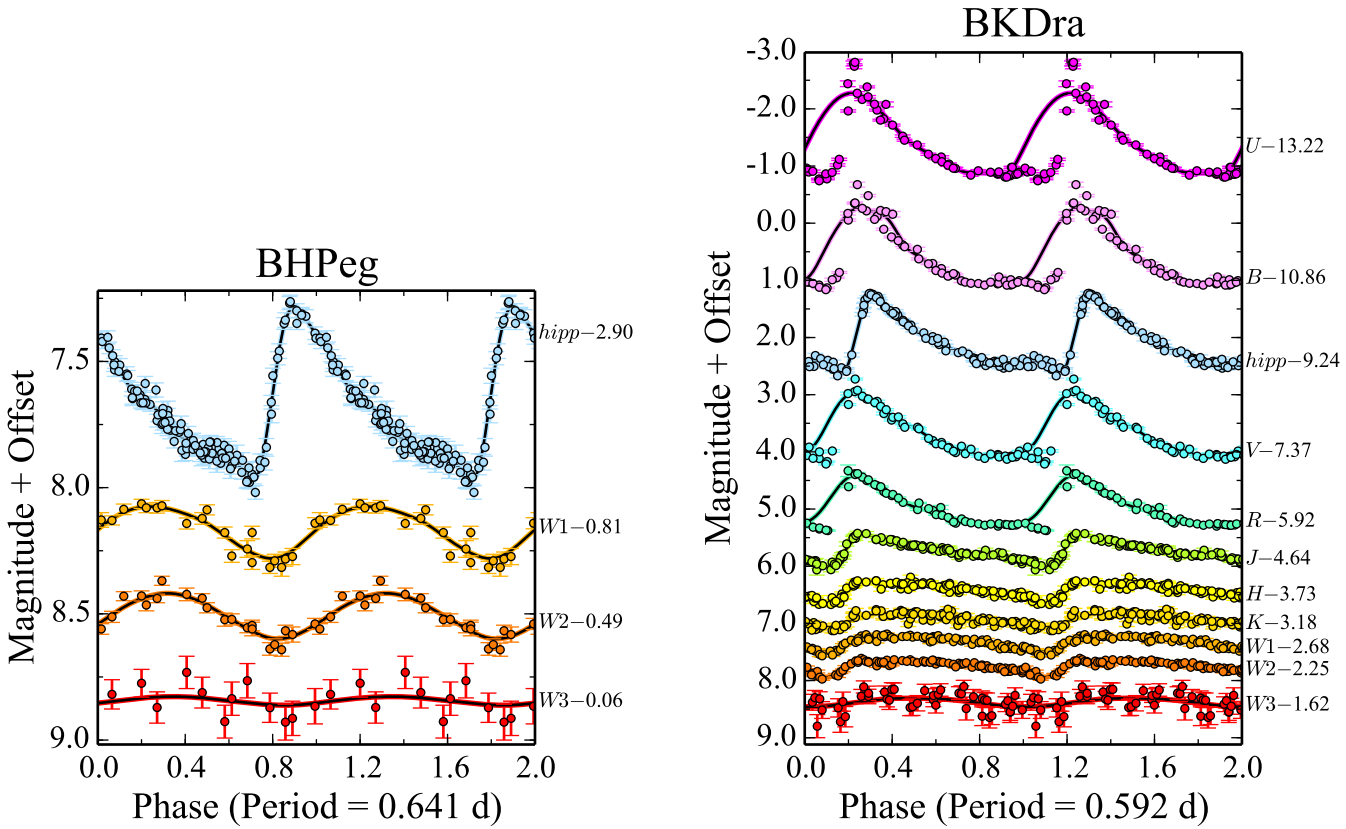

Figure B.10: Observed light curves for BHPeg and BKDra.

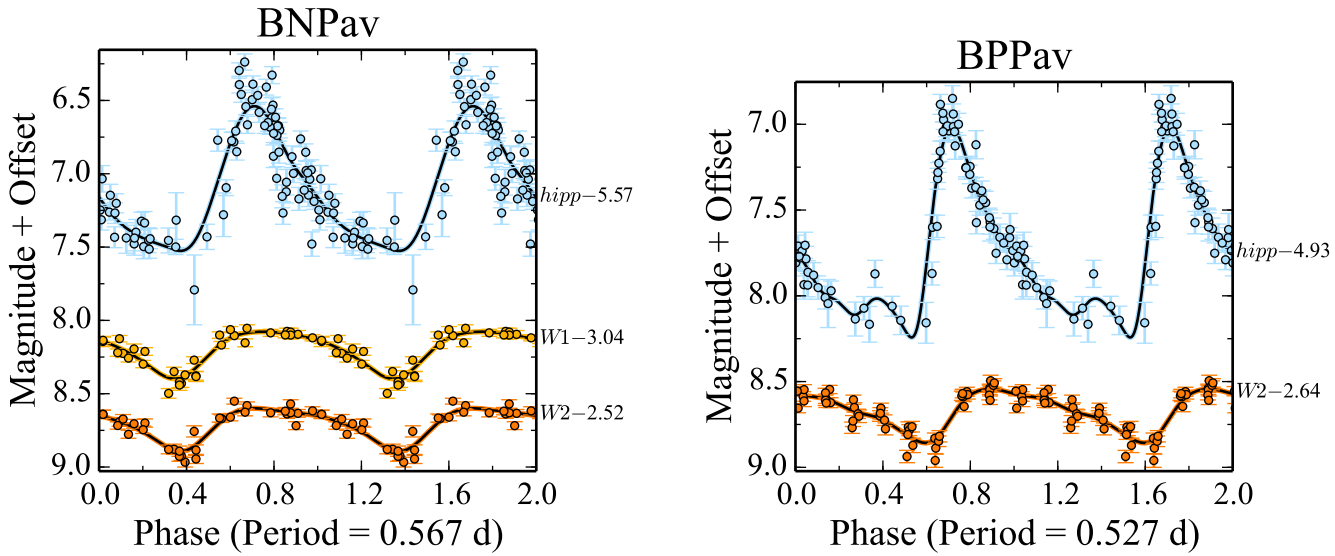

Figure B.11: Observed light curves for BNPav and BPPav.

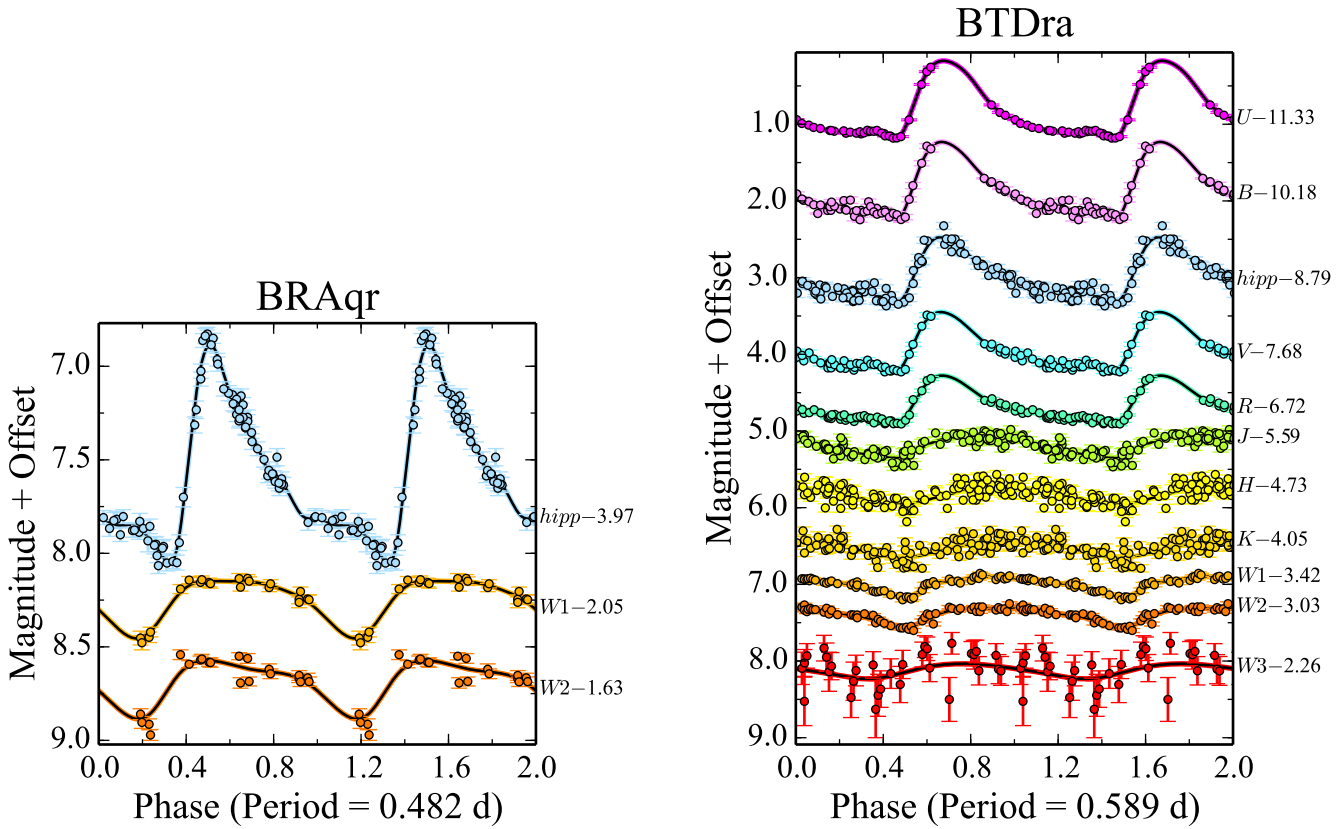

Figure B.12: Observed light curves for BRAqr and BTDra.

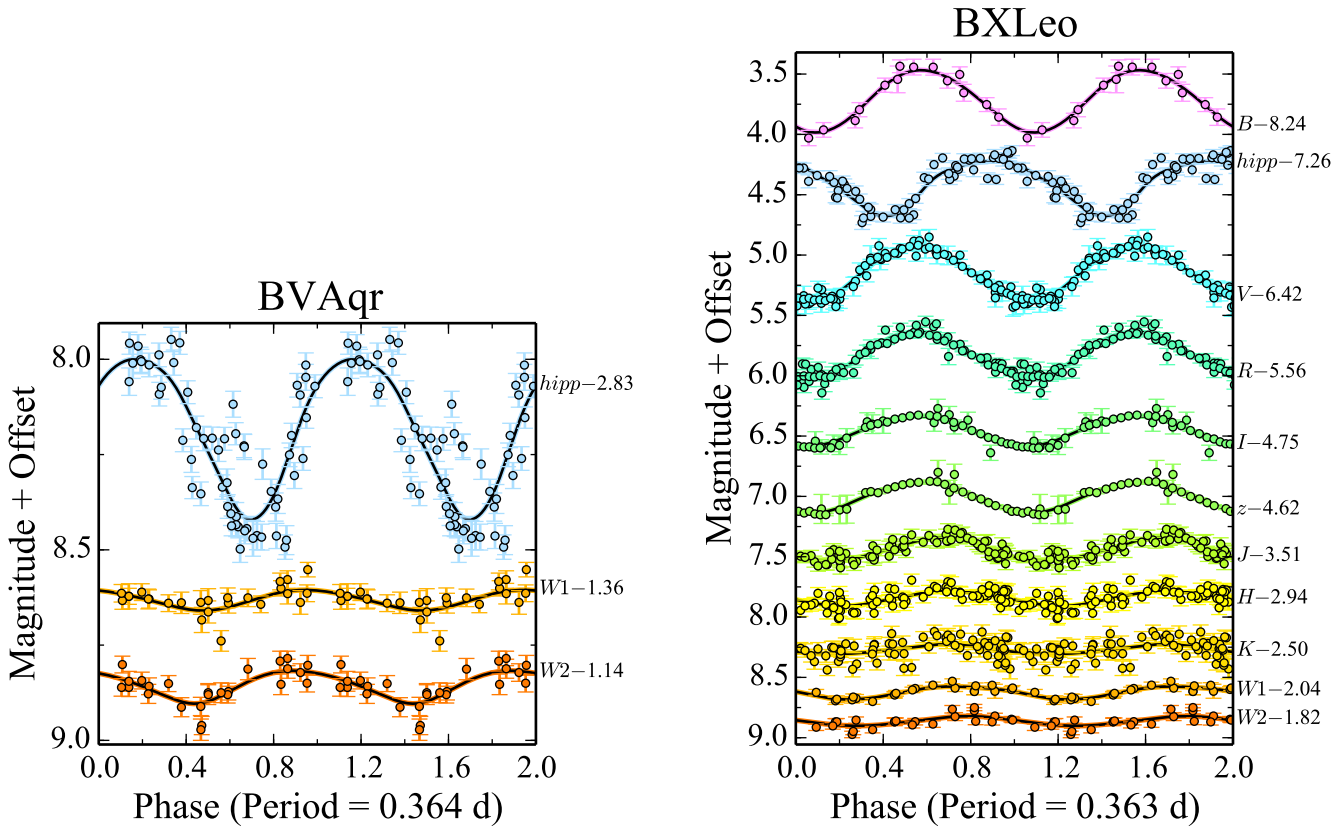

Figure B.13: Observed light curves for BVAqr and BXLeo.

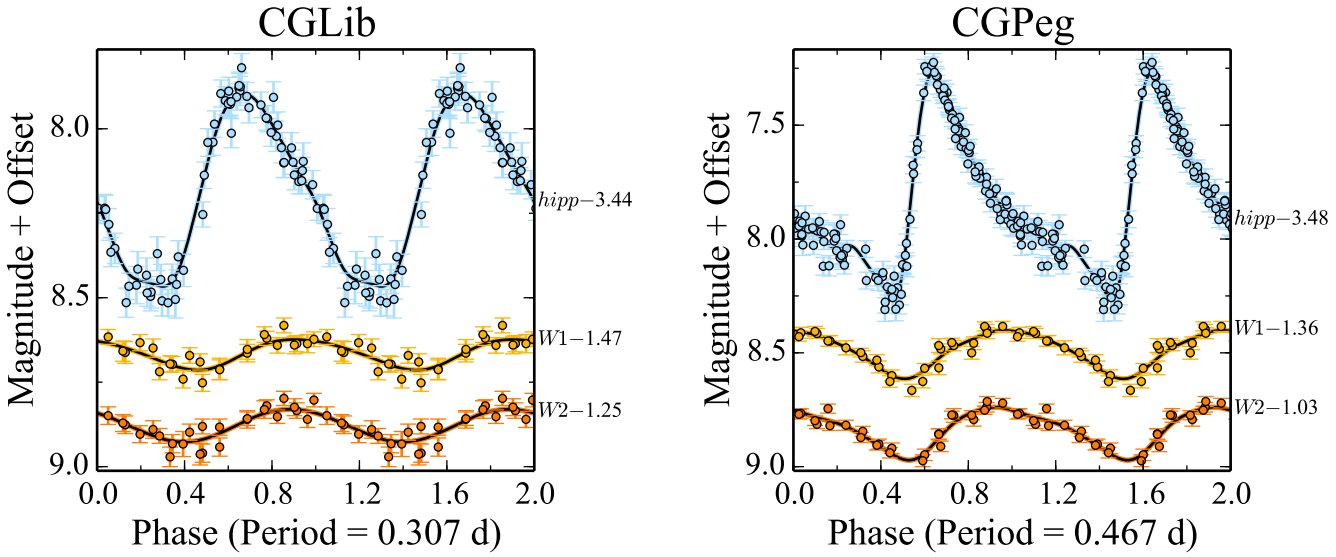

Figure B.14: Observed light curves for CGLib and CGPeg.

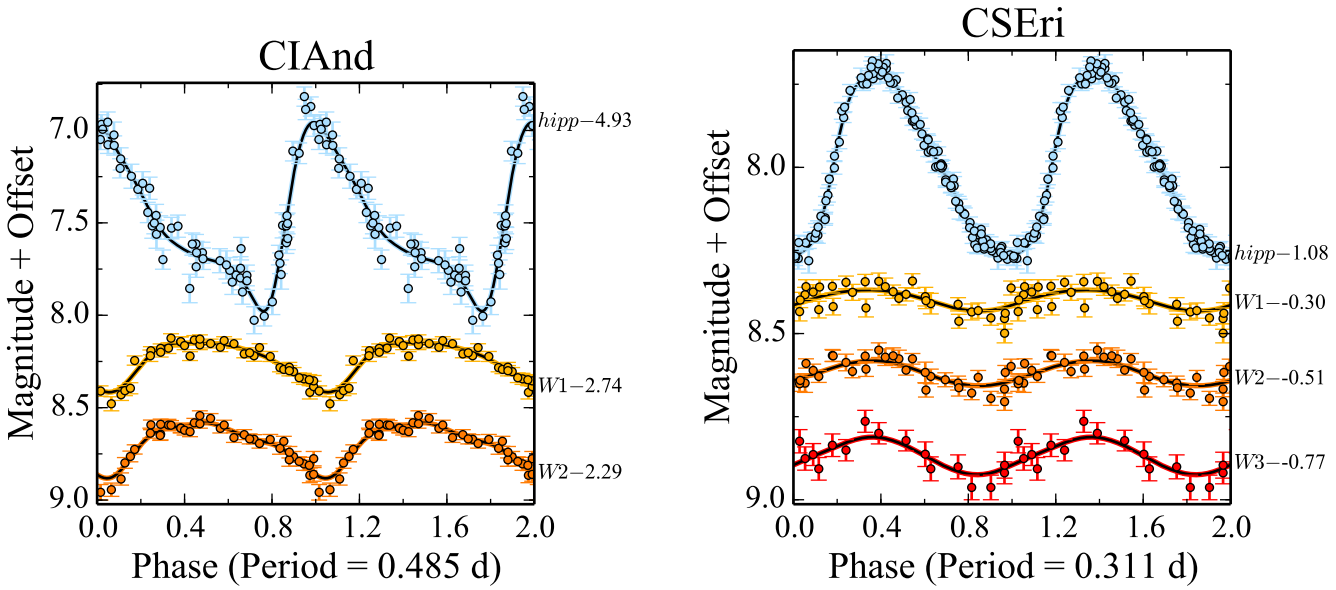

Figure B.15: Observed light curves for CIAnd and CSEri.

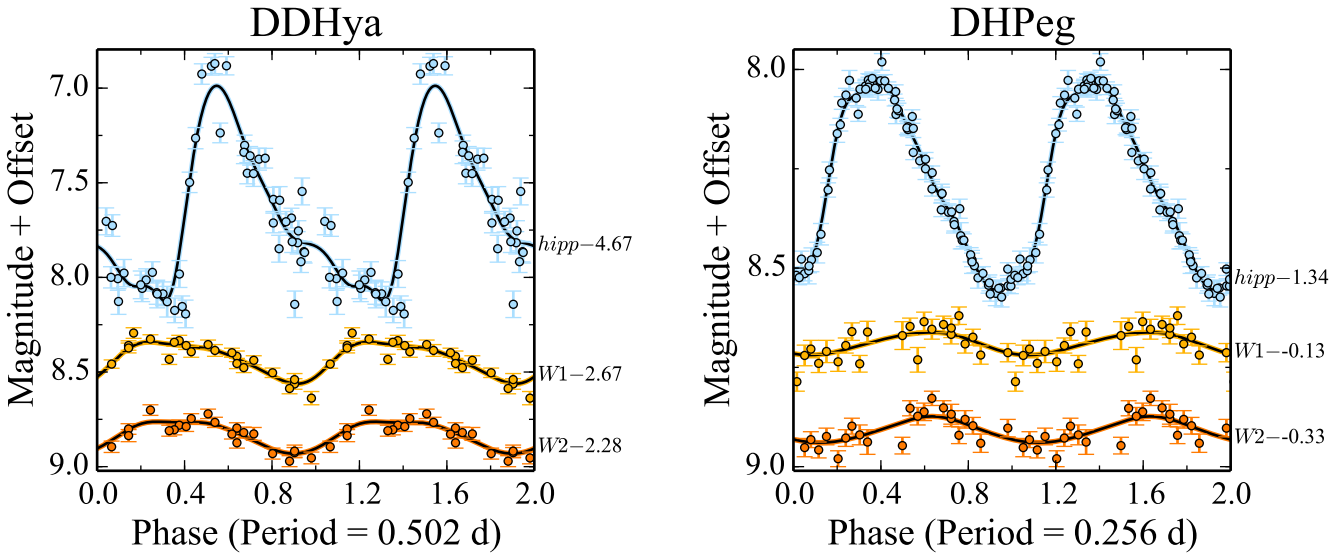

Figure B.16: Observed light curves for DDHya and DHPeg.

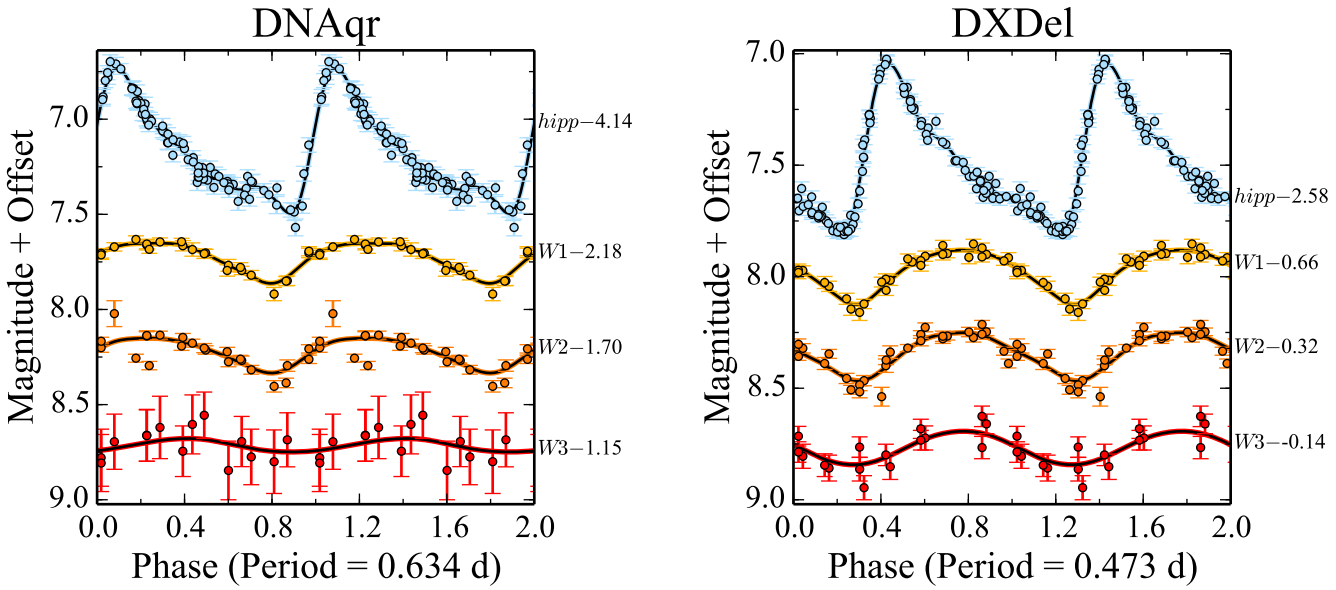

Figure B.17: Observed light curves for DNAqr and DXDel.

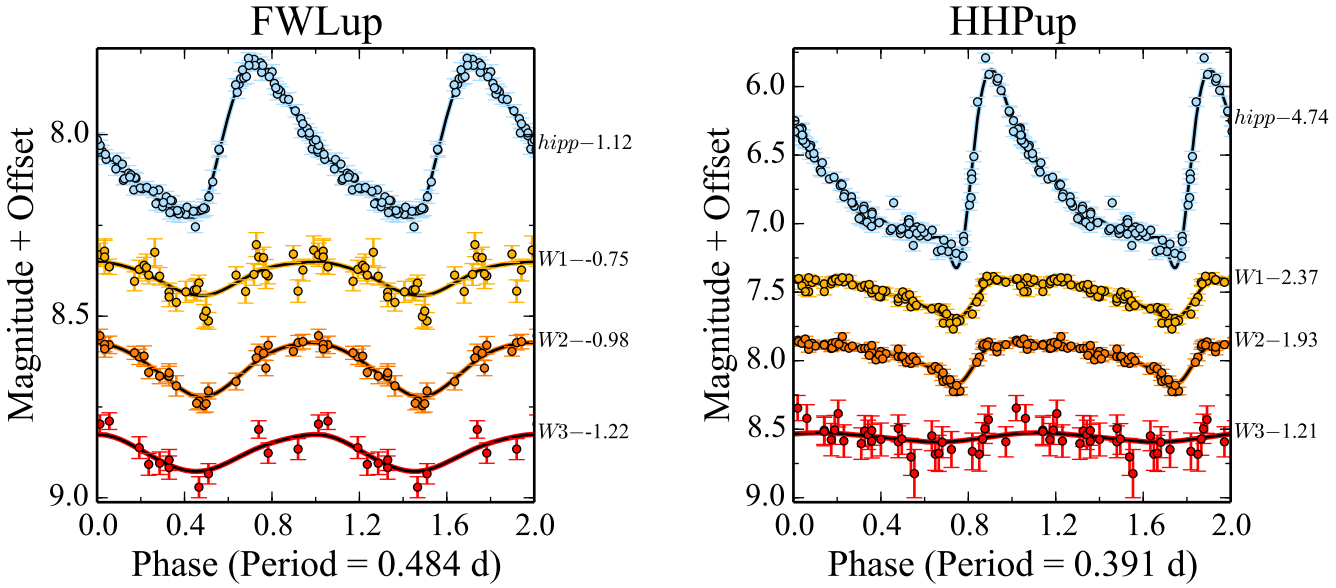

Figure B.18: Observed light curves for FWLup and HHPup.

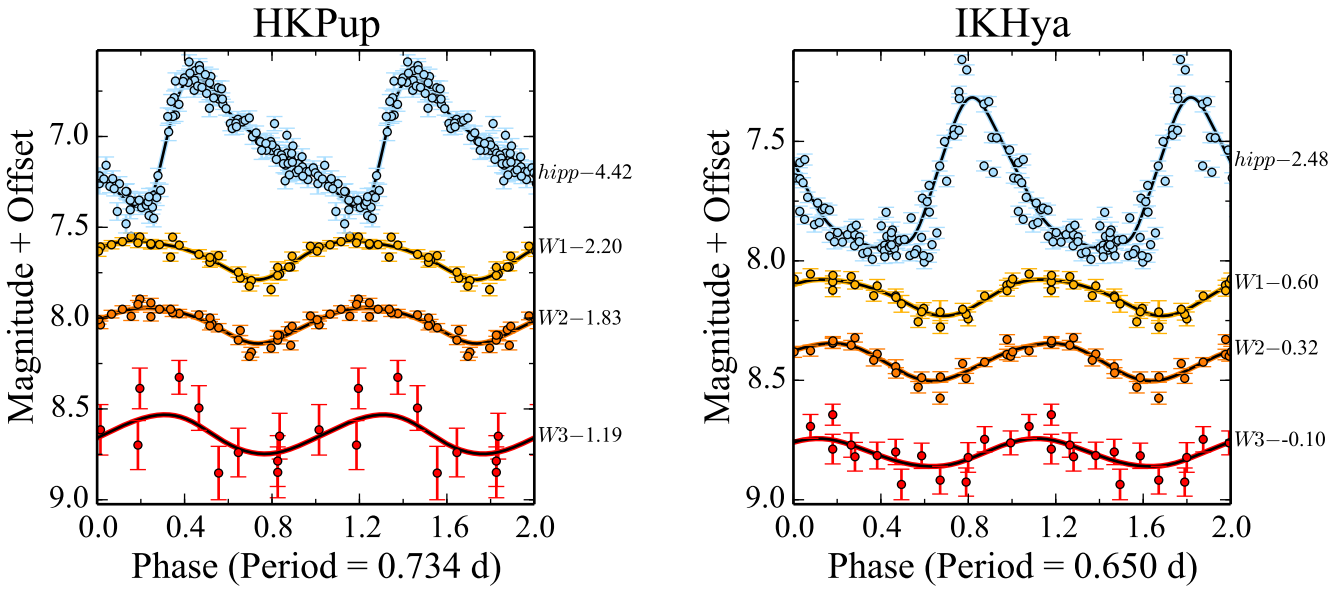

Figure B.19: Observed light curves for HKPup and IKHya.

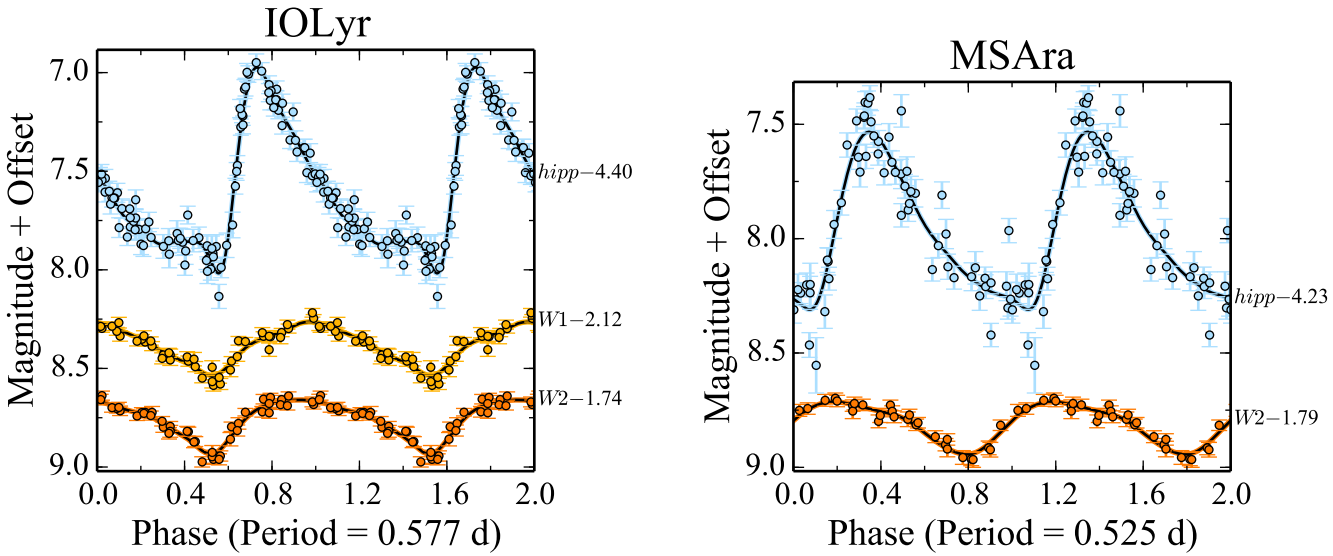

Figure B.20: Observed light curves for IOLyr and MSAra.

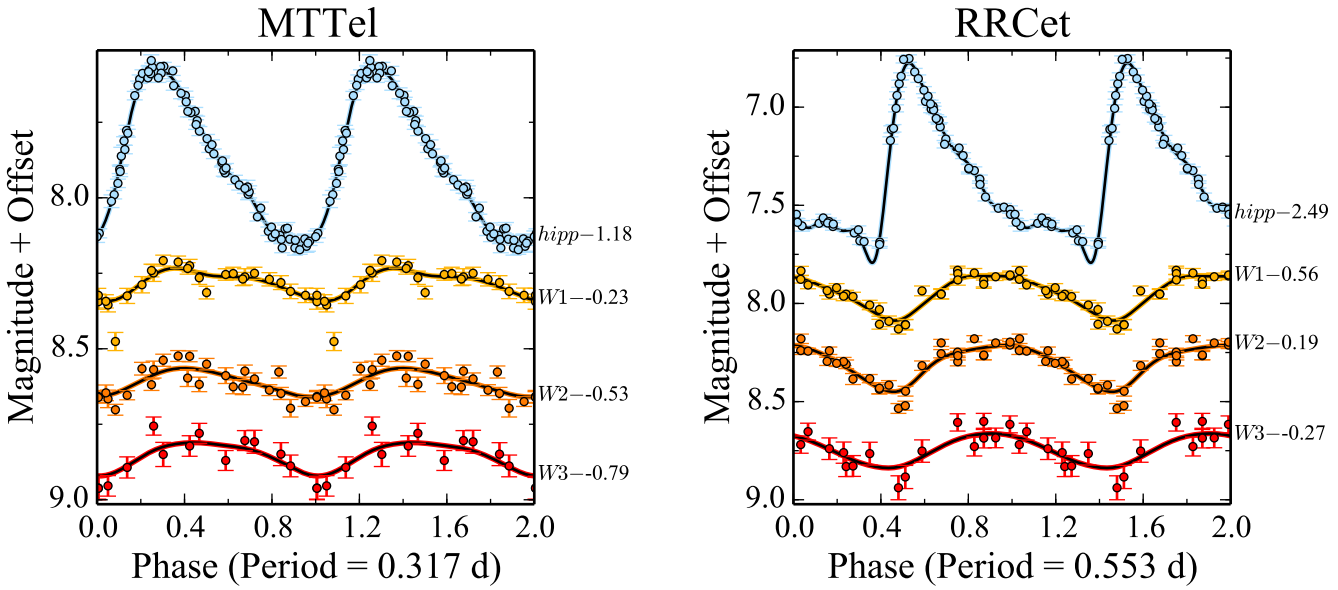

Figure B.21: Observed light curves for MTTel and RRCet.

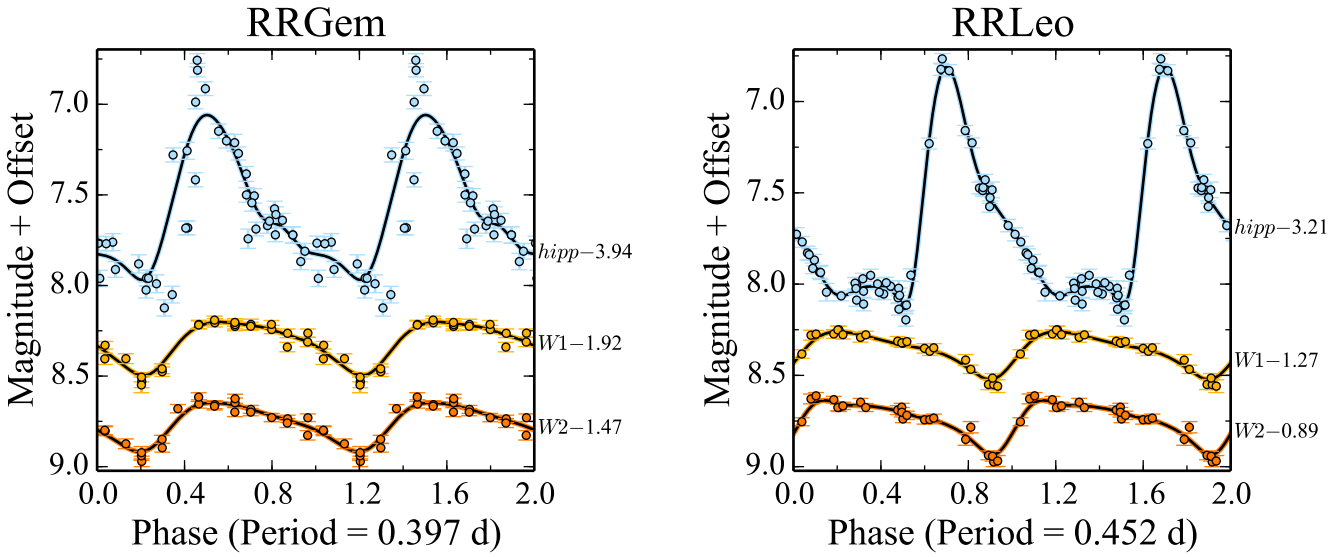

Figure B.22: Observed light curves for RRGem and RRLeo.

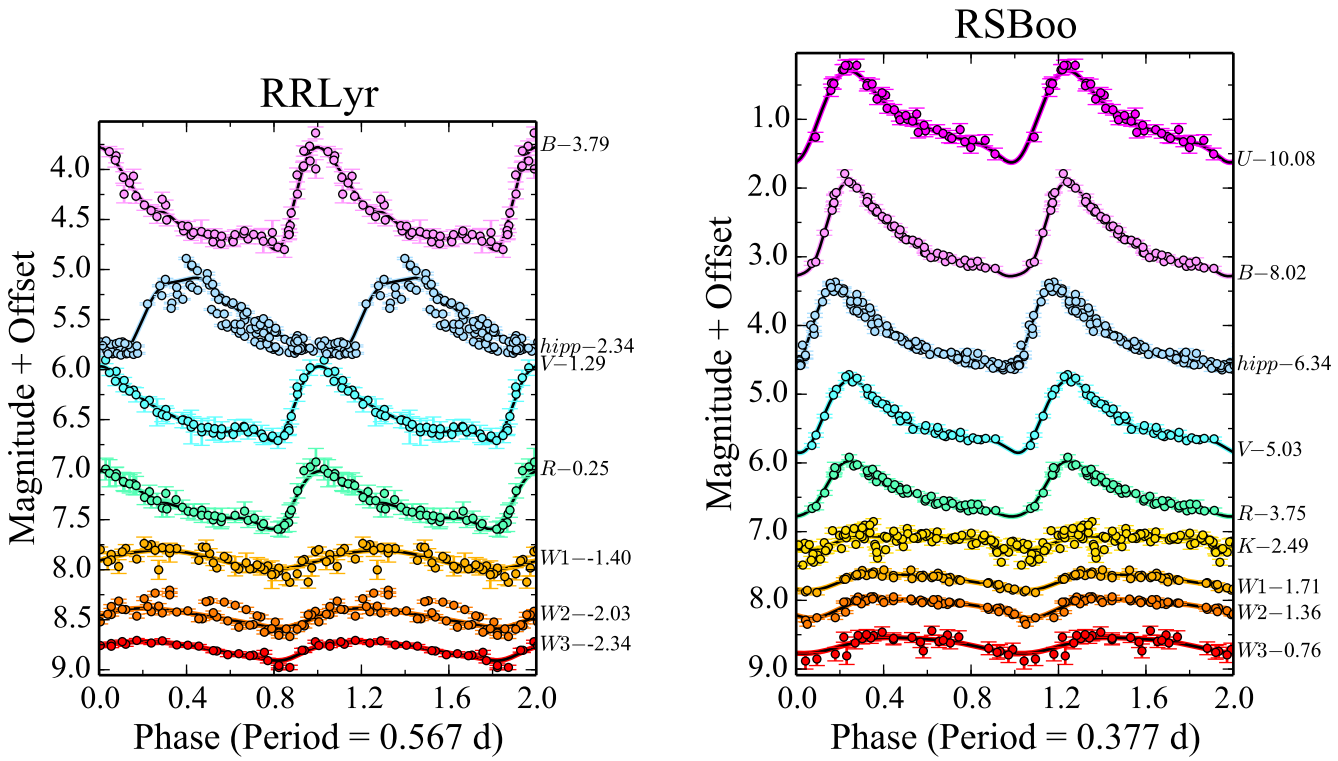

Figure B.23: Observed light curves for RRLyr and RSBoo.

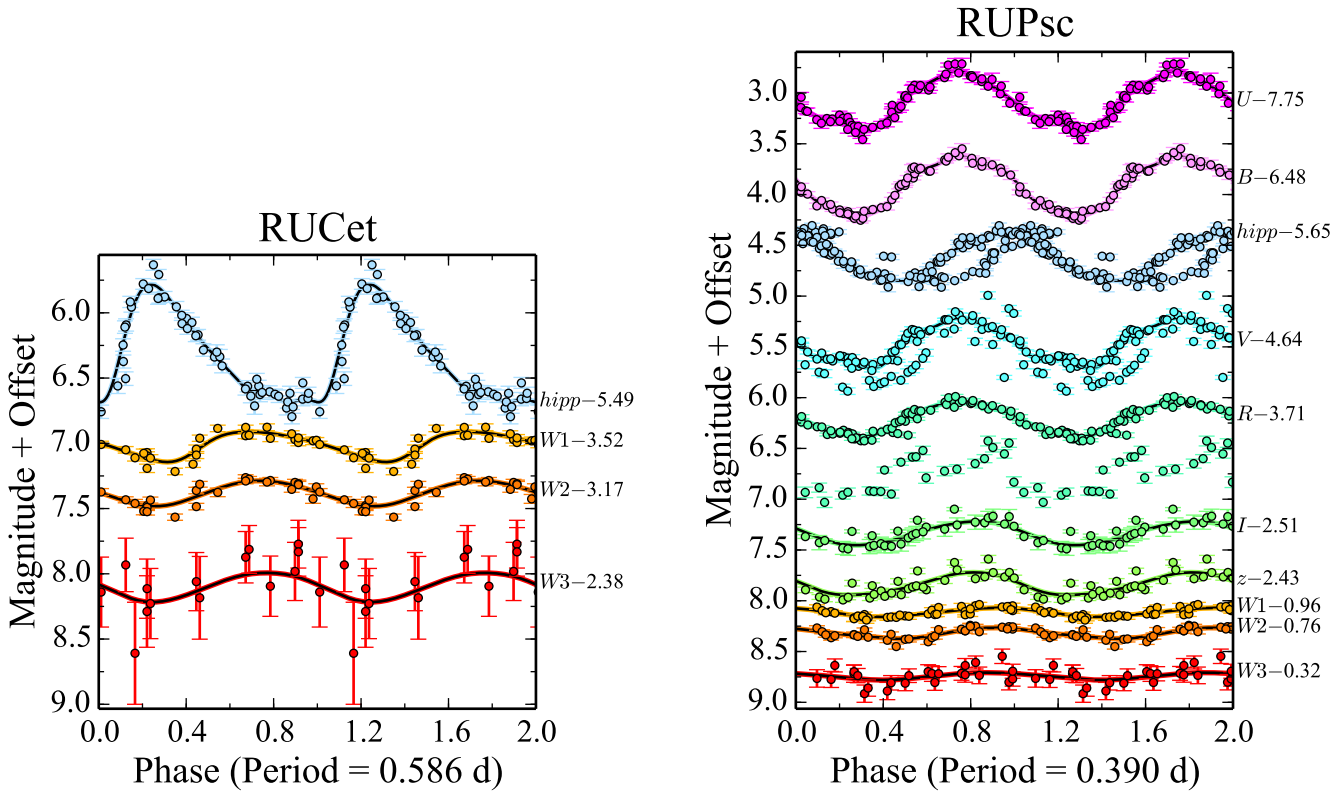

Figure B.24: Observed light curves for RUCet and RUPsc.

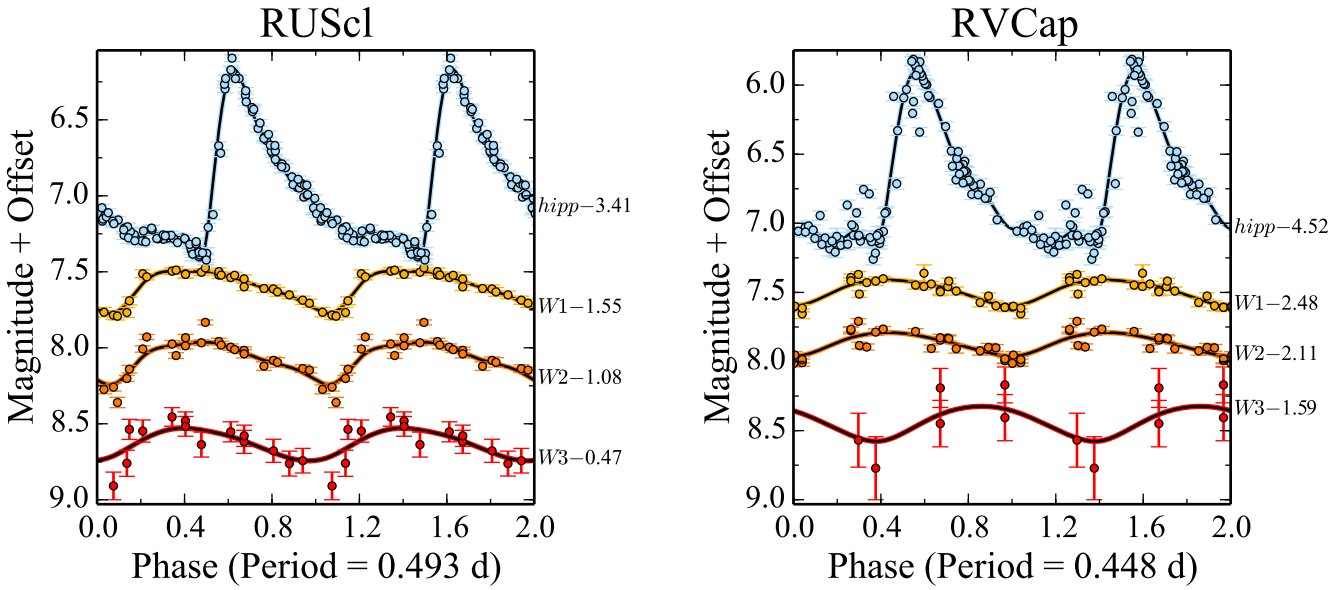

Figure B.25: Observed light curves for RUScl and RVCap.

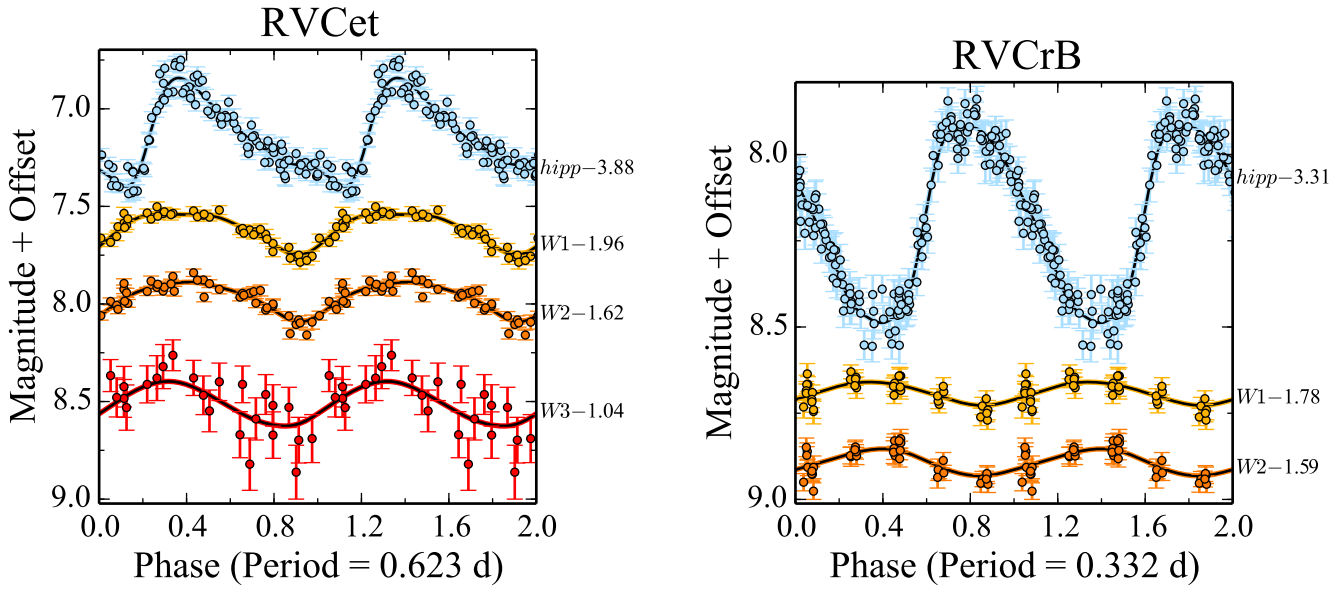

Figure B.26: Observed light curves for RVCet and RVCrB.

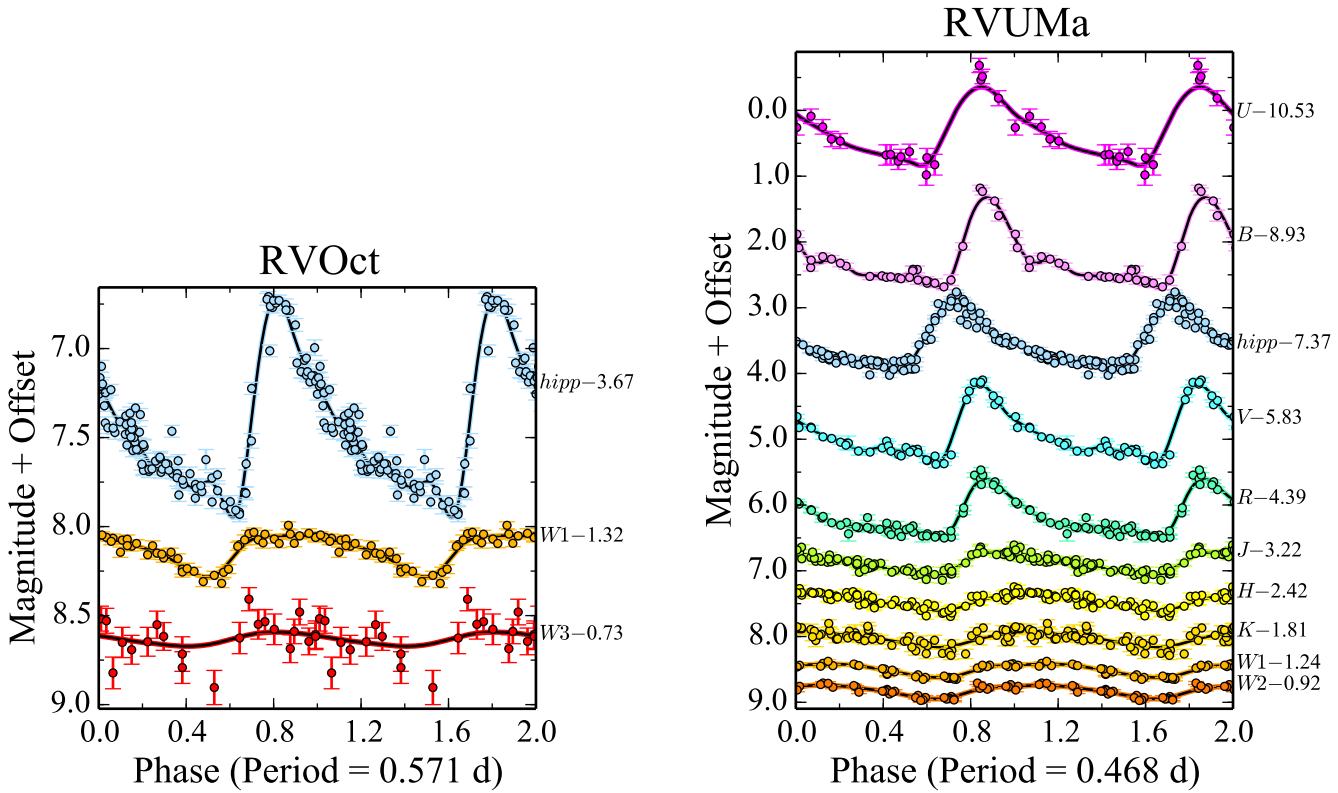

Figure B.27: Observed light curves for RVOct and RVUMa.

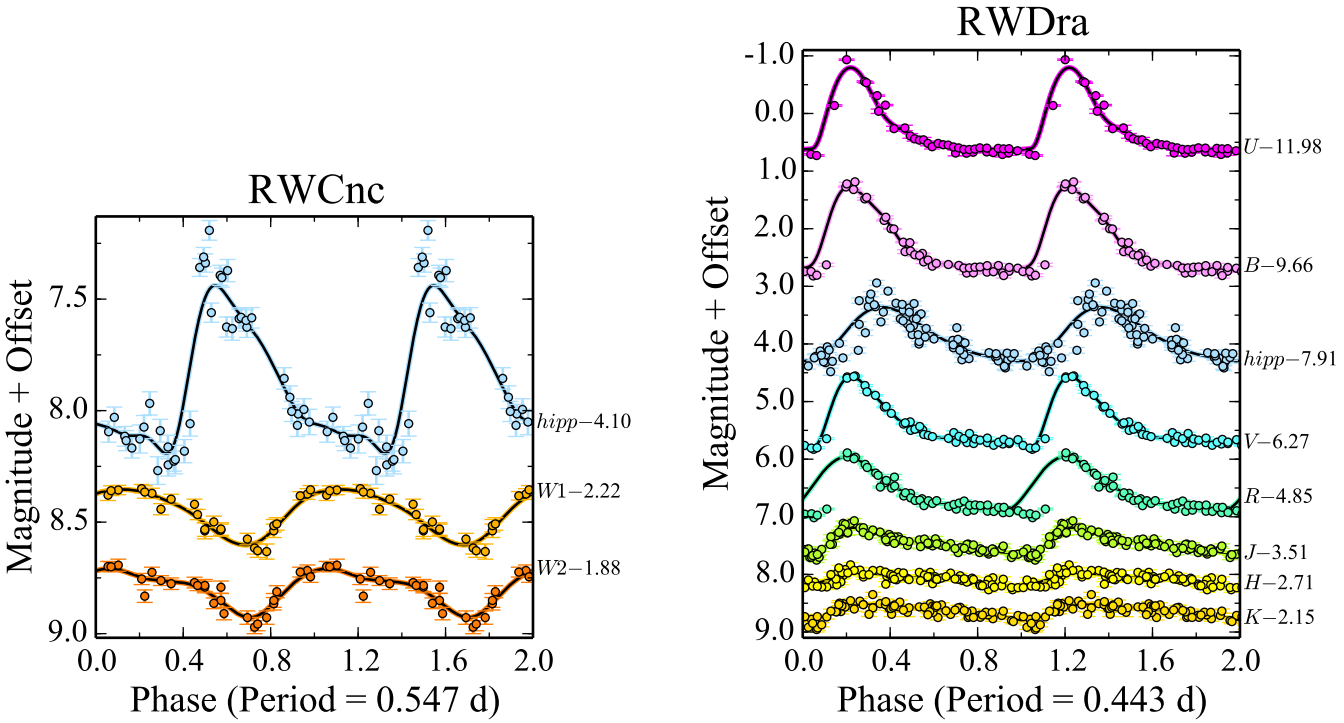

Figure B.28: Observed light curves for RWCnc and RWDra.

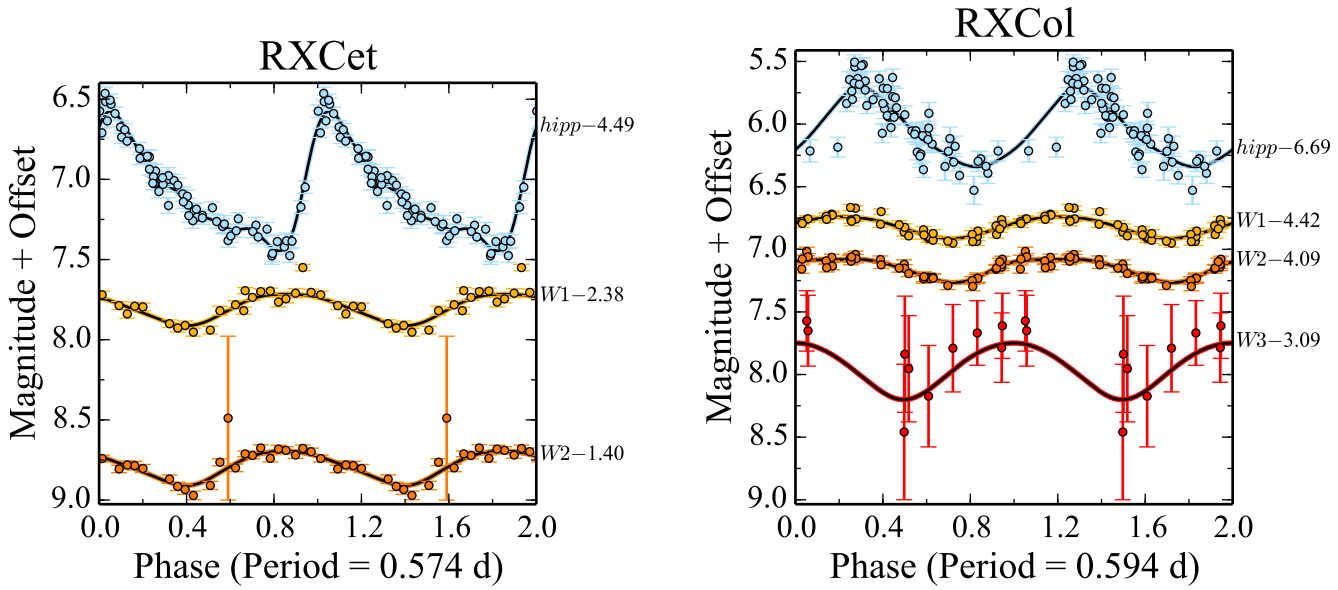

Figure B.29: Observed light curves for RXCet and RXCol.

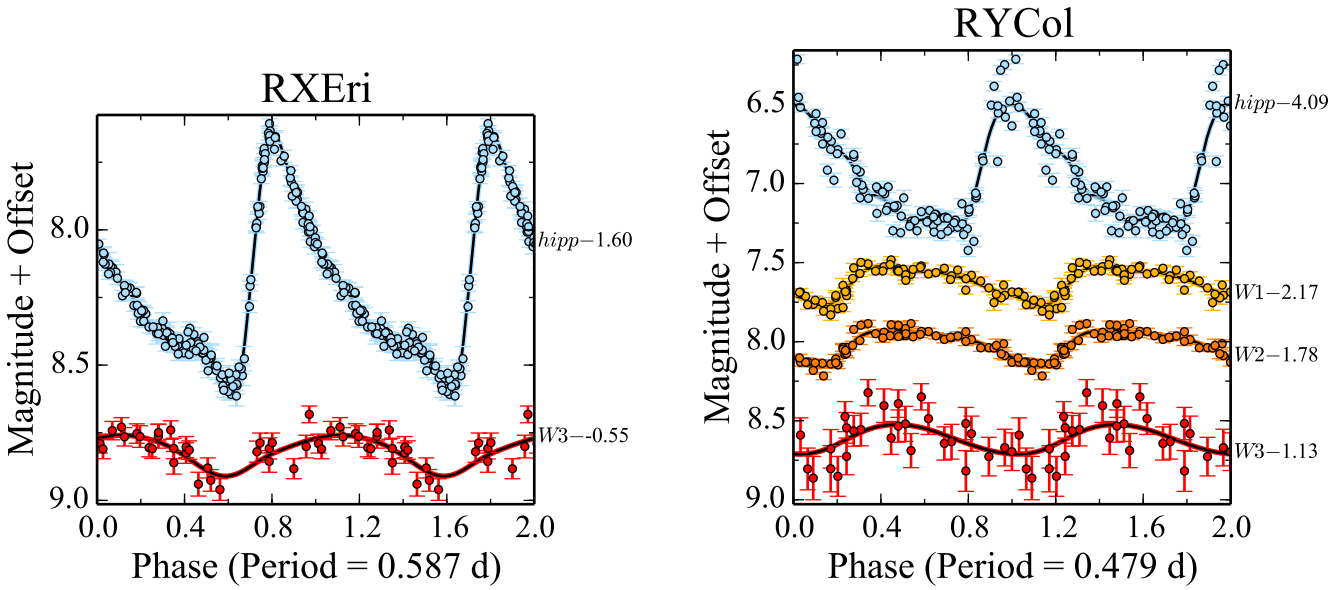

Figure B.30: Observed light curves for RXEri and RYCol.

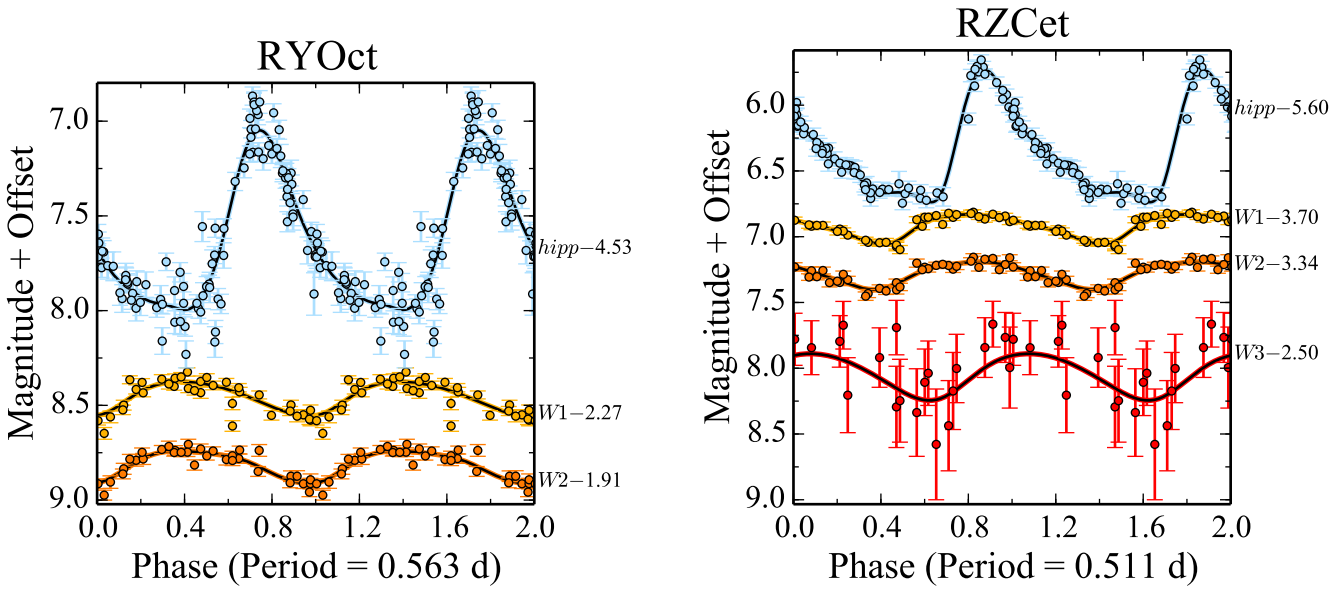

Figure B.31: Observed light curves for RYOct and RZCet.

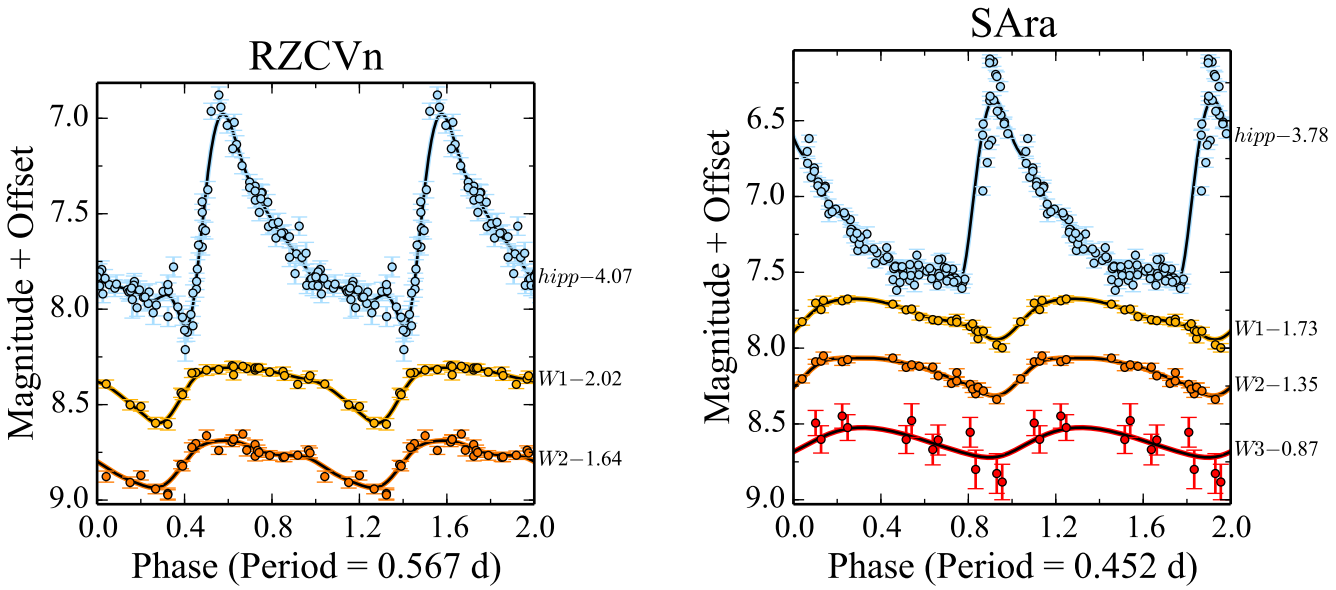

Figure B.32: Observed light curves for RZCVn and SAra.

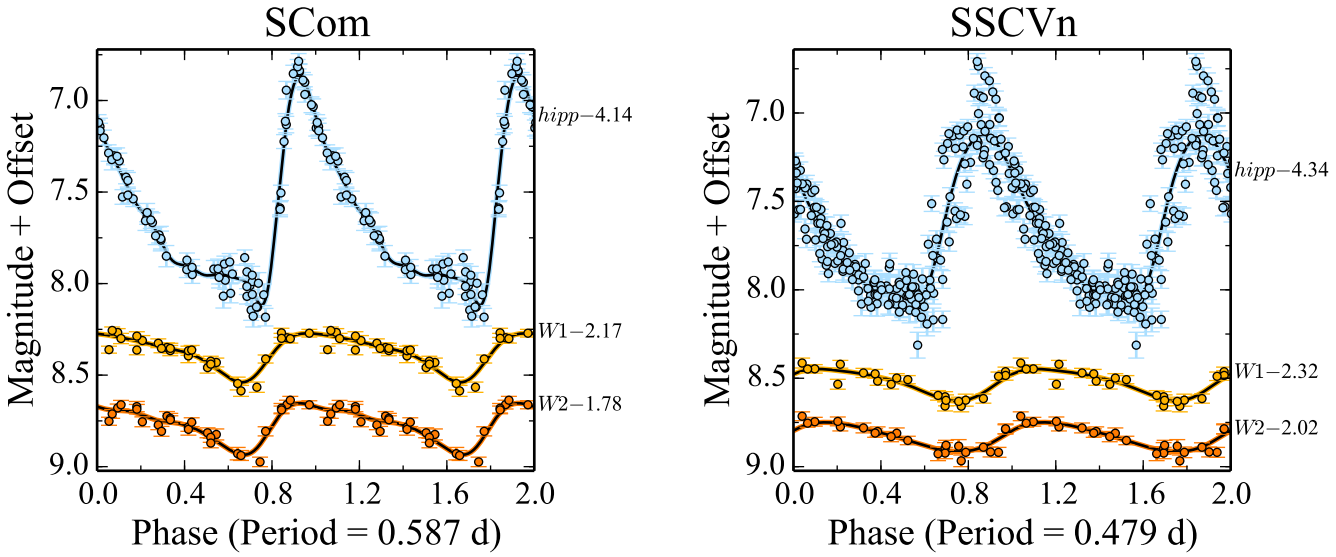

Figure B.33: Observed light curves for SCom and SSCVn.

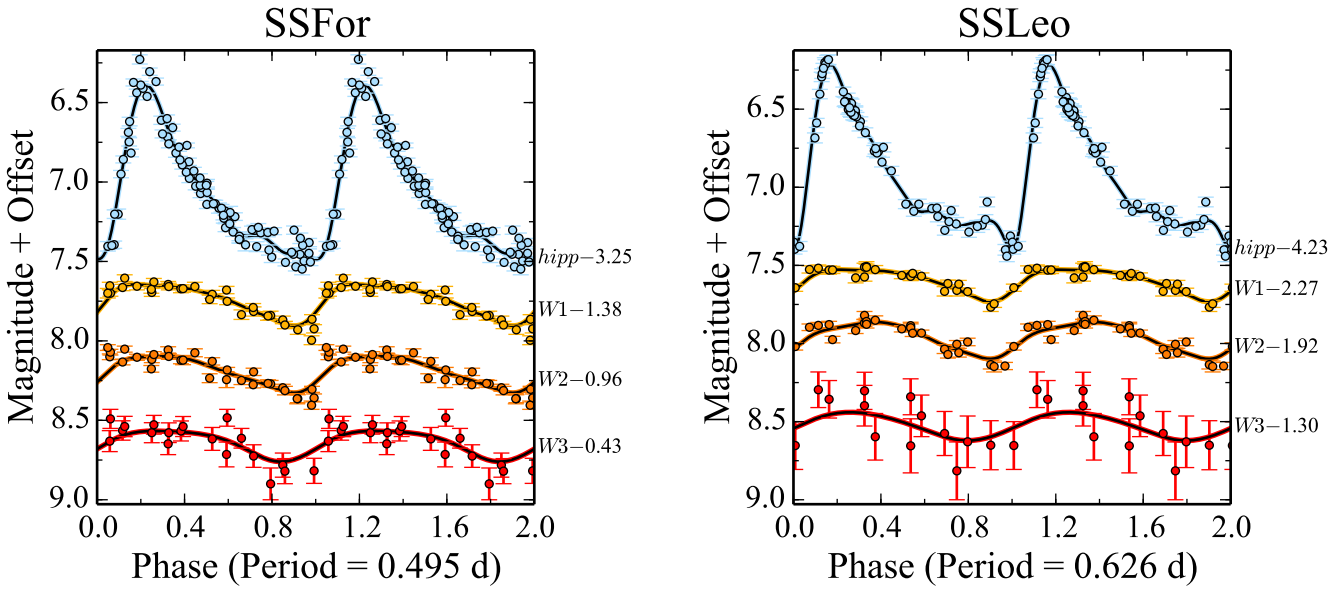

Figure B.34: Observed light curves for SSFor and SSLeo.

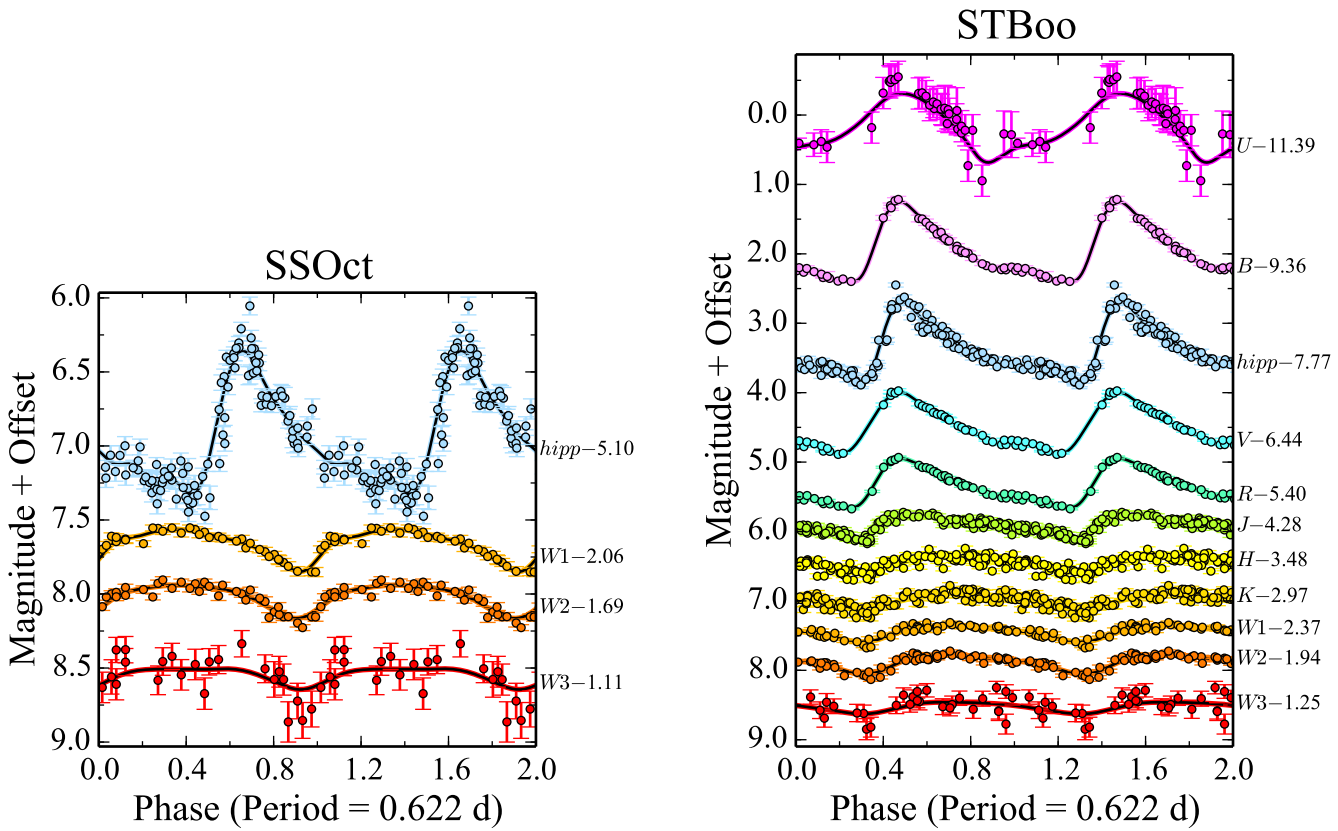

Figure B.35: Observed light curves for SSOct and STBoo.

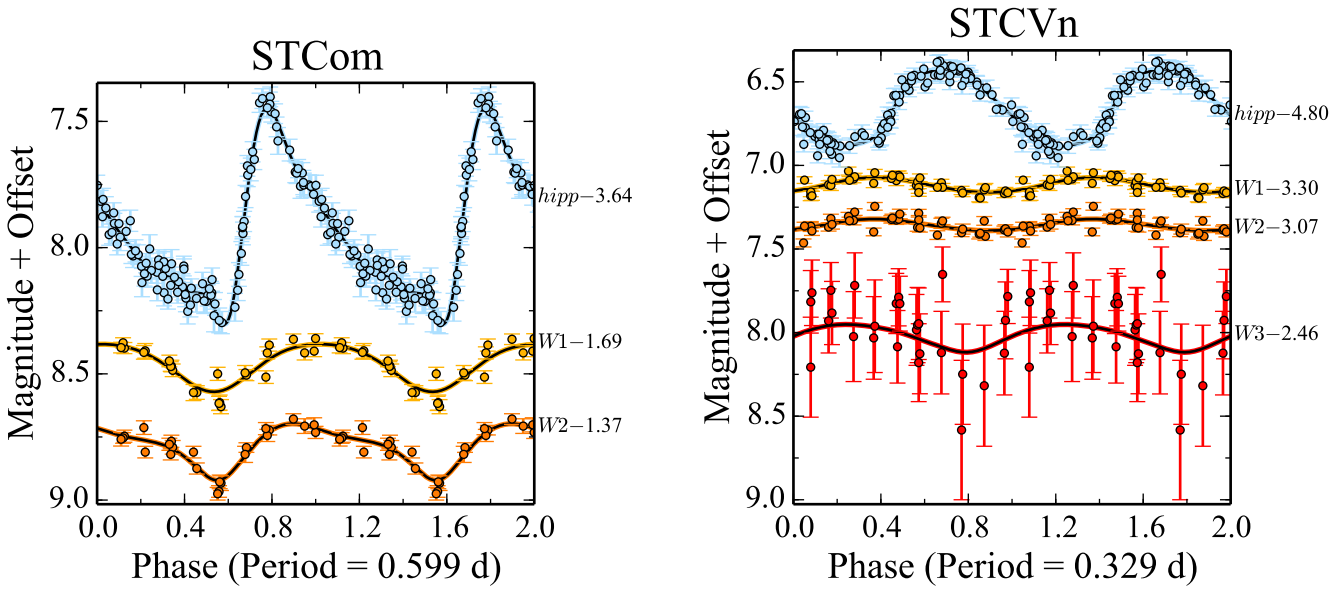

Figure B.36: Observed light curves for STCom and STCVn.

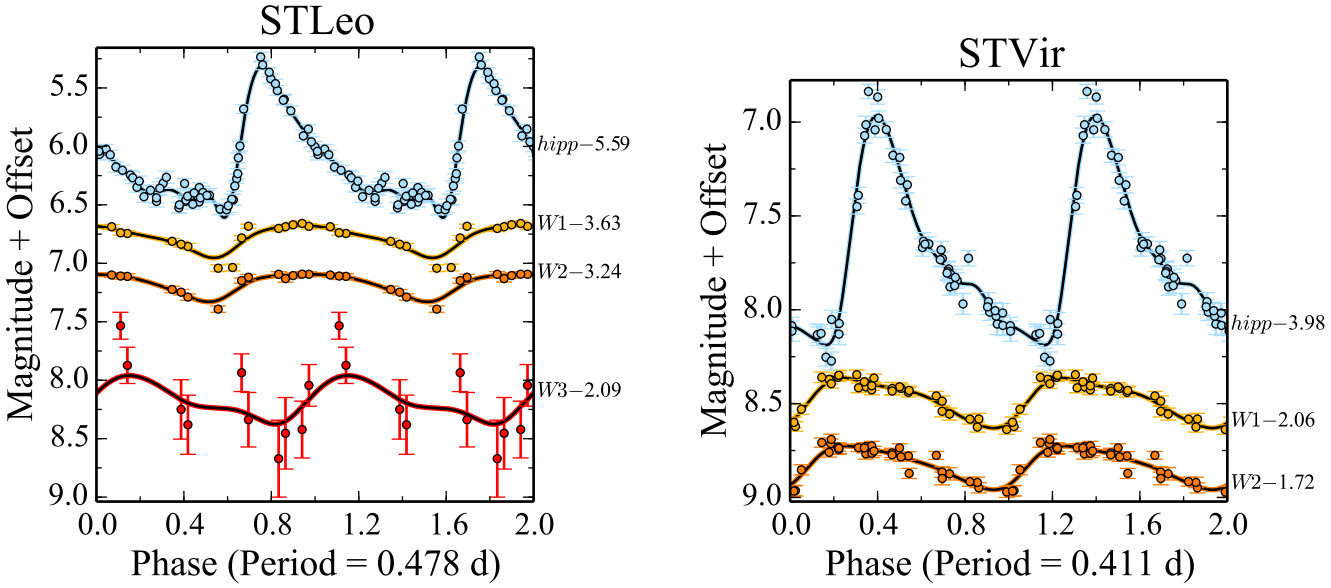

Figure B.37: Observed light curves for STLeo and STVir.

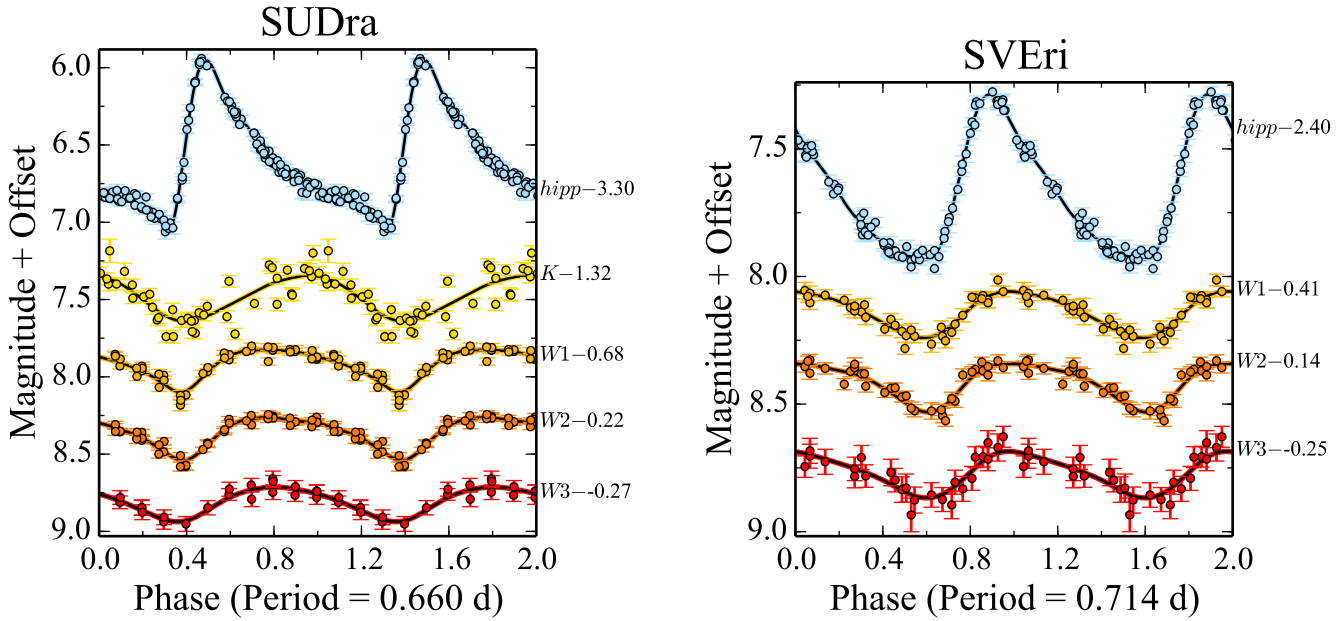

Figure B.38: Observed light curves for SUDra and SVEri.

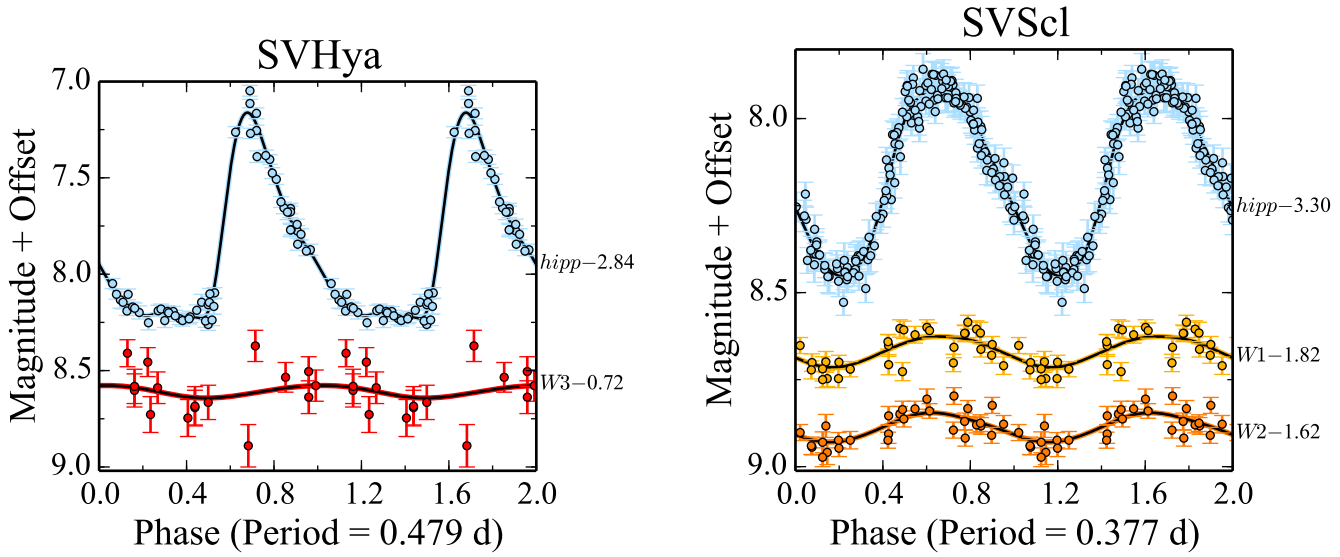

Figure B.39: Observed light curves for SVHya and SVScl.

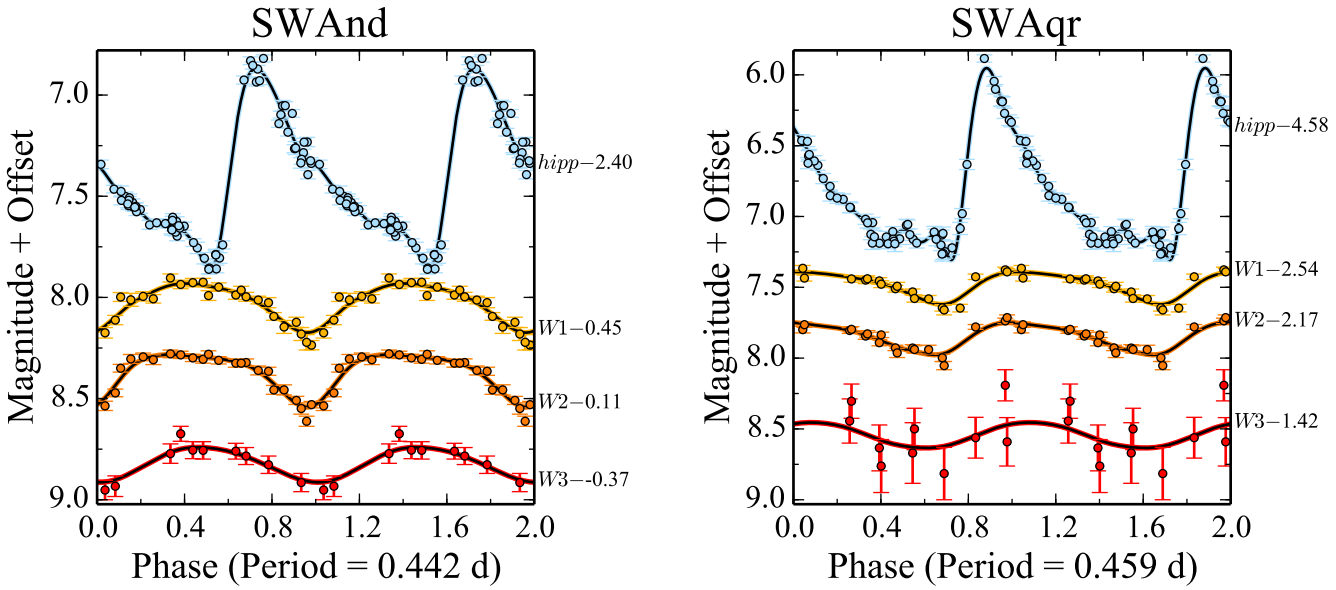

Figure B.40: Observed light curves for SWAnd and SWAqr.

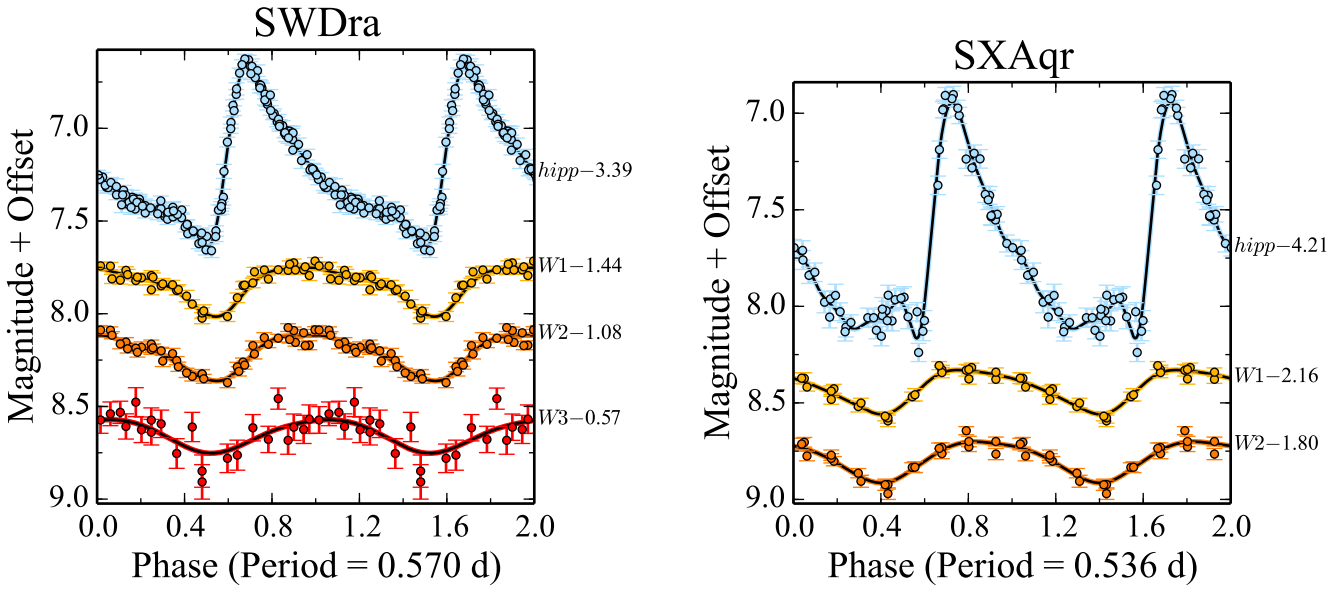

Figure B.41: Observed light curves for SWDra and SXAqr.

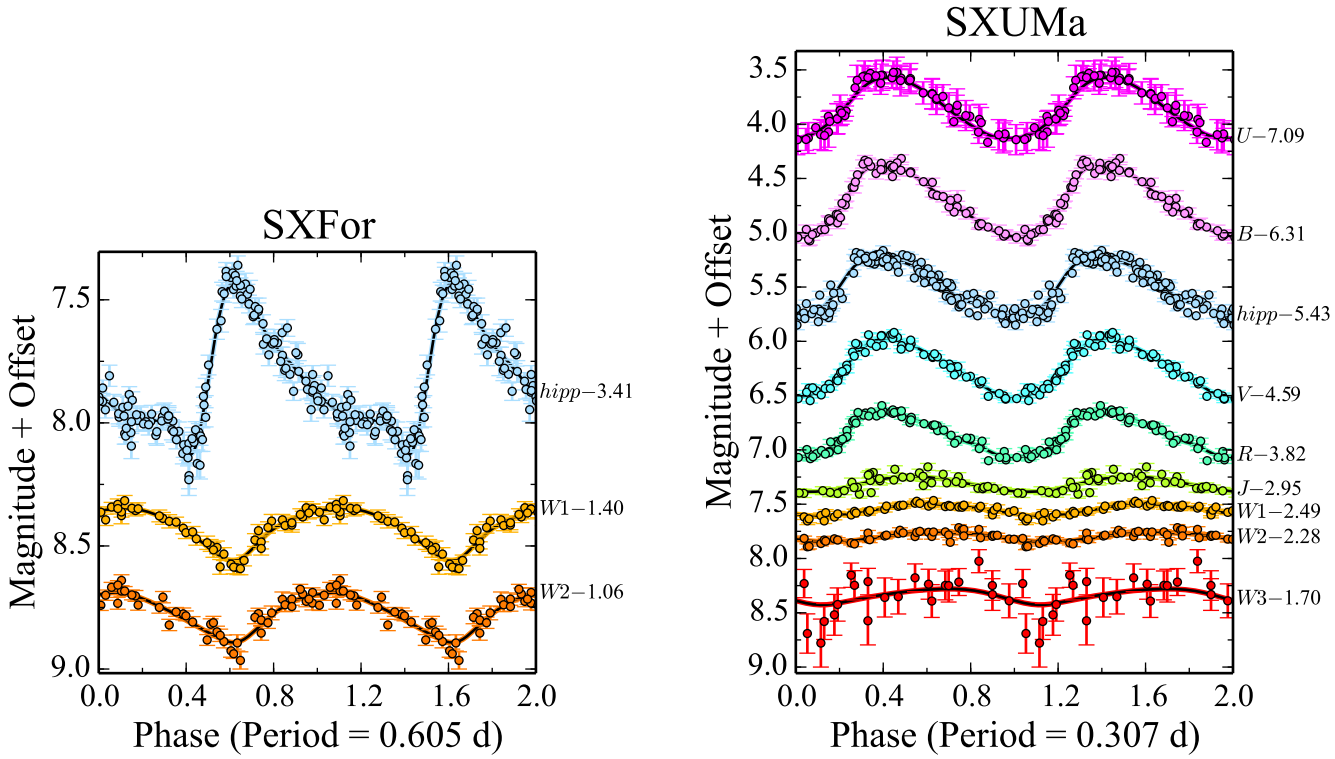

Figure B.42: Observed light curves for SXFor and SXUMa.

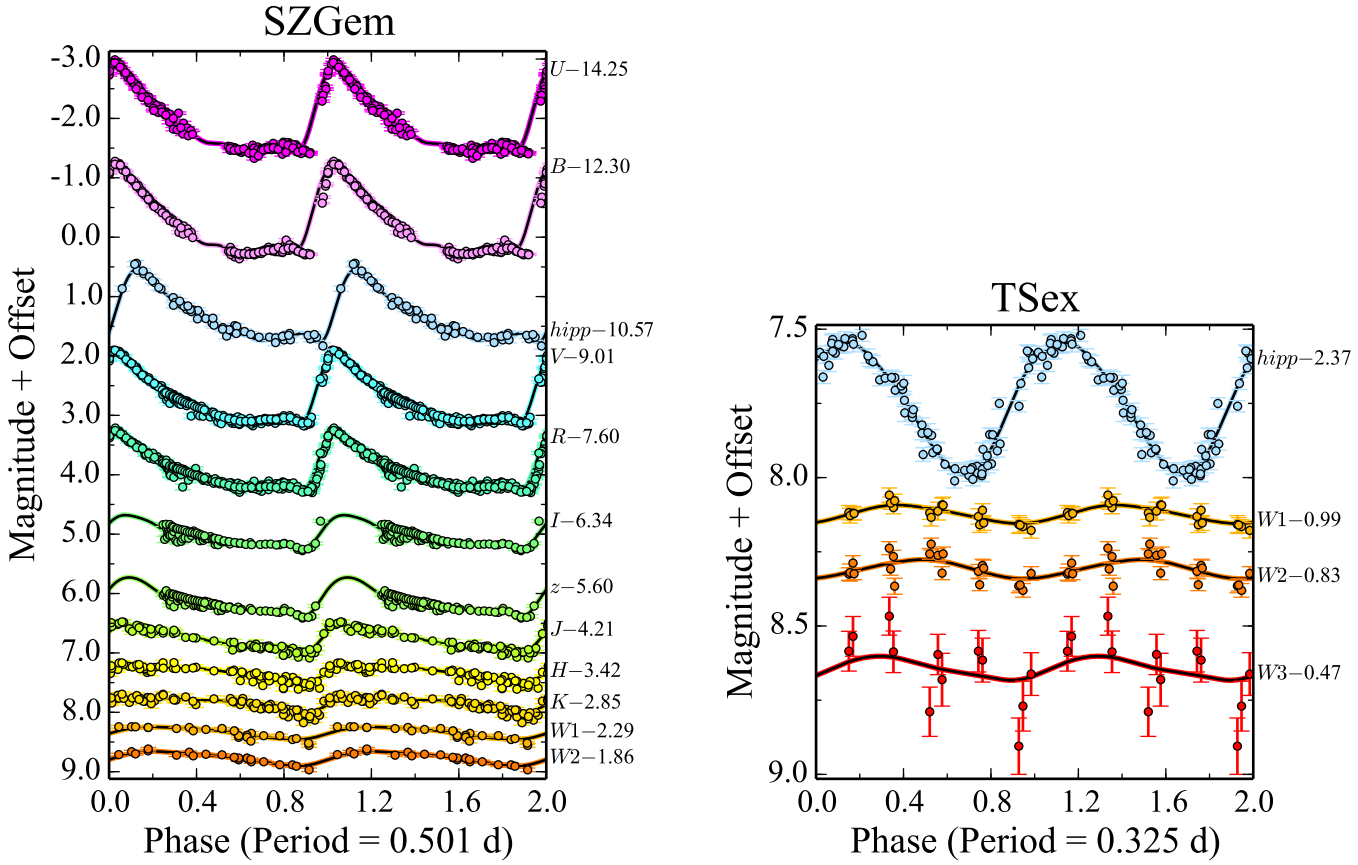

Figure B.43: Observed light curves for SZGem and TSex.

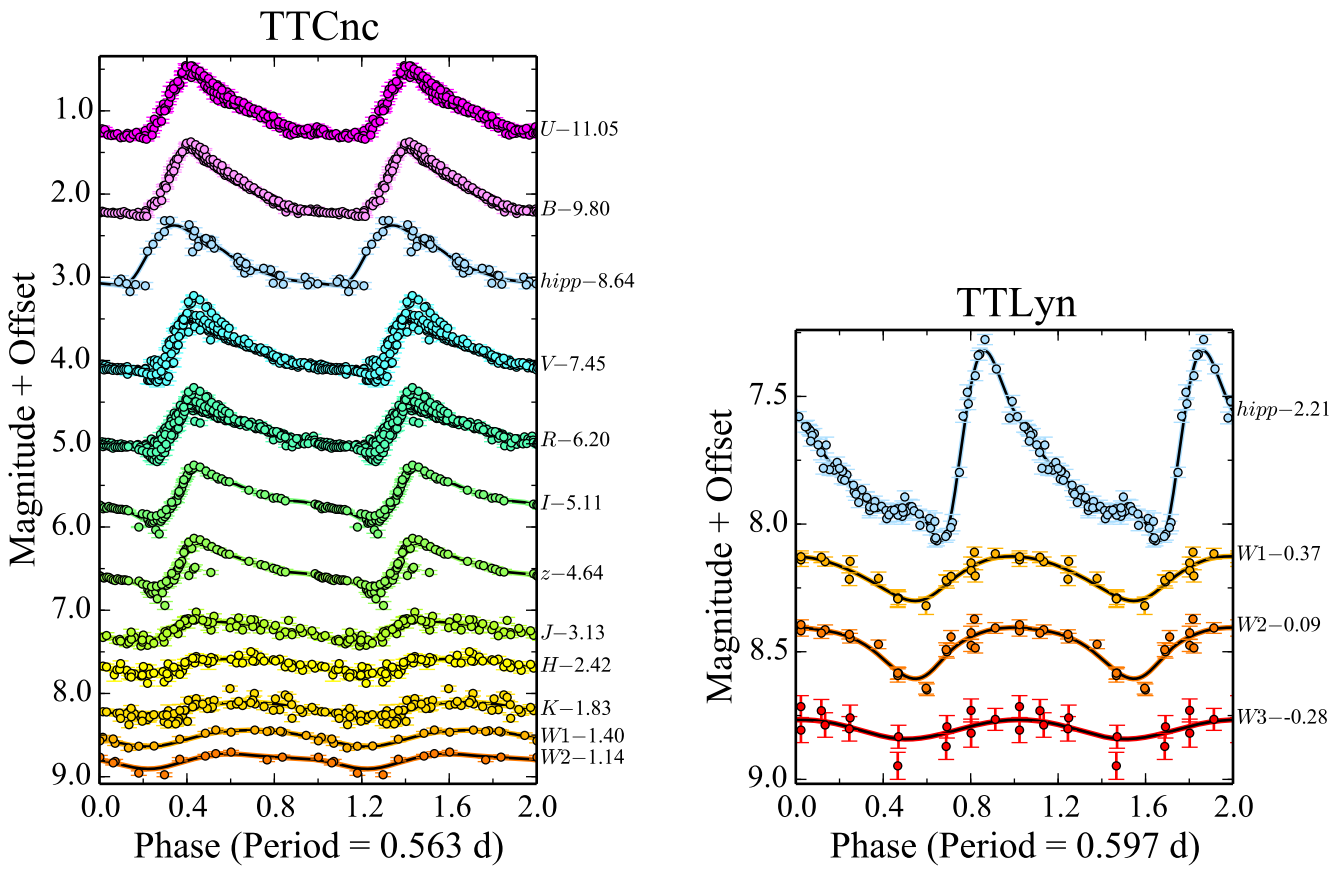

Figure B.44: Observed light curves for TTCnc and TTLyn.

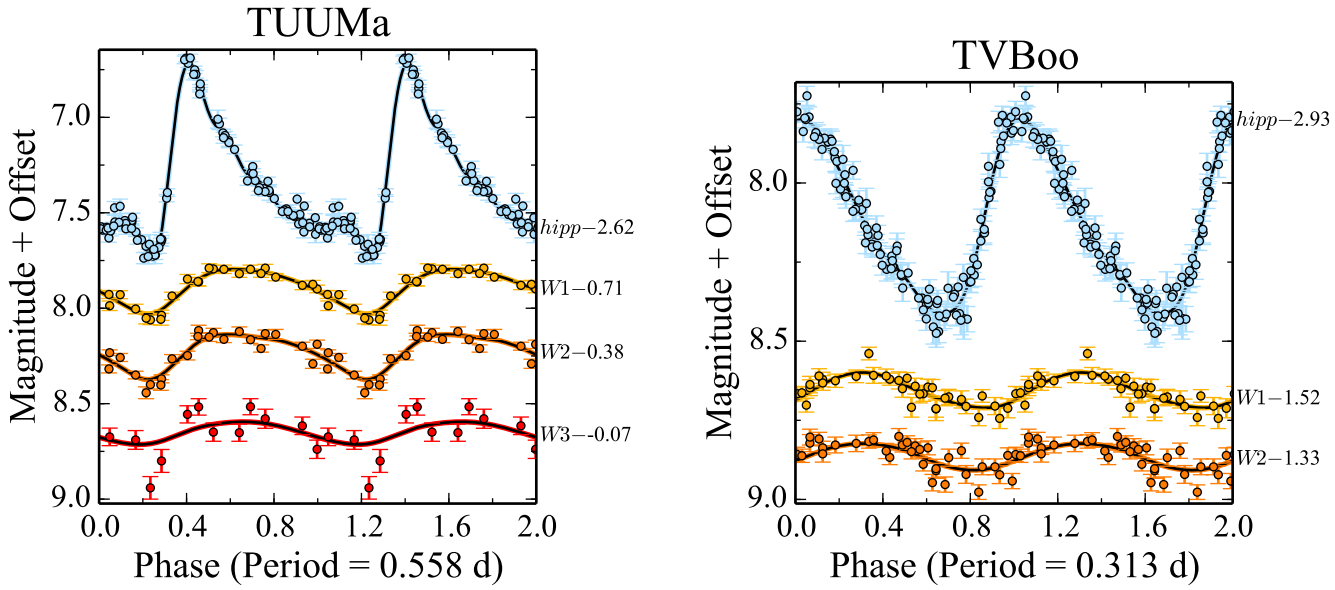

Figure B.45: Observed light curves for TUUMa and TVBoo.

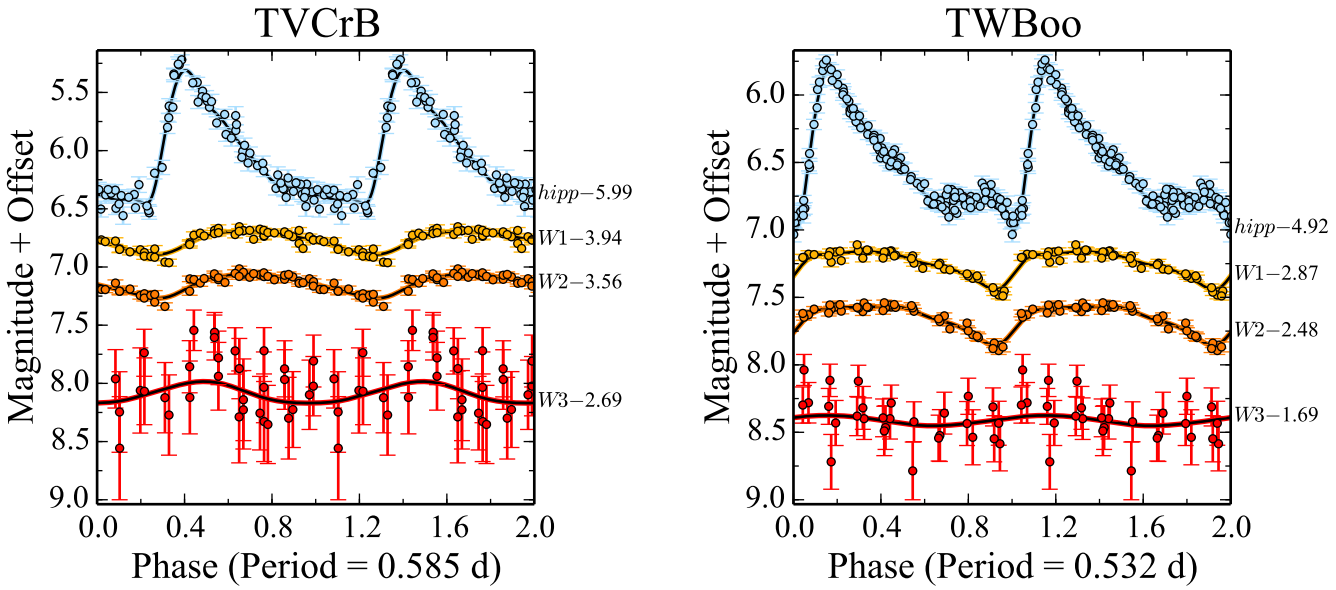

Figure B.46: Observed light curves for TVCrB and TWBoo.

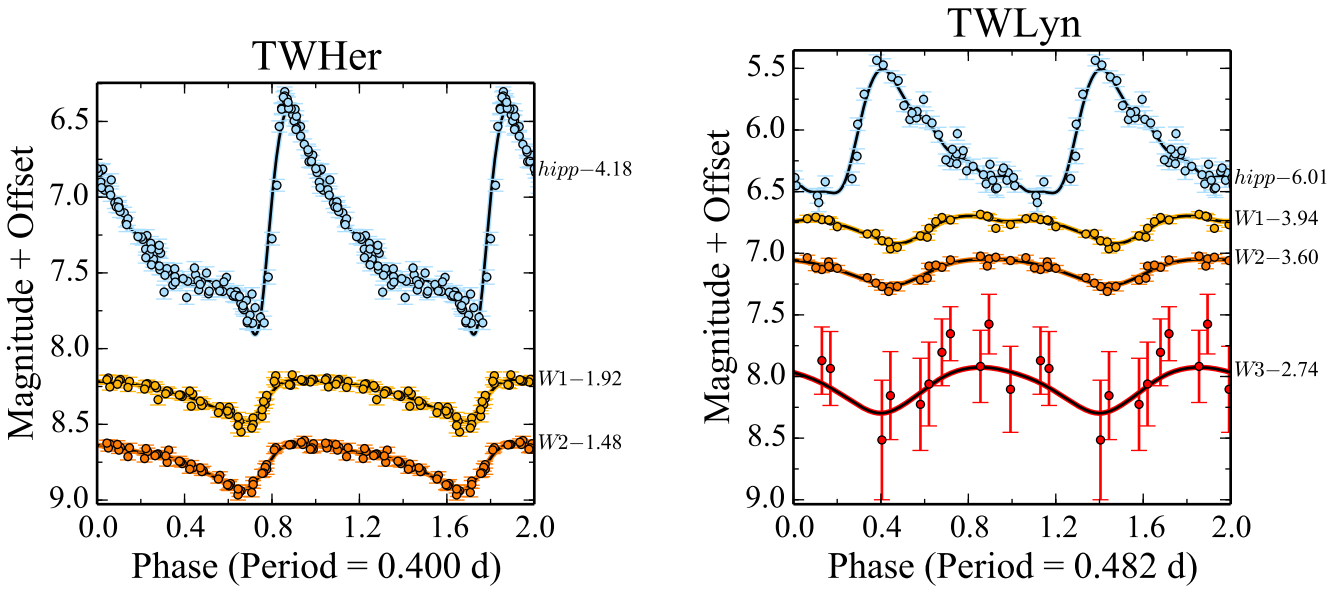

Figure B.47: Observed light curves for TWHer and TWLyn.

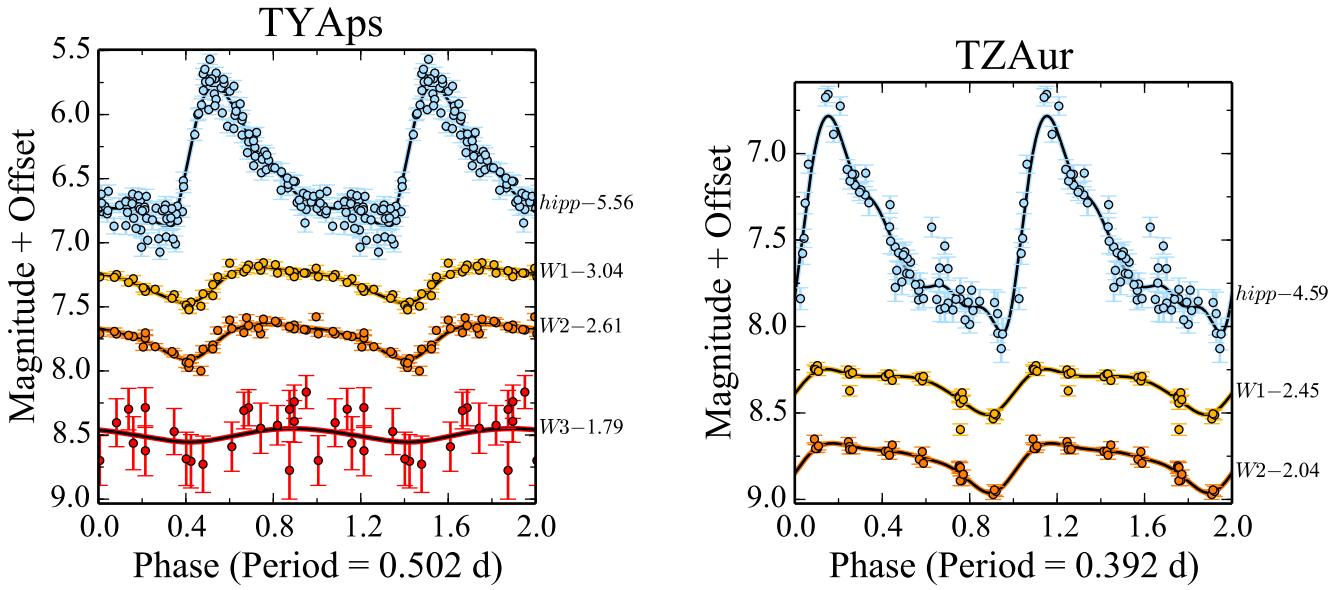

Figure B.48: Observed light curves for TYAps and TZAur.

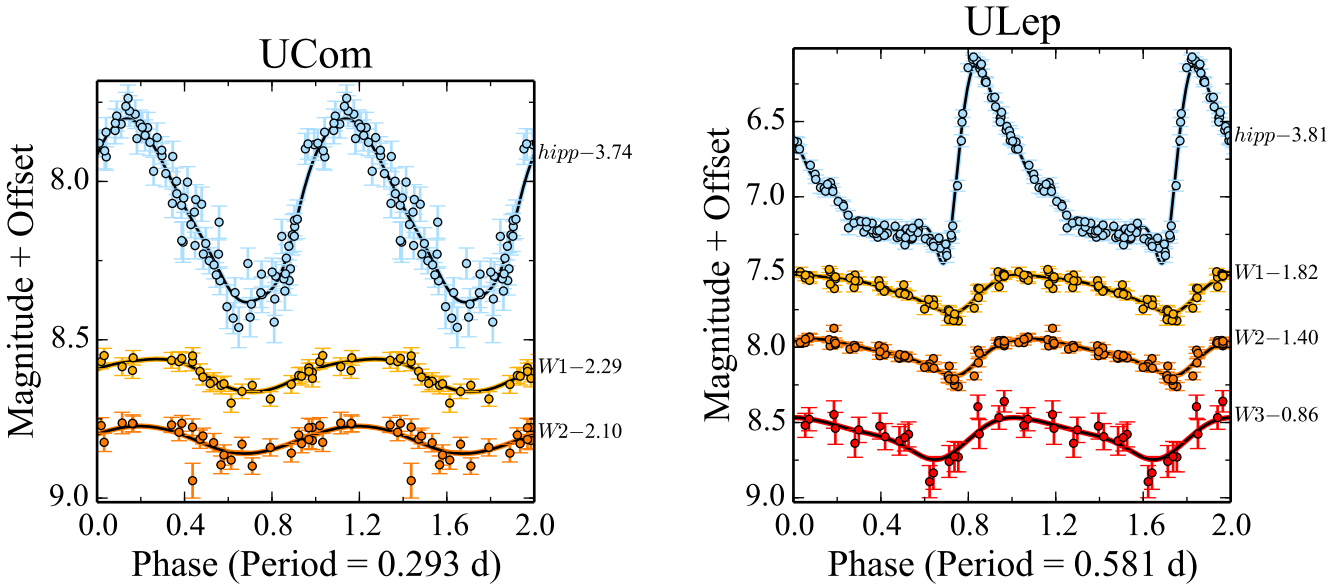

Figure B.49: Observed light curves for UCom and ULep.

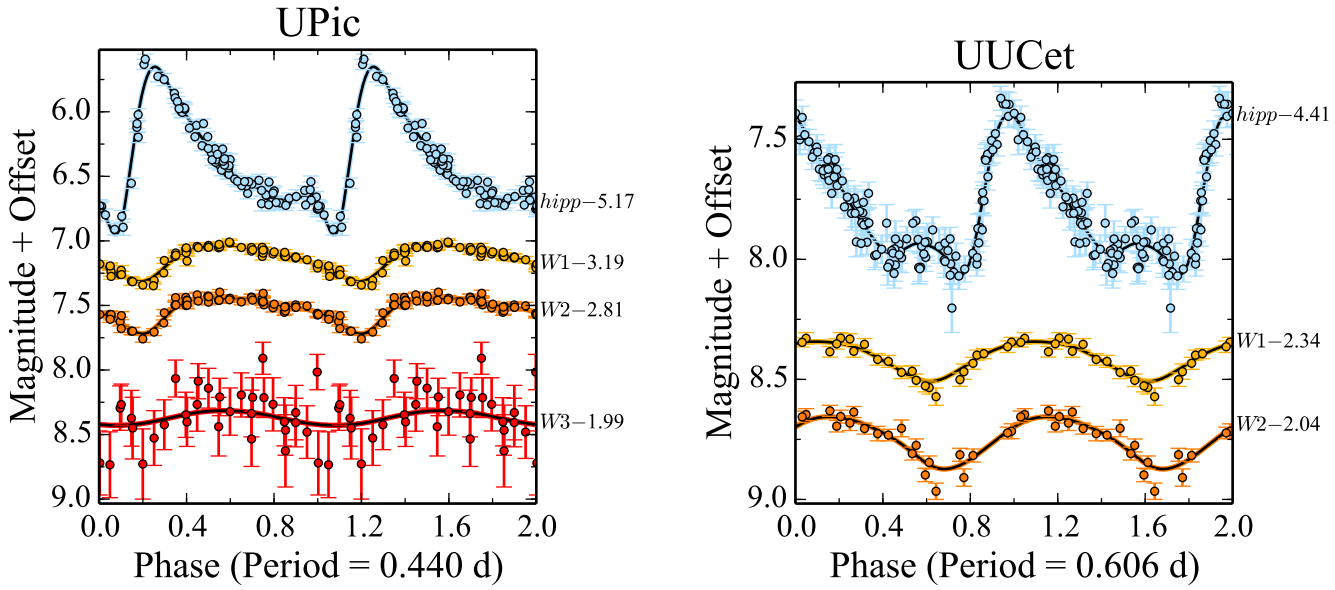

Figure B.50: Observed light curves for UPic and UUCet.

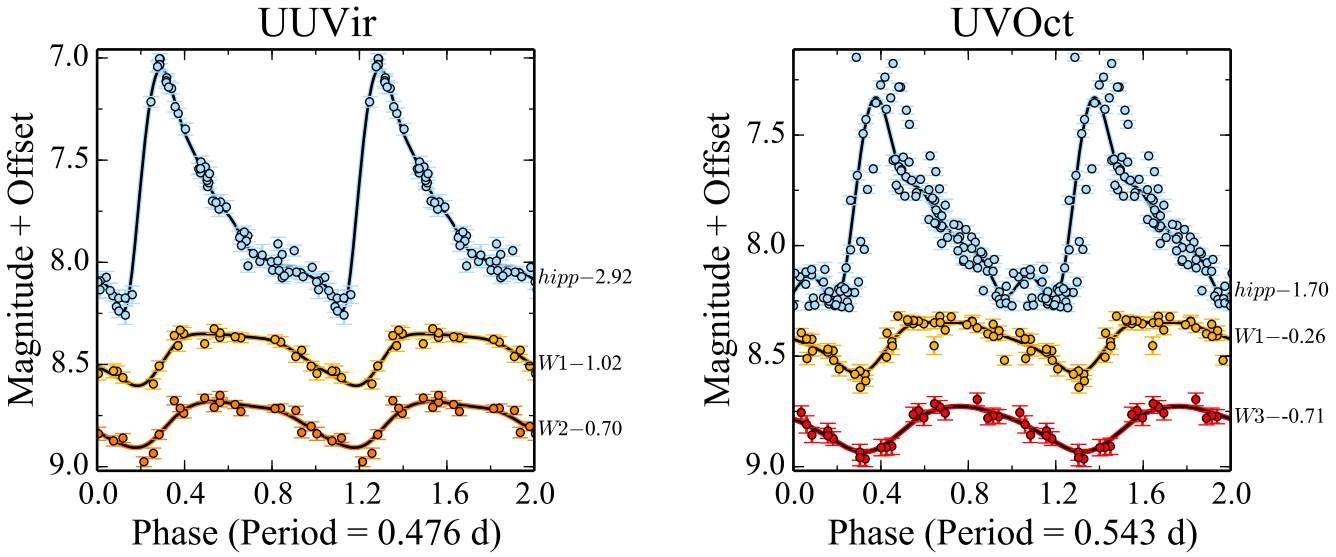

Figure B.51: Observed light curves for UUVir and UVOct.

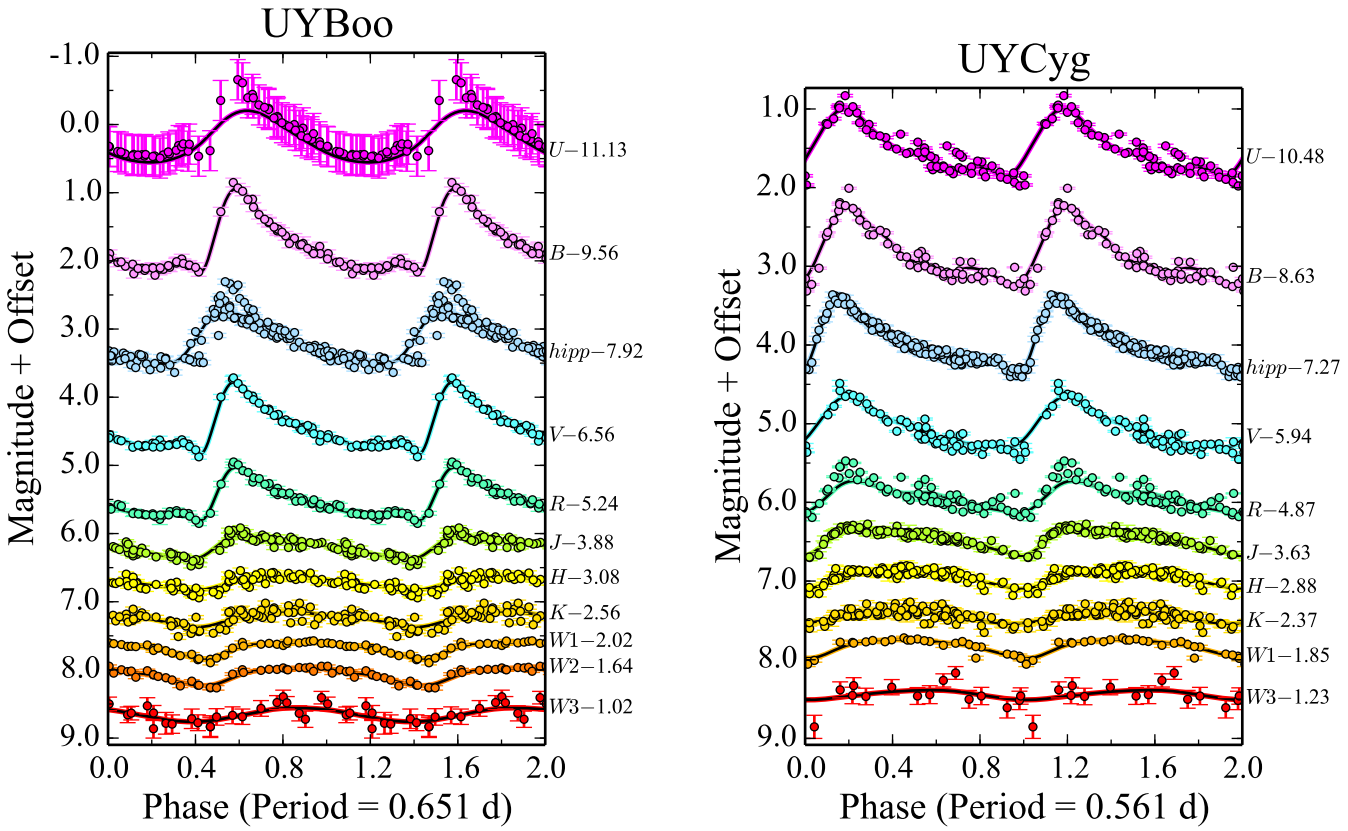

Figure B.52: Observed light curves for UYBoo and UYCyg.

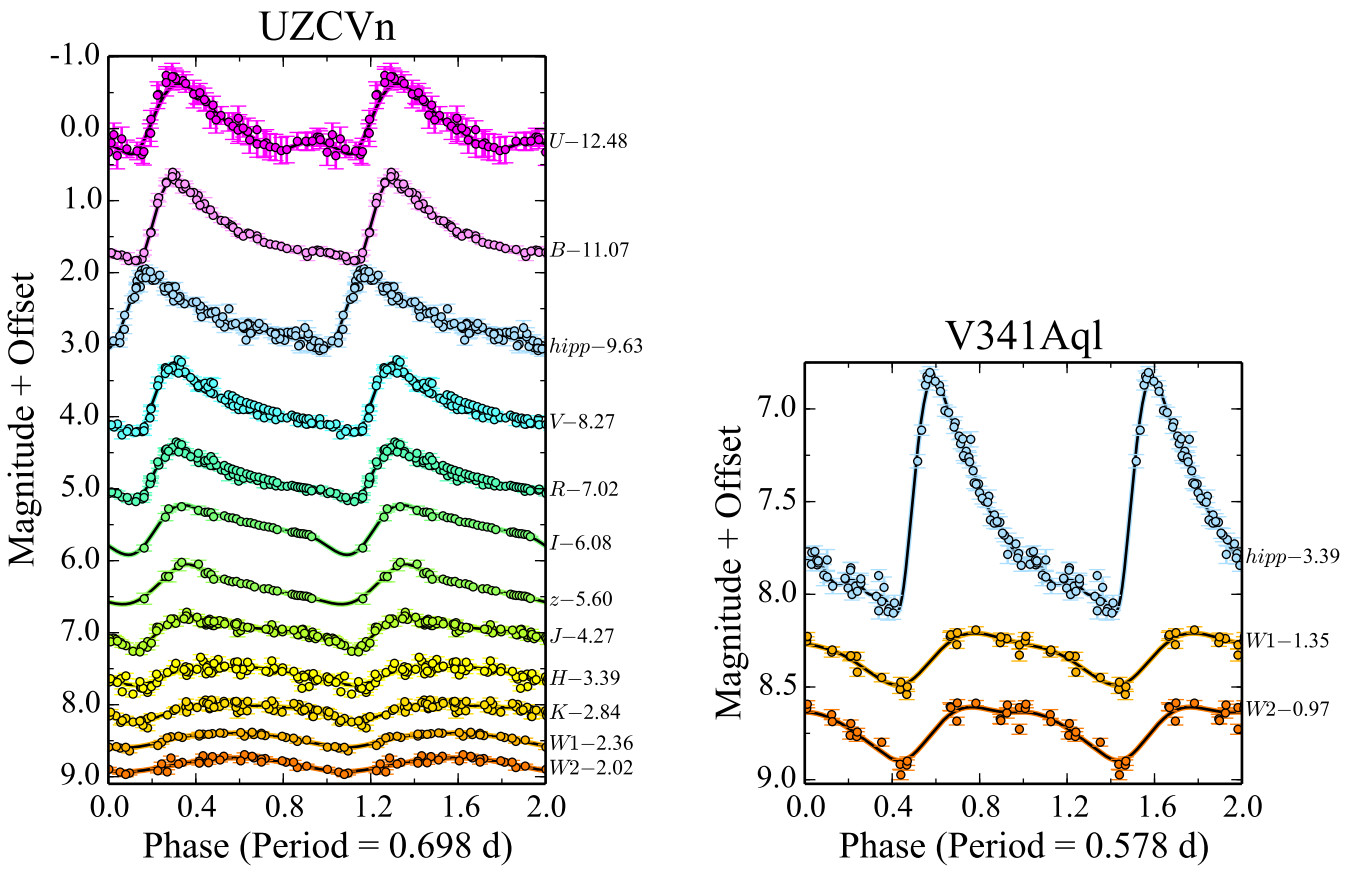

Figure B.53: Observed light curves for UZCVn and V341Aql.

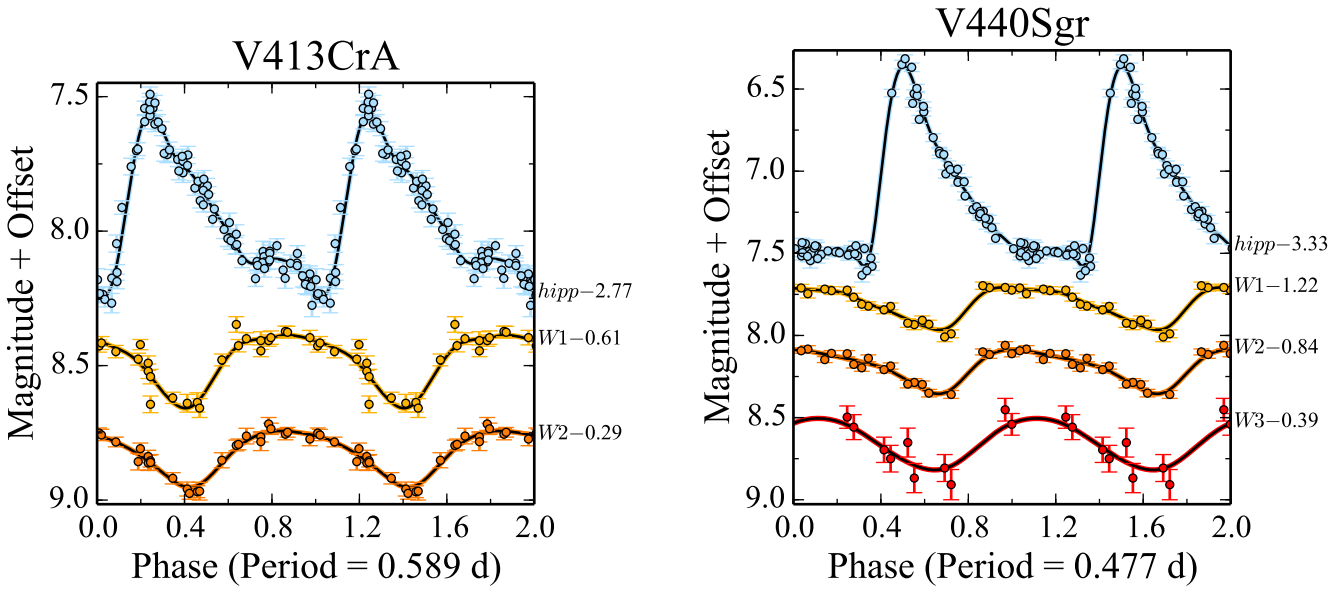

Figure B.54: Observed light curves for V413CrA and V440Sgr.

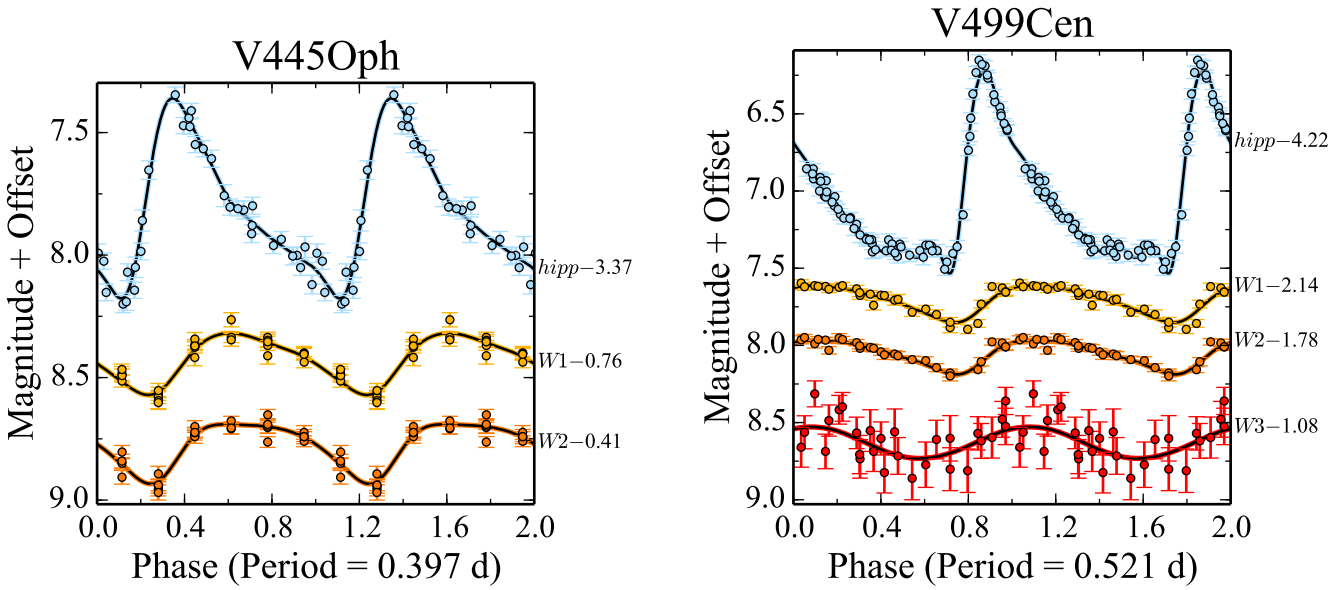

Figure B.55: Observed light curves for V445Oph and V499Cen.

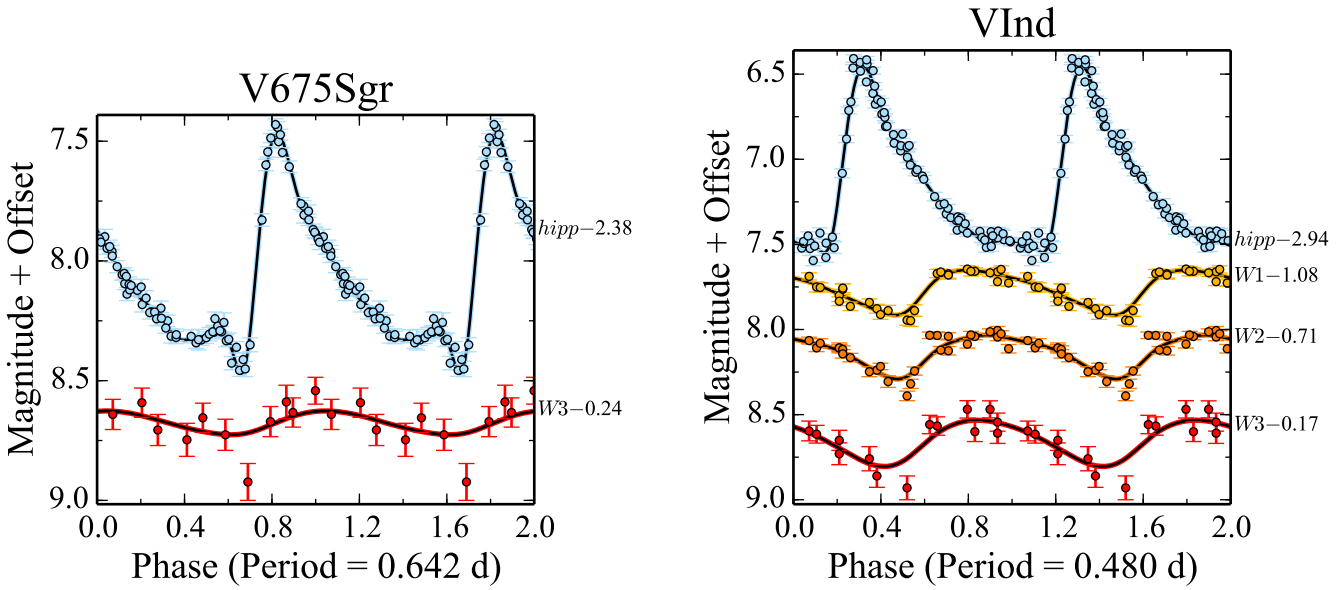

Figure B.56: Observed light curves for V675Sgr and VInd.

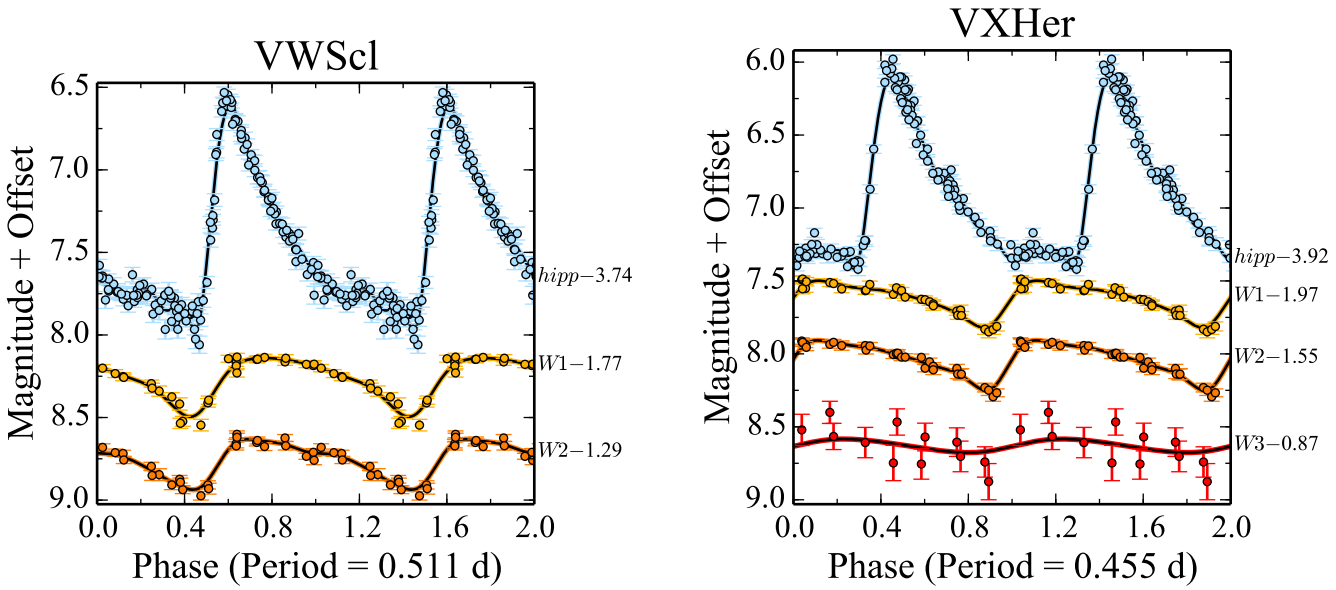

Figure B.57: Observed light curves for VWScl and VXHer.

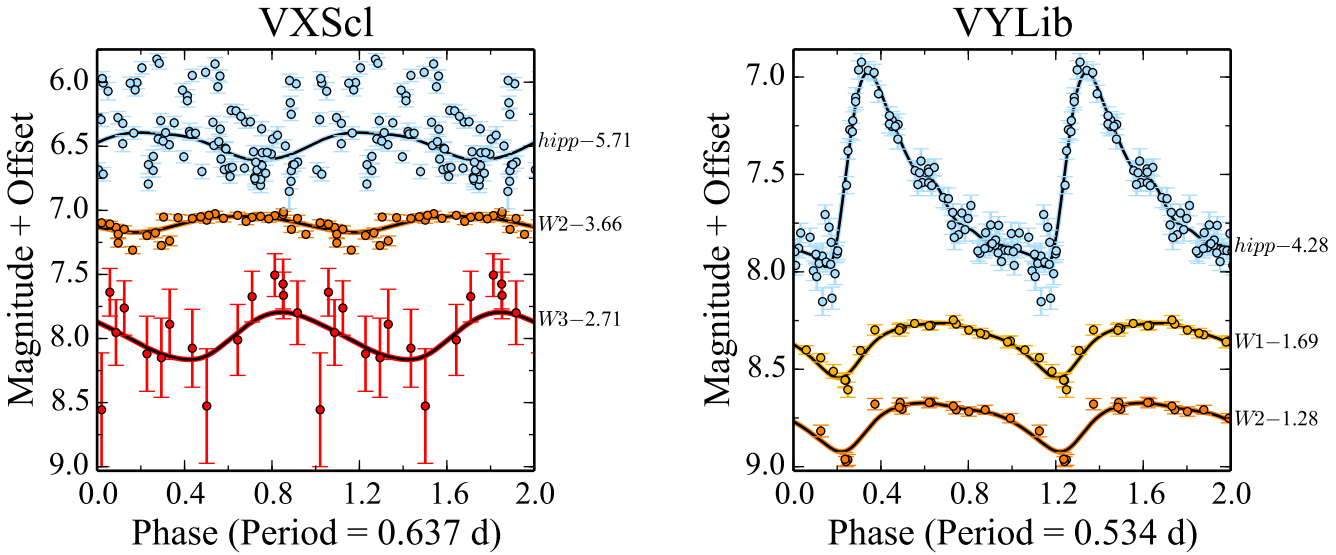

Figure B.58: Observed light curves for VXScl and VYLib.

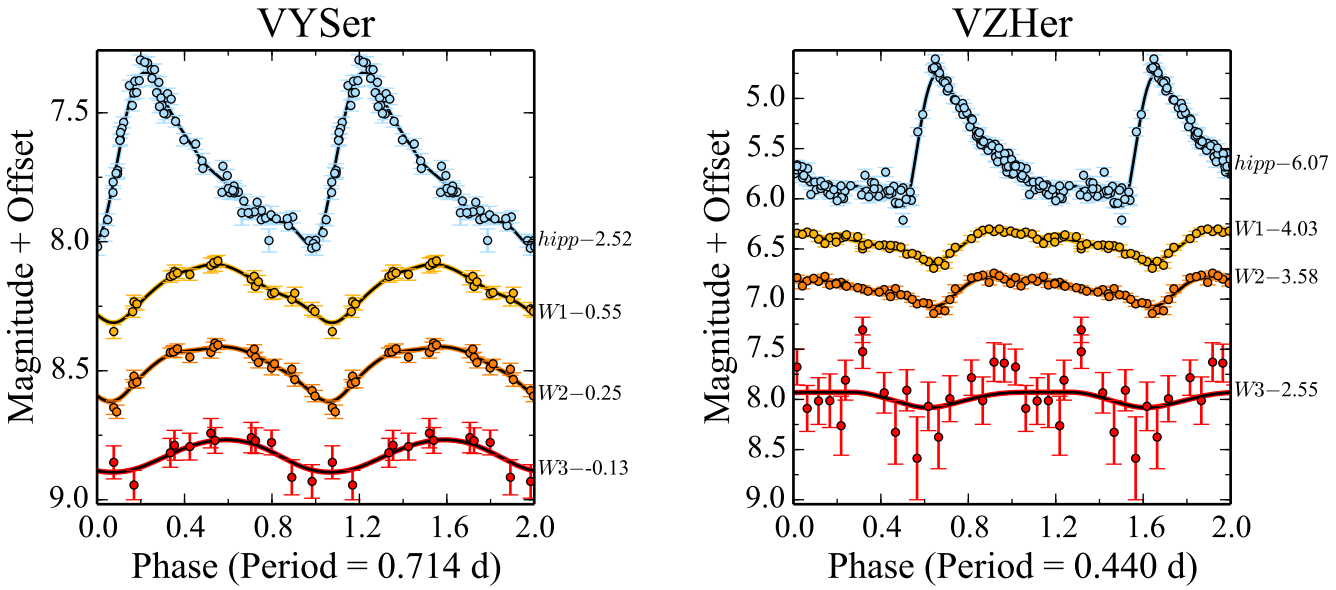

Figure B.59: Observed light curves for VYSer and VZHer.

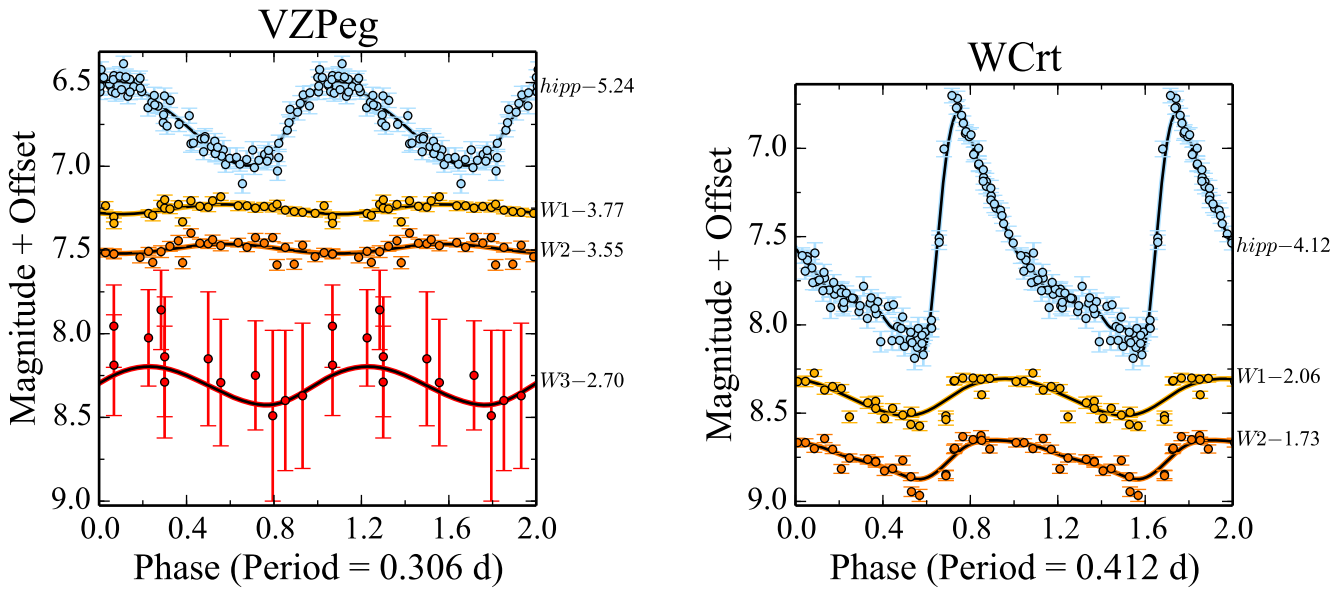

Figure B.60: Observed light curves for VZPeg and WCrt.

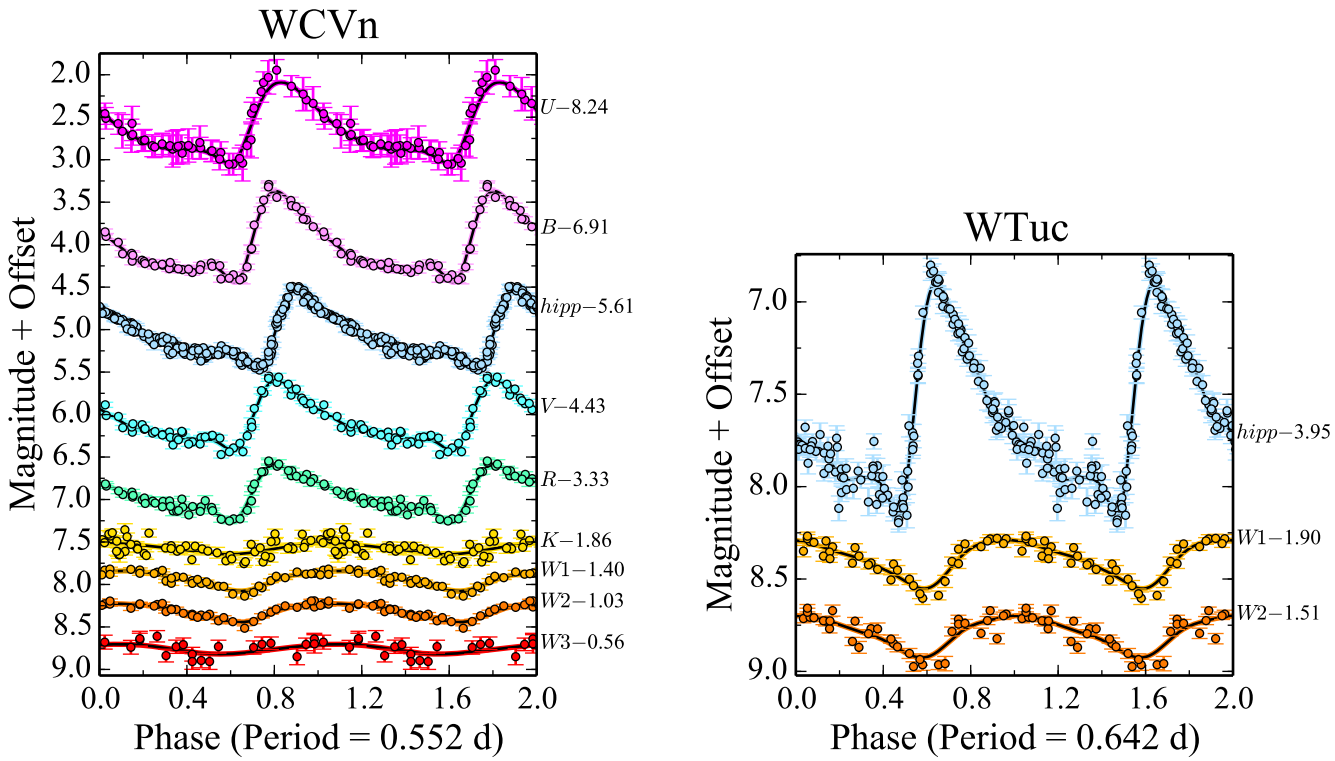

Figure B.61: Observed light curves for WCVn and WTuc.

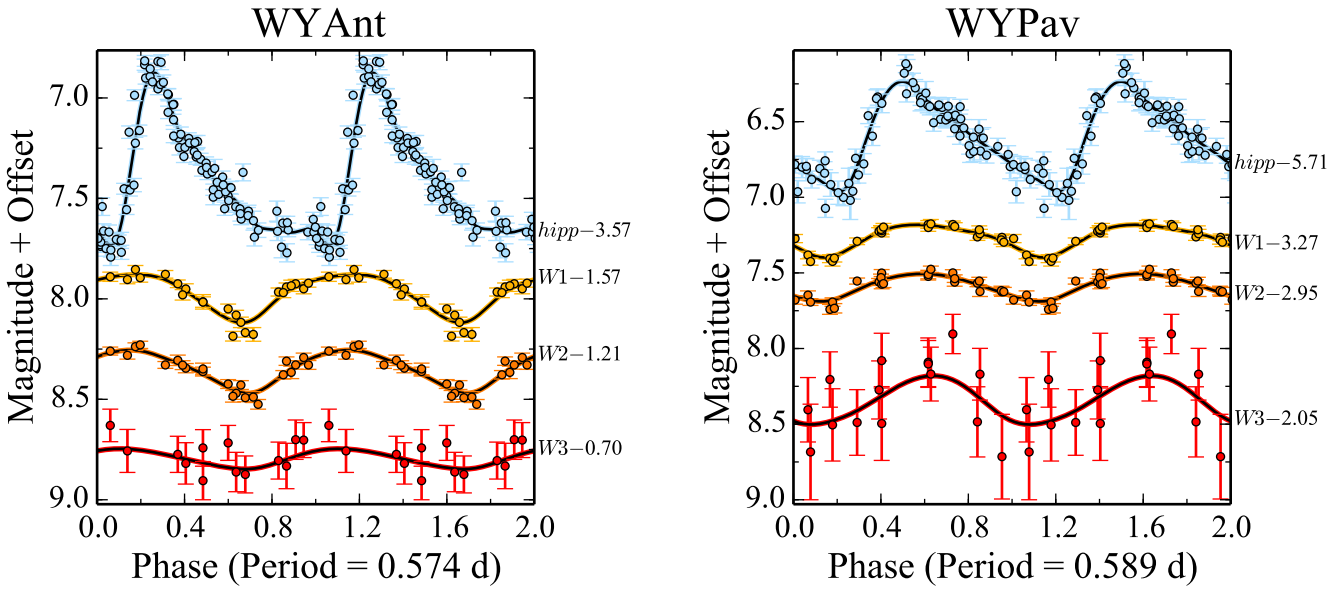

Figure B.62: Observed light curves for WYAnt and WYPav.

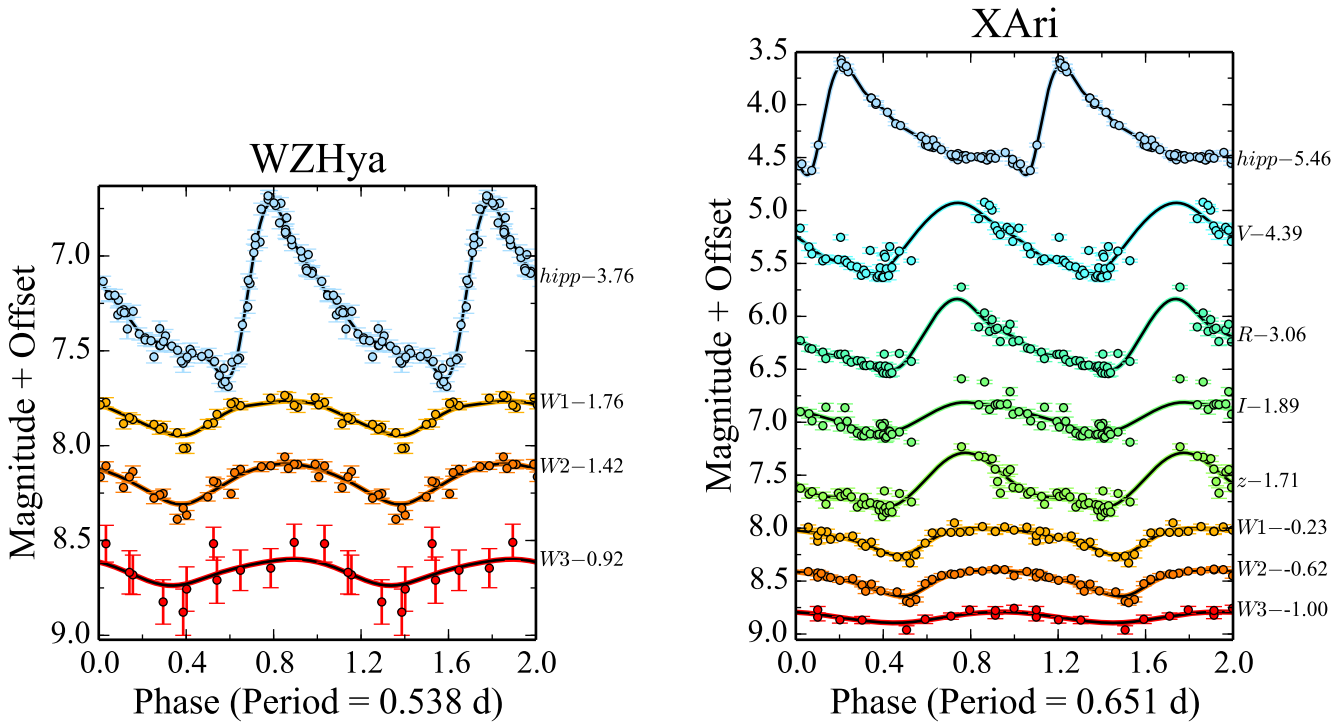

Figure B.63: Observed light curves for WZHya and XAri.

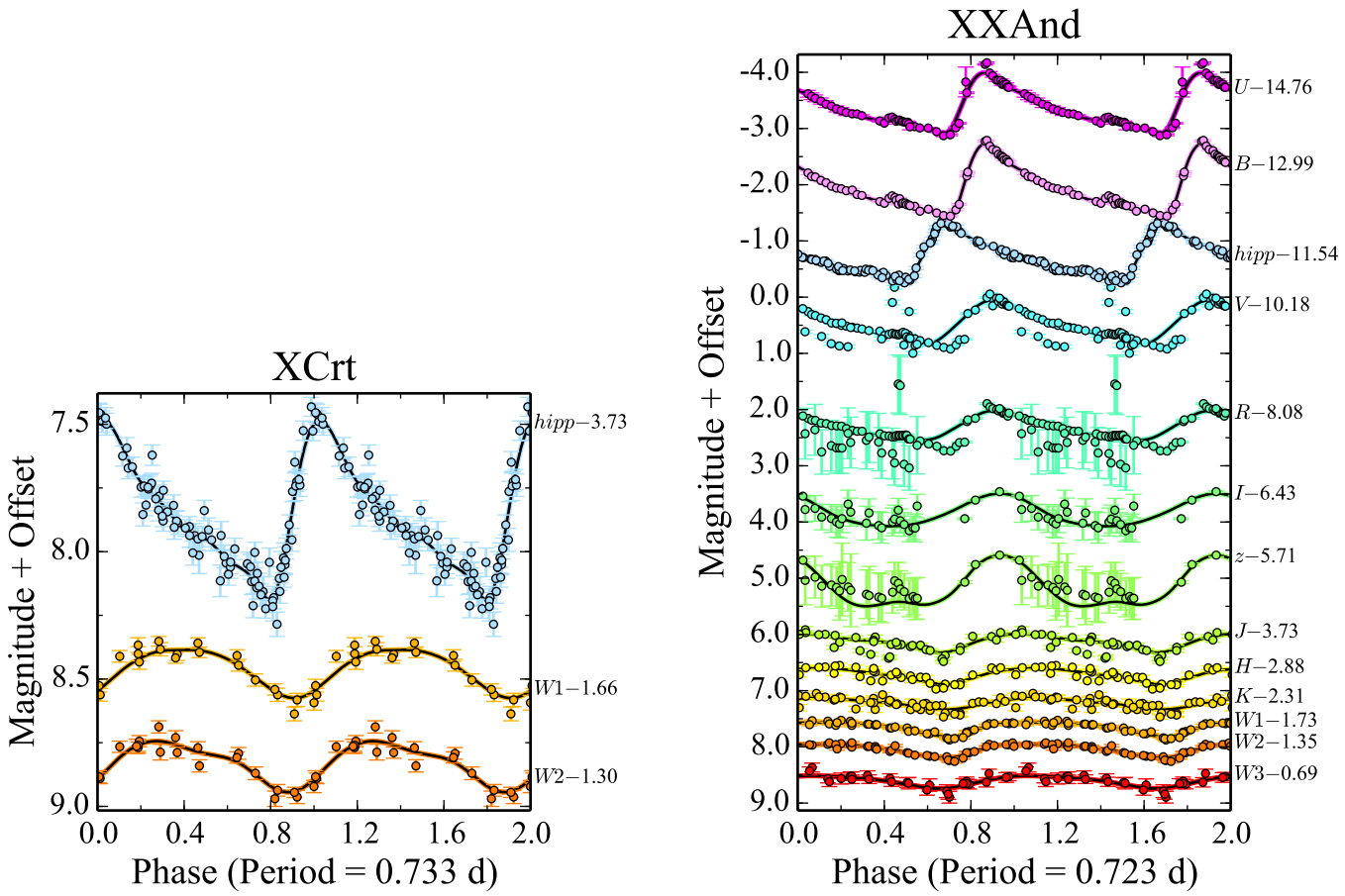

Figure B.64: Observed light curves for XCrt and XXAnd.

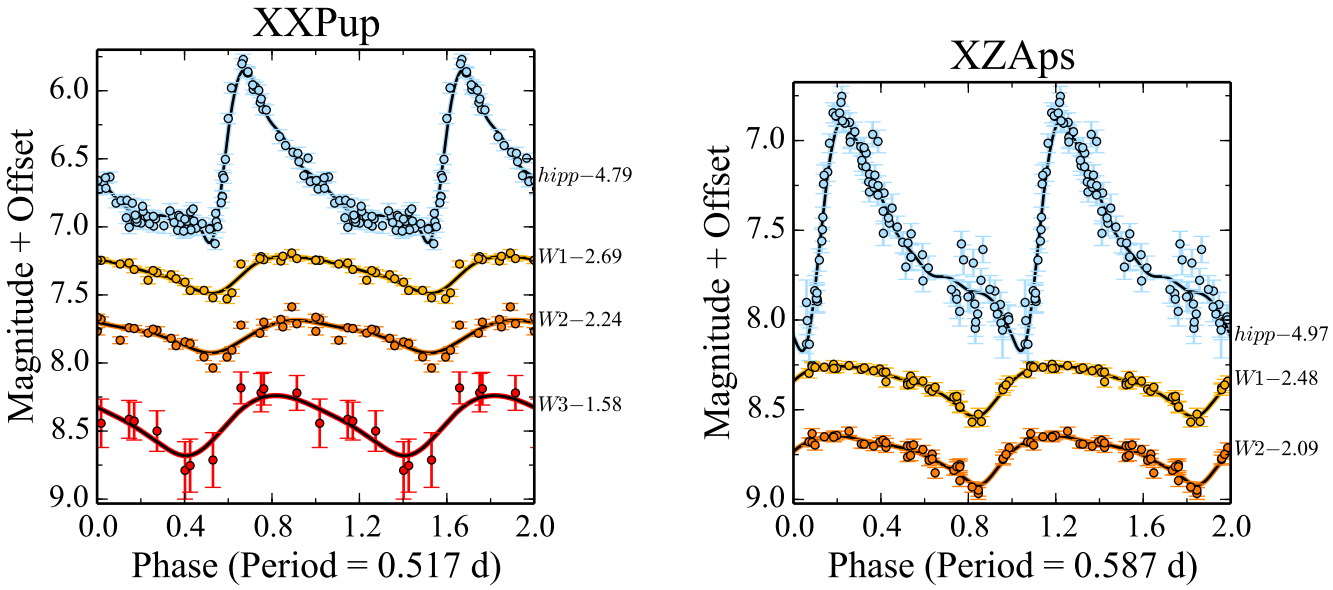

Figure B.65: Observed light curves for XXPup and XZAps.

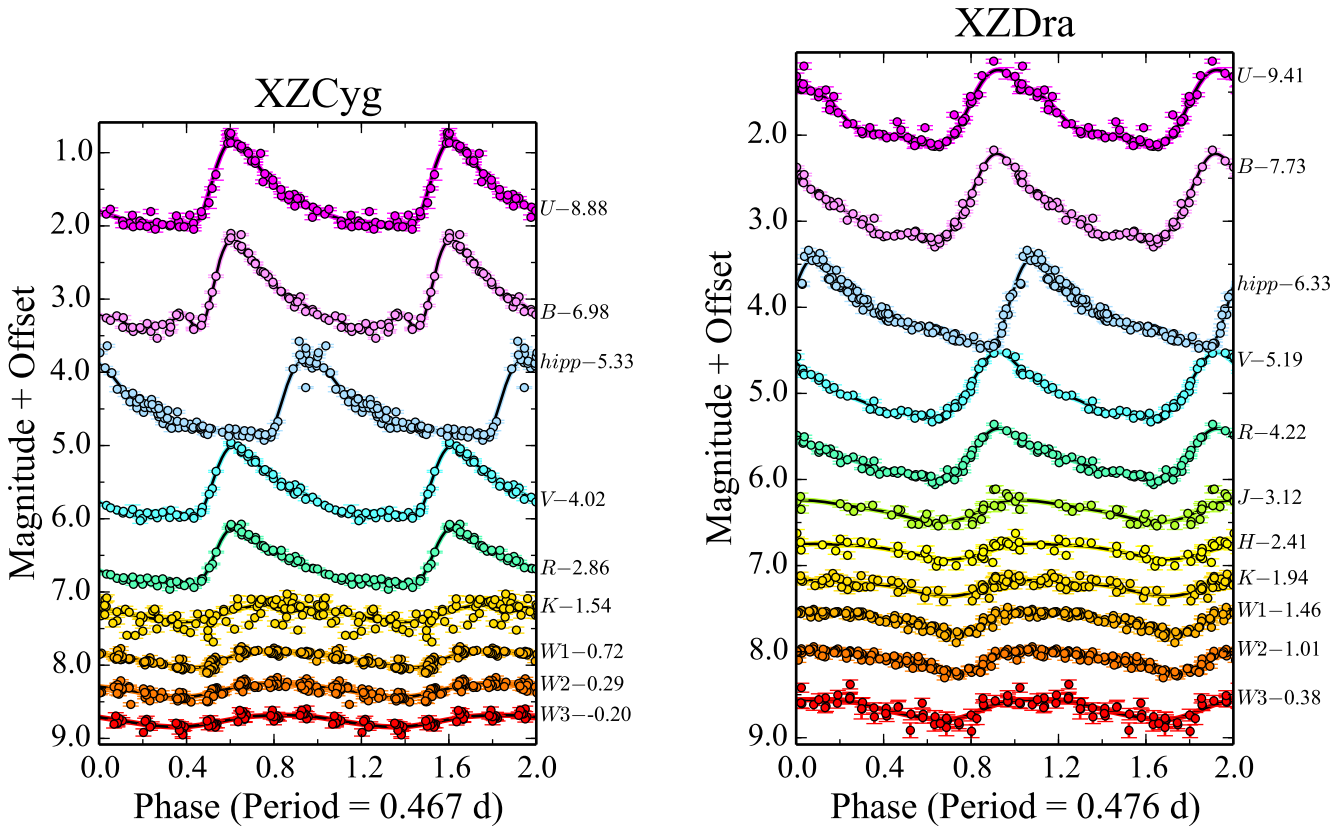

Figure B.66: Observed light curves for XZCyg and XZDra.

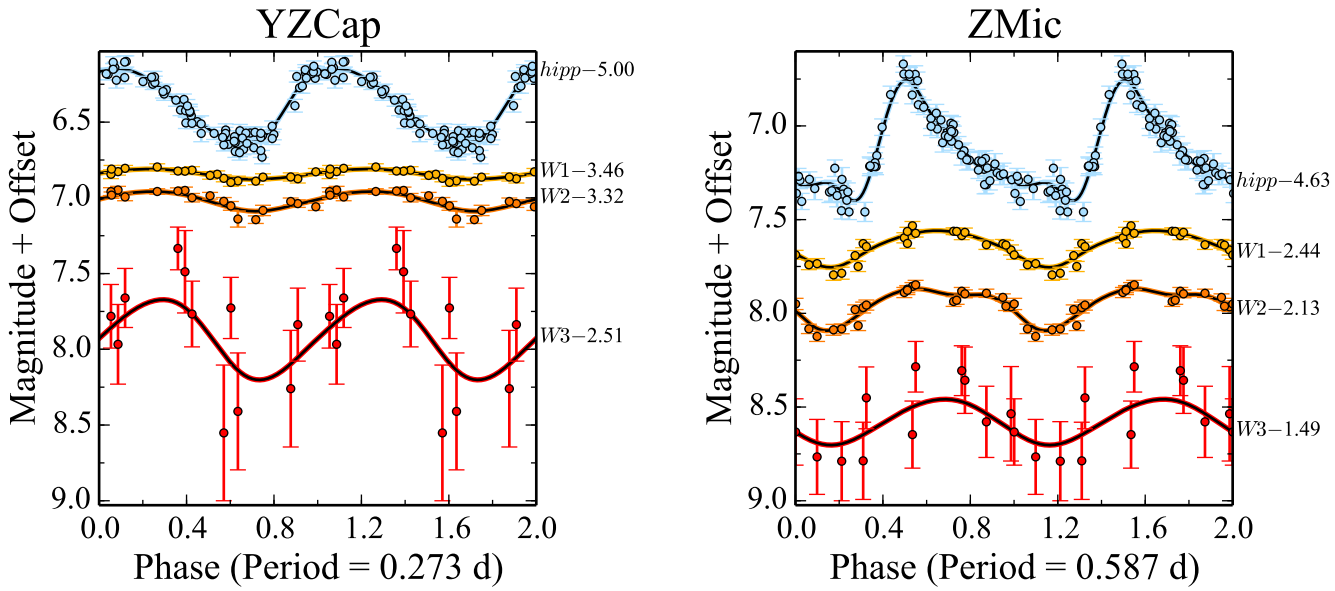

Figure B.67: Observed light curves for YZCap and ZMic.

Bibliography

Alcock, C., Allsman, R. A., Alves, D. R., et al. 1999, AJ, 117, 920

Bailer-Jones, C. A. L. 2011, MNRAS, 411, 435

Barnes, III, T. G., Jefferys, W. H., Berger, J. O., et al. 2003, ApJ, 592, 539

Barning, F. J. M. 1963, Bull. Astron. Inst. Netherlands, 17, 22

Barrett, P. E., & Bridgman, W. T. 1999, in Astronomical Society of the Pacific Conference Series, Vol. 172, Astronomical Data Analysis Software and Systems VIII, ed. D. M. Mehringer, R. L. Plante, & D. A. Roberts, 483

Benedict, G. 2008, in HST Proposal, 11789

Benedict, G. F., McArthur, B. E., Fredrick, L. W., et al. 2002, AJ, 123, 473

Benedict, G. F., McArthur, B. E., Feast, M. W., et al. 2007, AJ, 133, 1810

—. 2011, AJ, 142, 187

Berry, M., Ivezić, Ž., Sesar, B., et al. 2012, ApJ, 757, 166

Bertin, E. 2006, in Astronomical Society of the Pacific Conference Series, Vol. 351, Astronomical Data Analysis Software and Systems XV, ed. C. Gabriel, C. Arviset, D. Ponz, & S. Enrique, 112

Bertin, E. 2011, in Astronomical Society of the Pacific Conference Series, Vol. 442, Astronomical Data Analysis Software and Systems XX, ed. I. N. Evans, A. Accomazzi, D. J. Mink, & A. H. Rots, 435

Bertin, E., & Arnouts, S. 1996, A&AS, 117, 393

Bertin, E., Mellier, Y., Radovich, M., et al. 2002, in Astronomical Society of the Pacific Conference Series, Vol. 281, Astronomical Data Analysis Software and Systems XI, ed. D. A. Bohlender, D. Durand, & T. H. Handley, 228

Bessell, M. S. 2000, PASP, 112, 961

BICEP2 Collaboration, Ade, P. A. R., Aikin, R. W., et al. 2014, ArXiv e-prints, arXiv:1403.3985 [astro-ph.CO]

Bloom, J. S., Starr, D. L., Blake, C. H., Skrutskie, M. F., & Falco, E. E. 2006, in Astronomical Society of the Pacific Conference Series, Vol. 351, Astronomical Data Analysis Software and Systems XV, ed. C. Gabriel, C. Arviset, D. Ponz, & S. Enrique, 751

Bullock, J. S. 2010, ArXiv e-prints, arXiv:1009.4505 [astro-ph.CO]

Butler, N., Klein, C., Fox, O., et al. 2012, in Society of Photo-Optical Instrumentation Engineers (SPIE) Conference Series, Vol. 8446, Ground-based and Airborne Instrumentation for Astronomy IV

Cacciari, C. 2009a, Mem. Soc. Astron. Italiana, 80, 97
Cacciari, C. 2009b, in IAU Symposium, Vol. 258, IAU Symposium, ed. E. E. Mamajek, D. R. Soderblom, & R. F. G. Wyse, 409
Cardelli, J. A., Clayton, G. C., & Mathis, J. S. 1989, ApJ, 345, 245
Catelan, M., Pritzl, B. J., & Smith, H. A. 2004, ApJS, 154, 633
Chaboyer, B. 1999, Post-Hipparcos Cosmic Candles, ed. A. Heck & F. Caputo, 1 No. 111 (Dordrecht: Kluwer)
Clark, S., & Quartz, E. J. R. 2012, ESA Brochure, BR-269, 1
Dall'Ora, M., Storm, J., Bono, G., et al. 2004, ApJ, 610, 269
Dambis, A. K., Rastorguev, A. S., & Zabolotskikh, M. V. 2014, MNRAS, 439, 3765
de Bruijne, J. H. J. 2012, Ap&SS, 341, 31
de Grijs, R., Wicker, J. E., & Bono, G. 2014, AJ, 147, 122
Deb, S., & Singh, H. P. 2014, MNRAS, 438, 2440
Dorn, R. J., Eschbaumer, S., Hall, D. N. B., et al. 2008, in Society of Photo-Optical Instrumentation Engineers (SPIE) Conference Series, Vol. 7021, High Energy, Optical, and Infrared Detectors for Astronomy III
Eyer, L., Palaversa, L., Mowlavi, N., et al. 2012, Ap&SS, 49
Farah, A., González, J. J., Kutyrev, A. S., et al. 2012, in Society of Photo-Optical Instrumentation Engineers (SPIE) Conference Series, Vol. 8446, Ground-based and Airborne Instrumentation for Astronomy IV
Feast, M. W., & Catchpole, R. M. 1997, MNRAS, 286, L1
Feast, M. W., Laney, C. D., Kinman, T. D., van Leeuwen, F., & Whitelock, P. A. 2008, MNRAS, 386, 2115
Fernley, J., Barnes, T. G., Skillen, I., et al. 1998, A&A, 330, 515
Flaugher, B. L., Abbott, T. M. C., Angstadt, R., et al. 2012, in Society of Photo-Optical Instrumentation Engineers (SPIE) Conference Series, Vol. 8446, Society of Photo-Optical Instrumentation Engineers (SPIE) Conference Series
Fox, O. D., Kutyrev, A. S., Rapchun, D. A., et al. 2012, in Society of Photo-Optical Instrumentation Engineers (SPIE) Conference Series, Vol. 8453, High Energy Optical and Infrared Detectors for Astronomy V
Freedman, W. L., Madore, B. F., Rigby, J., Persson, S. E., & Sturch, L. 2008, ApJ, 679, 71
Freedman, W. L., Madore, B. F., Scowcroft, V., et al. 2012, ApJ, 758, 24
Freedman, W. L., Madore, B. F., Gibson, B. K., et al. 2001, ApJ, 553, 47
Fritz, T. K., Gillessen, S., Dodds-Eden, K., et al. 2011, ApJ, 737, 73
Gavrilchenko, T., Klein, C. R., Bloom, J. S., & Richards, J. W. 2013, arXiv:1312.4643 [astro-ph.SR], arXiv/1312.4643
Gelman, A., Carlin, J., Stern, H., & Rubin, D. 2003, Bayesian Data Analysis, Second Edition, 2 edn. (Chapman and Hall/CRC)
Gelman, A., & Rubin, D. B. 1992, Statistical Science, 7, 457
Glass, I. S., & Evans, T. L. 2003, MNRAS, 343, 67
Gould, A., & Popowski, P. 1998, ApJ, 508, 844
Green, G. M., Schlafly, E. F., Finkbeiner, D. P., et al. 2014, ApJ, 783, 114

Hanson, R. J., & Bailer-Jones, C. A. L. 2014, MNRAS, 438, 2938
Haschke, R., Grebel, E. K., & Duffau, S. 2011, AJ, 141, 158
—. 2012, AJ, 144, 106
Hastie, T., Tibshirani, R., & Friedman, J. 2009, The Elements of Statistical Learning: Data Mining, Inference, and Prediction, 2 edn., Springer Series in Statistics (Springer)
Hawley, S. L., Jefferys, W. H., Barnes, III, T. G., & Lai, W. 1986, ApJ, 302, 626
Herschel, W. 1785, Royal Society of London Philosophical Transactions Series I, 75, 213
Ichikawa, K., & Takahashi, T. 2008, J. Cosmology Astropart. Phys., 4, 27
Ivezić, Ž., Smith, J. A., Miknaitis, G., et al. 2007, AJ, 134, 973
Johnson, H. L. 1968, Interstellar Extinction, ed. B. M. Middlehurst & L. H. Aller (the University of Chicago Press), 167
Klein, C. R., & Bloom, J. S. 2014, ArXiv e-prints, arXiv:1404.4870 [astro-ph.SR]
Klein, C. R., Cenko, S. B., Miller, A. A., Norman, D. J., & Bloom, J. S. 2014a, ArXiv e-prints, arXiv:1405.1035 [astro-ph.IM]
Klein, C. R., Richards, J. W., Butler, N. R., & Bloom, J. S. 2011, ApJ, 738, 185
—. 2012a, Ap&SS, 341, 83
—. 2014b, MNRAS, 440, L96
Klein, C. R., Kubánek, P., Butler, N. R., et al. 2012b, in Society of Photo-Optical Instrumentation Engineers (SPIE) Conference Series, Vol. 8453, High Energy, Optical, and Infrared Detectors for Astronomy V
Kubánek, P. 2010, Advances in Astronomy, 2010, arXiv:1005.1014 [astro-ph.IM]
Kubánek, P., Jelínek, M., Vítek, S., et al. 2006, in Society of Photo-Optical Instrumentation Engineers (SPIE) Conference Series, Vol. 6274, Advanced Software and Control for Astronomy
Kubánek, P., Jelínek, M., Nekola, M., et al. 2004, in American Institute of Physics Conference Series, Vol. 727, Gamma-Ray Bursts: 30 Years of Discovery, ed. E. Fenimore & M. Galassi, 753
Landolt, A. U. 1992, AJ, 104, 340
—. 2009, AJ, 137, 4186
Lang, D., Hogg, D. W., Mierle, K., Blanton, M., & Roweis, S. 2010, AJ, 139, 1782
Liu, T., & Janes, K. A. 1990, ApJ, 354, 273
Łokas, E. L., Gajda, G., & Kazantzidis, S. 2013, MNRAS, 433, 878
Lomb, N. R. 1976, Ap&SS, 39, 447
Longmore, A. J., Fernley, J. A., & Jameson, R. F. 1986, MNRAS, 220, 279
Loose, M., Lewyn, L., Durmus, H., et al. 2003, in Society of Photo-Optical Instrumentation Engineers (SPIE) Conference Series, Vol. 4841, Instrument Design and Performance for Optical/Infrared Ground-based Telescopes, ed. M. Iye & A. F. M. Moorwood, 782
Loose, M., Beletic, J., Blackwell, J., et al. 2005, in Society of Photo-Optical Instrumentation Engineers (SPIE) Conference Series, Vol. 5904, Cryogenic Optical Systems and Instruments XI, ed. J. B. Heaney & L. G. Burriesci, 293
LSST Science Collaboration, Abell, P. A., Allison, J., et al. 2009, ArXiv e-prints, arXiv:0912.0201 [astro-ph.IM]

Madore, B. F., & Freedman, W. L. 1998, in Stellar astrophysics for the local group: VIII Canary Islands Winter School of Astrophysics, ed. A. Aparicio, A. Herrero, & F. Sánchez, 263
Madore, B. F., Freedman, W. L., Rigby, J., et al. 2009, ApJ, 695, 988
Madore, B. F., Hoffman, D., Freedman, W. L., et al. 2013, ApJ, 776, 135
Maintz, G., & de Boer, K. S. 2005, A&A, 442, 229
Mainzer, A., Bauer, J., Grav, T., et al. 2011, ApJ, 731, 53
Marengo, M., Evans, N. R., Barmby, P., et al. 2010, ApJ, 709, 120
Mateo, M. L. 1998, ARA&A, 36, 435
Matsunaga, N., Fukushi, H., Nakada, Y., et al. 2006, MNRAS, 370, 1979
Meixner, M., Gordon, K. D., Indebetouw, R., et al. 2006, AJ, 132, 2268
Ofek, E. O., Laher, R., Law, N., et al. 2012, PASP, 124, 62
Patil, A., Huard, D., & Fonnesbeck, C. J. 2010, Journal of Statistical Software, 35, 1
Perryman, M. A. C., & ESA, eds. 1997, ESA Special Publication, Vol. 1200, The HIPPARCOS and TYCHO catalogues. Astrometric and photometric star catalogues derived from the ESA HIPPARCOS Space Astrometry Mission
Pietrzyński, G., Graczyk, D., Gieren, W., et al. 2013, Nature, 495, 76
Planck Collaboration, Ade, P. A. R., Aghanim, N., et al. 2013, arXiv:1303.5076 [astro-ph.CO], arXiv/1303.5076
Preston, G. W. 1964, ARA&A, 2, 23
Richards, J. W., Starr, D. L., Butler, N. R., et al. 2011, ApJ, 733, 10
Rieke, G. H., & Lebofsky, M. J. 1985, ApJ, 288, 618
Riess, A. G., Macri, L., Casertano, S., et al. 2011, ApJ, 730, 119
Sale, S. E. 2012, MNRAS, 427, 2119
Sandage, A., & Tammann, G. A. 2006, ARA&A, 44, 93
Scargle, J. D. 1982, ApJ, 263, 835
Schaefer, B. E. 2008, AJ, 135, 112
Schlafly, E. F., & Finkbeiner, D. P. 2011, ApJ, 737, 103
Schlegel, D. J., Finkbeiner, D. P., & Davis, M. 1998, ApJ, 500, 525
Schultz, G. V., & Wiemer, W. 1975, A&A, 43, 133
Sesar, B., Ivezić, Ž., Grammer, S. H., et al. 2010, ApJ, 708, 717
Skrutskie, M. F., Cutri, R. M., Stiening, R., et al. 2006, AJ, 131, 1163
Smith, H. A. 1995, Cambridge Astrophysics Series, 27
Smith, J. A., Tucker, D. L., Kent, S., et al. 2002, AJ, 123, 2121
Sollima, A., Cacciari, C., & Valenti, E. 2006, MNRAS, 372, 1675
Soszyński, I., Udalski, A., Szymañski, M. K., et al. 2010a, Acta Astron., 60, 165
Soszyński, I., Poleski, R., Udalski, A., et al. 2008, Acta Astron., 58, 163
Soszyński, I., Udalski, A., Szymański, M. K., et al. 2009, Acta Astron., 59, 1
Soszyński, I., Poleski, R., Udalski, A., et al. 2010b, Acta Astron., 60, 17
Spergel, D., Flauger, R., & Hlozek, R. 2013a, ArXiv e-prints, arXiv:1312.3313 [astro-ph.CO]
Spergel, D., Gehrels, N., Breckinridge, J., et al. 2013b, ArXiv e-prints, arXiv:1305.5425 [astro-ph.IM]

—. 2013c, ArXiv e-prints, arXiv:1305.5422 [astro-ph.IM]
Tucker, D. L., Allam, S. S., Annis, J. T., et al. 2014, in American Astronomical Society Meeting Abstracts, Vol. 223, #254.11
Udalski, A., Szymanski, M. K., Soszynski, I., & Poleski, R. 2008a, Acta Astron., 58, 69
Udalski, A., Soszynski, I., Szymanski, M. K., et al. 2008b, Acta Astron., 58, 89
van Leeuwen, F., ed. 2007, Astrophysics and Space Science Library, Vol. 350, Hipparcos, the New Reduction of the Raw Data
Vivas, A. K., Zinn, R., Andrews, P., et al. 2001, ApJ, 554, L33
Wagner-Kaiser, R., & Sarajedini, A. 2013, MNRAS, 431, 1565
Watson, A. M., Richer, M. G., Bloom, J. S., et al. 2012, in Society of Photo-Optical Instrumentation Engineers (SPIE) Conference Series, Vol. 8444, Ground-based and Airborne Telescopes IV
Webb, S. 1999, Measuring the Universe
Wester, W., & Dark Energy Survey Collaboration. 2005, in Astronomical Society of the Pacific Conference Series, Vol. 339, Observing Dark Energy, ed. S. C. Wolff & T. R. Lauer, 152
Whitelock, P. A., Feast, M. W., & van Leeuwen, F. 2008, MNRAS, 386, 313
Wright, E. L., Eisenhardt, P. R. M., Mainzer, A. K., et al. 2010, AJ, 140, 1868